Engineering nanobody fusion proteins for nanoparticle stabilisation and application in biosensing

John-Paul Ayrton

January 2025

A dissertation submitted in partial fulfilment
of the requirements for the degree of
Doctor of Philosophy
of
University College London

Department of Biochemical Engineering and London Centre for Nanotechnology
University College London

Declaration

I, John-Paul Ayrton, confirm that the work presented in this thesis is my own. Where information has been derived from other sources, I confirm that this has been indicated in the work.

Abstract

The development of point-of-care diagnostics, crucial for containing infectious diseases, is often hindered by the time-consuming search for suitable antibody pairs. Nanobodies, with their facile production and design flexibility, present a promising alternative for lateral flow assays (LFAs). This work explores protein engineering strategies to optimise nanobodies for these applications, enhancing their stability and functionality upon integration into LFAs

A key challenge addressed in this thesis is the inherent instability of nanobody-gold nanoparticle bioconjugates formed through physisorption. This instability, particularly relevant in the context of nanoparticle functionalisation, poses a significant hurdle in LFA development, where bioconjugates must withstand harsh processing steps like drying and exposure to complex biological samples. A trivalent nanobody is developed through innovative protein engineering that demonstrates efficient and stable bioconjugation through physisorption. Compared to its monovalent and divalent counterparts, these engineered bioconjugates exhibit enhanced stability, retaining picomolar sensitivity to the target antigen and withstanding storage processes like freeze-drying, making them ideal candidates for real-world diagnostic applications.

Current LFA manufacturing and deployment can be subject to manufacturing bottlenecks and disruptions in supply chains, especially during global emergencies. This vulnerability underscores the need for robust and adaptable diagnostics. Leveraging the versatility of nanobodies, a modular display LFA based on in vivo biotinylation is also established. Nanoparticle and nitrocellulose functionalisation with streptavidin enables the simultaneous display of biotinylated nanobodies on the nanoparticle and test line. The system's design is validated through mechanistic mathematical modelling. The "plug-and-play" integration of nanobodies into prefabricated cassettes promises to accelerate LFA development significantly. This modular approach, coupled with rapid nanobody development and the

exceptional streptavidin-biotin interaction, would be less affected by manufacturing bottlenecks and supply chain disruptions. This could enable a quicker response to infectious diseases, leading to improved patient outcomes and more effective disease control.

Impact statement

This thesis addresses the development, manufacturing, and deployment bottlenecks of lateral flow assays (LFA) by integrating nanobodies as biorecognition elements and developing versatile LFAs. This thesis is expected to contribute to the following sectors:

Impact on public health and diagnostics

A key benefit of using nanobodies over traditional antibodies is the potential for accelerated development of LFAs. Nanobodies offer straightforward development and cost-effective production, promising a quicker response to emerging infectious threats. This thesis successfully addresses a critical challenge hindering the use of nanobodies in LFAs: the instability of nanobody-gold nanoparticle bioconjugates prepared through physisorption. By employing protein engineering strategies, this instability has been overcome, enabling the integration of nanobodies into LFAs. Furthermore, developing a universal "plug-and-play" LFA can significantly reduce the time and resources required to create new diagnostic assays. Rapid LFA development and deployment for new disease threats enhances global pandemic preparedness. By enabling early and accurate detection of infections, this research contributes to more effective control and management of outbreaks, minimising their impact on public health and the global economy.

Enhanced access to diagnostics is crucial for combating communicable diseases, disproportionately affecting low-income countries with limited access to life-saving diagnostic tools. This research contributes to increased accessibility by aiming to reduce LFA development costs through simplified optimisation processes and the use of cost-effective biorecognition molecules like nanobodies. These reductions in development costs can translate to lower end-user prices, making LFAs more affordable and accessible in resource-limited settings. Additionally, the development of universal LFA cassettes enables their distribution and storage in high-risk areas for rapid deployment when needed. Furthermore, the ease of nanobody production facilitates a decentralised production model, empowering research groups, diagnostic companies, and even local manufacturers in resource-limited settings to produce their own nanobody-based diagnostic tools. This would foster a globally accessible and responsive diagnostic ecosystem, contributing to health equity and improved disease control in underserved populations.

Environmental impact

Universal LFAs offer a more sustainable alternative to traditional, disease-specific LFAs. Their adaptability to various targets through interchangeable biorecognition pairs allows for repurposing and utilising stockpiled tests, minimising expiration and waste. This versatility reduces the environmental impact compared to specific LFAs, which risk becoming obsolete and discarded if demand for their designated purpose decreases.

Impact on industry

The universal LFA platform and engineered nanobodies offer new opportunities for diagnostic companies to develop and commercialise innovative and adaptable point-of-care tests. This can lead to the growth of the diagnostics industry and create new economic opportunities.

Impact on nanobiotechnology

This work contributes to a deeper understanding of protein-nanoparticle interactions and the stabilisation of bioconjugates. This knowledge can be applied to various applications beyond diagnostics, including drug delivery, biosensing, and imaging. The development of engineered nanobodies and modular display systems provides valuable tools for researchers in various fields. These tools can be used to create new bioconjugates and assays for diverse applications, fostering innovation in biotechnology and related disciplines.

Publications

Ayrton, J. P., Ho, C., Zhang, H., Chudasama, V., Frank, S., & Thomas, M. R. (2024). Multivalent nanobody engineering for enhanced physisorption and functional display on gold nanoparticles. *Nanoscale*, *16*(42), 19881-19896.

Ho, C., McMahon, C., **Ayrton, J. P.**, Chudasama, V., & Thomas, M. R. Triggered ‘capture-and-release’ enables a high-affinity re-binding strategy for sensitivity enhancement in lateral flow assays. *ACS Nano* **(In peer-review)**

Conference presentations

34th Anniversary World Congress on Biosensors, Busan, South Korea (2023). “Improving and characterising paratope display of nanobodies on gold nanoparticles”

RSC Analytical Biosciences group Early Career Researcher Meeting (2022). “Engineering Affinity Reagent Presentation on Rapid Tests”

Keynote presentation RSC Analytical Biosciences Group Annual General Meeting (2022). “Engineering Affinity Reagent Presentation on Rapid Tests”– Invited speaker

Acknowledgements

I would like to express my deepest gratitude to my advisor, Michal Thomas. I feel incredibly proud to have been one of the first members of the Thomas lab. I am deeply grateful for the welcoming, encouraging, and intellectually stimulating environment he fostered within the group and for his scientific and moral support. His exceptional mentorship and commitment to excellence over the past four years have profoundly shaped my approach to research.

To my secondary supervisor, Stefanie Frank, I am deeply grateful for our many insightful discussions, her encouragement and support, and for introducing me to the fascinating world of synthetic biology. Her expert guidance has been invaluable to the success of this project.

To my buddies from the LCN, Chapman and Alyssa, you have fostered what would have otherwise been a bearable experience into an enjoyable one. Our conversations and shared experiences, academic and beyond, will always hold a special place in my memory.

I would also like to thank Dr. Ben Miller for the training in lateral flow assay fabrication and discussions in mathematical modelling.

Thank you to all the project students who contributed to the Thomas lab's work. Your work is highly valued and has contributed to our group's research excellence. Special gratitude to Andrew, who joined the lab at a pivotal point in my research and has helped with the design, expression, and characterisation of many protein constructs that have shaped this thesis.

I would like to express my deepest gratitude to my partner, Katerina. Your emotional and intellectual support has been fundamental these last four years. Thank you for all the proofreading, the presentation practices and the mathematical discussions.

Finally, I would like to thank my mother, Nasy, grandmother Soula, and sisters Katerina and Alexandra. Thank you for motivating me to keep going more times than I can count. None of this would have been possible without you.

Table of contents

Table of figures

List of abbreviations

AuNP	Gold nanoparticles
BLI	Bio-layer interferometry
BSA	Bovine serum albumin
BirA	Biotin protein ligase
CDRs	Complementarity-determining regions
CI	Confidence interval
CD	Circular dichroism
DH	Hydrodynamic diameter
DLS	Dynamic light scattering
DoE	Design of experiment
DTSSP	3,3'-Dithiobis(sulfosuccinimidylpropionate)
EDC	1-Ethyl-3-(3-dimethylaminopropyl) carbodiimide
ELISA	Enzyme-linked immunosorbent assay
Fab	Fragment antigen binding
Fc	Crystallisable fragment
Fv	Fragment variable
GST	Glutathione-S-transferase
HIV	Human immunodeficiency virus
HRP	Horseradish peroxidase
IC50	Half-maximal inhibitory concentration
IEP	Isoelectric Point
IPTG	Isopropyl β-D-1-thiogalactopyranoside
λSPR	Surface plasmon resonance wavelength
LC-MS	Liquid chromatography-mass spectrometry
LoD	Limit of detection
LFA	Lateral flow assay
LSPR	Localized surface plasmon resonance
mAb	Monoclonal antibodies
MWCO	Molecular weight cut-off

NAAT	Nucleic acid amplification test
NMM	N-methylmaleimide, a thiol-reactive reagent
NMR	Nuclear magnetic resonance
NHS	N-hydroxysuccinimide
NHS-PEG12-Biotin	N-hydroxysuccinimide polyethylene glycol-12 biotin
Ni-NTA	Nickel-nitrilotriacetic acid
OD	Optical density
PBS	Phosphate-buffered saline
PDB	Protein data bank
PoC	Point-of-care
PCR	Polymerase chain reaction
PSA	Poly streptavidin
RBD	Receptor binding domain
RBS	Ribosome binding site
SA	Streptavidin
SARS-CoV-2	Severe acute respiratory syndrome coronavirus 2
scFv	Single-chain variable fragment
SDS-PAGE electrophoresis	Sodium dodecyl sulfate-polyacrylamide gel
sdAb	Single-domain antibody
SNR	Signal-to-noise ratio
SPR	Surface plasmon resonance
TCEP-HCl	Tris(2-carboxyethyl)phosphine Hydrochloride
TEM	Transmission electron microscopy
TL	Test line
tRNA	Transfer RNA
UV-Vis	Ultraviolet-visible spectroscopy
VHH	Variable domain of heavy-chain only antibodies
WHO	World Health Organization

1 Introduction

1.1 Disease diagnosis

Communicable diseases have always posed a challenge to global health, but the severe acute respiratory syndrome coronavirus 2 (SARS-CoV-2) pandemic underscored the critical need for the quick availability of rapid and accessible point-of-care (PoC) diagnostics. The accurate and robust diagnosis of infectious diseases, including COVID-19, is paramount in ensuring effective treatment and interruption of the chain of transmission to mitigate the spread of pathogens, minimising the enormous socioeconomic burden caused by the disease.[1] This is particularly important in low-income countries as well as communities facing complex emergencies, which are disproportionately affected by communicable diseases and have unequal access to medical tools.[2,3] A 2021 WHO report highlighted this stark disparity, revealing that 8 out of the 10 leading causes of death in these populations were communicable diseases. In contrast, only 2 out of the 10 leading causes of death in high-income countries were attributed to such diseases. As a result, individuals in low-income countries are far more likely to die from a communicable disease.[4]

Clinical specimens, such as saliva and blood, contain a wealth of molecular information indicative of infection. These biofluids may contain the fragments of the pathogen itself (antigens), its genetic material (RNA in the case of SARS-CoV-2), or evidence of the host's immune response, such as pathogen-specific antibodies or inflammatory cytokines.[5] The detection of these biomarkers necessitates highly sensitive and specific diagnostic assays. Molecular tools such as nucleic acid amplification (NAAT), including polymerase chain reaction (PCR) and biochemical assays such as enzyme-linked immunosorbent assays (ELISA) are often the gold standard tools for the detection of communicable diseases.[6,7] However, these tools typically require centralised testing in controlled laboratory environments with trained personnel and complex infrastructure. Combined, these requirements make these diagnostic tools too costly, lengthy and complex to implement in low-income countries, limiting their throughput for deployment at the scales required during global crises.[8] The WHO has published a set of criteria that would make diagnostic tests available at all levels of healthcare in developing countries. The criteria state that a test must be affordable, sensitive, specific, user-friendly, rapid and robust, equipment-free, and deliverable to end users. These criteria have received the acronym ASSURED.[9] This has since been extended to include two extra criteria: real-time connectivity to adapt to the rapid advancements in digital technology and ease of specimen collection, making the new acronym REASSURED.[10]

Over the last 20 years, since these criteria were published, various diagnostic platforms have been developed to fulfil these requirements and enable reliable PoC diagnosis. Among these advancements, paper-based analytical devices, particularly lateral flow assays (LFAs), have emerged as prominent tools, notably demonstrated by their widespread use during the SARS-CoV-2 pandemic.[8] While antigen LFAs may exhibit lower sensitivity compared to gold-standard NAATs or biochemical assays, their simplicity, affordability, and ease of use make them invaluable in resource-constrained environments and emergencies. These qualities enabled their rapid deployment at an unprecedented scale during the COVID-19 pandemic, facilitating testing in communities with limited laboratory infrastructure. LFAs enable self-testing in decentralised settings such as homes, schools, and remote locations, which has significantly expanded access to diagnosis and enabled more effective disease detection and management of spread.[11]

1.2 Biorecognition in immunoassays

LFAs have become indispensable tools for rapid diagnostics, extending far beyond the realm of infectious disease detection. Their applications span diverse fields, including non-communicable disease diagnostics, forensic science, environmental monitoring, and food safety analysis.[12] LFAs demonstrate remarkable versatility in detecting a wide range of biomarkers, from large macromolecules like antibodies and antigens to nucleic acids and small molecules such as food contaminants and illicit drugs.[11,13–15]

The success of any PoC test, including LFAs, relies on the effective biorecognition of the target biomarker. This is achieved through the use of affinity macromolecules, such as antibodies or aptamers, which bind specifically to the target and initiate a detectable signal. In the context of protein detection (e.g. antigens and antibodies), LFAs commonly employ a sandwich immunoassay format.[8] This involves two distinct affinity macromolecules that simultaneously capture the target analyte. One of these is immobilised on the nitrocellulose membrane (capture bioreceptor) at the test line, while the other is conjugated to a detection nanoparticle (detection bioreceptor).[16]

LFAs are designed to be very simple and straightforward to operate and interpret. The test is performed with the user applying a sample at a designated space on the LFA cassette. Within a few minutes, the test result is developed, which can be read by eye depending on the appearance of a test line, indicating a positive test.

In its more common form, LFA consists of several porous pads attached to a laminated card. These pads consist of the sample pad, the conjugate pad, the test membrane and the absorbent pad.[5] A schematic representation of a LFA and its components is shown in Figure 1.1. Upon sample application to the sample pad, capillary action draws the sample to the conjugate pad. Here, the sample rehydrates the dried bioconjugate label decorated with the detection bioreceptor. The detection bioreceptor binds to the analyte in the sample. The

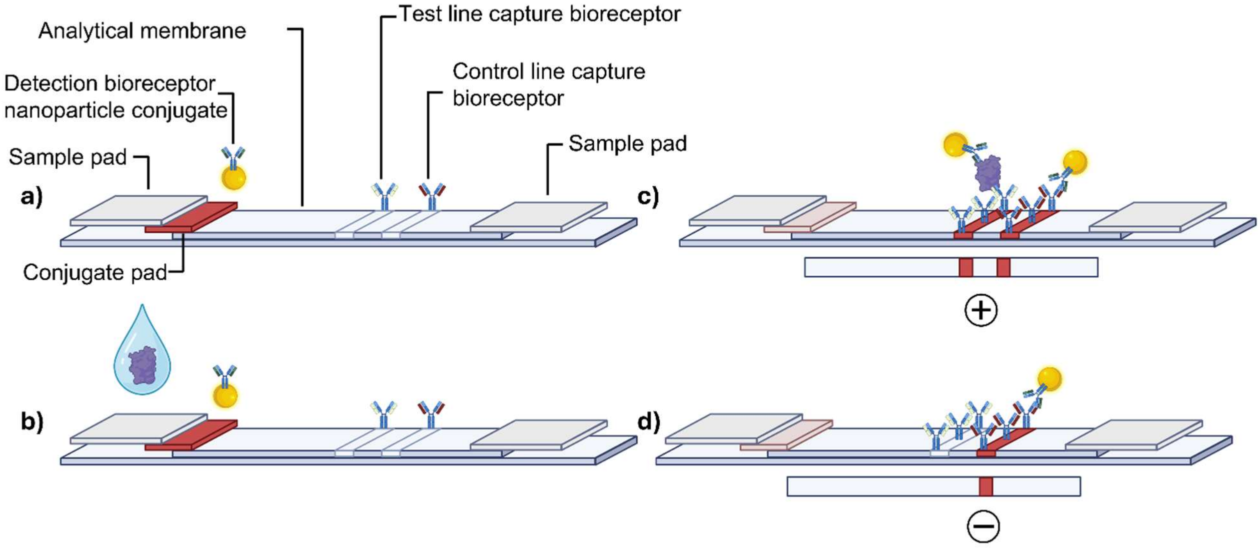

Figure 1. 1 **a**) Schematic of an LFA showing the four main pads. **b**) The addition of the sample to the sample pad activates the assay. **c**) Shows the formation of immunocomplex at the test line in the presence of the analyte and the capture of the nanoparticle probe at the control line, causing the development at both lines indicating a valid and positive result. **d**) In the absence of the analyte, the nanoparticle is only captured at the control line causing the development of a single line indicating a negative result.

conjugate pad and analytical membrane are in contact, ensuring the transfer of the assay reaction mixture. Once on the analytical membrane, the sample and conjugate mixture migrate across the porous structure of the membrane through capillary forces. The analytical membrane contains a region decorated with a capture bioreceptor specific to the analyte of interest, called the test line. As the sample flows over the test line, the capture bioreceptor binds the bioconjugate-analyte complex, immobilising the label on the test line and generating a visible signal. The control line contains a capture bioreceptor specific to the detection bioreceptor. Since the capture bioreceptor in the control line does not require the analyte to immobilise the detection probe on the control line, a signal is generated even in the absence of the analyte in the sample. The control line serves as a quality control measure to confirm reagent stability and correct flow. The generation of a control line is required to ensure a valid test result. The analytical membrane is in direct contact with an absorbent pad. Finally, the sample conjugate mixture reaches the absorbent pad, which acts as a sink, ensuring continued flow until the sample is exhausted. The intensity of the signal at the test line, often assessed visually or with a dedicated LFA reader, correlates with the concentration of the target analyte in the sample.

1.3 Selection of bioreceptors

A range of bioreceptor types have been used in LFA. These include nucleic acids, such as aptamers and DNA, and proteins, with antibodies being the most extensively employed and the prime choice for LFA reagents.[17] Antibodies are complex glycoproteins composed of two identical light chains and two identical heavy chains linked together by disulphide bridges. Together, the antibody forms a Y-shape (Figure 1.2).[18] The two arms of the Y make up the fragment antigen-binding (Fab) domains, and the “tail” makes up the fragment crystallisable (Fc) region. Each Fab domain contains the variable fragment (Fv), which is the part of the antibody responsible for binding to a specific target antigen. An antibody and its target interact through six complementarity-determining regions (CDRs) located within the Fv domain. Three

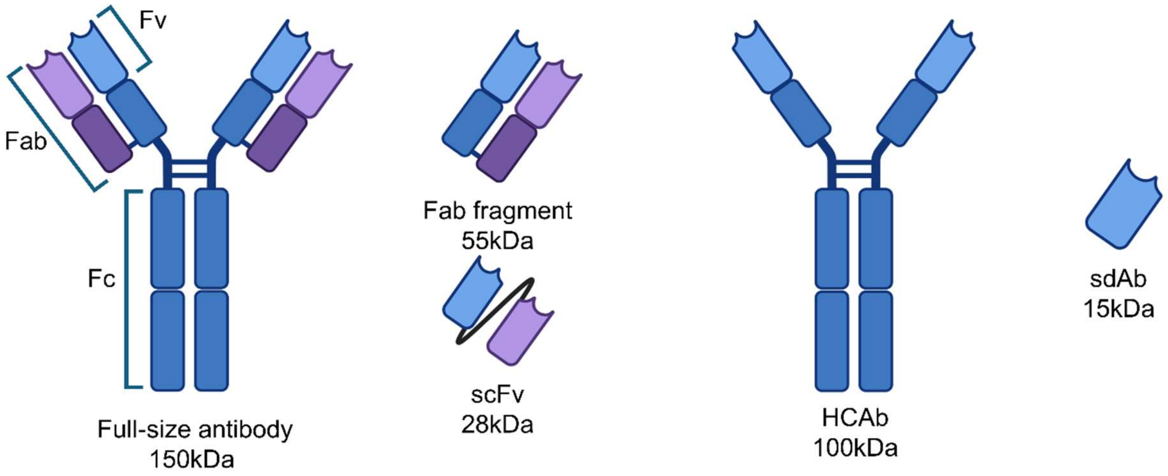

Figure 1. 2 Scheme of different antibody formats and fragments with their respective approximate molecular weights (MW)

of these are located on the light chain, and the other three are located on the heavy chain.[19] These CDRs form a unique surface called the paratope, which binds to a corresponding region on the antigen called the epitope. Amino acid sequences located on the epitope and paratope interact with each other and form a series of hydrogen bonds, hydrophobic interactions and charge interactions that enable their binding.[20]

The binding of antigens to antibodies is a reversible, noncovalent interaction that follows the law of mass action and takes the form

$$Ab + Ag \underset{k_{off}}{\overset{k_{on}}{\rightleftharpoons}} AbAg \tag{1.1}$$

where k_{on} is the association and k_{off} is the dissociation rate of the complex.[21] Techniques such as surface plasmon resonance (SPR) and bio-layer interferometry (BLI) can be used to measure the association and dissociation rates.[22] This provides a measurement of the complex affinity, most commonly reported as the equilibrium dissociation constant (K_D), which is calculated using the formula:

$$K_D = \frac{k_{off}}{k_{on}} \tag{1.2}$$

K_D and antibody affinity are inversely related. A lower K_D value indicates a higher affinity interaction, meaning the antibody binds more tightly to its target antigen.[20] K_D is typically expressed in molar units (M, mM, µM, nM, pM). Antibodies with K_D values in the low nanomolar to picomolar range ($K_D = 10^{-8} - 10^{-10}$ M) are considered to have very high affinity. In traditional immunoassays such as ELISA, where lengthy incubation times enable equilibrium, K_D plays a crucial role in determining assay sensitivity. A higher affinity antibody will bind more antigen at a given concentration, leading to a greater signal and improved sensitivity.[23]

However, LFAs operate under non-equilibrium conditions due to their rapid timescales.[24] This means that the reaction does not have sufficient time to reach equilibrium. Consequently, the sensitivity of an LFA becomes more dependent on the k_{on}, which dictates how quickly the antibody binds to the antigen rather than the overall K_D. A higher k_{on} allows for faster antigen capture during the limited timeframe of the assay, leading to improved sensitivity.[25]

1.4 Antibody development

The traditional development of monoclonal antibodies (mAb) involves the immunisation of an animal, typically a mouse or rabbit, with a specific antigen to stimulate the production of antibodies.[26] B-lymphocytes, involved in the immune response are isolated from the immunised animals and fused with myeloma cells to create immortal hybridomas, each secreting a unique mAb. These hybridoma cells are cultured and screened for activity against the target from which the best antibody candidates can be selected.[26]

The emergence of antibody display technologies has since provided alternative discovery routes. Among those, the most successfully applied method is using phage display.[27] Phage display technology involves the fusion of several billion antibody clones derived from immune libraries with the coat protein of a phage virus.[28] This results in the display of the antibody on the phage surface with the genetic material residing within the phage particle. This technology enables the barcoding of each antibody to its genetic material in a process called the genotype-phenotype coupling. Phages undergo several rounds of selection against the antigen of interest, where successful clones can be isolated and sequenced. Fragments of antibodies are typically utilised for phage display selection since these are compatible with expression in the *E. coli* host. These include fab fragments, single chain-variable fragments (ScFv) and single domain antibodies (SdAb). While the aim of phage display for the discovery of antibodies relies on the transition from fragment to full antibody, this is not always straightforward. Fusion of the selected fragments back to the full-size antibodies can result in instability and changes in affinity.[29] Full-length antibodies require sophisticated expression systems and purification processes, which can be resource intensive.

Antibody fragments are increasingly valuable tools in biomedical research, extending beyond their role as intermediates in developing full-size antibodies.[30] Among these fragments, single-domain antibodies, known as nanobodies, have gained significant attention.[31] Nanobodies are fragments of heavy chain-only antibodies found in animals of the *Camillidae* family (e.g., llamas and alpacas). Heavy chain-only antibodies, devoid of the light chain, consist of two heavy chains, each possessing a single variable antigen binding domain (VHH). Due to the absence of the light chain, heavy-chain only antibodies have evolved to maintain comparable affinity to traditional antibodies even though they only have 3 CDR regions. Nanobodies have an enlarged CDR1 and an extended CDR3, which contributes to a larger paratope and allows for a wider range of loop shapes. This unique structural feature, combined with the small size (~15 kDa) of nanobodies, enables them to access more complex and cryptic epitopes that may be inaccessible to conventional antibodies. They possess remarkable biochemical properties, including high thermal stability (even after denaturation), resistance to proteases and pH changes, and high solubility, preventing aggregation.[32] Nanobodies are easily produced in bacteria, and their discovery using phage display is more straightforward than that of traditional antibodies, bypassing the need for heavy and light chain pairing.

Nanobodies have emerged as promising therapeutic agents, with several nanobody-based therapies gaining approval for various applications, including oncology, autoimmune diseases, and infectious diseases. Notably, studies by Schoof et al. and Koenig et al. have demonstrated the development of highly potent neutralising nanobodies that target the SARS-CoV-2 S1 protein. These studies also highlight the ability to engineer nanobodies, such as incorporating them into multivalent nanobody fusions, to enhance their affinity and efficacy.[33,34]

Beyond their therapeutic potential, the unique features of nanobodies make them ideal affinity reagents for diagnostics. Researchers have recognised this potential and employed nanobodies in various diagnostic formats, including immunoassays like LFA and ELISA in vivo diagnostic imaging, as well as biosensors.[35–39]

In this thesis, nanobodies VHHV and VHHE from the study by Koenig et al. and nanobody Nb6 from the study by Schoof et al. are utilised to investigate their application in LFAs.

1.5 Diagnostic nanoparticles in LFA

The choice of nanoparticle probe significantly influences the sensitivity potential of an LFA. Consequently, substantial research has focused on developing novel nanomaterials to enhance LFA sensitivity. In recent years, quantum nanodiamonds, quantum dots, nanocatalysts, and magnetic beads have emerged as LFA labels, offering exceptional sensitivity gains.[8,38,40,41] However, these advancements often necessitate sophisticated instrumentation and multi-step assay procedures, increasing complexity and cost. Despite these innovations, gold nanoparticles (AuNPs) remain the dominant LFA label, with approximately 90% of current LFAs utilising them.[42]

AuNPs have exceptional optical properties and can absorb and scatter light with extraordinary efficiency.[43] The collective oscillation of conduction electrons, known as localised surface plasmon resonance (LSPR), is induced by specific wavelengths of light, resulting in pronounced absorption and scattering (Figure 1.3a). This phenomenon causes very strong absorption within the UV-Vis band, displaying extinction coefficients in the order of $10^9 – 10^{11}$ $M^{-1}\cdot cm^{-1}$.[44,45] The LSPR frequency, and consequently, the perceived colour of the AuNPs, is highly dependent on the particle size, shape, and the surrounding dielectric environment.

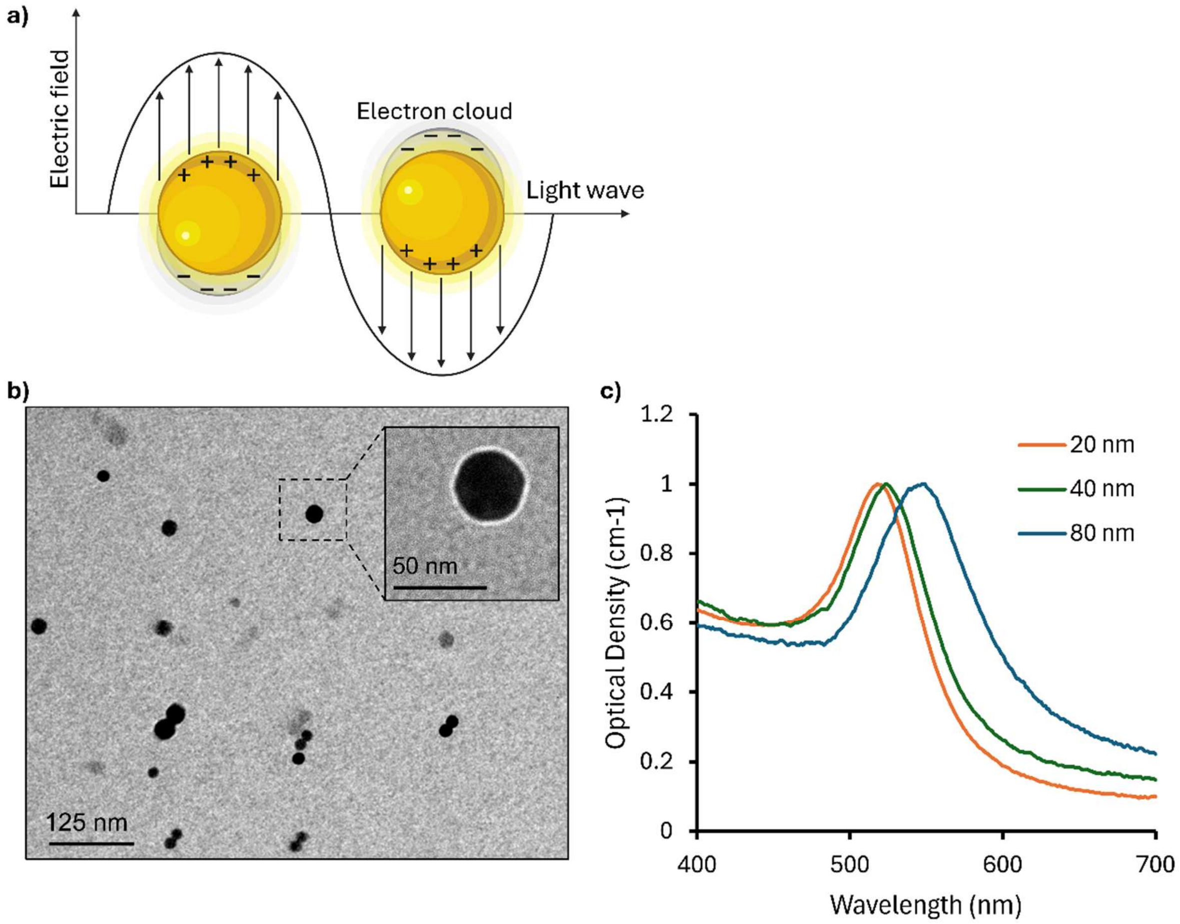

Figure 1. 3 AuNP optical properties a) Schematic illustration of LSPR in an AuNP induced by incident light waves. **b**) Representative transmission electron microscopy (TEM) image of 40 nm AuNPs. **c**) UV-Vis spectra of AuNPs with diameters of 20, 40, and 80 nm, demonstrating the size-dependent LSPR and corresponding colour variation.

For spherical AuNPs, an increase in diameter results in a redshift of the LSPR peak and a corresponding colour change from red to purple (Figure 1.3b and 1.3c). This gives nanoparticles a distinct bright red to purplish colour, depending on the nanoparticle size. This intense colour enables the naked-eye visualisation of test lines formed using AuNPs on LFAs.

The synthesis of AuNPs is commonly achieved through adaptations of the Turkevich method, where tetrachloroauric acid ($HAuCl_4$) is reacted with sodium citrate under boiling conditions.[46] Sodium citrate acts as a reducing and stabilising reagent. This method typically yields highly homogeneous AuNPs, with size control achieved by adjusting the sodium citrate concentration.[47] The resulting AuNPs are coated with sodium citrate, which gives the AuNPs a negative surface charge crucial for maintaining colloidal stability. Furthermore, AuNPs are biocompatible, have a large surface-to-volume ratio for functionalisation with biorecognition molecules and are chemically stable. Combined with their optical properties, AuNPs make ideal labels for LFA applications.[5]

AuNPs in solution remain stable due to a balance of attractive and repulsive forces, as explained by Derjaguin–Landau–Verwey–Overbeek (DLVO) theory.[48] This theory explains that colloidal stability arises from the balance between van der Waals attraction, which promotes aggregation, and electrostatic repulsion, which prevents it. While inherently unstable and prone to irreversible clumping upon contact, AuNPs remain dispersed due to their surface charge potential.

The surface charge of AuNPs often quantified as the ζ-potential, is affected by changes in pH and the concentration of electrolytes in solution. Increasing the electrolyte concentration compresses the diffuse electric double layer on the nanoparticle surface, crucial for maintaining the repulsive electrostatic forces.[48] AuNPs yielded using the Turkevich have a negative surface charge due to the negatively charged citrate on the surface and have a negative ζ-potential (ζ-potential < -25 mV).[49] An increase in electrolyte concentration leads to an increase of the ζ-potential towards zero, reducing the electrostatic repulsive forces and increasing the likelihood of aggregation.

This theory is often used to understand the behaviour of colloidal systems. Protein functionalisation of colloidal AuNPs can enhance their stability and impart protection to elevated ionic strengths and changes in pH.[50] The stability observed is owed to steric and electrostatic forces. The proteins act as a steric layer that prevents individual AuNPs from getting into close proximity to enable aggregation.

Maintaining colloidal stability is very important for sensing applications. Aggregation compromises their performance by inducing a red shift in the LSPR spectrum coupled with a reduction in per particle extinction cross-section, leading to a reduction in extinction coefficient.[51] This not only reduces their optical signal but also conceals binding sites on AuNP bioconjugates, hindering their ability to interact with target analytes. Consequently, the sensitivity and reliability of AuNP-based sensors are significantly reduced.

AuNP size is a critical parameter influencing the sensitivity of LFAs. Larger AuNPs offer several advantages, including an increased surface area for bioreceptor conjugation, leading to enhanced reactivity with the target analyte.[52] Additionally, larger particles possess greater extinction cross-sections, resulting in stronger signal generation per nanoparticle immobilised on the test line. However, these benefits must be weighed against the drawbacks associated with increased size. Larger AuNPs exhibit reduced diffusivity, potentially hindering their transport through the porous LFA membrane. Furthermore, they are more susceptible to aggregation, as they experience greater Van der Waals attraction, which can compromise assay performance by altering flow characteristics and reducing signal intensity. Therefore, careful optimisation of AuNP size is crucial to maximise assay sensitivity. This optimisation process must consider not only the inherent properties of the AuNPs but also the sample viscosity and LFA flow rate, as these factors influence the transport and immobilisation of the nanoparticles within the assay.

1.6 AuNP protein functionalisation

AuNP surface functionalisation with recognition proteins, such as antibodies, enables the nanoparticles to recognise and bind to specific target antigens. This process, crucial for applications like LFAs, relies on effective protein conjugation. These methods can be broadly classified as physisorption or chemisorption, each with its own set of advantages and challenges.[53]

Passive adsorption, also known as physisorption, is the simplest and most straightforward immobilisation method of proteins to AuNPs. The simplicity is due to the attachment of the protein without the need for chemical modification of the protein or the AuNP. Physisorption is based on the ability of proteins to adsorb on the surface of bare AuNPs spontaneously. This adsorption process is primarily driven by a combination of forces: electrostatic interactions, hydrophobic and van der Waals forces.[54] The physiochemical properties of the protein, particularly its surface-accessible amino acid residues, influence its adsorption characteristics. During physisorption, long-range electrostatic forces initially attract the protein to the negatively charged AuNP. Once near the surface, the protein reorients itself to maximise interactions and achieve stable binding.[55] The binding of proteins to the surface of AuNPs can be monitored through subtle changes in the local dielectric field. This interaction induces a small redshift in the LSPR peak, which can be readily detected using UV-Vis spectroscopy. Alternatively, the increase in hydrodynamic diameter caused by protein binding can be measured with dynamic light scattering (DLS).[56]

Successful conjugation of proteins to AuNPs relies on optimising the solution pH and protein concentration. For antibody-AuNP conjugates, this typically occurs around pH 8-9. Optimum adsorption of proteins onto AuNPs occurs at a pH slightly above the protein's isoelectric point (IEP).[57] At this pH, positively charged patches on the protein are attracted to the negatively charged AuNP despite the slightly net negative charge of the protein. [58]

The orientation and density of antibodies on nanoparticles influence the overall particle binding kinetics.[59] Essentially, increasing the number of accessible antibodies on a nanoparticle surface enhances its association rate with the target analyte. This means a higher density of antibodies leads to faster binding.[60]

Gasperino *et al.* introduced the application of effective on/off rate calculations (originally used for ligand-receptor binding) to diagnostic nanoparticles, used to describe the association and dissociation of polyvalent nanoparticle conjugates with their antigen pairs.[25] These effective rates, denoted as $\mathrm{k}_{\mathrm{on,\ particle}}$ and $\mathrm{k}_{\mathrm{off,\ particle}}$ consider the collective polyvalent behaviour of antibody-decorated nanoparticles.

$$k_{on,\ particle} = \frac{4\pi\alpha DNK_{on}}{NK_{on} + 4\pi\alpha D} \tag{1.3}$$

$$k_{off,\ particle} = K_{off}\left(1 - \frac{NK_{on}}{4\pi\alpha D + \quad {}_{on}}\right) \tag{1.4}$$

Where α is the nanoparticle radius, D is the nanoparticle diffusivity, N is the number of antibodies correctly presented on the nanoparticle surface, and $\mathrm{k_{on}}$ is the associative rate of individual antibody-antigen[25]. Others have calculated the effective particle association scaling with the number of antibodies on the surface, such as $\mathrm{k_{on,\,particle} = NK_{on}}$. However, at the size and diffusivity scales of diagnostic nanoparticles where $4\pi\alpha\mathrm{D} >> \mathrm{NK_{on}}$, meaning that the binding of antigen to the particle is not diffusion-limited, the $\mathrm{k_{on,\,particle}}$ calculation from both methods is a very close match.[52]

The number of accessible fab domains on an antibody-AuNP bioconjugate greatly affects the efficiency of antigen capture and is critical to the success of LFA.[60] Zhan *et al*. showed that LFA sensitivity can be significantly improved when using larger nanoparticles due to the greater number of antibodies presented on the nanoparticle surface.[52] While performing the physisorption at a higher concentration would, in principle, yield a high degree of decoration, the randomised orientation achieved through physisorption greatly reduces the paratope display on the AuNP surface. Ruiz *et al*. demonstrated that by fine-tuning antibody surface electrostatics with small changes in the solution pH, antibody orientation on the nanoparticle surface can be controlled, yielding a greater proportion of “tail-on” antibodies.[61]

While physisorption relies on weaker interactions, chemisorption involves the formation of covalent bonds between the protein and the AuNP.[54] In its simplest form, chemisorption can occur when the protein has free cysteine residues. The thiol group in cysteine residues readily forms a dative covalent bond with gold.[62] Strategic positioning of cysteines within the protein structure can, therefore, be used to improve binding affinity and offer some control over orientation on the AuNP.[63,64] Antibodies typically have limited accessible cysteine residues due to disulfide bridge formation. To overcome this, disulfide bridges can be reduced, or lysine residues can be modified to introduce thiols, enabling covalent coupling to the AuNPs.[54,65,66] Other chemisorption techniques include the modification of lysine residues using NHS esters. Filburn and Driskell used DTSSP, a disulphide-containing NHS ester linker, to covalently immobilise antibodies on AuNPs.[67] NHS-EDC chemistries covalently bind antibodies to pre-activated carboxyl-end-functionalized AuNPs. While these modifications are limited to the lysine residues, there is still little control over antibody orientation.

The natural diversity of proteins means that each protein requires a unique optimisation strategy when conjugated to AuNPs, with conjugation strategies limited to individual proteins. Factors such as protein size, shape, charge distribution, and the location of available cysteine or lysine residues all influence the optimal conjugation conditions. This inherent complexity necessitates careful consideration and experimentation to achieve efficient and functional protein-AuNP conjugates.

A major challenge in this process is that proteins can undergo conformational changes upon conjugation, leading to a loss of functionality and bioconjugate instability.[68,69] To mitigate this, researchers have developed modular bioconjugation approaches. These strategies employ a sacrificial protein adsorbed onto the AuNP surface, providing an anchor point for the functional protein via protein-protein interactions.

For example, Ma *et al*. utilised an engineered glutathione-S-transferase (GST) fused to the SpyCatcher protein. GST, with its multiple surface-exposed cysteines, binds strongly to gold surfaces. SpyCatcher can efficiently form interpeptide bonds with a corresponding peptide tag called SpyTag. In this system, GST acts as a sacrificial protein, shielding the functional protein from unfolding while providing a strong anchoring point to the AuNP.[70] Functional proteins fused with SpyTag can then be easily attached to the surface of the bioconjugate. Furthermore, the GST enables oriented attachment of the functional protein, which can be crucial for preserving its activity. Similarly, Richards *et al*. developed a versatile method for functionalising AuNPs by utilising the strong interaction between BSA and AuNPs.[59] The adsorbed BSA, chemically modified to present functional linkers, was used as an intermediate protein to bind antibodies on the bioconjugate. This approach resulted in improved performance of the bioconjugates. When used in LFA, the bioconjugates displaying antibodies via BSA showed a 3.7-fold improvement in sensitivity compared to those with physisorbed antibodies. In another approach, Robson *et al*. used an *E. coli* protein engineered with a free cysteine to improve binding to AuNPs. Fusing the engineered protein to an ScFv enabled an oriented display of the paratope and enabled its use as a diagnostic probe in LFA.[64]

1.7 LFA Development process

The overlapping pads in an LFA ensure an ‘automated’ assay where the different reagents sequentially mix and react with each other following sample addition. Despite the simplicity of its operation, LFAs require meticulous optimisation to ensure compatible and optimised interaction of the LFA components and proteins at the nanoscale.[5] This optimisation process is highly specific to each LFA and is influenced by several parameters such as the bioreceptor selection and affinity, the type of sample, the biomarker, and its clinically relevant concentration in the selected sample.

Often, LFA tests are developed and optimised by relatively small-scale manufacturers funded by donor programs or in low-resource settings. This often leads to limited research and development resources.[25]

LFA development is a multi-stage, empirically driven process exploring a complex multivariate parameter space.[71] It begins with identifying a suitable biomarker and establishing sensitivity and specificity requirements. Antibody pairs are then screened for compatibility as detection and capture reagents. Subsequent stages involve depositing reagents onto LFA pads, optimising buffer conditions, and assessing the assay's sensitivity and stability using the target analyte within its native matrix. During this iterative process, the selected antibody pair may fail to meet the required sensitivity or stability criteria, necessitating a return to reagent screening.

While biological reagents for well-characterised targets are often readily available, sourcing materials for emerging infectious threats can be challenging due to surging demand and potential supply chain disruptions. This challenge underscores the need for readily available, adaptable diagnostic tools.[72]

Even though the development of LFA diagnostics can take years, antigen LFAs for SARS-Cov-2 were developed and deployed within months. This was mainly due to the large sums of funding directed to the development of new diagnostics.[72] Despite this achievement, public availability of COVID-19 antigen LFAs was delayed until 2021, primarily due to insufficient manufacturing capacity. A report to the G7 by the pandemic preparedness partnership urges policymakers to enable pandemic control deployment, including rapid diagnostic tools, within 100 days.[3] This ambitious goal highlights the need for a comprehensive 100-day action plan to mitigate the impact of future infectious disease outbreaks. Research focused on enabling rapid LFA deployment by accelerating LFA development and minimising manufacturing bottlenecks is crucial to realising this plan.

1.8 Accelerating LFA development process

To accelerate and improve the traditional, labour-intensive LFA development process, often characterised by a trial-and-error approach, new methods are needed. Hsieh *et al*. provide a review of analytical tools typically employed by researchers developing LFA to guide optimisation.[71] Huynh *et al*. describe an accelerated LFA development workflow that employs design-of-experiments (DoE) theory, automation and image analysis to rapidly screen the multitude of parameters considered in an LFA.[73] DoE, a statistical tool commonly used in the pharmaceutical industry and immunoassay development, guides the efficient screening and optimisation of parameters within a multivariate space. Their automated system utilises a liquid handling robot with integrated image capture to set up and perform assays based on pre-defined reagents and parameters. By incorporating DoE principles, the system minimises experimental runs while effectively mapping the relationships between various parameters and assay performance. Results obtained from this automated system were comparable to those obtained through conventional, manual methods. This efficient, strategically driven optimisation process not only accelerates assay development but also allows researchers to shift their focus from manual experimentation to data analysis and explore new avenues of investigation.

The inefficient trial-and-error approach to optimisation risks missing the exploration of true optimal parameters and missing out on assay sensitivity. The employment of mechanistic mathematical models can help guide the optimisation process. These models can function as "digital twins" of LFAs under development, providing strategic guidance toward maximising sensitivity. By incorporating analyte-specific parameters like sample viscosity and target concentration, along with bioreceptor affinities, these models can pinpoint sensitivity-limiting factors and predict the likelihood of achieving desired performance. Gasperino and colleagues recently reviewed the application of mathematical modelling to LFA development, highlighting the prevalent use of advection-diffusion-reaction models.[25] Early work by Qian demonstrated these models' ability to capture key features of LFA signal generation, including non-linear responses at high analyte concentrations.[74] Subsequent studies by Ragavender and Anmol, Liu *et al*. and Zhan *et al*. leveraged similar models to optimise binder density, investigate particle size effects, and determine optimal test line placement, respectively.[52,75,76] With continued effort, these computational models are poised to empower experimentalists with a tool for more efficient exploration of the solution space, strategic optimisation, and a deeper mechanistic understanding of each component's impact on analytical performance.

While the discussed improvements in the optimisation methods enhance development speed and potentially improve assay performance, they do not fully address manufacturing bottlenecks. This thesis proposes that employing alternative, readily producible and versatile biorecognition reagents, such as nanobodies, presents a promising avenue for accelerating LFA deployment, reducing development time and cost compared to traditional antibodies. Nanobodies can be quickly produced using phage display, synthetic libraries, or even de novo design, significantly reducing development time and cost compared to traditional antibodies.[77,78] Their production in bacterial systems is simpler, higher-yielding, and more amenable to decentralised manufacturing.[79] This could provide a quicker and more cost-effective response for generating bioreceptors for LFA applications, speeding up the assay development process.

There are examples of LFAs employing nanobodies for biorecognition within a range of assay formats. In a paper by Colleen *et al.*, a chemically biotinylated version of an anti-p24 nanobody was employed to detect HIV in a nanocatalyst-based LFA.[38] The biotinylated nanobody acts as the capture reagent and binds to streptavidin-coated test lines. In another paper, the development of an LFA was demonstrated, using a green fluorescent protein nanobody fusion to act as the detection probe for Aflatoxin B1 in milk.[80] Wang *et al*. developed an LFA using a biotinylated nanobody displayed on streptavidin-coated gold nanoparticles for the detection of aflatoxin B1.[35] Maher *et al*. developed an LFA based on a chemically conjugated nanobody onto gold nanoparticles to detect the SARS-CoV-2 S1 protein in saliva samples.[81]

While examples of nanobody-based LFAs exist, few utilise the simple and cost-effective physisorption for AuNP immobilisation and often involve chemical modification of the protein. This is likely due to the instability of AuNP-nanobody bioconjugates made through physisorption. This effect was highlighted by Goossens *et al.*, where a panel of nanobodies was physisorbed onto AuNPs and was shown to lose stability when exposed to high ionic strength, showing limited stability of the bioconjugate.[58] Similarly, Chen *et al*. have observed nanobody-induced aggregation of AuNPs when these are physisorbed onto the surface, suggesting that this is a universal property of nanobodies.[82]

Recognising the limitations of physisorption, researchers have turned to protein engineering to enhance nanobody-AuNP binding and bioconjugate stability. This involves strategically modifying the nanobody's structure, either by positioning key amino acids involved in AuNP immobilisation or by fusing the nanobody to AuNP anchor proteins. These approaches have shown mixed results. Hattori *et al*. developed a nanobody with high affinity to gold that was later fused to another nanobody for directed immobilisation and was shown to improve nanoparticle bioconjugate stability.[83] Goossens *et al*. and Anderson *et al*. attempted incorporating free cysteines onto the nanobodies to improve binding and bioconjugate stability but found conflicting results.[58,84] Furthermore, these studies primarily evaluated stability in conjugation buffers without the downstream processing required for long-term storage in LFAs.

Further research is therefore needed to explore these and alternative engineering approaches to determine if engineered nanobodies can withstand rigorous conditions and function reliably as LFA detection bioreceptors. If successful, the ease of nanobody development and manufacture promises to significantly accelerate the LFA development process.

1.9 Modular display of binders on LFA surfaces

Functionalisation of LFA surfaces such as AuNPs and nitrocellulose membranes with biorecognition molecules is a critical step in the development process. The inherent diversity of proteins and the complex protein-solid interface necessitate thorough optimisation of functionalisation conditions. Similar to AuNP functionalisation, nitrocellulose functionalisation has a direct impact on the assay performance. Test line formation on nitrocellulose membranes involves antibody dispensing using contact or non-contact dispensing systems. Electrostatic interactions primarily drive antibody immobilisation, and the immobilisation buffer composition can be modulated to enhance both the presentation and stability of the dispensed reagents.[85] Optimisation of antibody immobilisation during LFA development involves adjusting the buffer composition to maximise capture bioreceptor adsorption and maintain its reactivity on the membrane. Key components include buffering agents with low ionic strength and a pH near the IEP of the bioreceptor, stabilisers like sugars to preserve the bioreceptor during drying, and alcohols to improve binding and drying time. Optimisation aims to enhance the sensitivity and specificity of the LFA by promoting strong bioreceptor binding while minimising non-specific interactions. These conditions are typically not universally applicable across different LFAs, requiring individual optimisation for each assay.

This optimisation process constitutes a major portion of LFA development, raising the question of whether alternative protein immobilisation methods could be employed. Ideally, these methods would be broadly applicable to different proteins or antibodies, irrespective of their inherent diversity, thereby streamlining the optimisation process and reducing development time. Such an approach could potentially enhance the efficiency and versatility of LFA development. Addressing the inherent complexities of protein binding to nitrocellulose, Holstein and colleagues investigated novel immobilisation techniques with the potential for broader applicability, improved binding, and preservation of functionality, particularly when using smaller binders.[85] Their study focused on immobilising small molecular weight binders (7.8 – 13.3 kDa) onto nitrocellulose membranes using three distinct methods: covalent attachment of a cysteine-presenting binder to an epoxide-functionalised membrane, fusion of the binder to a nitrocellulose anchor protein for directed immobilisation, and modular attachment employing a biotinylated binder and a streptavidin-functionalised membrane. The effectiveness of each method was evaluated by quantifying binder immobilisation and assessing the ability of the immobilised binder to capture its target in an LFA format. While all tested methods demonstrated advantages over direct adsorption, the modular approach, displaying biotinylated binders on streptavidin surfaces, produced the strongest signal in the LFA format. These novel immobilisation methods offer a promising avenue for overcoming the limitations posed by the complex protein-solid interface, paving the way for a more streamlined and efficient LFA development process.

The potential of these novel immobilisation methods has been recognised within the LFA industry. One such example is the generic rapid assay device (gRAD) developed by Bioporto.[86] gRAD is an optimised generic LFA strip where the test line is decorated with a biotin-binding protein that can bind to any biotinylated antibody. In this way, the assay can be adopted for different analytes. The assay is performed by mixing a detection antibody-gold conjugate with the analyte and biotinylated capture antibody and running on the gRAD LFA test strip. This method eliminates the need for optimisation of the antibody immobilisation, simplifying development.

1.10 Fully modular LFAs

LFAs are invaluable for rapid, PoC diagnostics. However, their traditional manufacturing often leads to rigid designs, susceptible to supply chain vulnerabilities, significant waste from expired assays, and slow adaptation to new threats. While the concept of modularity in LFA components holds immense potential for boosting sensitivity and speeding up development, current approaches typically offer it for either the detection or capture binder, leaving the other tied to traditional, time-consuming optimization. Moreover, existing methods for improved immobilisation often rely on complex chemical modifications of binders, hindering scalability and demanding extra optimization and characterization with sophisticated tools.

This thesis will introduce a novel, fully modular LFA system that overcomes these limitations. The work here leverages the inherent advantages of nanobodies, their straightforward protein engineering and cost-effective production, as ideal candidates for modular display. A key concept will be the development of a streamlined in vivo biotinylation system. This scalable method enables the simultaneous, highly efficient, and orthogonal biotinylation of nanobodies, anticipated to yield nanobodies presenting a single biotin. This facilitates easy and cost-effective production essential for our modular LFA design. A fully modular LFA employing streptavidin-coated AuNPs and streptavidin-coated nitrocellulose membranes will be generated to display both detection and capture nanobodies. This approach will allow for the stockpiling of "blank" LFA cassettes that can be readily functionalised with target-specific nanobodies in the field. This strategy is anticipated to mitigate supply chain challenges and reduce waste associated with expired assays by enabling a "plug-and-play" approach to LFA development. With the emergence of a new disease, nanobody pairs can be rapidly developed and used to activate the pre-fabricated, stockpiled modular LFAs. This minimises the manufacturing bottlenecks associated with traditional LFAs, which require significant time and resources to re-design and manufacture for each new target. Furthermore, the modular display of reagents eliminates the complex protein-solid interface, enabling oriented attachment of nanobodies and improving sensitivity while eliminating the need for extensive optimisation. Combined, these advancements will enable a more robust and effective response to emerging infectious threats by facilitating quicker and more robust development of LFA diagnostics.

1.11 Thesis aims

The main aim of this thesis is to explore the potential of nanobodies as effective bioreceptors in LFA. It aims to address the inherent challenges of nanobodies at the nanoparticle protein-solid interface when prepared through physisorption and the vulnerability of nanobody-bioconjugates to salt-induced aggregation. The use of protein engineering is intended to enhance nanobody immobilisation and improve the resistance of nanobody-AuNP-bioconjugates to aggregation. It is expected that this will lead to the successful integration of nanobody bioconjugates into LFA, displaying sufficient sensitivity to enable the diagnostic potential of nanobodies. Furthermore, this thesis explores the generation of a novel universal LFA to which engineered nanobodies can be used to activate the assay through a plug-and-play approach. Ultimately, it is anticipated that this research will contribute to the acceleration of LFA development, harnessing the ease of development, versatility and production of nanobodies.

The specific objectives of this thesis are:

1. **Investigate the limitations of nanobody-AuNP bioconjugate stability via physisorption.** This involves systematically testing nanobodies with varying IEPs, different nanoparticle sizes, and diverse ionic strength conditions to understand stability constraints, the impact of environmental factors, and the underlying mechanisms of salt-induced aggregation.
2. **Enhance the stability of physisorbed nanobody bioconjugates through protein engineering.** This objective will explore established and novel strategies, including the development of new nanobody constructs, to overcome current physisorption limitations. The impact of these stability improvements will be evaluated with a focus on enabling efficient downstream processing of bioconjugates (e.g., purification and lyophilisation) and assessing the performance of these stabilised bioconjugates as detection probes in LFAs, focusing on sensitivity and specificity. Ultimately, this aims

to translate enhanced stability into improved sensitivity, such as increased shelf-life and assay robustness, contributing to more reliable nanobody-based diagnostic tools.

3. **Develop a universal "plug-and-play" nanobody-based LFA platform.** This objective involves engineering nanobodies and creating a novel modular display system on LFA surfaces, making the platform adaptable to any nanobody pair for rapid assay development against any target disease. This will involve developing a scalable production method for biotinylated nanobodies and functionalising LFA surfaces with streptavidin. This approach is hypothesised to accelerate LFA development for emerging infectious diseases by eliminating the need for extensive optimisation, allowing for rapid responses to outbreaks. Furthermore, the modular design will overcome protein-solid interface challenges and ensure consistent performance regardless of the specific nanobody used. Ultimately, this research aims to revolutionise PoC diagnostics by providing a versatile and adaptable platform for rapid LFA development and deployment, enabling the stockpiling of universal assays to prevent manufacturing and logistical bottlenecks that hinder rapid response to emerging threats.

1.12 Thesis overview

Chapter 1: This chapter provides a comprehensive overview of LFAs, emphasising their role in PoC diagnostics, particularly for emerging infectious diseases. It begins by highlighting the need for rapid and accessible diagnostics, especially in resource-limited settings, and positions LFAs as a key solution due to their simplicity and affordability. The chapter introduces the core components of LFA, discussing biorecognition elements like antibodies and the importance of diagnostic nanoparticles. Furthermore, this chapter discusses the inefficient development process of LFAs and the deployment bottlenecks that can emerge during global crises. It discusses strategies for accelerating LFA development and highlights the potential of nanobodies to further streamline the process. Finally, the chapter explores the concept of modular binder display on an LFA in order to overcome the protein interface challenges and accelerate assay development.

Chapter 2: Provides a detailed description of the materials and methods used in this thesis.

Chapter 3: This study systematically evaluates the adsorption characteristics of different nanobodies in their native form onto AuNPs and the stability of the resulting bioconjugates under various ionic strength conditions. By performing physisorption using nanobodies with different IEPs at different pH values, the relationship between pH and nanobody IEP is established in generating stable bioconjugates at low ionic strength conditions. The stability limitations of these nanobody-AuNP bioconjugates are then assessed by exposing them to increasing ionic strengths. Furthermore, two common approaches to improving bioconjugate stability are explored: 1) incorporating a single cysteine residue into the lead nanobody candidate and 2) supplementing the physisorption buffer with carbonate. The purpose of this chapter is to establish the exact limitations of nanobody bioconjugates and act as the benchmark for comparison with novel engineered nanobodies created for superior bioconjugate stability.

Chapter 4: This chapter explores the generation of multivalent nanobodies with the aim of improving the stability of nanobody bioconjugates generated through physisorption. Initially, the chapter explores the generation of a divalent and trivalent version of the lead nanobody candidate and identifies distinct adsorption characteristics between the monovalent, divalent and trivalent forms and distinct superior stability of the trivalent nanobody bioconjugate. The trivalent bioconjugate is studied for stability through different downstream processing stages required for LFA development and storage and is integrated into an LFA for the detection of the target analyte, the S1 protein of SARS-CoV-2. Through this, a relationship between multivalent form, bioconjugate stability and sensitivity in LFA is established. Finally, different nanobodies are incorporated into multivalent chains and studied for stability when bound to AuNPs.

Chapter 5: This results chapter reports the development of a plug-and-play LFA developed using the modular display of nanobodies on LFA. The chapter includes a theoretical study of different affinity systems to identify a suitable system for the plug-and-play LFA that will be activated and performed at the PoC. To create a scalable method for producing modular reagents, Avi-tagged nanobodies were developed using an in vivo orthogonal biotinylation system. The sensitivity of this fully modular assay was then established for the detection of the S1 protein.

Chapter 6: This chapter summarises the work in this thesis, highlights the conclusions and outlines the future work

2 Materials and methods

2.1 Description of plasmids used

Name	**Description**	**Predicted mass (Da)**	**Chapter**	**Reference**
pET-26b-VHHV	Anti SARS-CoV-2 S1 nanobody VHHV with N-terminal PelB leader sequence and C-terminal hexahistidine tag (HHHHHH*) under a T7 x`	14225.70	3	Koenig *et al.*
pET-26b-VHHE	Anti SARS-CoV-2 S1 nanobody VHHE with N-terminal PelB leader sequence and C-terminal hexahistidine tag under a T7 promoter	15335.96	3	Koenig *et al*.
pET-26b-Nb6	Anti SARS-CoV-2 S1 nanobody Nb6 with N-terminal PelB leader sequence and C-terminal hexahistidine tag under a T7 promoter	13937.58	3	Schoof *et al*.
pET-26b-VHHV-Cys	Anti SARS-CoV-2 S1 nanobody VHHV with N-terminal PelB leader sequence and C-terminal Hexa-histidine tag and single cysteine (HHHHHHC*) under a T7 promoter	14328.83	3	
pET-26b-Cys-VHHV	Anti SARS-CoV-2 S1 nanobody VHHV with N-terminal PelB leader sequence, single cysteine between VHHV and PelB and C-terminal hexahistidine tag under a T7 promoter	14328.83	3	
pET-26b-VHHV2	Divalent anti SARS-CoV-2 S1 nanobody VHHV fused together with a 15 aa flexible linker (GGGGS)x3 with N-terminal PelB leader sequence and C- hexahistidine tag under a T7 promoter	28125.87	4	
pET-26b-VHHV3	Trivalent anti SARS-CoV-2 S1 nanobody VHHV fused together with a 15 aa flexible linker (GGGGS)x3 with N-terminal PelB leader sequence and C-terminal hexahistidine tag under a T7 promoter	42026.04	4	
pET-26b-VHHV4	Tetravalent anti SARS-CoV-2 S1 nanobody VHHV fused together with a 15 aa flexible linker (GGGGS)x3 with N-terminal PelB leader sequence and C-terminal hexahistidine tag under a T7 promoter	55926.21	4	
pET-26b-VHHV5	Pentavalent anti SARS-CoV-2 S1 nanobody VHHV fused together with a 15 aa flexible linker (GGGGS)x3 with N-terminal PelB leader sequence and C-terminal hexahistidine tag under a T7 promoter	69826.38	4	
pET-26b-VHHV6	Hexavalent anti SARS-CoV-2 S1 nanobody VHHV fused together with a 15 aa flexible linker (GGGGS)x3 with N-terminal PelB leader sequence and C-terminal hexahistidine tag under a T7 promoter	83726.56	4	
pET-26b-VHHE2	Divalent anti SARS-CoV-2 S1 nanobody VHHE fused together with a 15 aa flexible	30346.40	4	

	linker (GGGGS)x3 with N-terminal PelB leader sequence and C-terminal hexahistidine tag under a T7 promoter			
pET-26b-VHHE3	Trivalent anti SARS-CoV-2 S1 nanobody VHHE fused together with a 15 aa flexible linker (GGGGS)x3 with N-terminal PelB leader sequence and C-terminal hexahistidine tag under a T7 promoter	45356.84	4	
pET-26b-Nb6x2	Divalent anti SARS-CoV-2 S1 nanobody Nb6 fused together with a 15 aa flexible linker (GGGGS)x3 with N-terminal PelB leader sequence and C-terminal hexahistidine tag under a T7 promoter	27549.63	4	
pET-26b-Nb6x3	Trivalent anti SARS-CoV-2 S1 nanobody Nb6 fused together with a 15 aa flexible linker (GGGGS)x3 with N-terminal PelB leader sequence and C-terminal hexahistidine tag under a T7 promoter	41161.68	4	
pET-26b-VHHV-AVI	Anti SARS-CoV-2 S1 nanobody VHHV with N-terminal PelB leader sequence and C-terminal AVI tag (GLNDIFEAQKIEWHE) followed by HRV 3C cleavage sequence (LEVLFQGP) followed by a hexahistidine tag under a T7 promoter	16920.72	5	
pET-26b-VHHV2-AVI	Divalent anti SARS-CoV-2 S1 nanobody VHHV fused together with a 15 aa flexible linker (GGGGS)x3 with N-terminal PelB leader sequence and C-terminal AVI tag followed by HRV 3C cleavage sequence followed by a hexahistidine tag under a T7 promoter	30820.89	5	
pET-26b-VHHV3-AVI	Trivalent anti SARS-CoV-2 S1 nanobody VHHV fused together with a 15 aa flexible linker (GGGGS)x3 with N-terminal PelB leader sequence and C-terminal AVI tag followed by HRV 3C cleavage sequence followed by a hexahistidine tag under a T7 promoter	44721.07	5	
pET-26b-Nb6-AVI	Anti SARS-CoV-2 S1 nanobody Nb6 with N-terminal PelB leader sequence and C-terminal AVI tag (GLNDIFEAQKIEWHE) followed by HRV 3C cleavage sequence (LEVLFQGP) followed by a hexahistidine tag under a T7 promoter	16748.68	5	
pET-26b-VHHE-AVI	Anti SARS-CoV-2 S1 nanobody VHHE with N-terminal PelB leader sequence and C-terminal AVI tag (GLNDIFEAQKIEWHE) followed by HRV 3C cleavage sequence (LEVLFQGP) followed by a hexahistidine tag under a T7 promoter	18030.99	5	
pBirAcm	pACYC184 biotin ligase (BirA) under Tac promoter		5	Avidity

Table 2.1. Names and descriptions of plasmids generated or used in this study. Custom plasmid constructs for this study were generated through synthesis by GenScript.

2.2 Nanobody periplasmic expression, purification and concentration

Nanobody sequences were fused with an N-terminal PelB signal sequence and a C-terminal hexahistidine sequence for periplasmic production and hexahistidine affinity purification, respectively. Plasmids containing the nanobody genes were transformed into chemically competent BL21 (DE3*) E. coli* cells and plated onto LB-agar plates supplemented with 50 µg/mL kanamycin. A single colony from the agar plate was used to inoculate 10 mL of LB media supplemented with 50 µg/mL kanamycin and incubated at 37°C in a shaking incubator at 180 RPM for 16 hours overnight. Starter cultures were used to inoculate 400 mL of LB media in a 2 L baffled Erlenmeyer flask supplemented with 50 µg/mL kanamycin to a cell concentration of OD_{600} = 0.05. Cultures were incubated at 37°C in a shaking incubator at 225 RPM until OD reached 0.7. Protein expression was induced with the addition of isopropyl β-D-1-thiogalactopyranoside (IPTG) to a final concentration of 1 mM and incubated in a shaking incubator for 16 hours overnight at 225 rpm and 25°C. Cells were collected by centrifugation at 10,000 × g for 15 minutes. Periplasmic extraction was performed by resuspending the cells in 15 mL of chilled TES (200 mM Tris HCl, 0.5 mM EDTA and 500 mM Sucrose, pH8) per L of culture and incubation for 2 hours on ice. The osmotic shock was performed by a 3-fold dilution with distilled water and incubation on ice for 1 hour. The periplasmic extract was collected by centrifugation for 30 min at 9,000 × g and recovering the supernatant. Nanobodies were separated from the periplasmic extract by Ni-NTA chromatography using a 1 mL His-trap HP column (Cytiva) by passing the sample through the column equilibrated in binding buffer (20 mM sodium phosphate, 500 mM NaCl, 30 mM imidazole, pH 7.4) and eluted from the column using elution buffer (20 mM sodium phosphate, 500 mM NaCl, 500 mM imidazole, pH 7.4) using a stepwise elution. Elution fractions containing the nanobodies were identified by measuring the protein concentration using a nanodrop (Thermo Fisher Scientific). Purified nanobodies were buffer exchanged into phosphate buffered saline (PBS) using a protein centrifugal filter (Amicon, 3 kDa MWCO). Purity was evaluated using a 4-20% gradient SDS-PAGE (BIO-RAD) and visualised using Coomassie stain (Abcam).

2.3 Sandwich ELISA

Sandwich ELISA was performed by immobilising nanobodies (VHHV, VHHE, or Nb6) onto polystyrene high-binding 96 well-plates at 1 µg/mL in PBS overnight. The plates were washed 3 times by adding 200 µL of wash buffer (PBS and 0.05% v/v Tween-20, pH 7.4) and removing the wash buffer. Plates were blocked by adding 200 µL of blocking buffer (3% w/v BSA, PBS and 0.05% v/v Tween-20, pH 7.4) and incubated for 1 hour at room temperature. The blocking buffer was removed, and the plate was washed 3 times with washing buffer. 100 µL of either 1 µg/mL or 0 µg/mL of SARS-CoV-2 receptor binding domain (RBD) antigen in blocking buffer was added to each well and incubated for 1 hour at room temperature with rocking. After washing 3 times, 100 µL of chemically biotinylated detector nanobodies were added to each well and incubated for 1 hour. Following a wash step, 100 µL of streptavidin-HRP (SA-HRP 1:200) conjugate was added and incubated for another hour. After washing 5 times, 100 µL of TMB substrate was added, and the reaction was stopped by adding 200 µL of 2 M H_2SO_4 after 10 minutes. The absorbance at 450 nm was measured using the SpectraMax i3 (Molecular Devices) plate reader to determine signal intensity.

2.4 Aggregation assays of AuNP bioconjugates

Nanobody physisorption studies were performed by mixing 5 µL of 100 mM buffer (pH 5.0 - 6.5 MES - Sigma, pH 7.0 - 8.5 HEPES - Sigma, 9.0 - 9.5 Borate – Fisher Chemical) with 5 µL of nanobody solution in a 384-well protein low-binding plate (Greiner). 40 µL of 40 or 20 nm AuNPs (Nanocomposix) at OD 1.25 (Absorbance at 530 nm) were added to each well and mixed thoroughly using a pipette. The plate was incubated for 1 hour at room temperature. Absorbance measurements at 530 and 580 nm were recorded for 40 nm AuNP conjugations and 520 and 580 for 20 nm AuNP conjugation. The aggregation index was calculated as the ratio of the absorbance at the shoulder of the plasmon peak (580 nm) over the absorbance at the plasmon peak (530 for 40 nm AuNPs and 520 for 20 nm AuNPs). To observe changes in the shape of the plasmon peak, absorption spectra (400 nm to 750 nm, 1 nm steps) were recorded using the SpectraMax i3 (Molecular Devices). Salt-induced aggregation was performed by the addition of 50 µL of 800 mM NaCl to each well. The plate was left to stand for 5 minutes, and the absorbance measurements were recorded.

2.5 DLS Nanoparticle size measurements

Dynamic light scattering (DLS) was performed to determine the size of AuNP and AuNP bioconjugates using the Litesizer DLS 500 (Anton Paar). Measurements were taken at 90° detection angle at 25 °C using a disposable cuvette with a 50 µL sample. Measurements were taken at AuNP concentration at OD 1. Equilibration time was set to 30 seconds, time for each run was set to 10 seconds. Maximum number of runs was set to 60.

2.6 Cys mutant reduction reaction

VHHV nanobodies containing a free Cys on the N-terminus or C-terminus are denoted as Cys-VHHV and VHHV-Cys respectively. Cys-bearing nanobodies were either used without reduction or with reduction. Reduced versions of the nanobodies are denoted with lowercase r (for example, rCys-VHHV). The reduction reaction was carried out by mixing 10 mM TCEP-HCL with up to 100 µg/mL of nanobody and incubated for 5 minutes at RT. TCEP-HCl was removed from the reaction using Zeba Spin Desalting Columns (7 KDa MWCO, Thermo Fisher Scientific). Reduction to monomers was observed using a non-reducing SDS-PAGE. The integrity of the internal disulfide bridge was investigated by reacting the reduced protein with N-methylmaleimide and characterised using LC-MS (Agilent 6530 Q-TOF).

2.7 Biotinylation reaction of proteins

Nanobodies and the S1 protein were biotinylated using the amine-reactive NHS-PEG12-Biotin. NHS-PEG12-Biotin (Thermo) was diluted in DMSO (Sigma) immediately before use. NHS-PEG12-Biotin was added to the protein mixture and incubated for 1 hour at room temperature and shaken at 650 rpm. Biotinylated proteins were passed through a ZebaSpin desalting column that was pre-equilibrated with PBS (pH 7.4, sigma) to remove the unreacted biotinylation reagent and elute in PBS. A NanoDrop One (Thermo Fisher) measured the final protein concentration.

2.8 Quantification of nanobody binding constants

Nanobody binding constants were measured by Bio-layer interferometry (BLI) using the ForteBio Octet RED96 (Molecular Devices). Nanobodies were biotinylated using NHS-PEG-12-Biotin in a 5:1 biotin-to-nanobody ratio. Unreacted biotin was removed using a Zebaspin desalting column. Streptavidin-functionalised sensors (Sartorius) were hydrated in kinetics buffer (Sartorius) for 10 minutes before being placed in fresh Kinetics buffer for a 5-minute baseline reading. Biotinylated nanobodies were loaded to the sensor at 1 µg/mL diluted in kinetics buffer for 15 minutes. Sensors were then placed in kinetics buffer for a baseline reading and equilibration for 10 minutes. The association step was performed by placing sensors in different concentrations of S1 (Abcam, His-tagged, 80, 40, 20, 10, 5, 2.5, 1.25, 0 nM) for 30 minutes. The dissociation step was performed by placing the sensors in kinetics buffer for 30 minutes. Analysis and determination of the affinity constants were performed using the ForteBio Data Analysis 8.2 software. The antigen concentrations that provided the highest R-squared value across all experiments were selected for the fitting.

2.9 Epitope mapping BLI

Streptavidin functionalised BLI sensors were hydrated, equilibrated and loaded with chemically biotinylated VHHV as described in the previous section. Sensors were placed in kinetics buffer for 30 seconds to equilibrate before moving to a well containing the 500 ng/mL S1 protein of SARS-CoV-2 in kinetics buffer and allowed to associate for 30 minutes. Sensors were then placed into wells containing kinetics buffer for 30 seconds to equilibrate before placing into wells containing the secondary binder at 1 µg/mL.

2.10 Cys mutant ELISA

VHHV and Reduced versions of Cys-VHHV and VHHV-Cys were used to coat the surface of Nunc maxisorb 96 well-plates (Thermo) at 100 nM in PBS and incubated for 2 hours at room temperature. The plate was washed 3 times with washing buffer (1×PBS and 0.05% v/v Tween-20, pH 7.4). The plate was then blocked with blocking buffer (3% w/v BSA, 1×PBS and 0.05% v/v Tween-20) for 1 hour and washed 3 times with washing buffer. Biotinylated S1 in blocking buffer was added to each well at different concentrations (1000, 333, 111, 37.0, 12.3, 4.1, 1.37, 0 ng/ml) and incubated at RT for 1 h. The plate was washed 5 times before adding horseradish peroxidase-conjugated streptavidin (HRP-SA) (1:200 in blocking buffer) and incubating for 1 h. The plate was washed 5 times before adding TMB one-step substrate and left to develop a signal for 5 minutes before adding 2 M H_2SO_4. Absorbance measurements at 450 nm were collected using the SpectraMax i3.

2.11 Multivalent nanobody ELISA

Nunc maxisorb 96 well-plates were coated with S1-Fc antigen (Abcam, ab272105, PBS) at different concentrations (500, 250, 125, 62.5, 31.25, 15.6, 7.81, 0 ng/mL) for 1 hour at room temperature. The plate was washed 3 times with washing buffer (PBS and 0.05% v/v Tween-20, pH 7.4) before being blocked with blocking buffer (3% w/v BSA, PBS and 0.05% v/v Tween-20, pH 7.4) for 1 h. The plate was washed 3 times with washing buffer before adding biotinylated nanobodies at 1 µg/ml in blocking buffer. The biotinylation ratio was confirmed using mass spectrometry. The detection steps were performed as previously described.

2.12 Adsorption isotherm

5 µL of mono-, di- or trivalent VHHV was mixed with 5 µL of 100 mM HEPES buffer pH 7.0 in a 384-well plate. 40 µL of 40 nm AuNPs OD1.25 (A530) were added to the plate and mixed thoroughly before incubating for 1 hour at room temperature. The final nanobody concentrations ranged from 3000 to 15.4 ng/mL using a 1.5-fold serial dilution. UV-Vis spectra were collected using the CLARIOstar Plus plate reader (BMG LABTECH, 220 – 1000 nm, 1 nm steps). The precise wavelength of the peak of the surface plasmon resonance (λSPR) was determined by fitting a Gaussian function to the plasmon peak from 500 nm to 550 nm and determining the maximum point by interpolation using a 0.05 nm precision. The λSPR was plotted against concentration and best fitted to the Hill equation (equation 1) where $\lambda SPR_{initial}$ is the λSPR of the bare AuNP, K_d is the dissociation constant of the interaction.

$$\lambda\mathrm{SPR} = \lambda\mathrm{SPR}_{initital} + \frac{\Delta\lambda\mathrm{SPR}_{max}[nanobody]^n}{{K_d}^n + [nanobody]^n} \tag{2.1}$$

2.13 VHHV3-AuNP conjugation for LFA

AuNP-VHHV3 bioconjugates were prepared by combining 100 µL of pH 7.5 HEPES buffer with 100 µL of VHHV3 (155 µg/mL) in 2 mL protein low-binding tubes. After brief vortexing, 800 µL of 40 nm AuNPs (OD 1.25 at 530 nm) were added and incubated for 1 hour on a thermal shaker at 650 rpm at room temperature. Bioconjugates were blocked by adding 1 mL of blocking buffer (1% w/v BSA, 0.05% v/v Tween-20 in PBS) and incubating for another hour. Bioconjugates were then centrifuged at 3,500 × g for 10 minutes, the supernatant removed, and the pellet resuspended in blocking buffer. This washing process was repeated once, and the final AuNP-VHHV3 bioconjugate was adjusted to OD 2 at 530 nm.

2.14 Preparation of polystreptavidin LFA strips

For LFA assembly, 100 mm x 20 mm SureWick absorbent pads (Millipore) were attached to 100 mm of FF80HP plus nitrocellulose membrane (Cytiva) using their adhesive backing. The assembled cards were cut to 100 mm, and the bottom adhesive was removed with a guillotine cutter. Test lines were printed using a Biodot AD1520 dispenser (dispensing rate of 1 µL/cm) with poly-streptavidin (BioTez, 1 mg/ml in purified water) positioned 10 mm below the absorbent pad. After printing, membranes were dried at 37°C in the oven for 1 hour. Finally, 3-mm half-stick LFAs were cut using a ZQ2002 Strip Cutter (Kinbio).

2.15 S1 LFA using VHHV3-AuNP

To perform the immunoassay, 10 µL of AuNP-VHHV3 bioconjugates (OD 2 at 530 nm) were added to a protein low-binding 96 well-plate (Greiner). Dilution series of the biotinylated S1-His antigen was prepared in blocking buffer (concentrations ranging from 2000 ng/ml to 0 ng/ml) and 5 µL of each dilution was added to the corresponding well containing the bioconjugates. After mixing well and a 5-minute incubation at room temperature, half-stick LFAs strips were inserted into each well. The assays were allowed to fully wick and air dry. Images of the LFAs were captured using a Canon PowerShot G15 camera in a lightbox and analysed using an in-house developed MATLAB software to analyse the maximum intensity of each assay's test line. Briefly, sections from the LFA images containing the test lines were manually selected, cropped, and separated to the green channel and the image was reduced to one dimension by averaging along the lateral axis. The background was determined by a 100-pixel area away from the test line and subtracted from the inverted trace. The signal is quantified as the maximum intensity point along the trace.

2.16 VHHV3-AuNP bioconjugate freeze-thaw and freeze-drying experiments

VHHV3-AuNP bioconjugates for storage stability studies were prepared as previously described. 10 µL aliquots of bioconjugate were dispensed into a 96 well-plate, covered with adhesive film, and frozen overnight at -80°C. For analysis, bioconjugates were thawed at room temperature for 30 minutes with shaking. Antigen dilutions were added directly to the 96 well-plate, and LFAs were performed as previously described. For freeze-drying experiments, nanoparticles were suspended in a running buffer containing 10% sucrose before dispensing into a 96 well-plate. The plate was covered with adhesive film and frozen overnight at -80 °C. Frozen bioconjugates were then freeze-dried overnight. To reconstitute, 10 μL of deionised water was added to each well containing freeze-dried bioconjugates and shaken on a plate shaker at 650 rpm for 10 minutes. Antigen was added directly to the same plate and incubated for 5 minutes before performing the LFAs.

2.17 Limit of detection analysis

Limit of detection analysis and statistical analysis of the dose-response data of the Cys mutant ELISA, the multivalent nanobody ELISA and nanobody-AuNP bioconjugate LFAs were performed using the software developed by Miller *et al*. based on methods developed by Holstein *et al.* by fitting a Langmuir function to the data.[87,88].LoD is defined as the calculated lowest concentration of analyte that can be statistically distinguishable from the blank.

2.18 In-vivo biotinylation of AVI-tagged nanobodies.

Chemically competent BL21 E. coli cells were transformed with the pBirAcm plasmid (AVIDITY) and plated onto LB-agar plates supplemented with 30 μg/mL of chloramphenicol and incubated for 16 hours at 37 °C. A single colony was picked from the plate and used to inoculate 10 mL of LB broth containing chloramphenicol and incubated at 37 °C in the shaker incubator at 180 rpm for 16 hours. Transformed cells were made chemically competent by inoculating 1 mL of starter culture to 100 mL of LB broth until the cells grew to an optical density (A600) of 0.3 – 0.5 (mid-log phase). Cells were harvested by centrifuging at 7,000 rpm. The cell pellet was resuspended in a chilled solution containing 100 mM $CaCl_2$ for 15 minutes and centrifuged again at 7,000 rpm. Cells were resuspended in a chilled solution containing 100 mM $CaCl_2$ and 15 %v/v glycerol. Aliquots of chemically competent cells transformed with the pBirAcm plasmid were retransformed with plasmids containing AVI-tagged nanobodies and plated on LB-agar plated supplemented with kanamycin and chloramphenicol. A single colony of the dual-plasmid strain was inoculated into 10 mL of sterile LB broth containing appropriate antibiotics and grown overnight at 37 °C with shaking at 250 rpm. Starter cultures were used to inoculate 400 mL of LB media and grown until OD reached 0.6. Protein expression was induced with the addition of IPTG to a final concentration of 1.5 mM and the addition of d-biotin (dissolved in 10 mM HEPES buffer pH 8.2) to a final concentration of 50 µM. Periplasmic expression, extraction and IMAC purification were completed as already described in section 2.2.

2.19 Nanobody-SA-AuNP LFA assay

The LFA developed in section 5.9 involves the use of biotinylated nanobodies decorated onto streptavidin AuNP bioconjugates mixed with samples containing the SARS-CoV-2 protein and running on nitrocellulose strips decorated an Anti-SARS-CoV-2 S1 mAb D003. For the nanobody decoration process, 240 µL of Streptavidin-AuNPs (SA-AuNP, Abcam) at a concentration of OD 2.5 (A530) were placed in a 1 mL protein low binding, microcentrifuge tube. 60 µL of 5× AVI tagged nanobody (VHHV-AVI or VHHV2-AVI) stock was added to the tube containing the SA-AuNP. The conjugation was left for 30 minutes on the thermal shaker at room temperature. 300 µL of blocking buffer (2% w/v BSA in pH 8.5 100mM HEPES, 0.1% v/v Tween 20) was added to the tube and incubated for another 30 minutes. Nanobody-decorated bioconjugates were washed twice through centrifugation, removal of the supernatant and replacement with blocking buffer. Bioconjugates were immediately used. Nitrocellulose strips bearing D003 mAb as a test line were prepared as described in section 2.13. Dispensing of the antibody onto nitrocellulose card was performed using the biodot dispensing system at 1 mg/mL antibody concentration diluted in water. LFA was performed by mixing 10 µL of nanobody decorated SA-AuNP with the 5µL of samples containing different concentrations of the S1 protein (concentrations ranging from 1000 ng/ml to 0 ng/ml) diluted in blocking buffer. After 5 minutes of incubation, nitrocellulose strips were added to each well and left to fully wick and dry. Signal capture and quantification were performed as described in section 2.14 S1 LFA using VHHV3-AuNP.

2.20 D003-AuNP nanobody-PSA LFA

The LFA developed in section 5.10 involved using D003-AuNP mixed with samples containing the S1 protein and biotinylated detection nanobodies (VHHV-AVI, VHHV2-AVI, VHHV3-AVI). D003 conjugation to AuNP was performed using physisorption. 100 µL of D003 antibody at 62.9 ug/mL (PBS) were added to 100 µL of 100 mM borate buffer at pH 9.0 and 800 µL of OD1.25 (A530) citrate capped AuNPs. Conjugation was performed for 1 hour, blocked for another hour in blocking buffer (2% w/v BSA in 100mM Borate pH 9.0 0.1% v/v Tween-20). Blocked bioconjugates were washed twice using centrifugation. PSA-bearing nitrocellulose strips were prepared as described. LFA was operated with the mixing of 10 µL D003-AuNP at OD2 (A530) with 5 µL of samples containing different concentrations of the S1 protein (concentrations ranging from 1000 ng/ml to 0 ng/ml) diluted in blocking buffer and 5 µL of capture nanobody dilutions in blocking buffer. After 5 minutes of incubation PSA LFA were placed into the wells containing the mixture and were left to fully run and dry. Signal capture and quantification were performed as described in section 2.14 S1 LFA using VHHV3-AuNP.

2.21 Fully modular LFA operation

The fully modular LFA is a 2-step assay. In the first step the capture nanobody (200 nM) diluted in running buffer (2% w/v BSA in 100mM Borate pH 9.0 0.1% v/v Tween-20) is mixed (96 well-plate low protein binding) with samples containing different concentrations of the S1 protein (concentrations ranging from 1000 ng/ml to 0 ng/ml) diluted in running buffer and were left to incubate for 5 minutes before running the LFA strips with PSA test lines. The second step involves applying the detection nanobody decorated SA-AuNPs to the LFA strip. 10 µL of bioconjugates suspended in a running buffer are added to a well. After 5 minutes the strips already containing the capture nanobody and sample are placed in the well containing the bioconjugates and left to fully run and dry. Nanobody-decorated bioconjugates prepared as described in section 2.18. PSA-bearing nitrocellulose strips were prepared as described.

Signal capture and quantification were performed as described in section 2.14 S1 LFA using VHHV3-AuNP.

3 Direct immobilisation of monomeric nanobodies on gold nanoparticles

3.1 Introduction

Antibodies have been extensively utilised as biorecognition molecules in lateral flow assays (LFA) due to their high specificity and affinity for target analytes.[89] However, the development and production of antibodies are costly and complex processes, often posing a significant bottleneck in the development of diagnostic immunoassays, which can have severe impacts when controlling rapidly spreading infectious diseases.[90] Nanobodies, which are single-domain antibody fragments derived from camelids, offer a promising alternative.[91] Nanobodies can be rapidly generated using phage display or synthetic libraries, often within a timeframe as short as three weeks.[33,78] This streamlined development process significantly reduces the time and cost associated with developing biorecognition molecules for LFA. More recently, developments in de novo binder design have enabled the generation of functional nanobodies with no reliance on animal use.[77] Unlike traditional antibodies requiring costly mammalian cell cultures, nanobodies can be easily produced in bacteria at high yields.[92] This simplifies production and enables a decentralised model, empowering diverse stakeholders to produce their own nanobody-based tools. Furthermore, nanobodies' smaller size and stability offer advantages in binding cryptic epitopes and resisting mutational escape.[93]

A crucial step in the LFA development is the bioconjugation of recognition molecules onto gold nanoparticles (AuNP), which serve as the labels in the assay.[5] The smaller size of nanobodies, compared to traditional antibodies, promises increased coating densities on sensor surfaces, which has been shown to improve sensitivity.[94] While various nanobody bioconjugation chemistries exist, including click chemistry, *N*-hydroxysuccinimide (NHS) and maleimide pre-activated kits, SpyTag/SpyCatcher mediated and site-specific biotinylation, passive adsorption offers a simple, cost-effective, and scalable approach.[35,81,95–97] However, as highlighted by Goossens *et al.*, nanobody-AuNP bioconjugates generated through passive adsorption are prone to nanoparticle aggregation.[58] Nanoparticle stability is a pressing issue for LFA bioconjugates, as LFAs are valued for their ability to be stored in ambient conditions and must, therefore withstand multiple processing steps, including blocking, washing, and drying.[5]

In this study, a comprehensive analysis of the stability limitations of AuNP-nanobody bioconjugates formed via physisorption was performed. Focusing on SARS-CoV-2 spike glycoprotein-specific nanobodies, the stability of AuNP-nanobody was investigated under varying ionic strengths and using two common AuNP sizes used in commercial LFAs. Typically, bioconjugation of antibodies to citrate-capped AuNPs relies on electrostatic interactions between charged and hydrophobic residues, occurring at a pH slightly above the antibody's isoelectric point (IEP). Recognising that nanobody charge and sequence diversity can influence AuNP interactions, three nanobodies with varying IEPs (6.70 – 9.39) were selected: VHHV and VHHE (developed by Koenig *et al.*), and Nb6 (developed by Schoof *et al.*), the nanobody sequences and charge distribution maps are shown in Figure 3.1. This selection allows the evaluation of how each nanobody undergoes physisorption onto AuNPs at different pHs. The chosen nanobodies, exhibiting high affinity for their target antigen (indicated by low dissociation constants), enhance their diagnostic potential.

Through this study, it was identified that nanobody bioconjugates, in their native form, are unable to withstand exposure to elevated ionic strengths when conjugated to larger 40 nm AuNPs, simulating the harsh processing steps they must endure during bioconjugate synthesis, purification, and preparation for storage, including lyophilisation. Only moderate resistance to aggregation was observed with smaller 20 nm nanoparticles under mildly

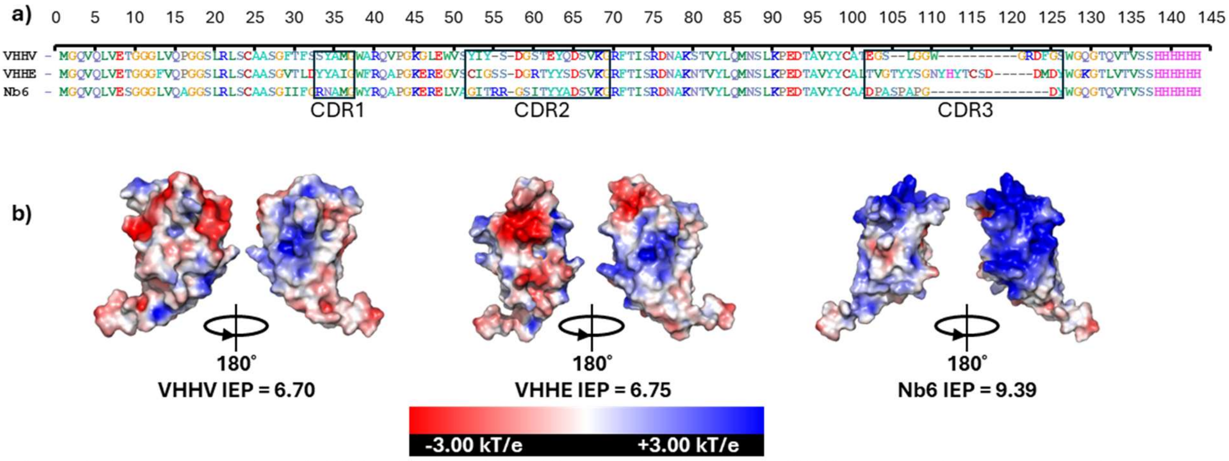

Figure 3. 1 Characteristics of VHHV, VHHE and Nb6 Nanobodies. (a) *ClustalW alignment of the amino-acid sequences* of the selected nanobody candidates. Boxes represent the three complementarity-determining regions (CDR) of each nanobody. (b)Surface charge distribution of the 3 nanobodies, blue represents positive potential and red represents negative potential from -3kT/e to +3kT/e at pH 7. Surface and IEP calculations were performed using the APBS biomolecular solvation.[146] Nanobody 3D structures predicted by AlphaFold 2 using the accessible colabfold server.[147,148]

elevated ionic strength conditions. To address this limitation, free cysteines were incorporated into the lead nanobody candidate (VHHV), aiming to improve loading density and stability by directly covalently coupling the nanobody to the nanoparticle surface.[36,63] This simple modification showed promise in preventing aggregation under elevated ionic strength conditions for the less stable but analytically more suitable 40 nm AuNPs, highlighting that both the presence and the position of the free cysteine can influence he stability of the resulting bioconjugates. While complete prevention of salt-induced aggregation was not achieved, significant insights were gained into the limitations of nanobody bioconjugates in their native form and the potential for improvement through cysteine protein engineering and selection of buffers.

3.2 Results and discussion

3.2.1 Recombinant nanobody design, expression and characterisation

The selected nanobody constructs were fused with PelB signal sequences and hexahistidine tags to enable expression in the bacterial periplasm and purification using Ni-NTA affinity chromatography. The final nanobody sequences are shown in Figure 3.1a. The activity of the recombinantly expressed nanobodies was confirmed through a direct ELISA that assessed the binding of each nanobody to the SARS-CoV-2 receptor binding domain (RBD). To enable signal generation using a horseradish peroxidase-streptavidin conjugate (SA-HRP), each nanobody was biotinylated using an NHS-PEG12-Biotin ester linker. Limit of detection (LoD) analysis (section 2.17) of the ELISA results revealed distinct analytical performance characteristics among the nanobodies. Using VHHE as the detection nanobody resulted in the lowest LoD at 196.4 pM, followed closely by VHHV at 200.4 pM (Figure 3.2). Notably, Nb6 displayed a considerably weaker analytical performance, generating a higher LoD of 4331 pM,

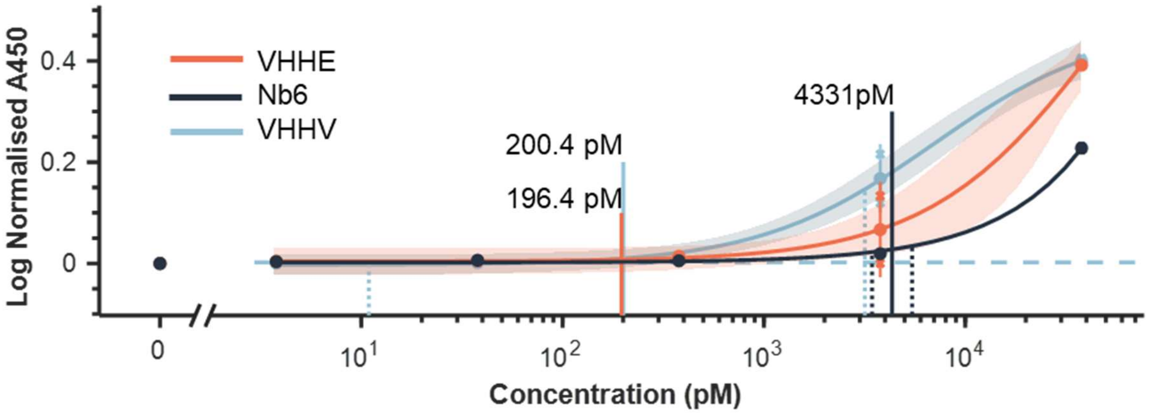

Figure 3.2 Native nanobody ELISA. Concentration-response curves for chemically biotinylated nanobodies VHHV, VHHE and Nb6 as ELISA detection reagents for SARS-CoV-2 RBD protein. Solid lines: fitted Langmuir functions for VHHV, VHHE and Nb6 with limits of detection presented as vertical lines. Solid circles show the mean value for each point (n=2) ± the standard deviation of the mean. Dotted vertical lines show the 95% confidence intervals for each series.

likely attributable to its higher dissociation constant (K_D) of 210 nM compared to VHHV and VHHE (8.92 nM and 1.86 nM, respectively). These findings confirm the binding of the recombinantly expressed nanobodies and underscore the importance of nanobody affinity in assay sensitivity, highlighting the potential of VHHV and VHHE as superior candidates for diagnostic applications.

3.2.2 Nanobody-AuNP bioconjugate formation and characterisation

The conjugation of immunoglobulin antibodies to citrate-capped AuNPs *via* physisorption relies on electrostatic interactions, typically yielding stable bioconjugates when the bioconjugation is performed at a pH slightly above the antibody's IEP.[61] This delicate balance in protein charge is essential. At pH values below the IEP, the overly positively charged antibody can overcome inter-particle repulsion, leading to cross-linking and aggregation. Conversely, at pH values much higher than the IEP, the net negative charge of the protein repels the negatively charged AuNP, preventing attachment. A common technique to assess protein physisorption onto AuNPs involves screening pH conditions during bioconjugation and monitoring changes in the stability of the nanoparticles or resulting bioconjugates.

In LFAs, AuNP size is crucial. Smaller AuNPs diffuse better (increasing reactivity) but produce weaker signals. Larger AuNPs offer stronger signals but diffuse less effectively. Generally, 40 nm AuNPs provide an optimal balance for LFAs. The physisorption of nanobodies VHHV, VHHE and Nb6 onto 40 nm AuNPs was evaluated at various pH values using a 3200:1 or 9600:1 molar excess of nanobodies to nanoparticles. These ratios were specifically chosen to ensure a high excess of nanobody relative to the nanoparticle surface area, thereby promoting saturation of the AuNP surface. Considering the dimensions of a typical nanobody (4 nm x 2.5 nm x 2.5 nm) and the surface area of a 40 nm AuNP, it was estimated that a close-packed monolayer would require approximately 500 to 800 nanobodies, depending on their orientation.[98] Localised surface plasmon resonance (LSPR) peak wavelengths were measured using UV-Vis spectroscopy to monitor transitions from stable to unstable states, as indicated by a decrease in intensity and broadening of the LSPR peak, indicative of nanoparticle aggregation. Aggregation was quantified using the aggregation index specific for 40 nm AuNPs (A50/530), defined as the ratio of absorbance at the plasmon shoulder (580 nm) to the absorbance at the plasmon peak (530 nm).[98]

A strong physisorption pH dependence on nanoparticle stability was identified for each nanobody during nanobody-AuNP bioconjugate formation. At low ionic strengths (10 mM), nanobody-AuNP bioconjugates with an A530/580 approaching 0.5 could be produced at defined pH ranges, indicating stable AuNPs. Using the most acidic nanobody VHHV (IEP = 6.70), physisorption yielded stable bioconjugates at pH conditions above 6.5 and aggregated

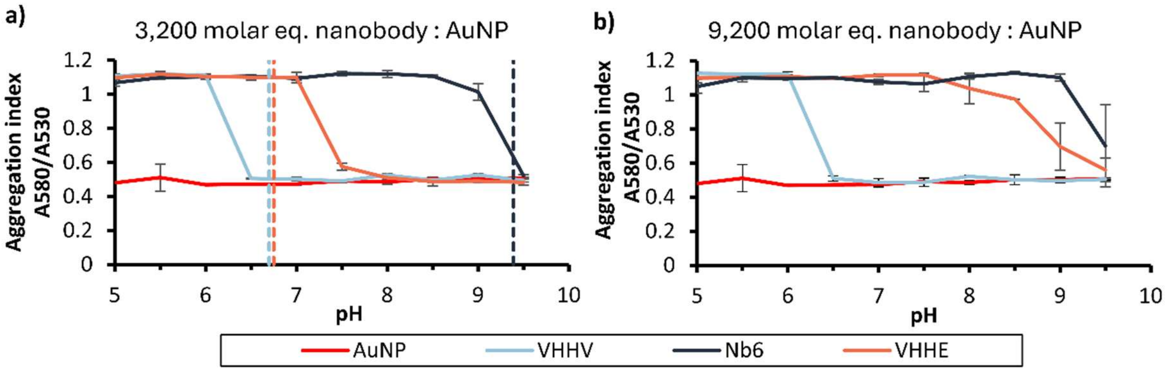

Figure 3. 3 Adsorption characteristics of anti-SARS-CoV-2 nanobodies on 40 nm AuNPs. Aggregation index plots for each nanobody conjugation across a range of pH conditions at either (**a**) 3,200 or (**b**) 9,200 molar equivalents. Dashed lines represent the IEP for each nanobody. Values are shown as the average (n = 3) and error bars indicate the standard deviation of the mean.

conjugates below pH 6.5 (Figure 3.3a). The most basic nanobody Nb6 (IEP = 9.39) yielded stable bioconjugates at a pH greater than 9.5. Nanobody VHHE (IEP = 6.75), however, required comparatively elevated pH conditions (pH >7.5) in order to obtain stable bioconjugates. Increasing the molar excess of VHHV and Nb6 (9,600 eq.) did not alter bioconjugate stability, suggesting no further modification is achieved with nanobody excess greater than 3,200 molar equivalents (Figure 3.3b). However, the same increase in molar excess of VHHE to AuNP was detrimental, causing aggregation across a wider pH range, potentially due to VHHE-VHHE interactions leading to nanoparticle bridging. To test this, a homologous sandwich ELISA was performed, using VHHE as both the capture and detection nanobody. Given that the VHHE-VHHE detection-capture pair generated the highest signal in the sandwich ELISA suggests potential protein-protein interactions between VHHE molecules, supporting the initial hypothesis (Figure 3.4). The presented data, being generated from single measurements, provides a qualitative assessment.

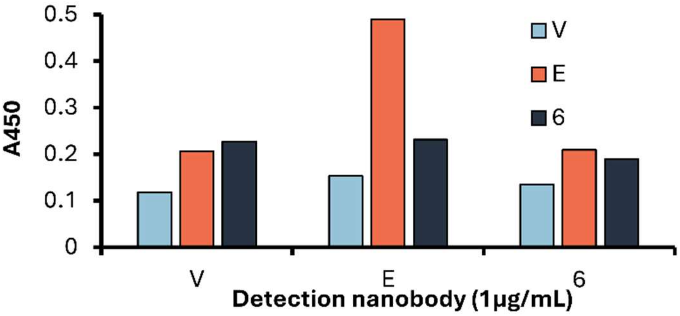

Figure 3. 4 Native nanobody sandwich ELISA. Assessing the background signal generated by the interaction of the capture and detection nanobodies in the absence of the antigen (RBD) n=1. V – VHHV, E – VHHE, 6 – Nb6.

The physisorption process was further analysed using two approaches: the emergence of a redshift in the LSPR maximum resulting from local dielectric changes on protein binding to AuNPs and the stability of the bioconjugates to elevated salt concentrations. The immobilisation of all 3 nanobodies onto AuNPs was found to result in a subtle redshift of about 5 nm as observed by UV-Vis spectroscopy, consistent with modification of the nanoparticle surface by protein (Figure 3.5a).[99] While a protein monolayer may exist on the AuNP bioconjugate, this does not necessarily mean the nanoparticle is sufficiently stable to endure

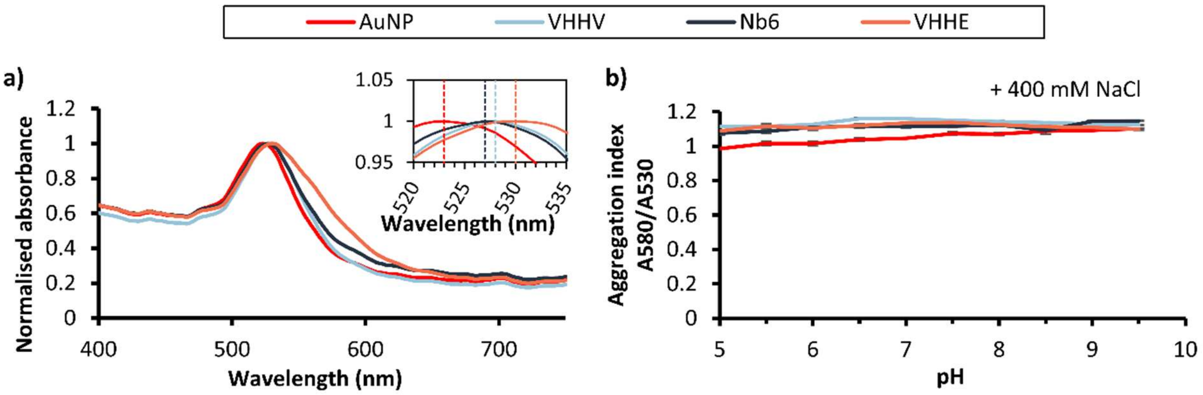

Figure 3. 5 Evaluation of bioconjugate stability from nanobody bioconjugation on 40 nm AuNPs. (**a**)UV-Vis spectra of each nanobody bioconjugation reaction at the first stable pH condition for nanobodies VHHV (pH 6.5), VHHE (pH 7.5) and Nb6 (pH 9.5). Dashed lines in the subplot show the position of the plasmon peak (**b**) Aggregation index plots for each nanobody after increasing the NaCl concentration to 400 mM. Values are shown as the average (n = 3) and error bars indicate the standard deviation of the mean

the harsh processing steps and operate within the conditions of an LFA. The bioconjugates were therefore tested for stability by increasing the ionic strength of the solution through the addition of 400 mM of NaCl. The choice of using a 400 mM final NaCl concentration is to expose the bioconjugates to a high ionic strength. This not only simulates the elevated ionic strengths of physiological samples, which can range from 50 - 150 mM depending on the sample, but also ensures a sufficient stress test to indicate the ability of the bioconjugates to endure downstream processing steps such as lyophilisation. High ionic strengths cause a shortening of the length of the electric double layer between two approaching bioconjugates, which is crucial for maintaining colloidal stability. If the surface has been sufficiently covered by protein, the colloid can be protected from salt-induced aggregation since the protein layer creates a steric, charged barrier around the nanoparticles, preventing the electron-dense gold from directly contacting each other *via* Van der Waals interactions.[100] Bare AuNPs readily aggregate in solutions with 50 mM NaCl. Operating the salt stress test in this excess enables probing for any stabilisation gained through the formed protein layer.[101] As shown in Figure 3.5b, physisorbed nanobodies do not prevent the salt-induced aggregation observed for bare AuNPs, consistent with previous findings.[58]

Dynamic light scattering (DLS) was used to characterise the nanobody layer formed through bioconjugation by measuring changes in hydrodynamic diameter (calculated by intensity)

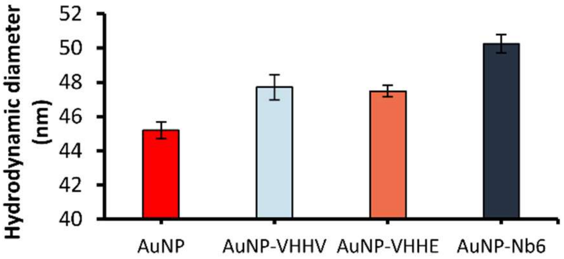

Nanobody	Dimensions (nm)	Measured change in diameter (nm)
VHHV	4.68 × 3.29 × 2.64	2.52
VHHE	5.36 × 3.29 × 3.60	2.29
Nb6	4.35 × 3.47 × 2.89	5.05

Figure 3. 6 DLS analysis of 40 nm AuNP nanobody bioconjugates. Hydrodynamic diameter of bare AuNP and bioconjugate for each nanobody immediately following physisorption. Values are shown as the average (n = 3), and error bars indicate the standard deviation of the mean. The table shows the dimensions of each nanobody calculated using the PDB structures and the measured change in hydrodynamic diameter compared to bare AuNP.

compared to bare AuNPs. An increase in hydrodynamic diameter was noted post-bioconjugation with VHHV (47.7 nm ± 0.7), VHHE (47.5 nm ± 0.3), and Nb6 (50.2 nm ± 0.5) compared to bare AuNPs (45.2 nm ± 0.5), confirming surface modification. However, given the dimensions of each nanobody, shown in the table in Figure 3.6, determined from the Protein Data Bank structures, the calculated diameter changes for each bioconjugate post-physisorption fall short of the expected changes following the formation of a protein monolayer. This finding is consistent with the results from Simões, where nanobodies were used to modify the surface of a gold sensor. In this example, the author claimed a similar 1.99 nm increase in thickness generated by the nanobody monolayer, which was much less than the expected value measured using ellipsometry.[102] Nb6 showed a larger increase of 5.05±0.73 nm, consistent with a monolayer, despite not providing enough steric repulsion at high ionic strengths. The values obtained by DLS suggest that the nanoparticles are either not fully covered by nanobodies or that nanobodies unfold upon binding to the particle surface.

The findings here are consistent with the literature studying nanobody physisorption onto AuNPs. In the studies by Goossens and Hattori, nanobodies in their native form were shown to produce stable bioconjugates at defined pH conditions. While exhibiting evidence for successful immobilisation, they failed to completely prevent salt-induced aggregation. However, Chen *et al*. utilise the nanobody-induced aggregation of AuNPs to generate a competitive SPR-based biosensor. In this study, the authors claim nanobody-induced aggregation to be a universal property of nanobodies. This is in striking contrast to the findings in this thesis and those by Hattori and Goossens, where stable bioconjugates are generated and remain stable at low ionic strengths. Indeed, the authors show that the nanobody used in the biosensor causes nanoparticle aggregation in the absence of a salt stress test (ionic strength is not reported), irrespective of the solution pH (pH 6-10), even though the calculated IEP of the nanobody is relatively low (IEP = 6.63). Furthermore, a panel of nanobodies was tested, displaying varying degrees of aggregation when physisorbed onto nanoparticles. It is possible that these are different mechanisms of aggregation. In the case of salt-induced aggregation, the bioconjugates fail to provide sufficient protection to the nanoparticles, causing aggregation. At low ionic strengths, when the pH is below the protein IEP, nanoparticle bridging is mediated by the overly positive charge of the protein. However, when aggregation is observed at a pH greater than the protein's IEP, this could be due to other mechanisms, such as protein-mediated interaction through aggregated nanobodies or interaction of the immobilised nanobodies with other nanoparticles. It is important to note that we have observed this effect with VHHE, where nanoparticle aggregation occurs at a pH greater than the protein's IEP and increasing nanobody concentration is detrimental to stability. The smaller size of nanobodies compared to IgG antibodies might limit their ability to stabilise AuNPs upon physisorption due to reduced steric repulsion. Additionally, proteins can be prone to unfolding on nanoparticle surfaces, further contributing to aggregation.[69]

3.2.3 Stability assessment of nanobody-functionalised 20 nm AuNPs under varying Ionic strengths

In the previous section, the ability of nanobodies to stabilise 40 nm AuNPs upon immobilisation was investigated. The size of AuNPs in LFAs significantly impacts their analytical performance.[103] Smaller nanoparticles exhibit greater diffusivity, leading to increased reactivity but they also have a smaller extinction cross-section, leading to weaker signal generation per binding event. Conversely, larger nanoparticles offer stronger signal generation but may have reduced diffusivity.[52] It is generally accepted that AuNPs around 40 nm in diameter strike an optimal balance between these factors for LFA applications, motivating their use in the previous section.[103,104] However, given the observed limitations of nanobodies in stabilising 40 nm AuNPs, their capacity to stabilise smaller 20 nm AuNPs was investigated. Although the resulting analytical performance might theoretically be weaker, 20 nm AuNPs tend to be more stable than AuNPs with larger diameters.[105]

Similar to the previous section, the stability profile of VHHV, VHHE, and Nb6 AuNP bioconjugates was monitored through the aggregation index profile as a function of pH during the conjugation reaction. However, since the surface area of 20 nm AuNPs is approximately four times smaller than that of 40 nm, the conjugation reaction was carried out at 800 nanobody equivalents to AuNPs to ensure a comparable ratio of nanobodies to the available surface area.

Prior to salt addition, the expected relationship between IEP, conjugation pH, and the stability of the resulting bioconjugates within specific pH ranges was observed. For VHHV, stable bioconjugates are formed at pH values above 6.5 (Figure 3.7a), mirroring the stability profile observed with 40 nm AuNPs. VHHE and Nb6 require pH values above 7.0 and 8.5, respectively, for stable bioconjugate formation. Compared to the conjugations using 40 nm AuNPs, VHHE and Nb6 form stable bioconjugates at lower pH values when 20 nm AuNPs are used. This likely reflects the enhanced colloidal stability of the smaller 20 nm nanoparticles, which are less prone to aggregation due to weaker Van der Waals forces. The formation of a

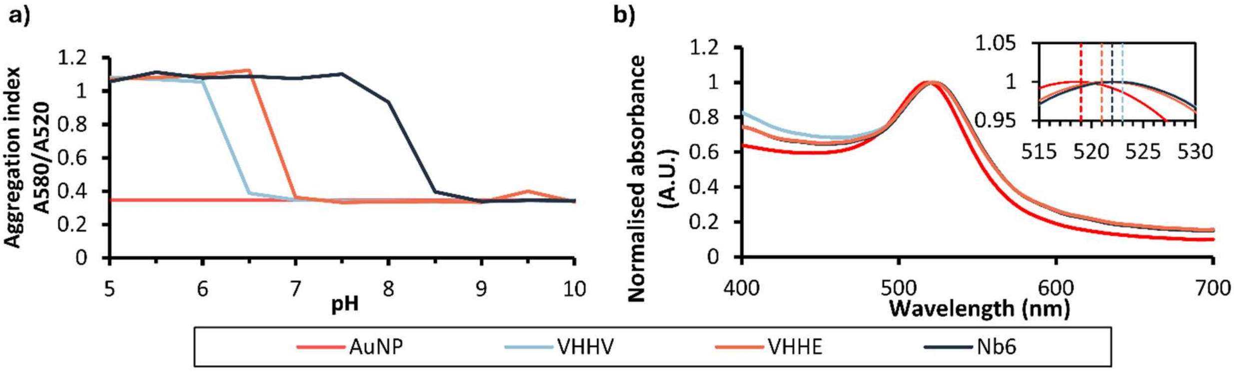

Figure 3. 7 Adsorption characteristics of anti-SARS-CoV-2 nanobodies on 20 nm AuNPs. (**a**) Aggregation index plots for each nanobody conjugation across a range of pH conditions n =1. (**b**) UV-Vis spectra of each nanobody bioconjugation reaction at the first stable pH condition for nanobodies VHHV (pH 7.5), VHHE (pH 8.0) and Nb6 (pH 9.5). Dashed lines in the subplot show the position of the plasmon peak.

protein layer on the surface of the 20 nm AuNPs is confirmed by the observation of a slight redshift of approximately 3 nm in the LSPR peak, consistent across all three nanobodies.

To assess the suitability of these bioconjugates for LFA applications, their stability was further examined by increasing the ionic strength of the solution through the addition of 400 mM of NaCl. Similar to the observations with 40 nm AuNPs, all three nanobodies failed to provide sufficient protection, as the bioconjugates rapidly aggregated upon NaCl addition (Figure 3.8). The only exception was VHHE, which showed a modest improvement in stability at high pH values (9.5 - 10.0). However, even at these pH conditions, complete stability was not maintained.

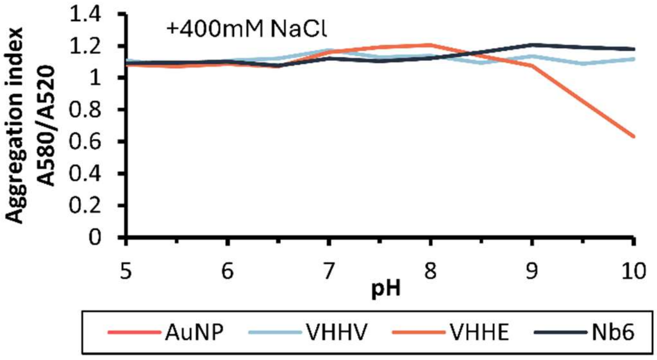

Figure 3. 8 20 nm AuNP bioconjugate aggregation assessment. Aggregation index plots for each nanobody after increasing the NaCl concentration to 400 mM (n = 1).

3.2.4 Establishing a benchmark for AuNP-nanobody bioconjugate stability

To further investigate the limitations of nanobody-AuNP bioconjugate stability against salt-induced aggregation, a side-by-side comparison of bioconjugates formed using 40 nm and 20 nm AuNPs was conducted under mildly elevated ionic strength conditions (200 mM NaCl). This intermediate salt concentration was chosen to assess whether the reduced Van der Waals forces in smaller 20 nm AuNPs could provide any advantage in resisting aggregation compared to the larger 40 nm AuNPs

By conducting this side-by-side comparison, the exact limitations of nanobody bioconjugates against salt-induced aggregation were identified, considering both the concentration of NaCl

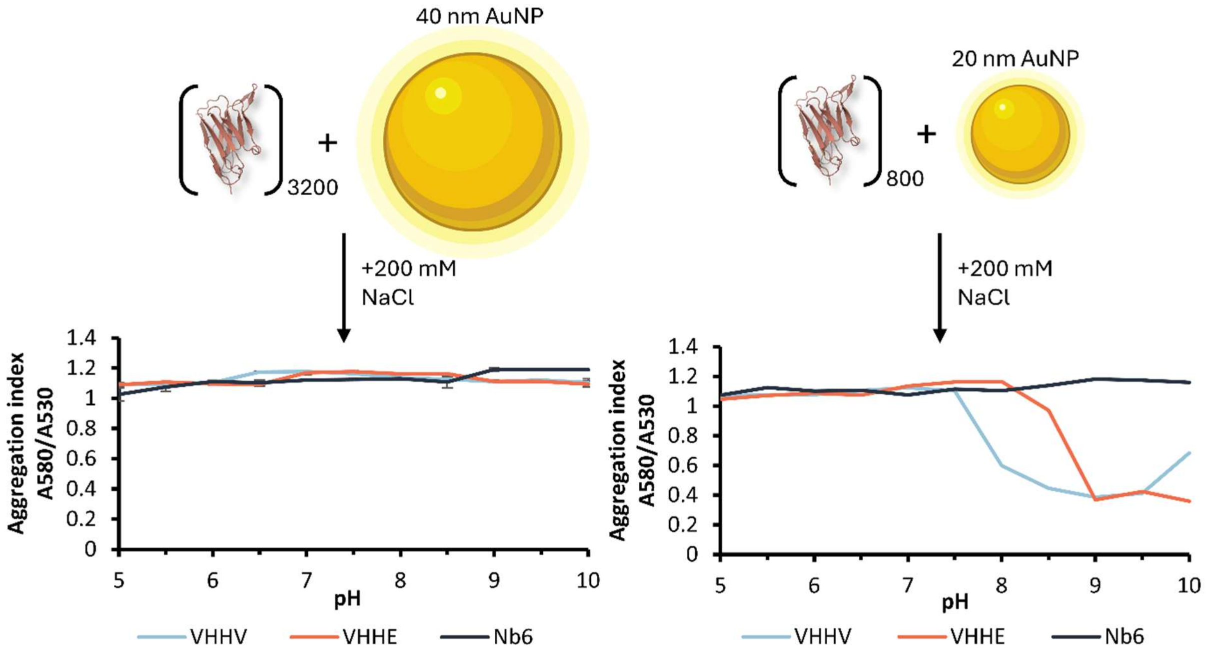

Figure 3.9 Comparison of stability of 40 nm AuNP bioconjugates against 20 nm AuNP bioconjugates after adding 200 mM NaCl simulating mild ionic strength test. (**a**) Aggregation index plots for nanobody conjugation to 40 nm AuNPs following the addition of 200 mM NaCl across a range of pH conditions. Values are shown as the average (n = 3), and error bars indicate the standard deviation of the mean. (**b**) Aggregation index plots for nanobody conjugation to 40 nm AuNPs following the addition of 200 mM NaCl across a range of pH conditions (n=1).

used for the salt stress test and the AuNP size. For the 40 nm conjugations the reduced concentration of NaCl (200 mM) was used for the salt stress, as all three nanobodies rapidly aggregated under these conditions (Figure 3.9). Interestingly, for the 20 nm bioconjugations at milder ionic strengths, VHHV and VHHE bioconjugates prevented salt-induced aggregation. This suggests that the reduced Van der Waals forces in the smaller AuNPs, combined with the specific properties of VHHV and VHHE, were sufficient to maintain stability under these conditions. However, Nb6 bioconjugates aggregated across all pH conditions, regardless of ionic strength. The reason for Nb6's inability to prevent salt-induced aggregation under these conditions remains unclear but could be due to the higher IEP of the nanobody compared to VHHV and VHHE. Our findings are in close agreement with the previous study by Goossens and colleagues, where they reported that their most acidic nanobody, possessing a low IEP, was the only one that maintained colloidal stability after salt-induced aggregation. Furthermore, the study was performed using 20 nm AuNPs and 1% NaCl concentration (~171 mM) used for the salt stress tests which closely match our experimental parameters.

The results here confirm that only VHHV and VHHE, both with lower IEPs than Nb6, resisted aggregation at 200 mM NaCl using 20 nm AuNPs.

While these findings confirm that nanobodies offer limited protection against salt-induced aggregation, with some protection observed when smaller nanoparticle sizes are used and no protection with larger ones, a clear benchmark for the stability of these nanobody bioconjugates was established. However, without a full titration to determine the precise salt concentration at which aggregation begins, the exact "point of failure" for the bioconjugates is not established. This benchmark will still be valuable for future research aimed at improving nanoparticle stability, as new approaches can be directly compared to the results presented here, providing a clear reference point for evaluating enhanced performance.

The following section will explore the incorporation of a free cysteine residue into the nanobody construct as a strategy to enhance nanoparticle stability. By enabling directed immobilisation through thiol-gold chemistry, the aim is to increase loading density and optimise nanobody presentation, potentially addressing the limitations observed in the passive adsorption approach and improving the overall performance of nanobody-AuNP bioconjugates for LFA applications.

3.2.5 Generation of cysteine-bearing nanobodies

Thiol groups, typically found in cysteine residues of proteins, can form stable dative covalent bonds with the AuNP surface.[55,106] While methionines also contain a thiol group, they interact poorly with gold.[102,107] Nanobodies usually possess two cysteine residues, which are typically involved in intramolecular disulfide bonds, rendering them inaccessible for AuNP immobilisation. Previous work has established that engineering cysteines on nanobodies can improve their binding to gold surfaces, including surface plasmon resonance gold chips and AuNPs, enabling increased nanobody immobilisation density and functionality.[84,102]

A strategy was implemented to engineer cysteines onto the VHHV nanobody, aiming to link the nanobody covalently to the surface in order to enhance the stability of nanobody-AuNP bioconjugates towards elevated ionic strength. The VHHV nanobody was selected for the Cys-bearing nanobody generation since VHHV-AuNP displayed the greatest stability over the broadest range of pH at low ionic strengths of the nanobodies studied. Two cysteine-bearing variants of VHHV were created with cysteine residues at different positions to study the influence of both the presence and location of the free thiols on bioconjugate stability. One of the variants contained a cysteine on the C-terminus, following the hexahistidine tag and distal to the paratope (VHHV-Cys), and the other presented a cysteine at the N-terminus (Cys-VHHV). A further nanobody was designed with a free cysteine at each terminus (Cys-VHHV-Cys) in order to act as an intermediate, but this construct was not successfully expressed.

Protein engineering enables tailoring of protein function, but it can also introduce unintended consequences such as misfolding and reduced affinity, requiring stringent characterisation. The presence of free cysteines in the engineered cys-bearing nanobodies can lead to dimerisation between two nanobodies linked *via* their free cysteines through a disulphide bridge since they are expressed in the oxidative conditions of the bacterial periplasm. SDS-PAGE analysis was performed under non-reducing conditions in order to examine any potential dimerisation. Matching its expected molecular weight (14.23 kDa), VHHV showed a single band around 15 kDa (Figure 3.10a, b). In contrast, Cys-VHHV and VHHV-Cys appeared as two distinct bands in the SDS-PAGE gel protein profile, one corresponding to the nanobody monomeric band and a heavier band consistent with dimer formation. To study the effect of the single free cysteine on AuNP physisorption, the dimers would have to be broken down into their monomeric form. To achieve this, each of the cys-bearing nanobodies, in their as-expressed form, were treated with 10 mM TCEP-HCl, which is a mild reducing agent and they were readily reduced down to monomers (Figure 3.10) as previously shown.[108] This is evident by the disappearance of the heavier band corresponding to the dimer in the Cys-VHHV and VHHV-Cys samples when run on an SDS-PAGE gel under non-reducing conditions. The reduction reaction also carries the risk of reducing the internal disulfide bridge, which could have an impact on functionality, protein stability and the creation of further unintended binding sites that could complicate binding to the AuNP.

Liquid chromatography-mass spectrometry (LC-MS) was employed to verify both the reduction of the dimerised VHHV-Cys construct to its monomeric form and the integrity of its internal disulfide bond. Prior to analysis, VHHV-Cys was reduced with TCEP-HCl, and the reaction was quenched using the thiol-reactive reagent N-methylmaleimide (NMM). The presence of a single peak corresponding to the molecular weight of one VHHV-Cys molecule bound to a single NMM molecule indicated successful dimer reduction (Figure 3.10d). Additionally, this result confirmed the integrity of the internal disulfide bond, as its reduction would have resulted in mass additions that would reflect multiple free sulfhydryl groups reacting with NMM.

To investigate potential functional changes caused by the cysteine addition or subsequent TCEP reduction process, the analytical performance of VHHV, VHHV-Cys, and Cys-VHHV

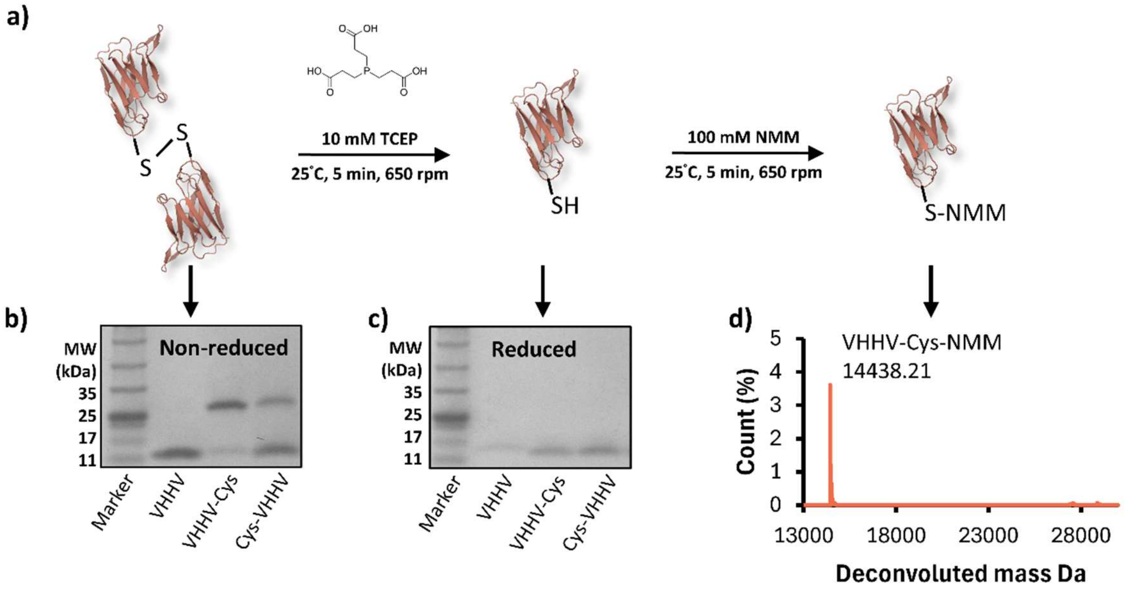

Figure 3.10 Cys-nanobody reduction and characterisation. (a) Schematic showing the reduction of the dimerised nanobody to the monomer using TCEP-HCL and the capping of the free cysteine with NMM for LC-MS characteriation. (**b,c**) SDS-PAGE showing the profile under non-reducing conditions before (**b**) and after reaction with TCEP-HCL (**c**) LCMS spectra for VHHV-Cys after reduction with 10 mM TCEP, desalting, and reaction with N-Methylmaleimide (NMM) using LCMS. The addition of one NMM molecule (111.1 g/mol) to VHHV-Cys (14328.83 g/mol) was observed. The absence of a peak at 28657.3 g/mol indicates complete reduction of the intermolecular disulfide bond, breaking the dimer into monomers. Additionally, the absence of peaks at 14,551.03 g/mol and 14,662.13 g/mol confirms that the internal disulfide bond remained intact. Reduction of this bond would enable the reaction of multiple NMM molecules per nanobody.

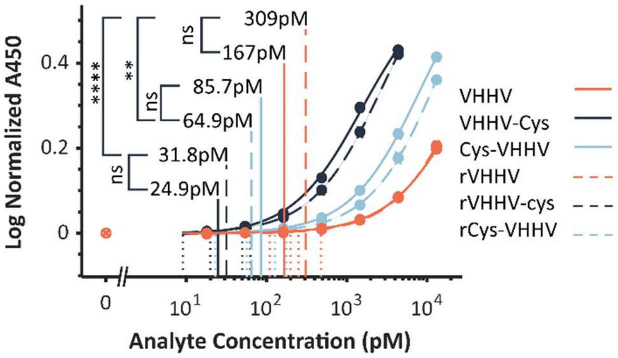

Figure 3.11 Cys bearing VHHV nanobody ELISA. Concentration-response curves for native and cysteine-bearing nanobodies (reduced and non-reduced) as ELISA capture reagents for biotinylated SARS-CoV-2 S1 protein. Dashed lines: fitted Langmuir functions for reduced nanobodies (VHHV, VHHV-Cys, Cys-VHHV) with limits of detection Solid lines: fitted Langmuir functions for non-reduced nanobodies with limits of detection. Solid circles show the mean value for each point (n=3), while dotted lines show the 95% confidence intervals for each series. Significance was calculated using a two-tailed t-test and denoted as ns – $p > 0.05$, **–$p < 0.01$, ****–$p < 0.001$.

was compared using an ELISA. Reduced and non-reduced versions of each nanobody were immobilised on polystyrene plates, and LoD analyses were conducted for the detection of the chemically biotinylated S1 protein. The amine-reactive crosslinker NHS-PEG12-Biotin was used to functionalise the S1 protein with biotin, enabling the use of streptavidin-HRP for signal generation. No significant differences in LoD between non-reduced and reduced versions of VHHV, VHHV-Cys, and Cys-VHHV (denoted as rVHHV, rVHHV-Cys and rCys-VHHV respectively) were observed as illustrated in Figure 3.11. Intriguingly, rVHHV-Cys and rCys-VHHV demonstrated significantly improved LoD compared to the non-Cys-bearing rVHHV. While rVHHV exhibited a LoD of 167 pM (110 – 252 pM, 95% CI), rVHHV-Cys and rCys-VHHV showed LoDs of 31.8 pM (19.9 – 50.0 pM, 95% CI) and 64.9 pM (23.0 – 177 pM, 95% CI), respectively. While the precise mechanism behind this observed effect remains elusive, the findings strongly indicate that the presence of the free sulfhydryl group plays a crucial role in enhancing the nanobody's performance as a capture affinity reagent within the direct ELISA framework.

Although the addition of the cysteine residue unexpectedly improved the LoD, the absence of significant differences between the reduced and non-reduced forms of each nanobody confirms that the reduction process itself does not significantly impact the binding affinity of these nanobodies, enabling further experimentation

3.2.6 Physisorption of cysteine-bearing nanobodies

To investigate the impact of cysteine modification on bioconjugate formation and stability, VHHV, VHHV-Cys and Cys-VHHV were conjugated to 40 nm AuNPs at varied pH at a ratio of 3200 nanobodies per nanoparticle, consistent with earlier native nanobody experiments. Their stability before and after 400 mM NaCl addition was assessed by monitoring the aggregation index. These measurements were performed for both reduced (rVHHV, rVHHV-Cys, rCys-VHHV) and non-reduced versions of each nanobody to assess the impact of any dimerisation on the non-reduced nanobodies. Initially, the pH-dependent aggregation index profiles for both reduced and non-reduced cysteine-modified VHHV nanobodies exhibited a similar response to the unmodified VHHV. Nanoparticles were stable at pH values above the protein's isoelectric point (6.70) and aggregated below it (Figure 3.12a). Successful immobilisation of

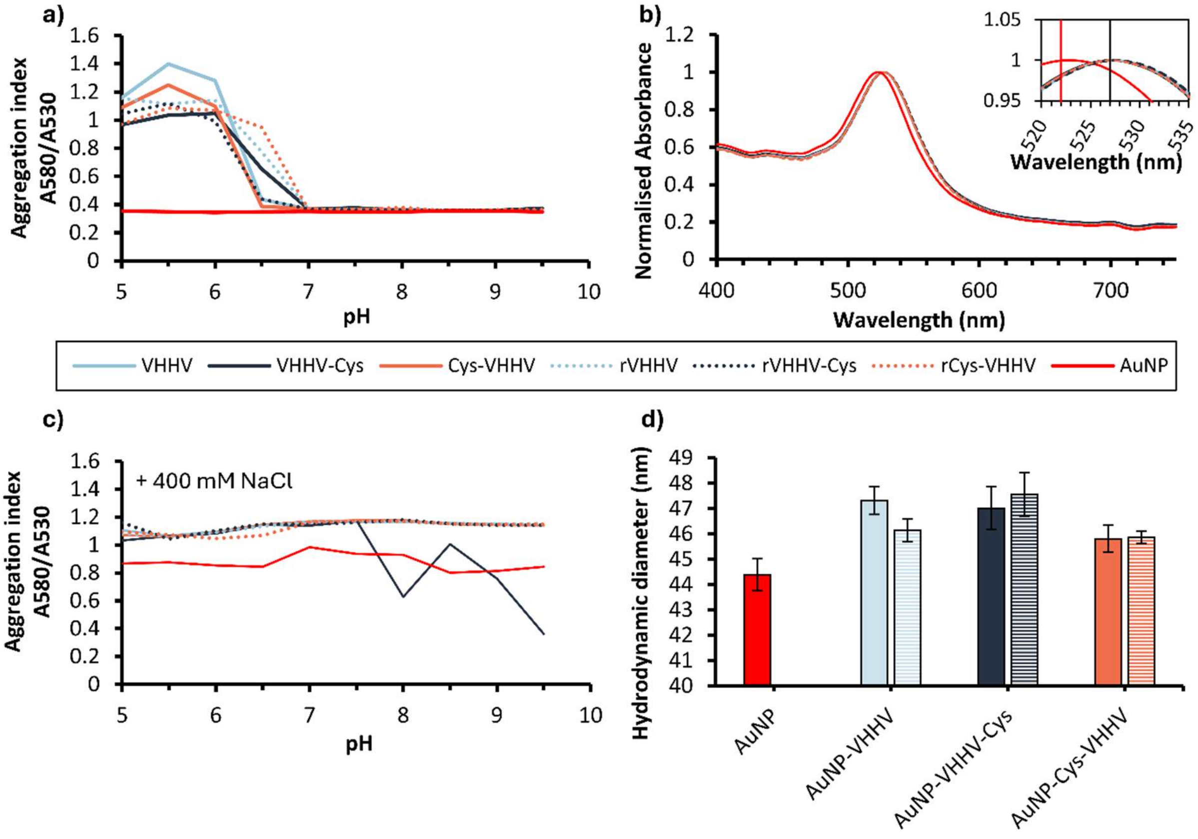

Figure 3.12 AuNP adsorption characteristics of VHHV and Cys bearing VHHV. Aggregation index plots for each Cys-nanobody conjugation across a range of pH conditions before (**a**) and after (**c**) increasing NaCl concentration to 400 mM. Reduced and non-reduced versions of each nanobody are represented by dashed and solid lines, respectively. (**b**) UV-Vis plot for Cys-nanobody bioconjugates. (**d**) The hydrodynamic diameter of bare AuNP and bioconjugates made from the reduced (dashed fill) and non-reduced (solid fill) versions of VHHV, VHHV-Cys and Cys-VHHV determined by DLS immediately following physisorption. Values are shown as the average (n = 3), and error bars indicate the standard deviation of the mean.

nanobodies onto AuNPs was indicated by comparable plasmon shifts of approximately 5 nm for all VHHV variants (Figure 3.12b). However, across all the nanobody cysteine variants, elevated salt concentrations were deleterious towards colloidal stability, leading to particle aggregation across all tested pH conditions (Figure 3.12c).

The exception to this is the non-reduced VHHV-Cys nanobody, which displayed enhanced colloidal stability and some resistance to salt-induced aggregation. In Figure 3.10b, a fraction of VHHV-Cys and Cys-VHHV in the dimerised form on SDS-PAGE was identified. In the case of VHHV-Cys, the dimer fraction was the dominant fraction, suggesting that nanobody dimerisation could influence particle stabilisation. This observation is consistent with the initial hypothesis that the nanobody, in its native form, may not provide sufficient protection against nanoparticle aggregation due to its small size. At the same time, the dimerised version shows some improvement in stability at higher pH. Despite this, DLS measurements revealed comparable increases in Dh for all VHHV variants (Figure 3.12d). This may indicate that there is an influence of the proteins approaching as a pre-formed dimer, or of a disulfide linkage itself, with its tendency to bind Au, influencing the particle stability.

3.2.7 Carbonate-mediated physisorption of Cys-nanobodies to AuNP

The fine-tuning of the solution pH during physisorption is key to providing favourable electrostatic forces of attraction between AuNPs and proteins. In the previous sections, common buffers such as MES (pH 5.0 – 6.5), HEPES (7.0 - 8.5) and borate (pH 9.0 – 10.0) were used to adjust the pH of the nanobodies prior to addition of AuNP. An alternative avenue for pH adjustment of the slightly acidic AuNP (pH 6.4) solution is through the addition of alkaline solutions. Carbonate-based solutions such as sodium carbonate (Na_2CO_3) and potassium carbonate (K_2CO_3) are common for the pH adjustment of AuNPs used for bioconjugation with small proteins such as nanobodies.[58,82,109–111]

To investigate the potential impact of carbonate-based buffers on nanobody bioconjugation efficiency and stability, the native VHHV nanobody and its cysteine mutants in their reduced forms (rVHHV-Cys and rCys-VHHV) were conjugated to 40 nm AuNPs. The conjugation process was carried out in buffers supplemented with varying concentrations of K_2CO_3 (5 mM or 10 mM), allowing the assessment of the effect of both the presence of the carbonate buffer and its concentration on the resulting bioconjugate stability. By systematically examining these conditions, the optimal pH and buffer composition for achieving the most stable nanobody-AuNP were established.

As shown in Figure 3.13a, before adding NaCl, the expected stability profile of VHHV and rCys-VHHV bioconjugates, as a function of conjugation pH, was observed when the reaction was supplemented with 5 or 10 mM K_2CO_3. Bioconjugates were stable at a buffer pH greater than 6.5 and aggregated below it. Conversely, rVHHV-Cys bioconjugates demonstrated stability across all tested pH ranges. This enhanced stability likely results from the slight pH increase caused by the carbonate buffer.

Figures 3.13b and 3.13c clearly demonstrate that carbonate supplementation during conjugation improves the stability of rVHHV-Cys bioconjugates against salt-induced aggregation. Unlike the aggregation profile without carbonate (Figure 3.13a), rVHHV-Cys bioconjugates formed in the presence of 5 mM carbonate remained stable across a range of pH conditions. From pH 7.0 onwards, a decrease in the aggregation index was observed with increasing pH, indicating improved stability. Nearly complete stability was maintained between pH 9.0 and 10.0 in the mild stress test (200 mM NaCl). A similar trend was observed under the full salt stress test (400 mM NaCl), but with a slightly increased aggregation index, indicating some loss of stability at higher ionic strengths. Notably, 5 mM carbonate concentration appeared optimal, as 10 mM carbonate showed a greater tendency for aggregation, although some stability improvement was maintained for rVHHV-Cys even at this higher concentration.

The addition of carbonate buffer improved the stability of rVHHV-Cys bioconjugates, conferring almost complete stability across the tested pH range (7-10). Notably, this stabilising effect exhibited a carbonate concentration dependence, with 5 mM K_2CO_3 providing greater stability

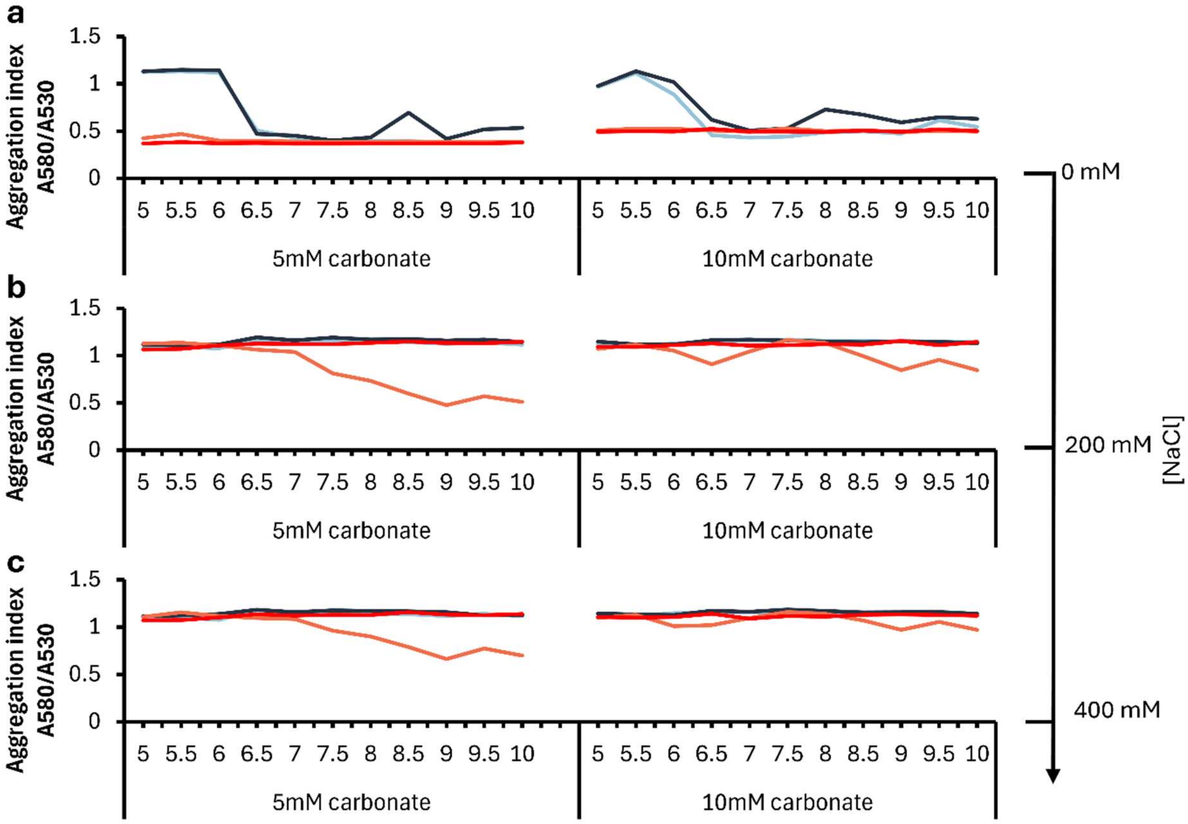

Figure 3.13 Physisorption characteristics in carbonate buffer. Aggregation index plots for conjugation of VHHV, VHHV-Cys and Cys-VHHV nanobodies to 40 nm AuNPs across a range of pH conditions in the presence of either 5 or 10 mM of buffer. **a**. Before the addition of NaCl, **b** mild salt stress test with 200 mM of NaCl and **c** full salt stress test using 400 mM of NaCl. N =1 for all data points.

to rVHHV-Cys bioconjugates compared to 10 mM K_2CO_3. Interestingly, the native VHHV nanobody, lacking free cysteines, and rCys-VHHV did not appear to benefit from the addition of carbonate. Complete loss of stability was observed for the native VHHV and rCys-VHHV bioconjugate across all pH conditions, carbonate concentrations, and NaCl concentrations, in contrast to the high improvement in stability observed for rVHHV-Cys. This suggests that the presence and the location of free cysteine as well as the use of carbonate buffer, may play a crucial role in mediating the observed stability enhancements.

The mechanism by which carbonate confers improved stability remains unclear. Carbonate-capped AuNPs possess a surface that is closer to "bare" than citrate-capped AuNPs, which can be attributed to the smaller size of the carbonate ligand. Similar to citrate, carbonate molecules impart a negative zeta potential over a broad pH range. However, unlike citrate, which has three carboxylic acid groups and a molecular weight of 189.10 g/mol, carbonate has only one carboxyl group and a lower molecular weight of 60.01 g/mol. This smaller size and reduced effective charge of carbonate facilitate its displacement, enabling higher surface loadings of physisorbed protein.[112] This surface chemistry may potentially allow for the loading of greater amounts of protein onto the particles, which could make them ideal starting materials for bioconjugation applications like LFAs, where a dense antibody layer enhances sensitivity.

One possible scenario is that an initial exchange of citrate for carbonate occurs on the nanoparticle surface due to the comparatively higher concentration of carbonate (sodium citrate 0.02 mM vs 5-10 mM potassium carbonate). This exchange could create a more favourable environment for the smaller nanobodies to displace the carbonate, leading to enhanced bioconjugation efficiency and stability. Further investigation employing experimentation and molecular dynamics simulations is needed to elucidate the precise molecular interactions involved in this process and to confirm the proposed mechanism.

3.3 Conclusions and future work

The ease of production and adaptability of nanobodies could significantly accelerate the development process of point-of-care diagnostics such as LFAs. LFAs are crucial for rapidly detecting infectious diseases, but their deployment is often hindered by the lengthy development of suitable antibody pairs, resulting in considerable burden on public health and economies. Nanobodies have the potential to change this, but their inherent limitations in forming AuNP bioconjugates that would remain stable in the harsh conditions required during bioconjugate processing and when they interface with complex matrices during LFA operation.

In this chapter, a panel of nanobodies against the SARS-CoV-2 was employed to characterise the adsorption characteristics of nanobodies on AuNPs and their limitations in preventing salt-induced aggregation. Aggregation studies revealed that nanobody charge and sequence diversity have a considerable influence towards the resulting stability of the nanobody bioconjugate, with bioconjugate produced with more acidic nanobodies such as VHHV and

VHHE demonstrating greater resilience under higher ionic strengths. Specifically, while all nanobodies failed to produce stable bioconjugates with 40 nm AuNPs under elevated ionic conditions, the more acidic nanobodies moderately improved the aggregation profile of bioconjugates formed with 20 nm AuNPs. This systematic study, utilising two common AuNPs sizes used for commercial LFAs, preparing bioconjugates under different pH conditions and by exposing the resulting bioconjugates to increasing ionic strength conditions, the extent of the resilience of nanobody based bioconjugates against salt aggregation was derived. Nanobody-based bioconjugates are only able to withstand moderate concentrations of NaCl when nanobodies with relatively low IEP and 20 nm AuNPs are used.

DLS analysis revealed a sub-maximal loading density of nanobodies on the nanoparticle surface. To address this, a free cysteine was introduced into the lead nanobody, VHHV, aiming to improve loading density and stability through direct covalent binding to the AuNP surface.

While this modification led to nanobody dimerisation, a simple reduction reaction successfully reverted them to monomers. Although rVHHV-Cys and rCys-VHHV did not initially show enhanced stability, using an optimised carbonate buffer revealed the distinct benefit of the free cysteine's presence and strategic positioning. Specifically, rVHHV-Cys demonstrated an improvement in stability when combined with the carbonate buffer, while VHHV and rCys-VHHV offered no protection against salt-induced aggregation.

While completely stable bioconjugates under high ionic strengths were not achieved, this work demonstrates the potential of protein engineering to overcome the inherent limitations of nanobodies in LFA applications. The detailed exploration of nanobody bioconjugate stability limitations and the identification of specific factors influencing stability provide a foundation for further optimisation. The findings here suggest that further experimentation could be used to optimise the physisorption of the Cys bearing VHHV to improve binding and the generation of salt-resistant bioconjugates. However, the results here strongly suggest that bioconjugates with physisorbed native nanobodies are incompatible with exposure to elevated ionic strengths, limiting their use in LFA.

In subsequent chapters, we will explore alternative protein engineering strategies to further enhance nanoparticle stability and meet the stringent requirements of LFAs. We will investigate the incorporation of nanobodies into multivalent chains, inspired by the improved stability observed with dimerised VHHV-Cys. Additionally, we will explore alternative recognition molecules and modular display platforms to potentially bypass the nanobody-nanoparticle interface entirely, opening up new avenues for robust LFA development.

4 Multivalent nanobody engineering for enhanced physisorption and functional display on gold nanoparticles

4.1 Introduction

Highly functional AuNP bioconjugates are essential for the development of sensitive LFAs, which must capture the target analyte within the relatively short timescales of the assay. It is both theoretically postulated and experimentally confirmed that bioconjugate functionality depends on the affinity of the surface-bound ligand and the number of immobilised ligands that retain their activity.[25,89,94,113,114] Bioconjugate diffusivity is another key factor influencing assay sensitivity, as larger nanoparticles, which are less diffusive, tend to be less reactive.[52,103] Bioconjugate aggregation can reduce diffusivity by forming larger amorphous clusters and concealing functional ligands within the aggregates, leading to a further loss of activity. Therefore, maintaining bioconjugate monodispersity is crucial for maximising assay sensitivity. This task is often challenging and requires optimisation at various stages of bioconjugate development and processing.[5] Nanobodies have been shown to produce bioconjugates with limited stability when conjugated through physisorption and are prone to aggregation when exposed to high ionic strengths, both in this work (previous chapter) and in previous studies.[58,83] This is a critical limitation for LFA bioconjugates, which must withstand harsh processing steps, such as washing and drying, and interface with physiological samples and complex matrices.[38]

Protein engineering strategies have been previously explored to improve nanobody-AuNP physisorption. Hattori *et al*. developed a novel anti-gold nanobody which, upon physisorption onto 20 nm AuNPs, maintained a degree of resistance to elevated ionic strengths.[83] They demonstrated the feasibility of a bispecific nanobody approach to promote particle assembly, where one nanobody (anti-gold nanobody) facilitated immobilisation while the other provided biorecognition of a secondary particle. However, while their gold-binding nanobody was able to form bioconjugates, complete suppression of salt-induced aggregation was not achieved under all tested conditions. Goossens *et al*. employed a similar bispecific construct incorporating the same anti-gold nanobody but found this did not prevent the aggregation of 20 nm AuNP bioconjugates.[58] Additionally, they conjugated a series of nanobodies to AuNPs in their native form through physisorption. While this approach generated functional nanobody-AuNP bioconjugates, the results showed varying degrees of susceptibility to salt-induced aggregation across different nanobodies. Furthermore, they explored dative covalent bond-mediated immobilisation using cysteine-bearing nanobodies, but again, this was not found to improve nanoparticle stability. Notably, the bioconjugates were prone to aggregation in the presence of blocker proteins, a critical factor for LFA applications, since the bioconjugates are required to interface with common blocking proteins such as bovine serum albumin (BSA), and complex sample matrices. In contrast, Anderson *et al*. investigated various nanobody modifications, including fusion with metal-binding peptides and cysteine-bearing peptides.[84] They found that incorporating a cysteine-bearing tag (hop-tail) was the optimal strategy for enhancing bioconjugate stability compared to native nanobody constructs, although at the cost of additional reduction steps in the production of AuNP bioconjugates. To date, these studies have involved the use of bioconjugates prepared and stored in the liquid phase, leaving the impact of harsher processes, such as drying, on the stability of bioconjugates unknown.

In the previous section, a comparative analysis of the physisorption characteristics of three distinct nanobodies with varying IEPs against the SARS-CoV-2 S1 protein was undertaken. The limitations of both native nanobody physisorption and terminal-cysteine modifications in achieving colloidally stable bioconjugates via physisorption were elucidated.

In this chapter, to address this challenge, a rational protein engineering approach was implemented, incorporating the lead nanobody candidate (VHHV) into multivalent nanobody chains. The generated multivalent nanobodies were characterised and were shown to have improved kinetics when binding the antigen and improved performance as recognition molecules in ELISA. Notably, a trivalent nanobody demonstrated superior analytical performance and enhanced nanoparticle stability under elevated ionic strength conditions. The resulting trivalent nanobody bioconjugate was also shown to be resilient to the presence of blocker proteins encountered during bioconjugate processing and drying stages while maintaining picomolar-level detection of the S1 protein in an LFA format. In this study, we also explored the extent of the improvement in nanoparticle stability gained by multivalent nanobodies by generating multivalent nanobodies of other nanobodies used in this thesis (VHHE and Nb6) and by generating higher-order polyvalent nanobodies, including tetravalent, pentavalent, and hexavalent VHHV constructs. We also studied the adsorption and nanoparticle stabilisation capabilities of these constructs.

4.2 Results and discussion

4.2.1 Generation and characterisation of multivalent nanobodies

Monovalent nanobodies appear to fail to provide sufficient charge or steric protection to the nanoparticle to prevent salt-induced aggregation. To overcome this limitation, a strategy was implemented to increase their molecular weight by incorporating the nanobodies into multivalent chains. This approach effectively increases both the protein size and the number of paratopes per protein. This strategy is supported by the observed improvement in stability with the dimerised form of the VHHV-Cys nanobody (Figure 3.12c).

The lead nanobody candidate, VHHV, was used to initially test this approach. Bivalent (VHHV2) and trivalent (VHHV3) nanobody chains were generated with each nanobody domain linked in tandem by flexible GGGGS×3 spacers. The spatial distance of CDR regions from both termini in monovalent nanobodies ensures that the binding of fused nanobodies is unaffected. Similar strategies have been employed to enhance nanobody activity by improving binding affinities, specificity, and suppression of target mutational escape of viral targets when used as neutralising therapeutics.[33,34]

The inclusion of the flexible linker ensures that the nanobody domains remain freely diffusive to maximise their functionality and reduce the chance of steric hindrance of the paratopes from other nanobody domains. Linker type and length can impact multivalent nanobody affinity and structure. Huang and colleagues generated multivalent nanobodies linked with different lengths of either a flexible (GGGGS) or rigid linker (EAAAK).[115] Using circular dichroism spectroscopy, they showed that while the nanobodies linked with GGGGS linkers showed comparable CD spectra, nanobodies with EAAAK showed distinct changes consistent with alpha-helix formation. Furthermore, the nanobodies connected with longer rigid linkers eluted more quickly during size exclusion chromatography, indicating an increased hydrodynamic diameter compared with nanobodies connected with a flexible linker of the same size. An improvement in affinity correlated with linker length for both linker types. Xiang and colleagues reported a much greater improvement in the neutralisation activity when nanobody NB21 is fused in a trivalent chain through the flexible linker compared to a rigid linker of similar length.[116]

In this study, a 15 amino acid GGGGSx3 flexible linker was chosen to maximise the affinity potential and ensure free diffusion of nanobodies in tandem. The multivalent nanobodies were cloned into pET-26b containing a PelB and hexahistidine tag. The PelB signal sequence directs the protein to the bacterial periplasm, where it is cleaved, enabling the formation of internal disulfide bonds due to the oxidative environment of the bacterial periplasmic space. The internal disulphide connects the CDR1 and CDR3 regions and is considered important for the nanobody to adopt its immunoglobulin fold.[92] The gene diagrams of the multivalent nanobodies are shown in Figure 4.1.

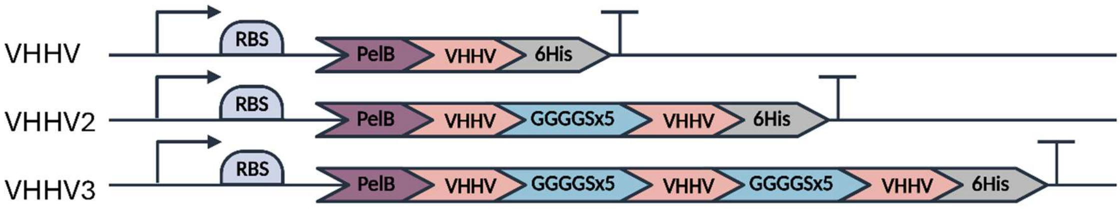

Figure 4. 1 Gene diagrams of the monovalent VHHV divalent - VHHV2 and trivalent - VHVH3 nanobodies. RBS - ribosome binding site. The arrow depicts the direction of translation.

Divalent (VHHV2), trivalent (VHHV3) and monovalent nanobodies (VHHV) were expressed in *E. coli* and purified under identical conditions. Successful expression and purification were confirmed by SDS-PAGE (Figure 4.2), which is used here as a qualitative assessment. All nanobodies were expressed in the bacterial periplasm, and purified samples presented a

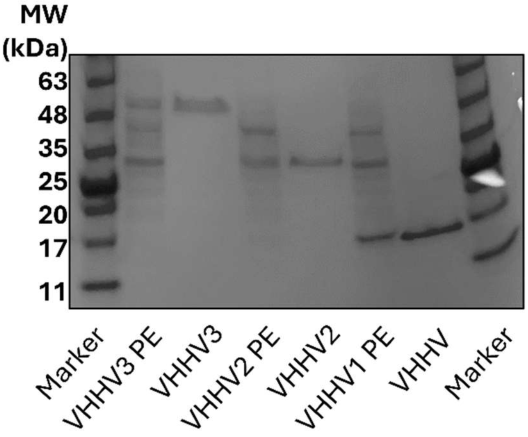

Figure 4.2 Reducing SDS-PAGE, Lanes 1 and 8 contain the protein MW reference marker, lanes 2 and 3 contain the periplasm and purified fraction from the VHHV3 expression, 4 and 5 contain the periplasm and purified fraction of VHHV2, lanes 6 and 7 contain the periplasm and purified fraction from the expression of VHHV. While the bands appear to consistently migrate slightly faster than their expected molecular weights, this gel was used primarily for qualitative assessment. The exact MW of the proteins were confirmed by Mass spectrometry.

single band. No additional bands were detected in the eluted samples, indicating sufficient purity through the one-step Ni-NTA purification process using the His-tag. While the SDS-PAGE bands consistently migrated slightly slower, appearing heavier than their expected molecular weights, the anticipated size increase between VHHV, VHHV2, and VHHV3 was observed, confirming the successful construction of the multivalent nanobodies.

The affinity of the multivalent nanobodies was assessed using biolayer interferometry (BLI) to determine dissociation constants, association and dissociation rates, and a direct ELISA to evaluate their performance in the analytical assay. To enable immobilisation on streptavidin-functionalised BLI sensors, nanobodies were biotinylated via chemical means using an NHS-PEG$_{12}$-biotin linker targeting primary amines. Nanobodies, rather than antigens, were loaded onto the sensor to minimise potential avidity effects caused by one multivalent nanobody binding to multiple antigens. Chemical biotinylation was performed under identical stoichiometries for each nanobody to reduce heterogeneity in the biotinylation load. Subsequent LC-MS analysis of the biotinylated nanobodies revealed a distribution of biotinylation loads ranging from 1 to 4 biotins per nanobody, with the majority presenting 2-3 biotins, as shown in Figure 4.3 a-c.

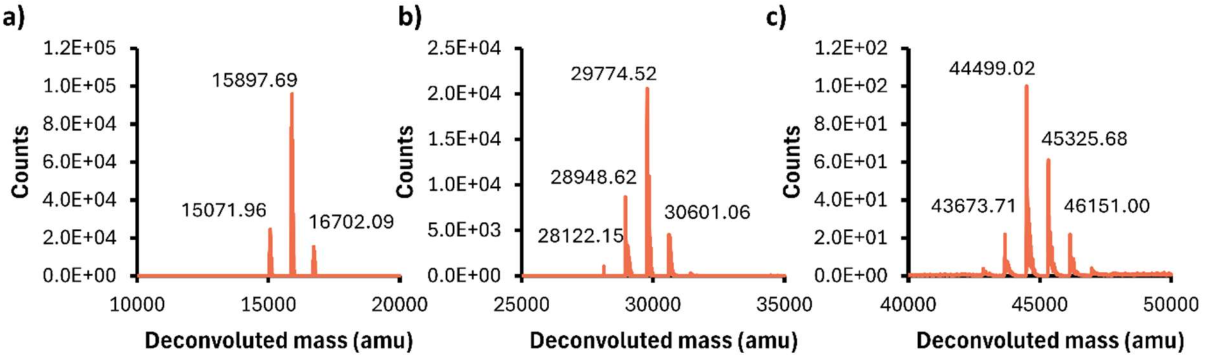

Figure 4.3 LC-MS spectra for VHHV-biotin conjugates showing the mass additions of NHS-PEG$_{12}$-Biotin (941.09 g/mol). The expected increase in molecular weight is 825.64 g/mol per NHS-PEG$_{12}$-Biotin. (**a**) VHHV (14225.70 g/mol), observed masses of 15071.96, 15897.69 and 16702.09 correspond to 1, 2 and 3 NHS-PEG$_{12}$-Biotin additions to VHHV nanobody, respectively. (**b**) VHHV2 (28125.87 g/mol) observed masses of 28948.62, 29774.52 and 30601.06 correspond to 1, 2 and 3 NHS-PEG$_{12}$-biotin additions to VHHV2 nanobody, respectively. The observed mass of 28122.15 corresponds to the unmodified VHHV2 nanobody (**c**) VHHV3 (42026.04 g/mol) Observed masses of 43673.41, 44499.02, 45325.68 and 46151.00 correspond to 2, 3, 4 and 5 NHS-PEG$_{12}$-biotin additions to VHHV3 nanobody respectively.

Nanobodies bearing double and triple valency exhibited a modest improvement in binding affinity when compared to the monomeric form of VHHV. This is indicated by a decrease in the dissociation constant (K_D) from 1.77±0.01 nM for VHHV to 0.97±0.01 nM for VHHV2 and 0.92±0.01 nM for VHHV3 (Figure 4.4). This modest improvement in affinity is consistent with previous findings by Koenig *et al.*, who reported a K_D of 8.92 nM for monovalent VHHV and 2.58 nM for the divalent form[34]. The consistently lower K_D values reported here could be

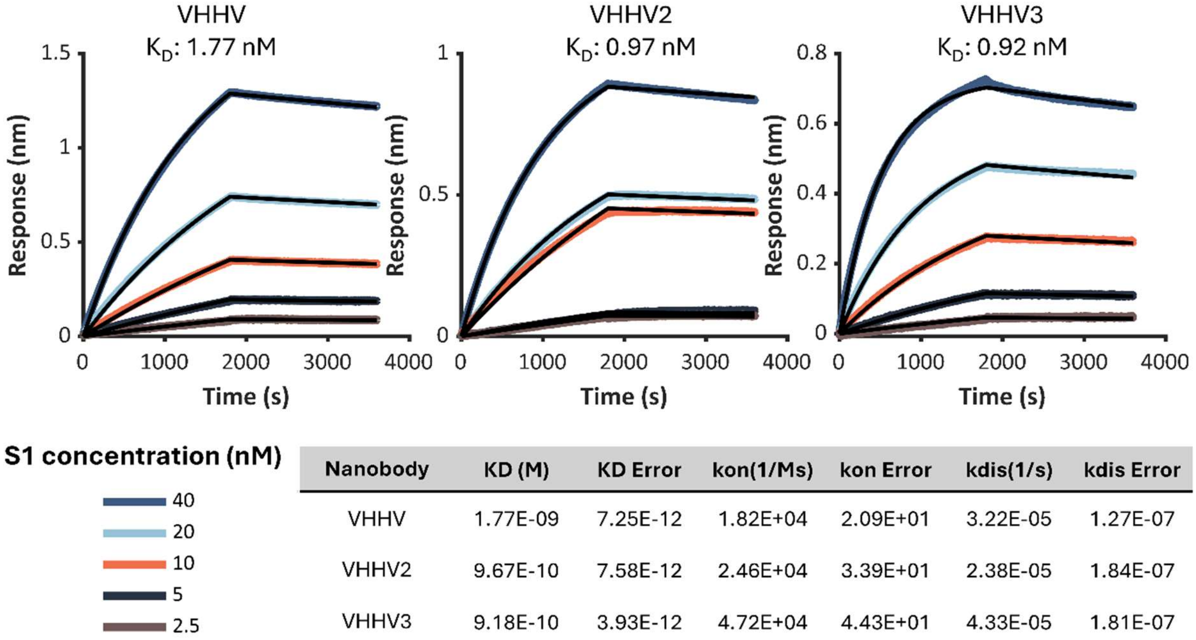

Nanobody	KD (M)	KD Error	kon(1/Ms)	kon Error	kdis(1/s)	kdis Error
VHHV	1.77E-09	7.25E-12	1.82E+04	2.09E+01	3.22E-05	1.27E-07
VHHV2	9.67E-10	7.58E-12	2.46E+04	3.39E+01	2.38E-05	1.84E-07
VHHV3	9.18E-10	3.93E-12	4.72E+04	4.43E+01	4.33E-05	1.81E-07

Figure 4. 4 Bio-layer interferometry of biotinylated VHHV, VHHV2 and VHHV3 against the SARS-CoV-2 S1-His antigen. Solid black lines show the global fit used to calculate the kinetic parameters shown in the table.

attributed to differences in assay setup. Koenig *et al*. used an SPR system with immobilised antigens, whereas a BLI system with immobilised nanobodies was used in this study.

Direct ELISA was performed with a flipped configuration to probe how the affinity differences due to multivalency translate to sensitivity. In this ELISA, the Fc-tagged S1 antigen was immobilised on the solid phase of polystyrene plates. The chemically biotinylated versions of VHHV, VHHV2 and VHHV3 served as the detection reagent that bound the S1 in solution. This direct ELISA format enabled a free configuration of the multimeric nanobodies, ensuring a fair comparison by minimising any potential impact on the LoD that might arise from differences in immobilisation between monovalent, divalent and trivalent nanobody constructs. HRP-conjugated streptavidin was used to generate signal corresponding to the immunocomplex formation. Comparative analysis was achieved by calculating the LoD, which indicates the lowest concentration of S1 that can be detected with this assay setup. A significantly improved LoD was measured for VHHV3 at 29.8 pM (17.4 – 50.3 pM, 95% CI) when compared to VHHV's LoD of 79.7 pM (56.6-111.7 pM, 95% CI, p = 0.0034) as shown in Figure 4.5. A similar, though statistically non-significant, LoD decrease was observed for VHHV2 (49.8 pM, 30.1-81.5 pM, 95% CI, p = 0.13). This improvement in LoD is likely attributed to the increase in affinity observed with increasing valency.

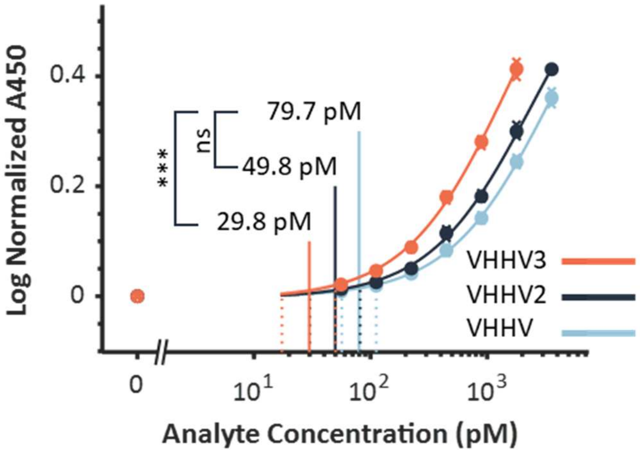

Nanobody	ELISA LoD pM (95% CI)
VHHV	79.7 (56.6-111.7)
VHHV2	49.8 (30.1-81.5)
VHHV3	29.8 (17.4 – 50.3)

Figure 4. 5 Direct ELISA using biotinylated nanobodies VHHV, VHHV2 and VHHV3 against the S1-Fc immobilised on the plate and LoD analysis. Solid curves show the fitted Langmuir functions for VHHV, VHHV2 and VHHV3. Circles show the average of 3 replicates for each concentration ± the standard deviation of the mean. Vertical dashed lines show the 95% CI of the LoD calculation, while solid vertical lines show the LoD.

4.2.2 Multivalent VHHV physisorption

The adsorption characteristics of the multivalent nanobodies and the stability of the bioconjugates were studied using UV-Vis spectroscopy comparing the monovalent VHHV against the divalent and trivalent VHHV2 and VHHV3. Nanobodies were physisorbed to 40 nm AuNPs at a molar excess of 3200 nanobodies per AuNP. The effect of pH on bioconjugation was tested by conjugating at a range of pH conditions (pH 5.0 – 9.5) and monitoring the aggregation index defined as A580/A530, matching experiments performed in the monovalent nanobody studies in Chapter 3 (Figure 3.3).

As anticipated, due to the similar IEPs of VHHV (6.70), VHHV2 (6.66) and VHHV3 (6.70), comparable aggregation index values were observed as a function of pH following physisorption. Nanoparticle stability was maintained during conjugation at pH greater than 6.0 for VHHV2 and VHHV3, and pH greater than 6.5 for VHHV (Figure 4.6a). However, the addition of salt rapidly compromised the stability of VHHV2 bioconjugates across all pH values, mirroring the behaviour of VHHV (Figure 4.6b). This is not improved at higher nanobody concentrations for VHHV2. This contrasts with the dimerised form of the disulfide-bridged VHHV-Cys, which retained some nanoparticle stability. While VHHV2 and dimerised VHHV-Cys nanobodies have similar molecular weights, they exhibit cross-linkers with different lengths and flexibility. It's hypothesised that the differences in linker flexibility (flexible in

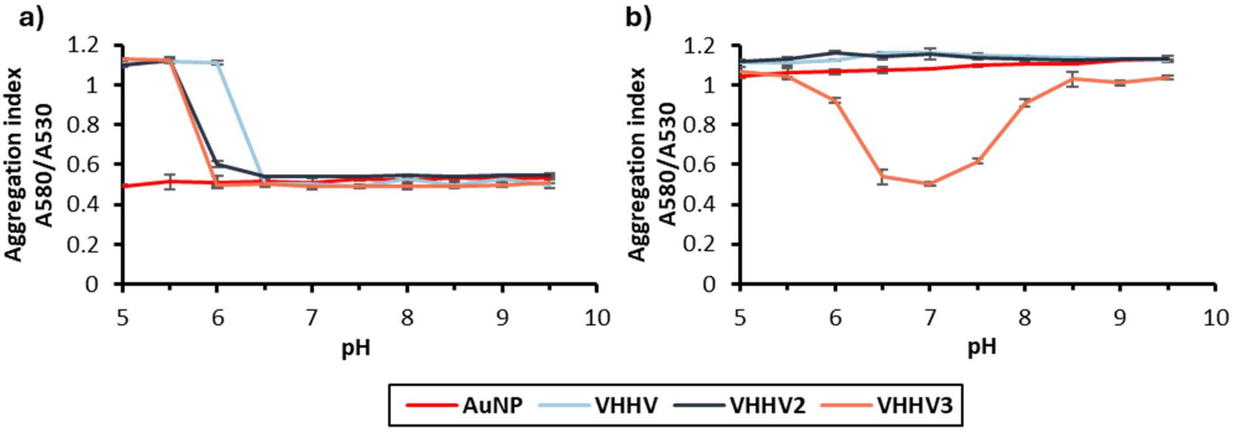

Figure 4.6. 40nm AuNP adsorption characteristics of VHHV, VHHV2, and VHH3. Aggregation index of VHHV, VHHV2 and VHHV3 bioconjugates before (**a**) and after (**b**) the addition of 400 mM of NaCl. Values displayed as the mean (n = 3) ± the standard deviation of the mean.

VHHV2, rigid in dimerised VHHV-Cys) and nanobody orientation (C-termini interfacing in the dimer) could lead to distinct approaches, binding mechanisms, and ultimately different protein structures upon adsorption to the AuNP surface, impacting the resulting bioconjugate stability.

In contrast to the low stability of VHHV and VHHV2 bioconjugates at elevated ionic strength, VHHV3 exhibited a stable region between pH 6.5 and 7.5 (Figure 4.6b). The presence of an additional nanobody on VHHV3 correlated with enhanced nanoparticle protection against salt induced aggregation, indicating improved colloidal stability likely due to differences in local charge and structure. The larger size of the VHHV3 nanobody likely creates a thicker protein layer on the bioconjugate surface preventing the AuNPs from coming into proximity where the Van der Waals attraction causes nanoparticle clumping, leading to aggregation. Increasing the molar ratio of VHHV3: AuNP to 6400:1 resulted in a similar aggregation index as a function of pH, suggesting that maximum coverage is achieved at or before 3200 VHHV3 nanobodies per nanoparticle (Figure 4.7).

This protection against salt-induced aggregation highlights the importance of balanced protein electrostatics. At pH values above 7.5, negatively charged proteins repel the negatively charged nanoparticles during conjugation, leaving them less effectively decorated and vulnerable to salt-induced aggregation. Conversely, at pH values below 6.5, strongly positively

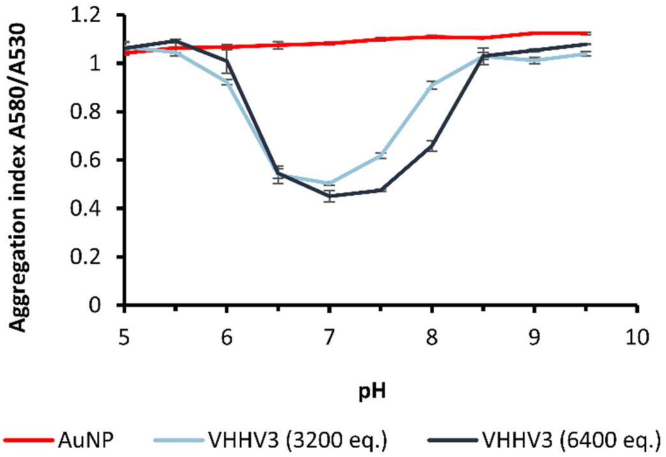

Figure 4. 7 VHHV3 physisorption at different concentrations. Comparison of the aggregation index plots of VHHV3 nanobody bioconjugations to 40nm AuNPs with a 3200 or 6400 nanobody to AuNP ratio at a range of pH conditions (5.0 – 9.5) under elevated ionic strength conditions (400 nM NaCl), Values are shown as average (n=3) and error bars indicate the standard deviation of the mean.

charged VHHV3 proteins cross-link AuNPs, leading to aggregation. Therefore, a pH range between 6.5 and 7.5 provides an optimal environment where a protective protein layer shields the nanoparticle surface from salt-induced aggregation without causing protein-mediated cross-linking.

The effect of multimer length on adsorption behaviour was studied by comparing the adsorption isotherms of each nanobody to AuNPs. Adsorption isotherms can be used to evaluate the adsorption characteristics of a protein to a surface and calculate the thermodynamic dissociation constants (K_d).[61] The adsorption isotherm of each nanobody was derived by monitoring the wavelength of the surface plasmon resonance peak (λSPR), which is expected to undergo a redshift as protein adsorbs to the surface.[106] Nanobody was titrated into an AuNPs solution during bioconjugation where the UV-Vis spectrum around the λSPR is fitted to a Gaussian function to determine the precise position of the SPR peak wavelength (Figure 4.8a). The mean λSPR is plotted against nanobody concentration and best fits the Hill equation, where $\lambda\mathrm{SPR}_{\mathrm{initial}}$ is the wavelength of the SPR derived from the AuNP at 0 ng/mL nanobody concentrations, $\Delta\lambda\mathrm{SPR}_{\mathrm{max}}$ is the maximum shift in λSPR, K_d provides a quantitative measure of the nanobody physisorption kinetics, n is an estimate of binding cooperativity. The adsorption isotherm equation is given by

$$\lambda\mathrm{SPR} = \lambda\mathrm{SPR}_{initial} + \frac{\Delta\lambda\mathrm{SPR}_{max}[nanobody]^n}{K_d^{\,n}+[nanobody]^n} \tag{4.1}$$

The dissociation constant determined reflects the rate at which the adsorbing protein is shifting the plasmon resonance. Notably, the equilibrium dissociation constant, K_d, was found to decrease with increasing nanobody valency (940.2, 789.4 and 759.2 nM for VHH1, VHH2 and VHH3, respectively). This likely reflects the larger size of the multivalent nanobodies that cause a greater change to local refractive index by binding event and cause a greater shift in the LSPR.. Furthermore, VHHV3 exhibited a larger max increase in the $\lambda\mathrm{SPR}_{\mathrm{max}}$. This shift is linked to nanoparticle local refractive index changes, as described by LSPR theory. The larger shift observed for VHHV3 suggests that it creates a more pronounced change in the dielectric environment surrounding the nanoparticle. This could be due to several factors related to the

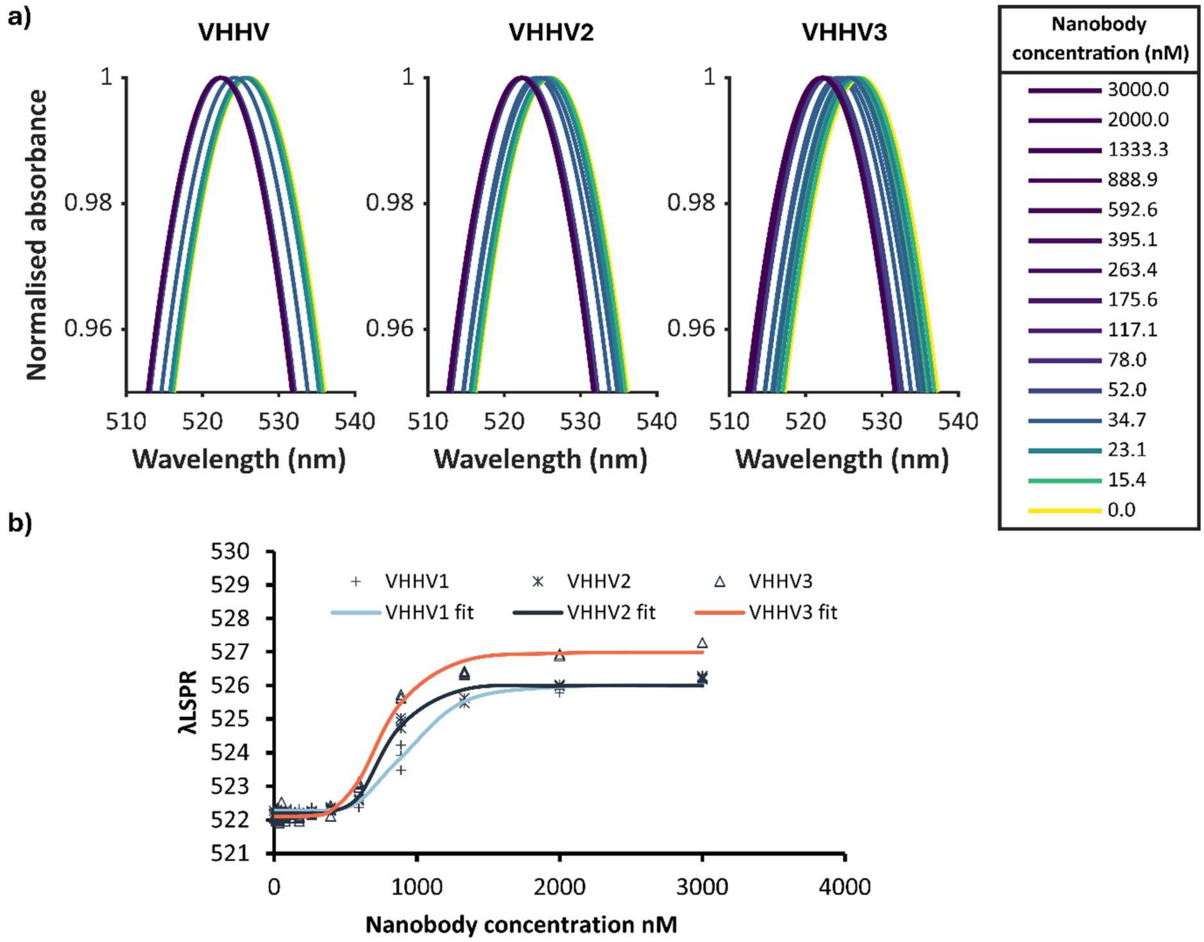

Figure 4. 8 Adsorption isotherm analysis (**a**) Normalised Gaussian functions of best fit of the SPR peak plots of the UV-Vis spectrum for VHHV, VHHV2 and VHHV3 AuNP bioconjugates generated at different concentrations of nanobody. (**b**) Adsorption isotherm plots based on the plasmon peak shift for each bioconjugate. Solid lines represent the fitted Langmuir equation (Equation 4.1).

protein's size and the density of the adsorbed layer. As the valency increases, the nanobody's effective size or its conformational footprint on the nanoparticle surface may change. The larger shift could be a result of the VHHV3 forming a thicker or more densely packed protein layer on the nanoparticle surface, leading to a greater perturbation of the local refractive index and a larger red-shift. This pronounced surface modification likely contributes to the observed superior salt stability of the nanoparticle-VHHV3 conjugate, as a more complete and robust protein corona can provide better electrostatic and steric stabilisation against aggregation in high-salt environments.[99]

The protein monolayer formed post-physisorption of the nanobody was further studied using dynamic light scattering (DLS). DLS of the AuNPs and AuNP-nanobody bioconjugates can be

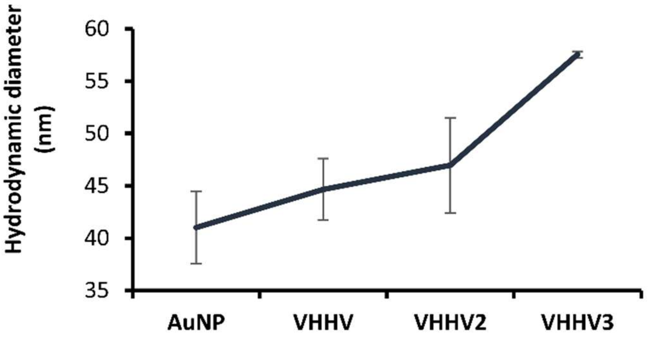

Figure 4. 9 Hydrodynamic diameter of VHHV, VHHV2 and VHHV3 AuNP bioconjugates determined by DLS. Values are displayed as mean (n=3) ± the standard deviation of the mean

used to determine the hydrodynamic diameter (Dh) which can be used to study the modification of the surface and the thickness of the protein layer formed.

DLS revealed a greater increase in the Dh of VHHV3 of 57.5 nm (±0.3 nm) in comparison to VHHV and VHHV2, which yielded Dh of 44.7 nm (±3.4 nm) and 47.0 nm (±4.5 nm), respectively (Figure 4.9). The significant increase in hydrodynamic diameter (Dh) for VHHV3 suggests that some nanobody domains act as anchors while others extend outwards.

VHHV3, with its three nanobodies connected by flexible linkers, likely adopts diverse conformations when interacting with the nanoparticle surface, unlike VHH2 and VHH1. This results in a more complex and sterically hindered interface, thus increasing Dh. The adsorbed protein layer is notably thicker than the largest dimension of VHHV, implying that flexible nanobody domains are likely to extend from the surface. This explains the enhanced stability of VHHV3, as these extended domains offer greater steric hindrance and a more protective protein layer. This thicker protein layer provides a steric protective layer, preventing the electron-dense AuNPs from approaching lengths where the Van der Waals forces of attraction overcome the repulsive electrostatic forces which ultimately lead to nanoparticle aggregation. While antibodies and other proteins have effectively created stable bioconjugates, VHHV3 presents an attractive alternative. It combines the ease of production and development inherent to nanobodies with a high density of paratopes, potentially leading to improved sensing capabilities.

4.2.3 Conjugate blocking optimisation

In this section, a brief optimisation of the conjugation and blocking buffers is performed with a scope to maximise the diagnostic capabilities of the bioconjugates when used as detection probes in LFAs. Typically, LFA development necessitates the optimisation of numerous parameters, including the selection of blocker proteins, running buffers, nitrocellulose membrane selection, sample volume, nanoparticle concentrations, and biomarker/antibody pairings.[5] However, the scope of this study is focused on evaluating the performance of nanobody bioconjugates derived from nanobodies of varying binder lengths rather than maximising the potential sensitivity. The aim is to assess whether the enhanced stability observed in trimeric nanobody-AuNP conjugates and their resistance to salt-induced aggregation translate to improved sensitivity. Therefore, initial optimisation efforts were concentrated on the conjugation pH and blocking buffer compositions, with the goal of establishing a working diagnostic with sufficient sensitivity to facilitate a comprehensive comparison.

A simplified half-stick LFA was assembled made of a nitrocellulose membrane attached to an absorbent pad. Polystreptavidin, dispensed onto the membrane using a BioDot system, served as the capture reagent. The S1 antigen was chemically biotinylated (S1-biotin) to facilitate capture by the polystreptavidin located at the detection zone (Figure 4.10). This streamlined assay design enabled the evaluation of the nanobody bioconjugates without the additional complexity of pairing them with antigen-recognition biomolecules. The immunoassay was performed by mixing the antigen and nanoparticles in a 96 well-plate, and then inserting the dipstick into the well. Once the dipstick interfaces with the bioconjugate and antigen mixture, capillary forces facilitate the transfer of the mixture onto the dipstick. The reaction mixture migrates across the nitrocellulose test membrane and over the test line where the bioconjugate can be immobilised to the PSA through the biotinylated antigen. In the presence of the antigen, bioconjugate accumulation on the test line causes the generation of

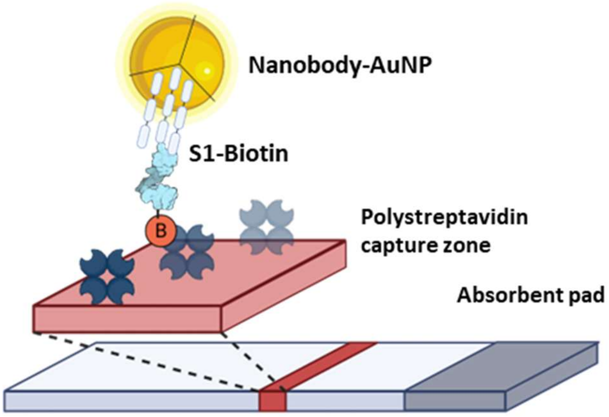

Figure 4.10 Scheme of nanobody LFA where nanobody-AuNPs are mixed in the well of a 96-well plate with S1-biotin. A half-dipstick LFA is inserted into the well to enable the flow of the immunocomplex through capillary action. An S1-biotin concentration-dependent deposition of nanobody-AuNPs generates signal quantified by a camera and image analysis.

signal due to the intense red colour of the bioconjugates. Signal quantification was achieved through image analysis of the LFA strips captured under controlled conditions using a camera.

The composition of both the conjugation and running buffers significantly impacts the sensitivity and specificity of the nanobody bioconjugates in the LFA. The conjugation buffer influences the number of nanobodies that are attached and properly oriented on the nanoparticle surface, which directly affects the binding efficiency to the target antigen.[61] The blocking buffer, by controlling the final pH and ionic strength of the assay, can modulate specific antigen-bioconjugate interactions as well as off-target interactions between the bioconjugate and other assay components, such as the polystreptavidin test line. Therefore, optimising the formulation of these buffers is crucial to maximising signal generation in the presence of the antigen while minimising non-specific binding, which could lead to false positive results.

VHHV3 nanobodies were conjugated to AuNPs across the optimum pH range identified in the aggregation studies (pH = 7.0 - 8.0 HEPES). Subsequently, the nanobody-AuNP complexes were blocked and washed using blocking buffers containing 1% BSA and Tween 20, prepared in either 1x PBS, diluted 0.1× PBS or HEPES buffer (Figure 4.11). 0.1× PBS was used to test the blocking buffer at the same pH but with reduced ionic strength. HEPES buffer was studied here to imitate the physisorption buffer that produced the most stable conjugates during

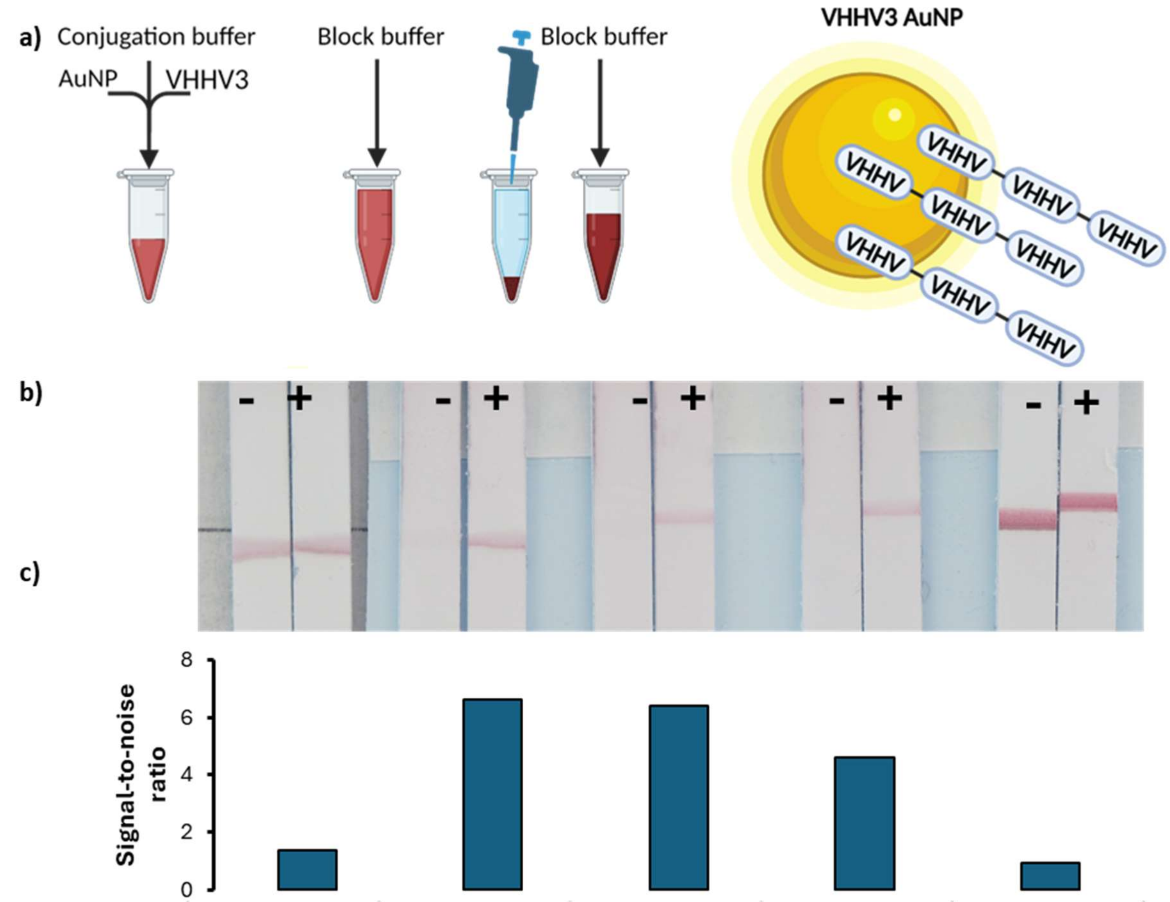

Conjugation Buffer	pH7.0 HEPES	pH7 .5 HEPES	pH8.0 HEPES	pH7 .5 HEPES	pH7.5 HEPES
Blocking/ running bufer	1×PBS 1%BSA 0.05% T-20	1×PBS 1%BSA 0.05% T-20	1×PBS 1%BSA 0.05% T-20	0.1×PBS 1%BSA 0.05% T-20	100mM HEPES 1%BSA 0.05% T-20

Figure 4. 11 VHHV3-AuNP optimisation for LFA (**a**)Process diagram for the conjugation, blocking and removal of unbound nanobodies through centrifugation. (**b**)images of lateral flow assays performed for the comparison of different conjugation and blocking buffer formulations, (-) indicated the blank where no antigen is present in the sample. (+) indicates a positive sample of 333ng/mL final concentration of S1-biotin in blocking buffer. (**c**) signal to noise ratio plots for each conjugate batch formulation.

physisorption. The washing step involved two rounds of centrifugation of the bioconjugates, removal of unbound nanobodies by the removal of the supernatant, and replacement of the volume with blocking buffer, additional centrifugation led to visual loss of stability of the bioconjugates (black precipitate and loss of solution intensity). The removal of unbound nanobodies is important since they would otherwise compete with the bioconjugates for the antigen and reduce the performance of the assay. Assay optimisation involved evaluating the signal-to-noise ratio (SNR), defined as the signal in the presence of S1biotin (333 ng/mL) divided by the signal in its absence (0 ng/mL). The optimal conjugation pH was established as 7.5 in HEPES buffer, as this condition yielded the highest SNR. Deviations from this pH, either lower (7.0) or higher (8.0), resulted in decreased SNR values, indicating less efficient binding. Blocking with 1x PBS proved to be the most effective while using 0.1x PBS produced a weaker SNR. Blocking with HEPES buffer resulted in an SNR of 1, signifying an inability to distinguish between the presence and absence of the antigen. The increase in ionic strength in this preparation could be driving non-specific interactions of the bioconjugate and the test line. Overall, these findings highlight the importance of optimising both conjugation pH and blocking buffer to achieve the most sensitive and specific assay performance. The optimum conditions identified in this study will be employed in subsequent experiments to compare nanobody bioconjugates generated with nanobodies of varying binder lengths.

4.2.4 Nanobody bioconjugate lateral flow assay

The trivalent VHHV nanobody afforded a clear advantage in physisorbed bioconjugate stabilisation; however, both stability and function are critical for effective application. The performance of VHHV3, VHHV2 and VHHV nanobody AuNP bioconjugates was evaluated as detection probes in LFA where the ability of the bioconjugates to withstand physiological ionic strengths, crowded protein environments and to demonstrate specific affinity interactions against the target protein could be assessed. The simplified half-dipstick LFA format comprising the nanobody conjugated AuNPs, a biotinylated SARS-CoV-2 S1 analyte S1-biotin and a membrane-bearing polystreptavidin as a capture region was used (Figure 4.12a, b). VHHV, VHHV2, and VHHV3 AuNP bioconjugates were prepared, blocked and washed under identical optimised conditions. The binding of the bioconjugate to the antigen, followed by immobilisation of the immunocomplex at the test line, leads to bioconjugate accumulation and the formation of a red line, indicating a positive signal. Signal quantification can then be performed by image analysis of photos of the LFA strips. Dose-response functions are

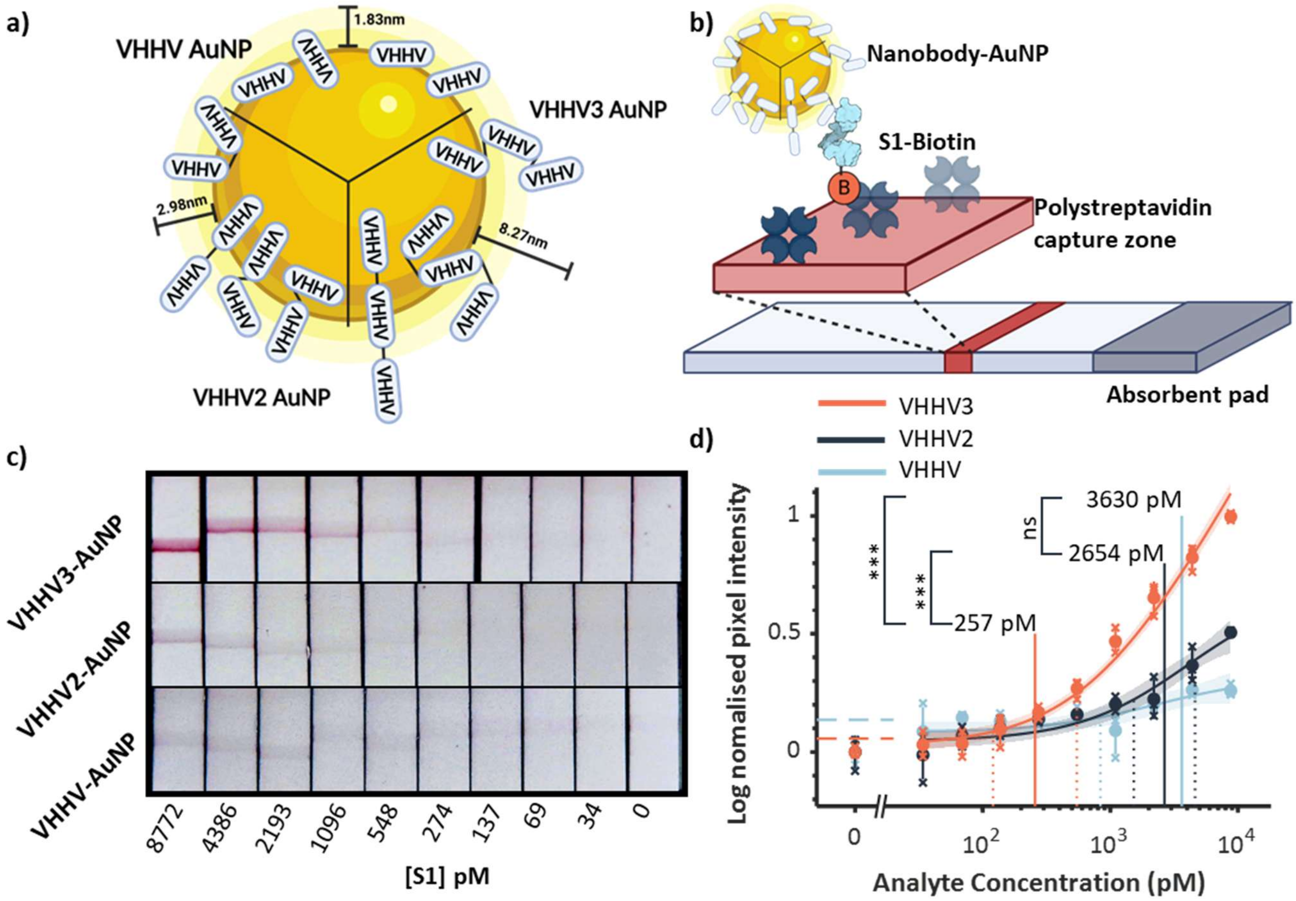

Figure 4.12 Evaluation of nanobody bioconjugates in LFA. **a)** Scheme indicating the three types of nanobody-AuNP bioconjugate and exemplar nanobody configurations **b)** Scheme of direct LFA showing capture of antigen-bound immunocomplex and immobilisation to the polystreptavidin test-line via the chemically biotinylated antigen. **c)** Images of LFA strips bearing test lines formed by bioconjugates immobilised at different antigen concentrations. **d)** Test line signal as a function of analyte concentration to establish LoD for each bioconjugate (n = 3), individual data points and their average is displayed as crosses and solid circles, respectively ± the standard deviation of the mean. Solid curves show the fitted Langmuir functions. Dashed lines show the 95% CI of the LoD calculation, while solid vertical lines show the LoD.

generated and the LoD is determined to provide a measure of the functionality and sensitivity of each bioconjugate.

Notably, VHHV and VHHV2 bioconjugates demonstrated weaker signal generation and significantly poorer limits of detection in the LFA format when compared to VHHV3 (Figure 4.12c, d). While the LoD of VHHV3 bioconjugate was 257 pM (120 – 546 pM 95% CI), the corresponding values for VHHV and VHHV2 were 3630 pM (836 - 15700 pM 95% CI $p < 0.005$) and 2650 pM (1530 – 4610 pM 95% CI $p < 0.005$) respectively. Importantly, the VHHV3-AuNP bioconjugate maintained its stability and functionality throughout the LFA process, including BSA blocking and multiple wash steps. Although VHHV and VHHV2 did not completely withstand the salt-induced aggregation test, a modest signal was generated at very high antigen concentrations following the completion of the bioconjugate preparation process, indicating some residual bioconjugate functionality. Comparing the signal profiles, VHHV3-AuNP produced significantly more signal in comparison to VHHV2-AuNP and VHHV-AuNP (Figure 4.13). VHHV-AuNP produced some signal even at zero antigen concentration, indicative of non-specific binding and a further reduction in the signal-to-noise ratio. Interestingly, VHHV2-AuNP, despite showing similar instability to VHHV-AuNP, prior to BSA blocking, displayed enhanced signal generation and signal-to-noise ratio, suggesting a relationship between nanobody length and LFA performance, even in the divalent form, potentially due to enhanced paratope display. Nevertheless, the test lines for VHHV-AuNP and VHHV2-AuNP displayed a bluish colour, indicative of nanoparticle aggregation, further highlighting the limitations of these constructs in LFA applications. It is worth noting that the VHHV3-AuNP signal profile is more intense towards the start of the test line where the AuNP-VHHV3 complex with S1 biotin would first interact with the test line. This effect is also observed with VHH2-AuNP and VHH-AuNP but to a much lesser extent. A high degree of concentrated signal at the start of the test line is indicative of a highly functional immunocomplex, potentially because of highly diffuse bioconjugates that maintain a high affinity to the antigen and therefore exhibit high affinity to the test line. While VHHV2-AuNP also shows some tendency

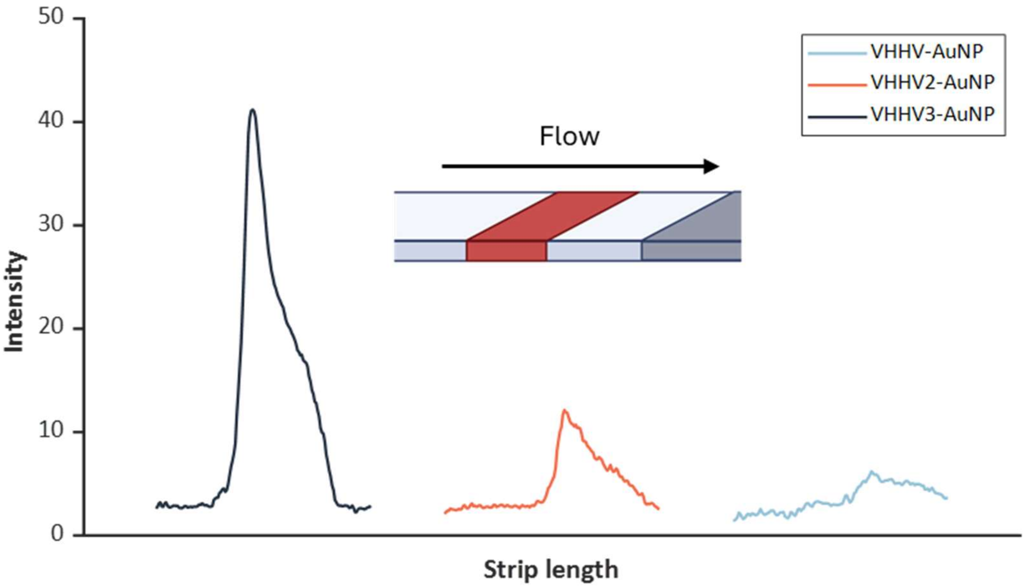

Figure 4. 13 Test-line signal intensity profiles at high antigen concentration (8772pM).

to generate more signal at the start of the test line it is much less pronounced than that of VHHV3-AuNP. This effect is absent in the intensity profile of VHHV-AuNP. The superior performance of VHHV3-AuNP likely reflects its enhanced nanoparticle stability, leading to greater availability of functional binding sites during assay operation and greater diffusivity. In addition, the presentation of nanobodies further from the AuNP surface, as indicated by the protein layer thickness determined by DLS, could indicate an increased proportion of nanobody paratopes presented appropriately for target interaction.[59]

4.2.5 Evaluation of resilience of VHHV3-AuNP bioconjugates to storage conditions

VHHV3 bioconjugates have been shown to accommodate the elevated ionic strengths associated with conditions in an LFA and the presence of high concentrations of BSA. However, LFA typically requires the bioconjugates to be in a desiccated format for improved storage and simplicity. The latter requirement is important to ensure the long-term stability of the assay and its resilience in rugged environments where a cold chain is not guaranteed.

To assess the stability of the VHHV3-AuNP bioconjugates towards harsher storage conditions, their function in LFA was measured using bioconjugates that were either used as prepared, freeze-thawed from storage at -80 °C in microtiter plates, or freeze-dried in microtiter plates prior to performing an S1-biotin antigen dose-response assay.

Initially, VHHV3-AuNP bioconjugates were frozen overnight at -80 °C in the original running buffer consisting of 1% w/v BSA in 1× PBS and 0.05% w/v Tween-20. Although bioconjugates are not typically stored frozen in solution, this serves as the intermediate step before lyophilising and is therefore a crucial point at which to evaluate any changes in stability. Bioconjugates were thawed prior to use and mixed with different concentrations of S1 biotin in running buffer before adding LFA bearing a polystreptavidin test line, matching previous experiments. The freeze-thawed bioconjugates were found to maintain their analytical sensitivity, with slightly higher LoD of 343 pM (235 - 500 pM 95% CI), when compared to unprocessed VHHV3 bioconjugates, LoD of 257 pM (120 – 546 pM 95% CI), showing no significant change (p > 0.05, Figure 4.14). Although the change in LoD is not significant, the increased LoD indicates a potential reduction in the performance of the bioconjugate. It's worth noting that there is increased non-specific binding in the freeze-thawed bioconjugates and a reduced signal intensity profile across S1 concentrations, potentially contributing to the increased LoD.

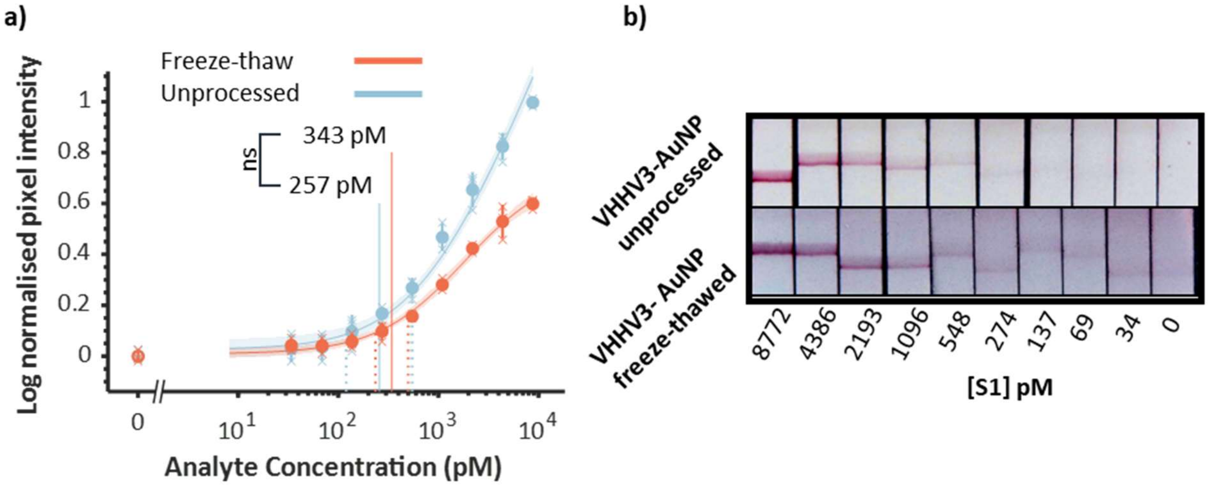

Figure 4. 14 VHHV3-AuNP freeze-thaw analysis **a)** LoD plots demonstrating the conservation of sensitivity of VHHV3-AuNPs after a freeze-thaw cycle. Each data point and their average (N = 3) are displayed as crosses and solid circles, respectively, ± the standard deviation of the mean. Solid curves show the fitted Langmuir functions. Dashed lines show the 95% CI of the LoD calculation, while solid vertical lines show the LoD. **b**) Contrast-enhanced images of LFA strips bearing test lines formed by bioconjugates immobilised at different antigen concentrations. ns – p >0.05

Following the freeze-thaw assessment, the stability of lyophilised VHHV3-AuNP bioconjugates was evaluated. Two batches were prepared: one in standard running buffer (1% w/v BSA in 1x PBS, 0.05% w/v Tween-20) and another supplemented with 10% w/v sucrose during the final wash step before lyophilisation. Visual inspection revealed distinct differences between the batches. The sucrose-supplemented batch formed a crystalline red solid, suggesting the preservation of monodispersity and plasmonic activity in the dried state. Conversely, the batch without sucrose appeared as clear crystals with black precipitates, indicative of bioconjugate aggregation (Figure 4.15).

Lyophilised bioconjugates were reconstituted with distilled water and mixed with varying concentrations of S1-biotin in running buffer before being run on LFA. As shown in Figure 4.15, the lyophilised bioconjugates containing 10% sucrose exhibited complete preservation of

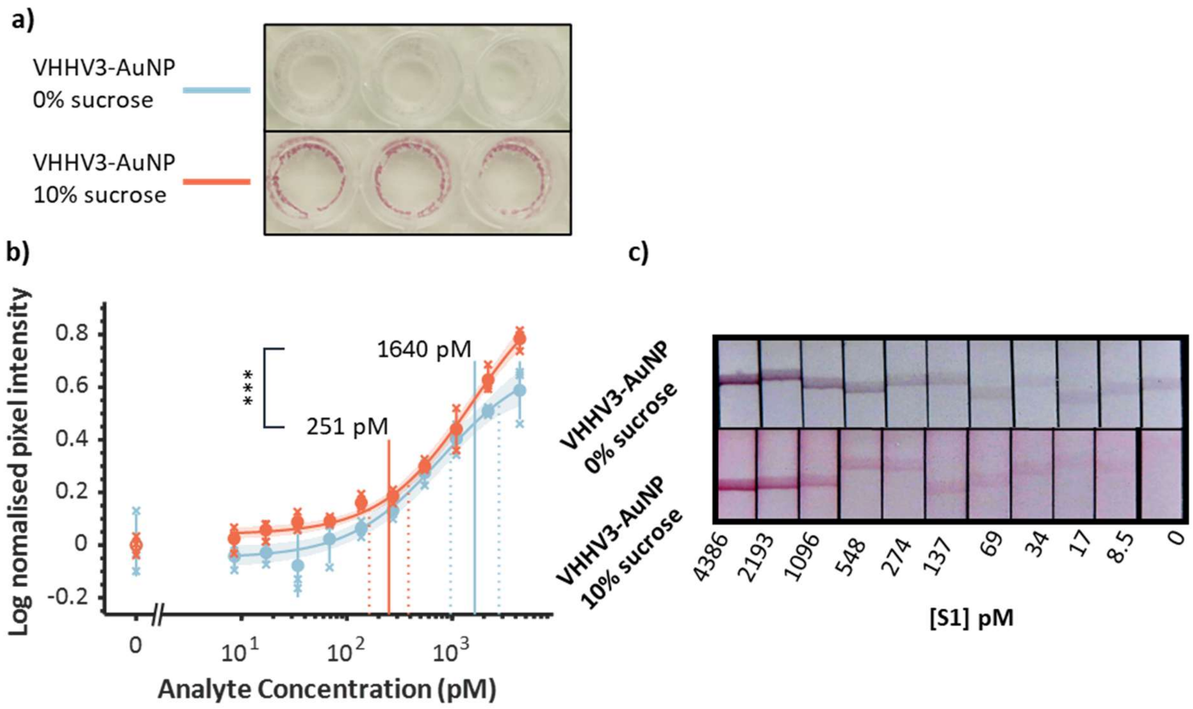

Figure 4. 15 VHHV3-AuNP lyophilisation analysis **a)** Images of VHHV3-AuNP bioconjugates lyophilised in running buffer or running buffer supplemented with 10% w/v sucrose. **b)** LoD plots comparing the sensitivity of the two batches of lyophilised VHHV3-AuNPs. Each data point and their average (N = 3) are displayed as crosses and solid circles, respectively, ± the standard deviation of the mean. Solid curves show the fitted Langmuir functions. Dashed lines show the 95% CI of the LoD calculation, while solid vertical lines show the LoD. **c**) Contrast-enhanced images of LFA strips bearing test lines formed by bioconjugates immobilised at different antigen concentrations. *** – $p < 0.005$

functionality with a calculated LoD of 251 pM (163 - 385 pM 95% CI) which was not significantly different compared to the LoD of the unprocessed VHHV3 bioconjugate LoD of 257 pM (120 – 546 pM 95% CI, $p > 0.05$). The bioconjugates lyophilised in the absence of sucrose were found to result in significantly higher limits of detection of 1640 pM (964 – 2780 pM 95% CI, $p < 0.001$). This increase in LoD and reduction in sensitivity is likely due to nanoparticle aggregation since the test line formed for the 0% sucrose bioconjugates appeared more bluish, indicative of aggregation, and an increased non-specific signal generated indicated by the generation of elevated signal at blank. While the signal profile between the two bioconjugates appear similar across the different concentrations the elevated signal at the blank likely causes the substantial increase in LoD.

These findings demonstrate that the nanobody-AuNP bioconjugates retain near-complete functionality even after freeze-drying and reconstitution, a highly promising result for LFA applications. The difference in sensitivity noted between the two different lyophilisation formulations highlights the need for optimisation to ensure maximal recovery of functionality post-storage.[5,38] During the freeze and lyophilisation process, the nanoparticles are exposed to a dramatic increase in nanoparticle concentration and increase in the ionic strength of the solution due to ice formation and solute exclusion.[117] The ability of VHHV3 bioconjugates to maintain stability and functionality after being exposed to these conditions highlights the potential of this construct for long term storage and use in LFAs

It's important to highlight that the sensitivity of the LFA using the freeze-dried VHHV3-AuNP is comparable to the nanobody ELISA detecting the S1 protein (29.8 pM vs LoD of 257 pM). This demonstrates remarkable sensitivity translation in the LFA, especially considering the significantly faster assay time (10 minutes vs 4 hours) and the lack of signal amplification used in the ELISA. Moreover, the sensitivity of the VHHV3-AuNP LFA is comparable to previously published LFAs. Shahdeo *et al*. reported a 1ng/mL (~40 pM) sensitivity for their RBD-targeting SARS-CoV-2 assay using a traditional antibody pair immunoassay.[118] Although the current LFA utilises a simplified format with biotin handles and a streptavidin test line, the comparison remains noteworthy as the nanobody LFA is still in the pre-optimisation phase and has significant potential for further improvement.

4.2.6 Polyvalent VHHV nanobody generation

In previous sections, the incorporation of VHHV into divalent and trivalent configurations was shown to enhance the diagnostic capabilities of the nanobody in an ELISA format. Moreover, the trivalent VHHV3 configuration facilitated the use of the nanobody in an LFA format due to improved nanoparticle stability. These results prompted further investigation into higher-order multivalent nanobodies, including quadrivalent (VHHV4), pentavalent (VHHV5), and hexavalent (VHHV6) versions of VHHV. These multivalent constructs were generated using previously described methods, with each VHHV domain linked by a GGGGSx3 linker (Figure 4.16a). However, protein yields for the higher-order multivalent nanobodies were significantly reduced. While typical nanobody yields are expected to be in the range of a few milligrams per litre of culture, VHHV4 yielded approximately 0.1 mg/L, VHHV5 yielded 0.05 mg/L, and VHHV6 was undetectable. This trend was confirmed by SDS-PAGE analysis, which revealed a distinct band corresponding to the purified quadrivalent fraction in VHHV4, a faint band corresponding to the pentamer in VHHV5, and no detectable band in the purified fraction for the hexavalent VHHV6 (Figure 4.16b). It is evident that protein yield decreases with an increasing number of nanobodies in tandem. This phenomenon could be attributed to the limitations of periplasmic expression for these protein constructs. The sec-dependent translocation machinery may struggle to translocate proteins of this size and complexity to the periplasm, reducing the yield. Furthermore, due to highly repetitive sequences, it is possible that the expression of the protein is reduced due to ribosome drop-off or tRNA depletion. De Groeve and colleagues also reported a decrease in protein yield per litre of culture with an increasing number of nanobodies in tandem when these are expressed in *Pichia pastoris.*[119]

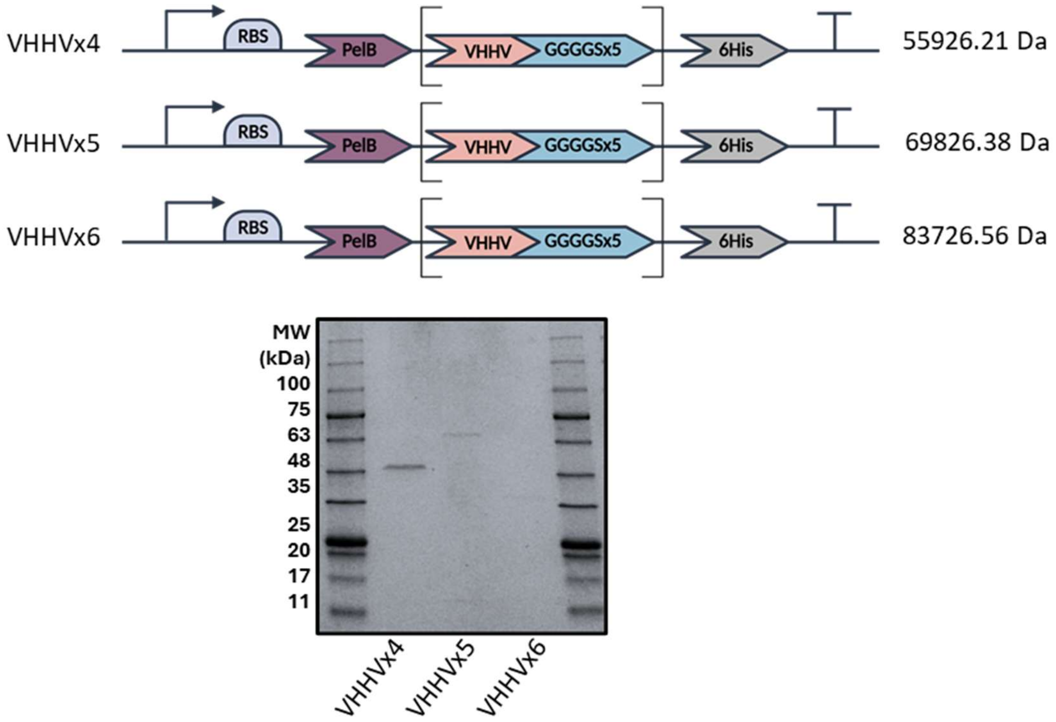

Figure 4. 16 (**a**) Gene diagram of the VHHV4, VHHV5 and VHHV6 nanobodies. RBS ribosome binding site. The arrow depicts the direction of translation. (**b**) Reducing SDS-PAGE, Lanes 1 and 5 contain the protein MW reference marker, lanes 2, 3 and 4 purified fractions from the VHHV4, VHHV5 and VHHV6 expression, respectively.

4.2.7 Tetravalent VHHV4 nanobody-AuNP physisorption

The significantly reduced yields of nanobodies VHHV4, VHHV5, and VHH6, in comparison to smaller nanobody chains, may hinder their diagnostic potential due to inefficient production. Despite this, VHHV4 was expressed in sufficient protein yields to enable experimentation for producing bioconjugates with AuNPs. In accordance with previous experiments, VHHV4 was physisorbed onto 40 nm AuNP at a 3200-fold molar excess across a pH range of 5.0-10.0, and the stability of the bioconjugates was monitored using the aggregation index (A580/A530) before and after the addition of 400 mM of NaCl.

Prior to salt addition, VHHV4 followed a similar aggregation profile to VHHV3, where colloidal stability was maintained at pH > 6.0 (Figure 4.17a). This is likely attributable to the similar isoelectric point of VHHV4, where the protein loses its excessive positive charge at pH greater than 6.0 and no longer induces nanoparticle aggregation due to protein-mediated nanoparticle bridging. After the addition of NaCl (400 nM), VHHV4 also exhibited a range of pH conditions where complete stability was maintained, mirroring the findings from VHHV3. However, VHHV4 enabled stability across a broader pH range. While VHHV3 appeared to prevent salt-induced aggregation when conjugation was performed at pH 6.5 to 7.5, VHHV4 appeared to reduce salt aggregation at pH 6.5 to 8.5 (Figure 4.17b). Furthermore, even at higher pH values

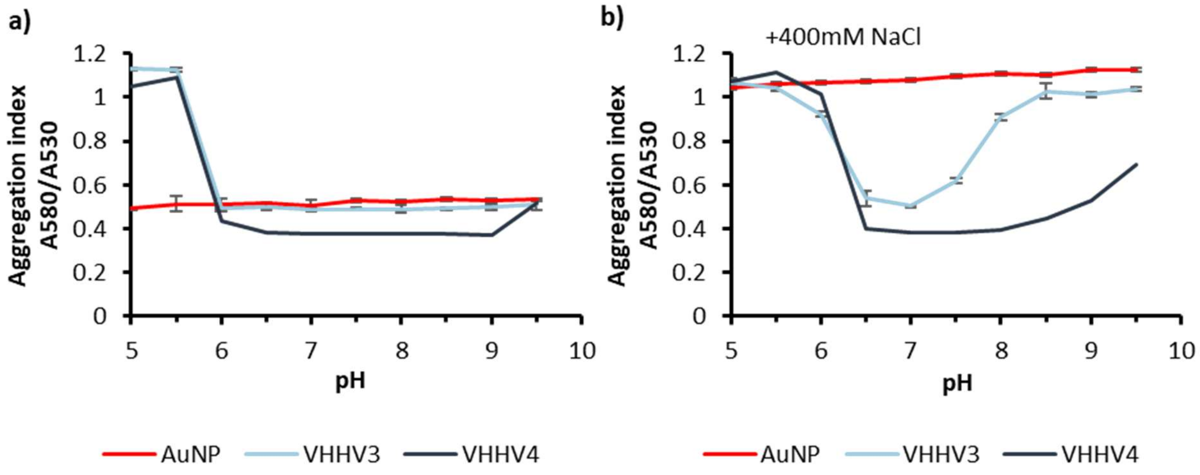

Figure 4. 17 Aggregation index of VHHV3 and VHHV4 bioconjugates before (**a**) and after (**b**) the addition of 400 mM of NaCl. Values displayed as the mean (n = 3) ± the standard deviation for VHHV3. N= 1 for VHHV4.

(>8.5), where complete stability was not maintained, a notable decrease in aggregation was observed, showing a greater protection against aggregation afforded by VHHV4 to AuNP. This indicated that VHHV4 possesses a distinct advantage over VHHV3 in preventing salt-induced aggregation, in accordance with the initial findings that stability improves with increasing protein size and, in this case, the number of nanobodies in tandem. Despite this, the significantly reduced protein yield may hinder the diagnostic potential of this nanobody and other higher-order multivalent nanobodies. Efforts to improve yields have been explored and may potentially mitigate the reduced expression of these nanobodies. For instance, cytoplasmic expression, rather than periplasmic expression, has been shown to be an efficient alternative for nanobody expression when sulfhydryl oxidase and disulfide-bond isomerase are co-expressed. This would be particularly beneficial if the limitation of larger polyvalent nanobodies' expression is due to inefficient periplasmic direction or failure to fold in the periplasm.[120] Furthermore, the co-expression of auxiliary proteins such as HAC1 has been shown to improve the protein yields of polyvalent nanobodies. HAC1 is a transcription factor activated by the cell unfolded protein response and activates the expression of chaperones, foldases, and proteins involved in glycosylation.[119]

VHHV4 bioconjugates demonstrate superior stability compared to VHHV3 bioconjugates, resisting salt-induced aggregation across a wider pH range. In the previous sections, it was shown that improved stability correlates with improved sensitivity in LFA. However, low VHHV4 yields hindered LFA experimentation in this study. Therefore, further research should focus on optimising VHHV4 production to enable a thorough evaluation of its potential for improved LFA sensitivity.

4.2.8 Multivalent VHHE and Nb6

To explore whether the improvement in stability gained by incorporating VHHV into multivalent nanobody chains applies more broadly to other nanobodies, nanobodies VHHE and Nb6 were also incorporated into divalent and trivalent formats, utilising the same GGGGSx3 flexible

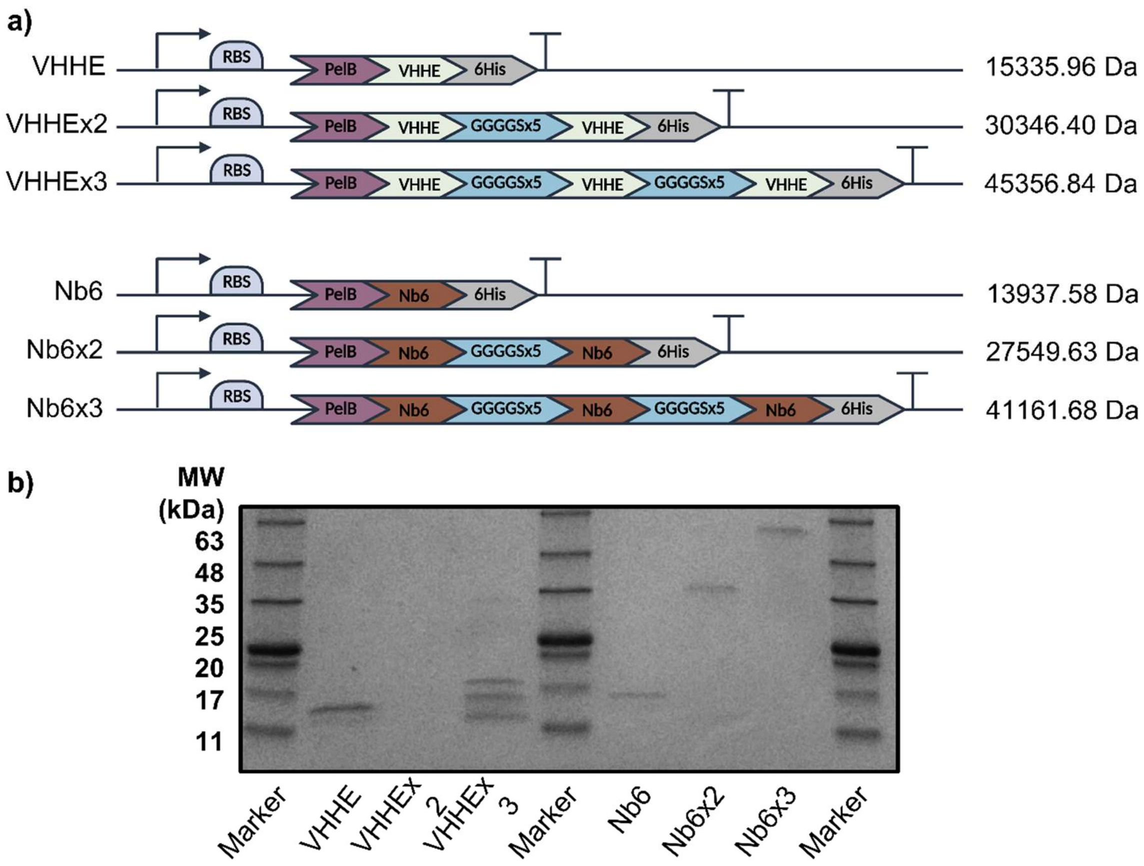

Figure 4. 18 (**a**) Gene diagram of the multivalent versions of nanobodies VHHE and Nb6 and their respective molecular weights based on the amino acid sequence. (**b**) Reducing SDS-PAGE, Lanes 1,5 and 9 contain the protein MW reference marker, and lanes 2, 3 and 4 contain the purified fraction of VHHE, VHHEx2 and VHHEx3 respectively. Lanes 6,7 and 8 contain the purified fractions of Nb6, Nb6x2 and Nb6x3, respectively.

linker. These nanobodies were expressed in *E. coli* within the bacterial periplasm (Figure 4.18a).

For Nb6, Nb6x2 (divalent), and Nb6x3 (trivalent), SDS-PAGE analysis revealed a single band in each sample, corresponding to the monovalent, divalent, and trivalent forms of Nb6, respectively. The bands appeared to migrate slower than their anticipated molecular weights, but the difference between each protein was as expected (Figure 4.18b).

Conversely, SDS-PAGE analysis of VHHE revealed no detectable bands for VHHEx2 and three bands at approximately the expected molecular weight for the monomer in the VHHEx3 sample. It appears that the multimeric VHHE was not efficiently expressed. Furthermore, the three bands in the trimeric sample indicate that the protein may be experiencing incomplete expression or protein degradation. This is in stark contrast to the study by Koenig *et al.*, where a trivalent version of VHHE was expressed in *E. coli*, although the authors did not report the yields or scales required for sufficient protein yield.[34] Importantly, the VHHE nanobody contains two internal disulfide bonds, classifying it as a type VHH1 nanobody, which has been shown to result in significantly poorer yields. It has been demonstrated that this can be addressed by co-expressing auxiliary proteins to assist in protein folding when these types of nanobodies are expressed in *Pichia pastoris* systems.[119] Furthermore, VHHE has a much longer CDR3 region (Figure 3.1a), which contributes to the added complexity and possibly hinders the expression of this nanobody.

4.2.9 Multivalent Nb6 AuNP physisorption

The physisorption characteristics of the monovalent and multivalent versions of Nb6 were compared by performing conjugation experiments across different pH conditions and monitoring the aggregation index of the resulting bioconjugates using UV-Vis spectroscopy. Similar to the previous conjugation experiments, the ratio of nanobody to AuNPs during bioconjugation was maintained at 3200 nanobodies to AuNPs and the stability of the bioconjugates was evaluated in low and high ionic strength conditions through exposure to elevated concentrations of NaCl.

Figure 4.19a shows the aggregation profiles of Nb6, Nb6x2, and Nb6x3 bioconjugates across a pH range after conjugation before the addition of salt. While Nb6 appears to yield relatively more stable conjugates at pH 9.5, Nb6x2 shows an earlier pH onset of maintaining colloidal stability at pH 9. This is unexpected, as the calculated isoelectric point (IEP) of Nb6x2 (9.75) is higher than that of Nb6 (9.39). A higher IEP would typically indicate that the protein would require a more elevated pH to lose the excess positive charge that normally causes aggregation. Conversely, Nb6x3 appears to require higher pH during conjugation to achieve bioconjugate stability, only showing improvement in aggregation index at pH 10. This aligns with the elevated calculated IEP of Nb6x3 (9.89) compared to the dimeric and monomeric Nb6. The observation that Nb6x3 demonstrates improved nanoparticle stability at the highest

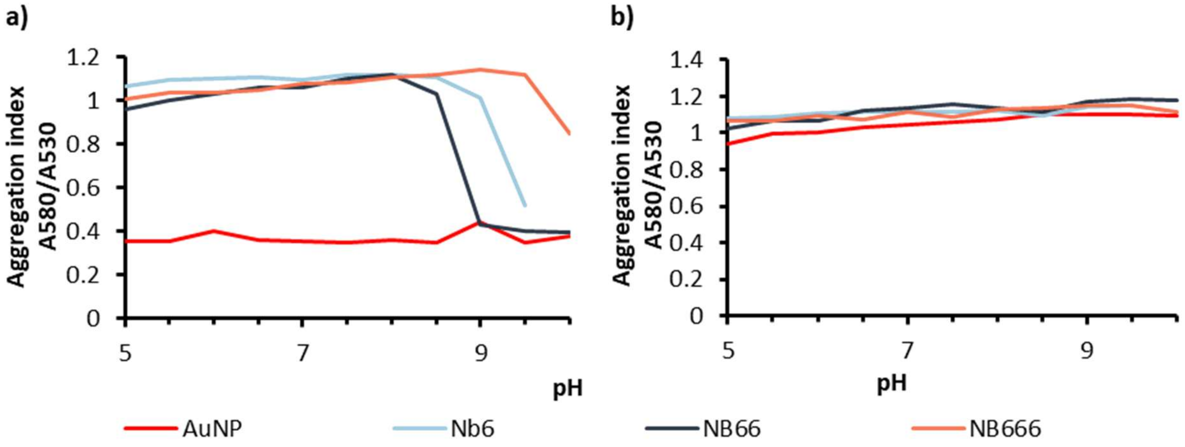

Figure 4.19 The stability profile of AuNP bioconjugates generated with monovalent Nb6, divalent Nb6x2 and trivalent Nb6x3 nanobodies at varying pH conditions (5.0- 10.0). (**a**) The aggregation index as a function of pH before the addition of 400 mM NaCl (n = 1). (**b**) The aggregation index as a function of pH before the addition of 400 mM of NaCl (n = 1).

pH tested but does not achieve complete stability suggests that the optimal pH condition for stability may lie outside the tested pH range.

Following the elevation of the ionic strength through the addition of 400 mM of NaCl, the aggregation profile of the trivalent and divalent nanobodies mirrors the aggregation profile of the monomeric Nb6 (Figure 4.19b). Across all tested pH conditions, all bioconjugates show no conservation of stability and aggregate following exposure to high ionic strengths. This is in contrast to the results obtained for VHH3 compared to VHHV in the previous sections. One possible explanation is that due to the elevated IEP of Nb6x3, the optimum pH condition required to yield stable bioconjugates resistant to salt-induced aggregation is greater than the pH range tested here.

The high IEP of Nb6 and its multimers may represent another challenge for producing stable bioconjugates. In the study by Goossens *et al.,* it was demonstrated that the only nanobody that conserved its stability and showed some degree of resistance to salt-induced aggregation was the nanobody with the lowest IEP (5.71). The other two tested nanobodies, each having a calculated IEP of 8.02 and 9.01, showed no resistance to salt-induced aggregation. This is in agreement with the findings in this thesis. In Chapter 3, monomeric nanobodies VHHV and VHHE showed some conservation of nanoparticle stability at mild ionic strength conditions, on which Nb6 showed none (Figure 3.6). Both VHHV and VHHE have relatively lower IEP of (6.70 and 6.75 respectively) compared to Nb6 (9.39). This demonstrates that nanobodies with lower IEP may have favourable binding kinetics to AuNPs and a greater tendency to generate stable bioconjugates resistant to elevated ionic strengths. At greater pH conditions needed for bioconjugation of high IEP nanobodies, the surface charge of the citrate-capped AuNPs will also become more negatively charged. This could result in the repulsion of negatively charged residues present in the protein despite its net neutral charge around its IEP, causing unfavourable binding kinetics. Based on this theory, nanobodies with low IEP may be required to generate robust AuNP bioconjugates, even in their multivalent forms.

4.3 Conclusions

Nanobodies can potentially improve point-of-care diagnostics by harnessing their ease of development and production, but their limitations must be addressed for successful implementation. This chapter outlines the creation of a stable nanobody bioconjugate capable of withstanding the rigorous processing steps required for nanoparticle storage in LFAs. The nanobody-bioconjugate stability issue was tackled through protein engineering, leading to the development of VHHV3, a trivalent version of VHHV targeting the SARS-CoV-2 Spike glycoprotein.

The systematic investigation into the diagnostic potential of multivalent nanobodies has revealed distinct advantages across various diagnostic platforms. The divalent and trivalent versions of VHHV demonstrated increased affinity, as evidenced by a decrease in the dissociation constant. This translated to significant improvements in the LoD when used in ELISA detecting the S1 protein. In the context of LFAs, the trivalent VHHV3 generated AuNP bioconjugates with superior stability compared to the monovalent and divalent forms of VHHV. Crucially, VHHV3 bioconjugates maintained stability and picomolar sensitivity to the S1 protein throughout various nanoparticle processing stages, including exposure to high ionic strength, interaction with blocker proteins, centrifugation cycles, freeze-thawing, and freeze-drying. The sensitivity achieved is comparable to that of commercial, antibody-based LFA. These results strongly suggest that this nanobody bioconjugate has the necessary stability to allow application in LFA diagnostics.

Despite these promising findings, a rational screening of nanobodies during LFA development, as with traditional antibody diagnostics, is still necessary to ensure commercial viability and fulfil various performance criteria. The nanobodies studied here, both in monovalent and multivalent forms, exhibited distinct differences in their ability to form stable bioconjugates, performance in analytical assays, and expression levels in bacterial cultures.

In this study, a type VHH1 nanobody (VHHE) was utilised, and consistent with previous findings, it exhibited significantly lower protein yields compared to other nanobodies. Additionally, attempts to incorporate VHHE into divalent or trivalent formats were unsuccessful, as the protein failed to express at detectable levels. This limitation was not unique to VHHE, as polyvalent VHHV nanobodies with more than three tandem repeats also demonstrated reduced yields. This reduction in yield could pose a significant challenge to the practical implementation of these polyvalent nanobodies in diagnostic applications, as it would necessitate larger-scale production processes to obtain sufficient quantities for widespread use. Interestingly, despite the yield limitations, the tetravalent VHHV4 demonstrated enhanced bioconjugate stability against salt-induced aggregation across a broader pH range. This suggests that increasing the valency of the nanobody may not only improve binding kinetics, as expected for polyvalent constructs but also confer greater stability to the bioconjugate, a critical factor for diagnostic applications where stability is paramount. The observed improvement in stability, combined with the potential for enhanced binding kinetics, suggests that polyvalent nanobodies like VHHV4 could offer significant advantages in diagnostic assays. However, the reduced yields associated with these constructs present a significant hurdle to their widespread implementation. Future research should, therefore, prioritise optimising the expression of these nanobodies in multivalent formats. This could involve exploring alternative expression systems, optimising fermentation conditions, or investigating novel protein engineering strategies to enhance yields. By addressing this limitation, the full potential of polyvalent nanobodies in diagnostics could be unlocked, leading to more sensitive, specific, and stable assays for various applications.

Another area for future work would be the study of different linkers within the multivalent nanobodies. While flexible linkers have been shown to maximise the affinity gains of multivalent nanobodies, using a rigid linker may benefit bioconjugate stability. The improved stability observed for the VHHV-Cys dimer, which was absent in the divalent VHHV, supports this hypothesis. Moreover, the rigid structure has been shown to produce nanobodies with a larger hydrodynamic radius, potentially leading to a more robust protein layer on the nanoparticle surface, further enhancing stability.

In this chapter, the results suggested that multivalent nanobodies may provide greater stability to nanobody bioconjugates by providing a more robust steric layer, preventing the contact of individual AuNPs. Alternative avenues to achieving this could be through the fusion of nanobodies with larger globular proteins, known to interact strongly with gold such as GST. Using a nanobody-GST fusion, where the GST would enable directed immobilisation, and act as an anchor protein, shielding the nanobody from the nanoparticle surface and providing a steric layer for improved stability. Furthermore, the combination of different nanobodies in tandem could be used to control the final IEP of the multivalent nanobody chain and provide favourable IEP for nanoparticle binding and stabilisation.

The findings of this study also underscore the importance of understanding the interplay between nanobody IEP and nanobody-bioconjugate behaviour. The observation of a potential relationship between acidic IEPs and increased resistance to salt-induced aggregation in VHHV, but not in Nb6, in both monovalent and multivalent forms, suggests that IEP may be a crucial factor to consider in nanobody selection and engineering for LFA development. Further investigation into this relationship, involving a larger and more diverse panel of nanobody candidates, could provide valuable insights for optimising nanobody performance in LFA applications.

In conclusion, the potential of multivalent nanobodies for advancing nanobody-based PoC diagnostics has been highlighted in this research. By addressing the limitations associated with yield and stability and by exploring the influence of linker design and protein IEP, the development of more sensitive, specific, and robust LFA-based diagnostic tools can be realised. The insights gained from this study lay the groundwork for future research aimed at unlocking the full potential of nanobodies in LFAs. The cheap bacterial production of nanobodies and their quick development can further accelerate the LFA development process, leading to improved global health outcomes.

5 Modular nanobody lateral flow assays: A plug-and-play diagnostic platform

5.1 Introduction

Controlling emerging infectious diseases is critical for public health and can prevent severe socioeconomic disruption. The COVID-19 pandemic highlighted the urgent need for inexpensive, high-performing point-of-care diagnostics. Lateral flow assays (LFAs) are cheap, quick, and easy to use. While their sensitivity is lower than the 'gold standard' nucleic acid amplification tests (NAATs), LFAs are among the few diagnostics deployable at the unprecedented scale required for population-wide testing.[8] Their use is integral for real-time monitoring and controlling outbreaks, enabling the disruption of transmission chains through contact tracing and self-isolation.

Remarkably, the first commercial rapid antigen LFA received emergency use authorisation in May 2020, just five months after the WHO declared COVID-19 a public health emergency. This rapid development is notable, considering that LFA development for other infectious diseases can take years. However, despite this initial progress, LFAs were not publicly available for self-testing at home until 2021, a strategy strongly endorsed by the WHO.[121]

A report by the pandemic preparedness partnership to the G7 task force urged policymakers to ensure the broad availability of rapid diagnostics within 100 days of an outbreak's onset. This report suggests that if such a plan had been in place for the SARS-CoV-2 pandemic, hundreds of thousands of deaths could have been prevented.[3]

The development of a rapid antigen LFA that meets the required specificity and sensitivity for a target disease is a lengthy and iterative process.[25] This optimisation necessitates a thorough exploration of the multivariate space through empirical testing.[71] There is a growing need to streamline and accelerate this optimisation process. Several approaches have been proposed to address this challenge. Anderson *et al.* demonstrated an automated approach to LFA optimisation using automated liquid handlers. This method successfully replicated results achieved through manual operation while significantly increasing throughput. By screening hundreds of antibody pairs and concentrations with minimal human intervention, this automated approach offers a promising avenue for rapid and efficient LFA development.[122] Alternatively, mechanistic models based on mass transport and reaction theory can identify optimal parameters and potential performance-limiting processes within a specific LFA. Gasperino *et al*. provide a detailed review of applying mathematical models in LFA development.[25] Sotnikov *et al*. employed a diffusion-advection-reaction model to identify parameters that increase the sensitivity of a serological antibody LFA, including reducing nanoparticle bioconjugate concentration, decreasing flow rate, and increasing test line receptor concentration.[110] Integrating mathematical models and automated LFA optimisation promises quicker development of sensitive LFAs and could improve our response to controlling the spread of infectious diseases. The COVID-19 pandemic highlighted additional challenges in LFA development and deployment during the global crisis, particularly concerning low capacity in supply chains and manufacturing.[72]

Previous chapters in this thesis discussed the benefits of using nanobodies in LFAs and focused on understanding and improving the physisorption of engineered nanobodies to AuNPs. Their quick and easy developability, as well as cheap and straightforward production in bacteria, at least in their monovalent form, make them compelling alternatives to traditional antibodies, with the potential to accelerate LFA development and manufacturing.[56] The work in this chapter capitalises on the adaptability of nanobodies and the straightforward protein engineering to further accelerate LFA development by developing an adaptable nanobody-based LFA. This involves the modular display of nanobodies onto LFA surfaces to generate a universal "plug-and-play" LFA cassette. This cassette is envisioned to be adaptable to any disease of interest through the use of appropriate nanobody pairs. Specifically, the modules in this system include tagged detection nanobodies, designed to bind to AuNPs, and tagged capture nanobodies, engineered for immobilisation onto functionalised nitrocellulose membranes. These nanobodies, along with their respective LFA-functionalised surfaces–AuNPs and nitrocellulose membranes–can bind the nanobodies in a modular fashion, thereby creating a versatile assay format. Developing adaptable, prefabricated LFA cassettes that can be readily modified for a target disease using the appropriate affinity agents can potentially minimise supply chain and manufacturing limitations during global crises. For the design of the modular display LFA, mathematical modelling is employed to identify appropriate affinity pairs for displaying nanobodies on LFA surfaces that meet the stringent criteria of point-of-care testing, including rapid binding kinetics and high sensitivity. Informed by these models, a popular in vivo biotinylation method for the simultaneous expression and orthogonal biotinylation of nanobodies in bacteria is utilised. By generating streptavidin-functionalised LFA surfaces, it is demonstrated that these biotinylated nanobodies can be used to generate highly sensitive (low pM) LFAs detecting the S1 protein of SARS-CoV-2. Notably, a dual modular LFA is generated and confirmed using a nanobody pair as the detection and capture reagents.

This research envisions a fully adaptable modular LFA platform employing streptavidin-coated gold nanoparticles (AuNPs) and streptavidin-coated nitrocellulose membranes for the display of both detection and capture nanobodies. This "plug-and-play" approach is intended to allow for the stockpiling of universal LFA cassettes that can be readily functionalised with target-specific nanobodies by the end user or local diagnostic facility, mitigating the effects of supply chain disruptions and reducing waste associated with expired assays. This approach not only facilitates the universal application of the LFA to any biotinylated nanobody pairs but also mitigates the challenges of direct binding of nanobodies onto surfaces, which, as demonstrated in previous chapters can cause issues such as poor bioconjugate stability and loss of functionality.

By decoupling the LFA architecture from the target-specific reagents, this strategy offers a rapid and flexible response to emerging infectious diseases. Upon identification of a new threat, nanobody pairs can be rapidly developed and integrated into the pre-fabricated, stockpiled LFAs, bypassing the manufacturing bottlenecks associated with traditional LFA

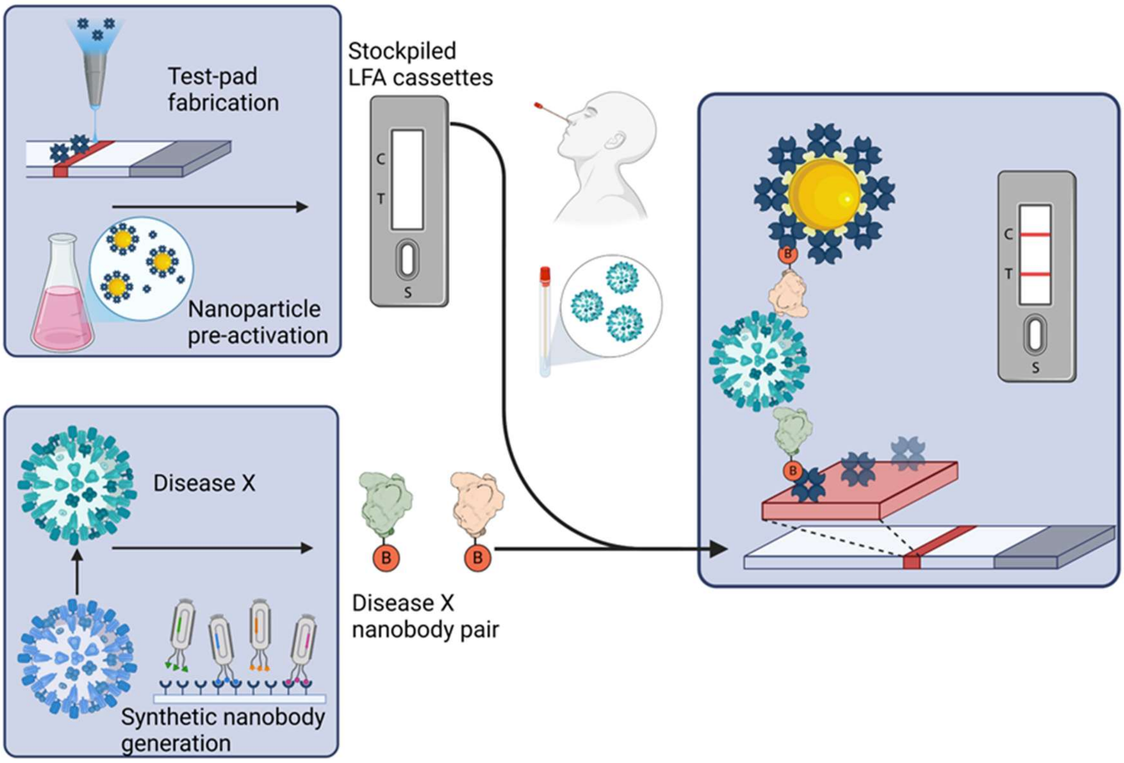

Figure 5. 1. Process diagram for the deployment of the proposed plug-and-play LFA against an emerging infectious agent – 'disease x'. The deployment begins with the fabrication and stockpiling of streptavidin bioconjugates and streptavidin functionalised nitrocellulose membranes. Upon the emergence of the infectious agent of concern, a suitable biomarker for the detection of the agent is identified and used to generate pairs of nanobodies. The nanobodies are produced at scale using an in vivo biotinylation system and deployed to the field to be used as the detection and capture reagents in the plug and play LFA using a modular display method. At the point-of-care, the sample containing the biomarker is collected and the nanobodies are used to activate the LFA diagnostic by the test operator. The test result is readable by the eye within a few minutes of sample collection.

design and production. A process diagram for the deployment of the proposed plug-and-play LFA is shown in Figure 5.1.

Furthermore, the modular display of nanobodies eliminates the complex protein-solid interface at the nanoparticle and nitrocellulose surface, enabling oriented attachment of nanobodies for improved sensitivity without extensive optimisation. This approach is expected to be applicable to a wide range of antigens with the use of appropriate nanobody pairs, though further investigation is needed to confirm universal compatibility with different reagent types.

This initial exemplar system demonstrates the feasibility of this modular LFA technology, highlighting its potential to significantly reduce LFA development time and bring the 100-day mission response to outbreaks closer to reality. The proposed platform promises a more robust and effective response to emerging infectious threats by facilitating quicker and more reliable development of LFA diagnostics.

5.2 Results and discussion

5.2.1 Computational modelling to guide the design of the modular bioconjugate

The modular display nanoparticle system employs AuNPs functionalised with an affinity macromolecule. This creates a base bioconjugate. Next, a detection nanobody, specifically engineered with an affinity "handle" positioned away from its antigen-binding site (paratope), is introduced. This handle allows the nanobody to bind specifically and efficiently to the affinity macromolecule on the AuNP. This nanobody is designed to target the biomarker of the target disease. This design enables the assembled bioconjugate complex to recognise the antigen and function as the label in the plug-and-play diagnostic. Different affinity molecules have unique binding affinities to their target handles (e.g., biotin-streptavidin, His-tag-NiNTA). This will ultimately mean that different affinity pairs will require different conditions (incubation time and nanobody concentration) to achieve the same level of decoration. To study the level of decoration of each system and identify potential limitations, a theoretical evaluation of system dynamics is conducted using mathematical modelling. The mathematical modelling is crucial to determine if the binding kinetics of different affinity pairs (e.g., biotinylated nanobody to streptavidin) are fast enough to achieve sufficient "decoration" within these very short, practical timeframes available to the end-user. If the decoration process takes hours, it would defeat the purpose of a rapid PoC diagnostic and would not be feasible for immediate on-site testing.

The kinetics of how molecules bind to cell surfaces was first described by Burg and Purcell and later validated by Erickson *et al.*, focusing on ligand interactions with cell membrane receptors.[123,124] Gasperino *et al.* introduced the application of this type of modelling in the realm of diagnostic nanoparticles, recognising its potential beyond its original context of cell surface receptor interactions.[25] Equations 5.1 and 5.2 are used to adjust the effective association rate, $K_{on,particle}$, and dissociation rate $K_{off,particle}$ of the polyvalent nanoparticles

$$K_{on,particle} = \frac{4\pi\alpha D N K_{on}}{NK_{on} + 4\pi\alpha D} \tag{5.1}$$

$$K_{off,particle} = K_{off}\left(1 - \frac{NK_{on}}{4\pi\alpha D + NK_{on}}\right) \tag{5.2}$$

taking into consideration the nanoparticle radius α, ligand diffusivity D, the intrinsic associative rate between the individual primary affinity macromolecule and the tagged nanobody K_{on}, and the number of binding sites on the surface of the bioconjugate – N. This theory dictates that the binding of an analyte to an antibody-coated nanoparticle occurs in two distinct phases. First, there's the approach of the analyte to the proximity of an antibody, a step primarily limited by the analyte's diffusivity. Second, there's the reversible binding of the analyte to the antibody itself, a phase that depends on both the number of antibodies present on the nanoparticle surface and the native association rate of the individual antibody-antigen interaction. Here, the adjusted Kon and Koff values of the polyvalent nanoparticle system were employed to model the interactions between the bioconjugate (displaying the primary affinity macromolecule) and the secondary tagged detection nanobody in a solution-based model. The change in the concentration of $[PN_n]$ complexes over time is described by the differential equation 5.3 where $[PN_n]$ is the concentration of particles bound to n number of secondary nanobodies and $[N]$ is the concentration of free detection nanobodies. The scheme in Figure 5.2 demonstrates this interaction.

$$\frac{d[PN_n]}{dt} = K_{on,particle} * [PN_{n-1}] * [N] - K_{off,particle} * [PN_n] \tag{5.3}$$

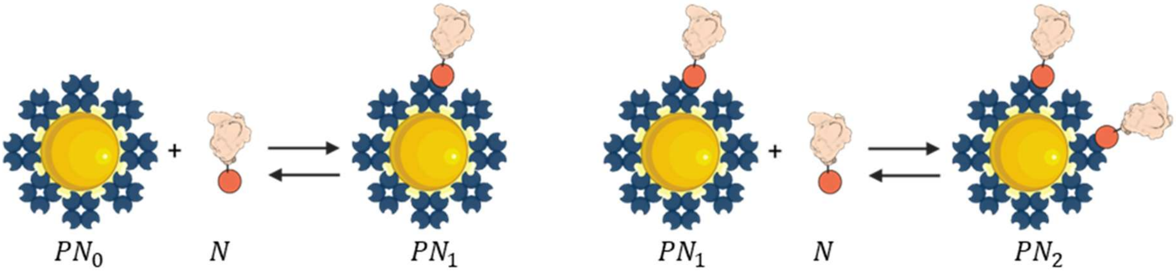

Figure 5. 2 Scheme demonstrating the binding of detection nanobody (N) to the surface of functionalised AuNP biocinjugates (P) to form nanobody decorated bioconjugates (PN).

5.2.2 Off-line decoration at the PoC

This section explores the off-line decoration of modular functionalised nanoparticles with tagged nanobodies for use in LFA. "Off-line decoration" refers to the process where the functionalised AuNPs are decorated with detection nanobodies in a separate tube before being applied to the test pad. This allows for pre-assembly of the detection complex.

The interaction of different affinity pairs was modelled using a range of dissociation constants from 250 fM to 0.01 nM. The lower limit of 250 fM corresponds to the strong interaction between streptavidin and biotin, with reported K_D values ranging from 250 to 10 fM.[125,126] The upper limit of 0.01 nM represents the range of affinities typically observed in antibody, nanobody, and aptamer recognition (ranging from 0.01 to 100 nM).[8] The modular LFA is intended to be performed at the point-of-care where the capture and detection nanobodies would be used to activate the prefabricated nitrocellulose pads and bioconjugates. To satisfy the WHO ASSURED criteria for point-of-care tests, the modular LFA must be simple to operate without the use of any equipment and provide results within 15-60 minutes of sample collection.[10] In addition to the time required for sample collection and assay operation, the modular LFA has the additional step of the decoration of the detection nanobody on the bioconjugate before the assay, which must also be considered for assay run time. To operate the assay, the user would mix the detection nanobody with the bioconjugate to activate the bioconjugate decoration step. With this proviso in mind, the bioconjugate decoration step should take no longer than 15 minutes to enable the performance of the entire assay in these timeframes. Furthermore, the decoration step should decorate the bioconjugate as much as possible for efficient analyte capture to maximise sensitivity and leave minimal amounts of free nanobody in the solution that could interfere with the assay. Since this would be operated at the PoC, the decoration should be performed without the need for separation of the unbound nanobodies. Based on these, the different affinity systems were evaluated when reacted with equimolar concentrations of detection nanobody to binding sites on the bioconjugate.

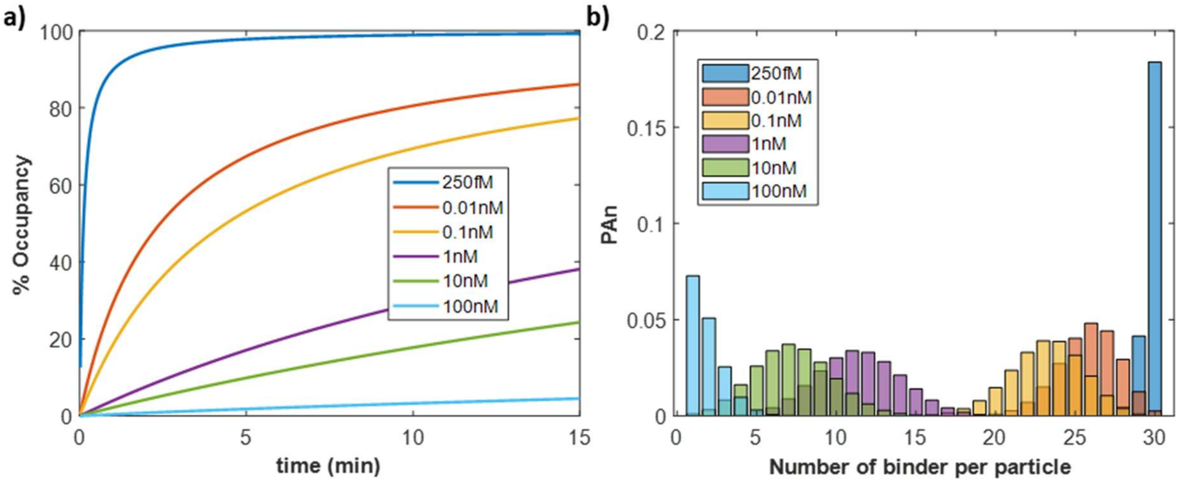

Figure 5. 3 Results of the PoC decoration simulation **a**) % occupancy plot of available binding sites on the gold nanoparticle bioconjugate by detection nanobodies. Each series represents a different affinity system. **b**) The distribution of the number of occupied receptors of bioconjugates by detection nanobodies after incubating with detection nanobodies for 15 minutes.

The system tested consisted of a polyvalent nanoparticle with 30 binding sites, reacted with a 30-fold molar excess of nanobodies. The bioconjugate concentration was set to 230 pM, a typical concentration used for LFA applications.[38,56,59] Figure 5.3a illustrates the formation of PN_ncomplexes, with each series representing the percentage occupancy of the bioconjugate receptors of different affinity systems over a timeframe of 15 minutes. The exceptional kinetics of the biotin-streptavidin interaction are demonstrated here, where equilibrium is achieved in a few minutes, reaching almost 100% occupancy (>99% at 12min) of the bioconjugate receptors. Figure 5.3 (b) illustrates the distribution of the number of detections nanobodies per bioconjugate for each affinity pair after 15 minutes of incubation. The streptavidin-biotin system shows that a very homogeneous distribution is achieved after 15, with the majority of bioconjugates bound to 30 detection nanobodies. Moreover, the concentration of the detection nanobody in the biotin-streptavidin simulation is reduced to 0.05 nM after 15 minutes, which is not expected to interfere with the assay. For the sub nM affinity systems, K_D = 0.1 and 0.01 nM, the occupancy percentages after 15 minutes were 86% and 77%, respectively, which resulted in higher concentrations of free detection nanobody after 15 minutes of 0.95 and 1.56 nM, respectively.

These results demonstrate that the modular nanoparticle system requires affinity reagents with exceptional kinetics, such as those of the biotin-streptavidin interaction, to achieve maximal decoration. Of the interactions tested, the streptavidin-biotin interaction appears to be the only one that reaches saturating conditions on the bioconjugate surface within the required timeframe. This not only maximises the resulting bioconjugate kinetics for efficient analyte capture but also minimises the remaining free nanobodies in solution that can compete for binding with the analyte and reduce assay sensitivity. The need for exceptional kinetics arises from the short timescales required for point-of-care assays, the dilute concentrations of the nanoparticles, and the inability to purify out unbound capture nanobodies during the assay.

5.2.3 In-line bioconjugate decoration

While the previous section demonstrated the feasibility of rapid nanobody decoration within PoC timeframes, the additional mixing and incubation step adds complexity compared to traditional LFAs. In traditional LFAs, sample application simultaneously rehydrates and mobilises the dried bioconjugate, initiating interaction with the analyte. The resuspended bioconjugate has a window to bind to the analyte from the time it is rehydrated until the bioconjugate-analyte mixture reaches the test line. The timeframe for this window is typically in the region of 10-30 seconds.[127] To streamline the modular LFA and potentially eliminate the separate decoration step, the possibility of "in-line" decoration was investigated. This approach utilises the solution-phase biotinylated nanobody to rehydrate and simultaneously decorate the dried streptavidin-coated conjugate while migrating towards the test line.

This in-line decoration strategy necessitates rapid and efficient conjugate decoration while minimising free nanobody concentration. To assess feasibility, the interaction was simulated using a polyvalent nanoparticle (30 binding sites) exhibiting streptavidin-biotin level affinity with varying ratios of an initial biotinylated nanobody (by adjusting initial detection nanobody concentration) to streptavidin binding site on the bioconjugate. This simulation explored different timeframes for the decoration window (10, 30, 60, and 120 seconds) representing the duration of nanobody interaction with the bioconjugate, simulating various flow rates and

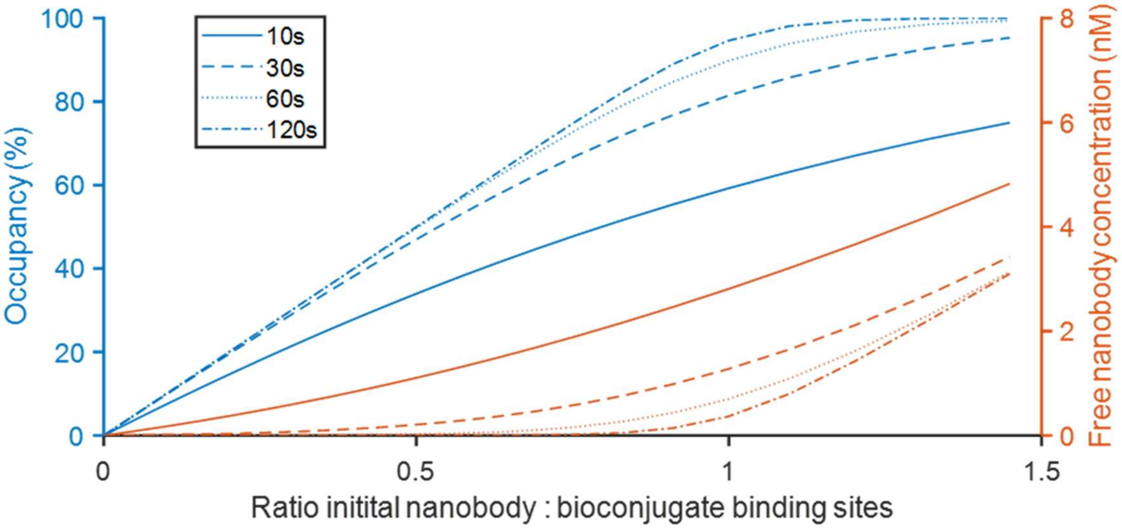

Figure 5. 4 In-line decoration simulation. Evaluation of in-line decoration of streptavidin-coated nanoparticles with biotinylated nanobodies during LFA operation. Blue lines: Show the percentage of occupied binding sites on the streptavidin-coated nanoparticles at different time points (indicated in the legend) and for varying initial concentrations of biotinylated nanobodies. Orange lines: Show the corresponding concentration of unbound (free) biotinylated nanobodies remaining in solution for each experiment.

assay configurations. This analysis aims to determine if sufficient decoration can be achieved within the typical timeframe of conjugate migration in a traditional LFA.

Figure 5.4 displays the percentage of occupied binding sites and the concentration of free nanobody at the end of the simulation, representing the point when the conjugate theoretically reaches the test line. The results demonstrate that increasing the initial nanobody concentration correlates with increased receptor occupancy (and thus, nanobody decoration). However, this also leads to a higher concentration of free nanobodies at the end of the experiment, potentially causing competition with bioconjugates and leading to a reduction in sensitivity. Careful optimisation would be required to achieve a balance of maximising nanoparticle decoration while minimising the free nanobody concentration. For instance, 80% occupancy is achieved when the 30mer bioconjugate is reacted with 25 times the nanobody for 120s, leading to the presentation of ~25 detection nanobodies per nanoparticle and low picomolar concentration (49.82 pM). Thorough experimentation would be needed to determine if this sufficient balance can be achieved for sensitive LFA using this in-line decoration step.

Furthermore, the results indicate that longer incubation times reduce this trade-off, potentially allowing a wider range of nanobody concentrations for sensitive LFA operation. Therefore, extending the decoration time could be beneficial. This can be achieved by slowing down conjugate migration using additives, employing nitrocellulose membranes with slower flow rates, or adjusting the device architecture to increase the distance between the conjugate pad and the test line.

5.2.4 Bioconjugate decoration away from the PoC

An alternative approach involves the decoration of bioconjugates with detection nanobodies in a laboratory setting before the assay. This allows for reacting the captured nanobody with the bioconjugate in greater excess, with unbound nanobodies removed through centrifugation and wash cycles. However, the added complexity of centrifugation and the longer preparation time make this approach more suitable for diagnostic centres or hospitals rather than field or home testing. In this scenario, bioconjugates would be produced in batches (e.g., weekly or daily) with the detection nanobody as they require lengthy incubation.

To evaluate the dynamics of this scenario with different affinity systems, the solution-based model was employed. The same affinity systems were tested as with the initial scenario but the concentration of initial detection nanobody was adjusted to 300-fold molar excess, or 10 times more nanobodies than would be required to saturate the 30 binding sites on the bioconjugates. This large excess was intentionally chosen to ensure efficient and rapid

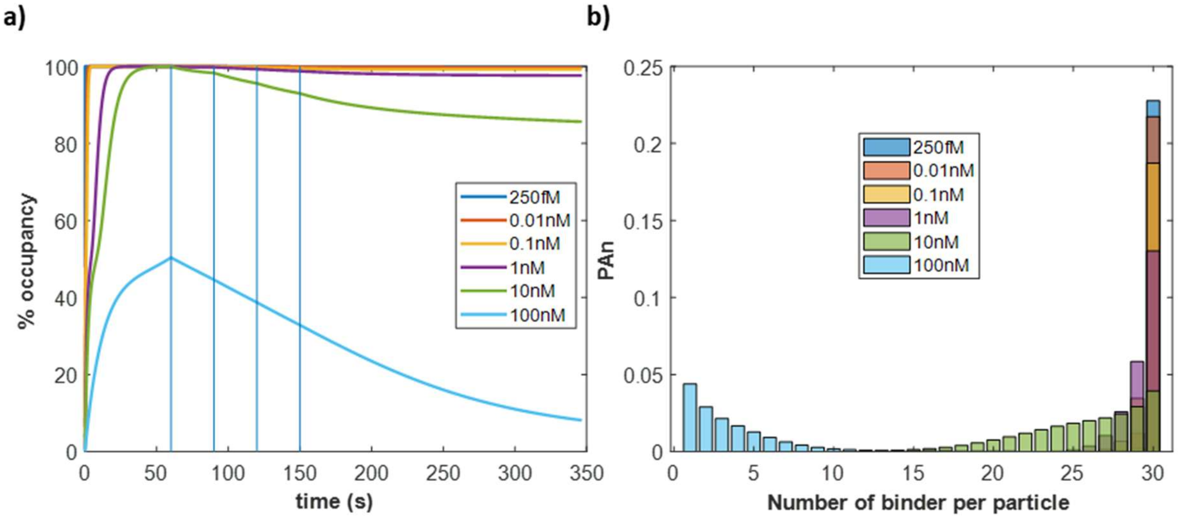

Figure 5. 5 Off-line decoration simulation **a**) % Occupancy plot of available binding sites on the gold nanoparticle bioconjugate by detection nanobodies. Each series represents a different affinity sysem. **b**) The distrivbution of number of occupied receptors of bioconuugates by detection nanobodies.

decoration of the bioconjugate, even with affinity pairs exhibiting lower association rates. By providing a surplus of nanobodies, the system is driven towards maximal occupancy, minimising the impact of weaker binding kinetics. This strategy mimics typical laboratory protocols where an excess of reagents is often used to promote efficient reactions. To simulate the wash cycles and determine how these might cause the elution of the detection nanobody off the bioconjugate, 100-fold dilutions of the remaining free detection nanobody were performed at 60, 90, 120, and 150 minutes. Figure 5.5a shows the percentage occupancy over time, with each series representing an affinity system with different dissociation constants. Here, the greater fold excess of detection nanobody favours quick binding to the bioconjugate. >99% occupancy was achieved for all except the 100 nM systems within the initial conjugation phase. The time required for these systems to achieve >99% occupancy was 6 seconds for the streptavidin-biotin system, ~109 seconds for the 0.01 nM, 197 seconds for the 0.1 nM, 18 minutes for the 1 nM interaction and 36 minutes for the 10 nM interaction. Interestingly, >99% occupancy is maintained after the four wash cycles and a further 1-hour incubation for the 250 fM, 0.01 nM and 0.1 nM affinity systems, and the majority of bioconjugates presented 30 nanobodies per nanoparticle (Figure 5.5b). While the 1 nM affinity quickly reached saturating conditions, the wash cycles caused the elution of some of the detection nanobodies, reaching 98% occupancy at the end of the experiment.

In the second scenario tested, it’s clear that the requirements for affinity kinetics are less demanding for efficient decoration of the modular bioconjugate in a laboratory environment. Here, the additional reaction times and the greater fold excess of detection nanobody allow for the achievement of nanoparticle saturation for the systems with affinities 0.01 and 0.1 nM in addition to the 250 fM system. Furthermore, the 4 wash cycles are effective in removing the unbound detection nanobodies from the solution as low picomolar concentrations of detection nanobodies remain in the solution after the 4 wash cycles and the further 1-hour incubation. This demonstrates that in this scenario, sub-nanomolar affinity pairs such as those found in good antibody and aptamer recognition could be used to generate the modular nanoparticle.[8]

Antibodies against FLAG and HA tags have been reported to display sub-nanomolar affinities.[128] While the simulations presented here focus on comparing different affinity systems for bioconjugate decoration, this type of modelling has broader applications. Once an affinity system is selected, this approach can be used to optimise loading conditions and estimate decoration times. For instance, this study used a 10x excess of detection nanobodies for comparison purposes. However, such excess might be unnecessarily high and wasteful in practical scenarios. By utilising the solution-based model and incorporating known kinetic parameters, researchers can precisely determine the minimal nanobody concentration required to achieve a desired level of decoration within a specific timeframe. This facilitates the efficient use of reagents and minimises waste, which is particularly crucial when working with costly or limited resources.

The results in the tested conditions demonstrate that in situations where the modular display nanoparticle must employ the affinity pair of antibody and tag recognition (K_D = 10 – 0.01 nM), the functionalisation of the bioconjugate will have to be performed in a laboratory environment with access to equipment such as micropipettes and a centrifuge. While this enables a broader space for affinity pair selection, it comes with the added cost of complexity and time, which ultimately prevent this type of testing from being fully assembled and executed in the field or at home.

The exceptional kinetics of the streptavidin-biotin interaction enable the user to perform the decoration step immediately prior to assay execution within the PoC timescale requirements. Likewise, the results from the in-line simulations show that it could be possible to have dried streptavidin bioconjugates decorated as they are resuspended and migrated towards the test line to enable automation and maximise assay simplicity. However, this would likely involve careful optimisation of the free nanobody flow rates and design architectures.

These results highlight the potential of a plug-and-play LFA to enable rapid response to emerging threats where stockpiling of prefabricated universal LFA cassettes and streptavidin functionalised AuNPs are ready to be deployed as needed. With the emergence of a disease of interest and the development of an appropriate nanobody pair, these LFAs will be ready to operate with the addition of the capture and detection nanobody.

It is important to acknowledge the inherent limitations of the model used. While the model calculates the interaction of polyvalent nanoparticles to its ligand, it assumes a perfectly homogeneous display of primary affinity macromolecule per particle. In reality, this will likely be highly heterogeneous, which could lead to deviations from the prediction. Furthermore, this model assumes that the affinity of the primary macromolecule is unaffected by its immobilisation on the nanoparticle. This is likely to change as the protein can undergo conformational changes after being bound to the nanoparticle, affecting its affinity. While this approach offers valuable predictive power, translating these theoretical findings into real-world performance may necessitate further optimisation and empirical validation. Factors such as non-specific binding, variations in reagent quality, and the complexities of real-world samples can all influence the interaction of the different assay components.

In the subsequent sections, the steps taken for the development of an exemplar modular LFA, intended to be used as a prototype for the plug-and-play diagnostic employing the streptavidin-biotin interaction, will be discussed. These include the design of an expression system capable of in vivo biotinylation of nanobodies, generation of streptavidin functionalised AuNP and streptavidin decorated nitrocellulose pads and evaluation of the sensitivity of the LFAs.

5.2.5 Design of dual expression system for in vitro biotinylation of nanobodies

To enable the binding to streptavidin on the nanoparticle surface and nitrocellulose pads, nanobodies need to be functionalised with biotin. This can be achieved in a number of ways, including the nonspecific amine modification already described in the previous chapters. However, this type of modification could result in inconsistencies in biotinylation, including the attachment of multiple biotins per nanobody. Multiple biotins can be problematic in the plug-and-play LFA immunoassay scenario for two reasons. 1) The detection nanobody bearing multiple biotins would cause the cross-linking of streptavidin-coated particles. 2) The capture and detection of nanobodies bearing multiple biotins could cause the bridging of streptavidin-coated nanoparticles to streptavidin-coated test lines and lead to the generation of non-antigen mediated signals.

Orthogonal biotinylation can be achieved by enzymatic methods using the biotin protein ligase reaction. In this method, proteins are fused with the recognition sequence AVI-tag.[129] AVI-tag is a 15 amino acid sequence GLNDIFEAQKIEWHE, recognised by the *E. coli* biotin ligase (BirA) enzyme, which covalently attaches a biotin on the lysine residue. The biotin protein ligase reaction can be performed in vitro where the AVI tagged proteins are reacted with the BirA after protein harvest, but this requires separate biotinylation reaction and multiple chromatography steps to separate the unbound biotin and enzyme from the purified or crude protein sample. A simpler method is in vivo biotinylation, where a dual expression system co-expresses the AVI-tagged protein and the BirA enzyme.[130] During induction, biotin is supplemented to the cell culture, and biotinylation is carried out in parallel to protein expression. This streamlined process does not require any additional reaction or separation steps since the biotinylated nanobody can be easily purified from the crude protein sample containing the BirA enzyme and residual free biotin.

To generate in vivo biotinylated nanobodies, AVI-tagged nanobodies were generated by the insertion of an AVI tag sequence on the C-terminus of the monovalent nanobody VHHV and its divalent and trivalent forms VHHV2 and VHHV3. These tagged nanobodies are named VHHV-AVI, VHHV2-AVI, and VHHV3-AVI. The AVI tag sequence was inserted on the C-terminus immediately after the nanobody sequence and before the hexahistidine tag. Each

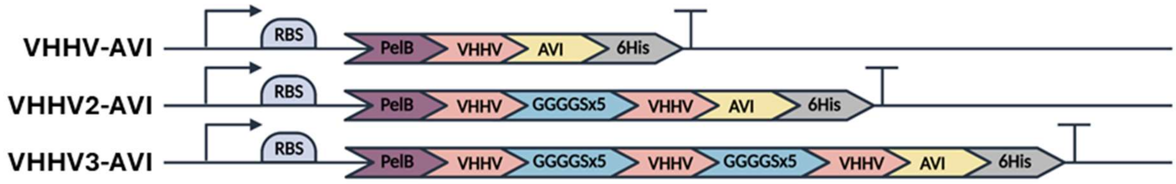

Figure 5. 6 Gene diagram of the AVI-tagged monovalent VHHV-AVI nanobody and multivalent VHHV2-AVI and VHVH3-AVI nanobodies. RBS - ribosome binding site. Arrow depicts the direction of translation.

plasmid contains a PelB signal peptide leading the nanobody sequence on the N terminus to enable the periplasmic expression of the biotinylated AVI-tagged nanobodies. Figure 5.6 shows the gene diagrams of the AVI-tagged nanobodies. The dual expression system was created by the sequential transformation of *E. coli,* first with the pBirAcm plasmid used for the expression of the biotin ligase (BirA) enzyme and plasmids containing the AVI-tagged nanobodies. The sequential transformation involved the transformation of chemically competent *E. coli* with pBirAcm, selecting for transformed colonies, making the transformed bacteria competent, transforming with the second plasmid containing the AVI-tagged nanobodies and re-selecting for colonies containing both plasmids.

5.2.6 Expression and characterisation of in vivo biotinylated nanobodies

AVI-tagged nanobodies were co-expressed with BirA in *E. coli* in the presence of free biotin. SDS-PAGE analysis revealed distinct bands corresponding to VHHV-AVI (16.9 kDa), VHHV2-AVI (30.8 kDa) and VHHV3-AVI (44.7 kDa), as shown in Figure 5.7. Western blot analysis was

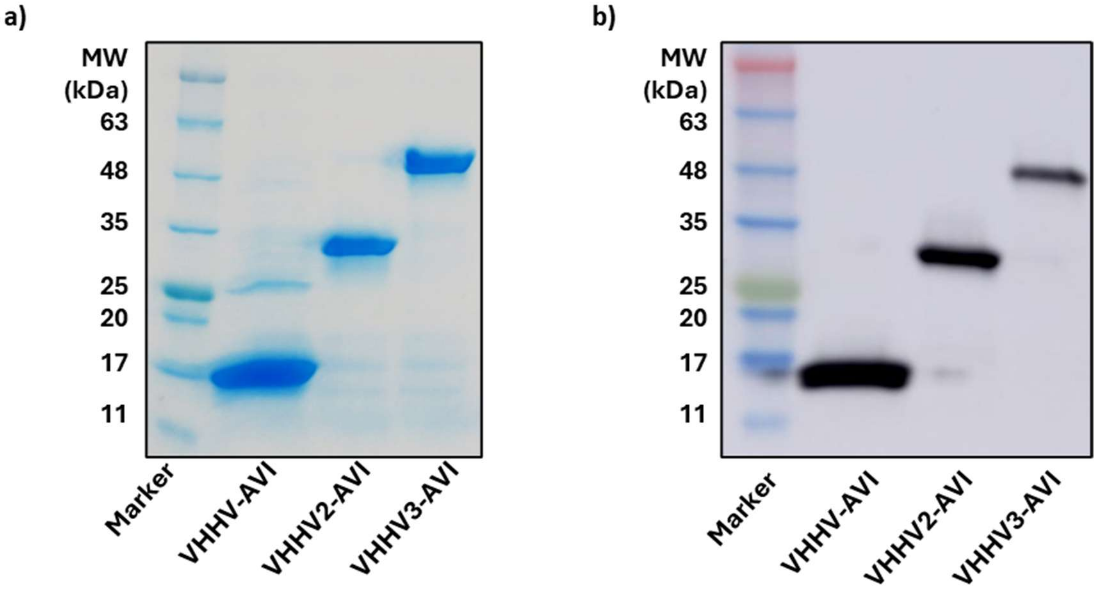

Figure 5. 7 AVI-tagged nanobody protein characterisation **a**) Purified fractions of Avi-tagged nanobodies co-expressed with BirA in E. coli. Lane 1 contains the protein molecular weight reference marker, and lanes 2-5 contain the IMAC purified fractions of the periplasm from the expression of VHHV1-AVI, VHHV2-AVI and VHHV3 -AVI, respectively. **b**) Western blot of the purified fractions of AVI-tagged nanobodies co-expressed with BirA. Detection was performed using HRP-conjugated streptavidin, and the signal was generated using chemiluminescence means. Lane 1 contains the protein molecular weight reference marker, and lanes 2-5 contain the IMAC purified fractions of the periplasm from the expression of VHHV1-AVI, VHHV2-AVI and VHHV3 -AVI, respectively.

performed using HRP-conjugated streptavidin to initially probe for the presence of biotin in the nanobody samples. All nanobodies appeared to produce a signal on the western blot, confirming the presence of biotin attached to the nanobodies. While western blot is a good qualitative assessment of the presence of the nanobodies, their respective weights and the presence of any biotin, it does not confirm that the AVI-tagged nanobodies have been biotinylated to completion.

By accurately measuring the mass distribution of the intact proteins using liquid chromatography-mass spectrometry (LC-MS), it is possible to distinguish between biotinylated and non-biotinylated forms. As shown by this analysis, VHHV2-AVI and VHHV3-AVI were biotinylated to completion, since single peaks appeared in the LC-MS analysis, with masses corresponding to the biotinylated forms (Figure 5.8b and c). This suggests that the biotinylation of these two nanobodies was highly efficient. In contrast, VHHV-AVI exhibited two distinct peaks, one corresponding to the mass of the biotinylated form and the other corresponding to the mass of the non-biotinylated form (Figure 5.8a). This result indicates that the biotinylation of VHHV-AVI was incomplete, with a mixture of modified and unmodified nanobodies present in the sample. Peak analysis revealed a 57% to 43% distribution of the non-biotinylated and biotinylated versions of VHHV, respectively. VHHV-AVI consistently expressed at much higher (~10-fold) yields compared to VHHV2-AVI and VHHV3-AVI. The incomplete biotinylation of VHHV-AVI could be due to biotin depletion during protein expression and biotinylation. This could be overcome by limiting the protein expression of VHHV-AVI by reducing the induction time or culture temperature post-induction. Alternatively, the depletion could be mitigated by supplementing more biotin during the induction phase.

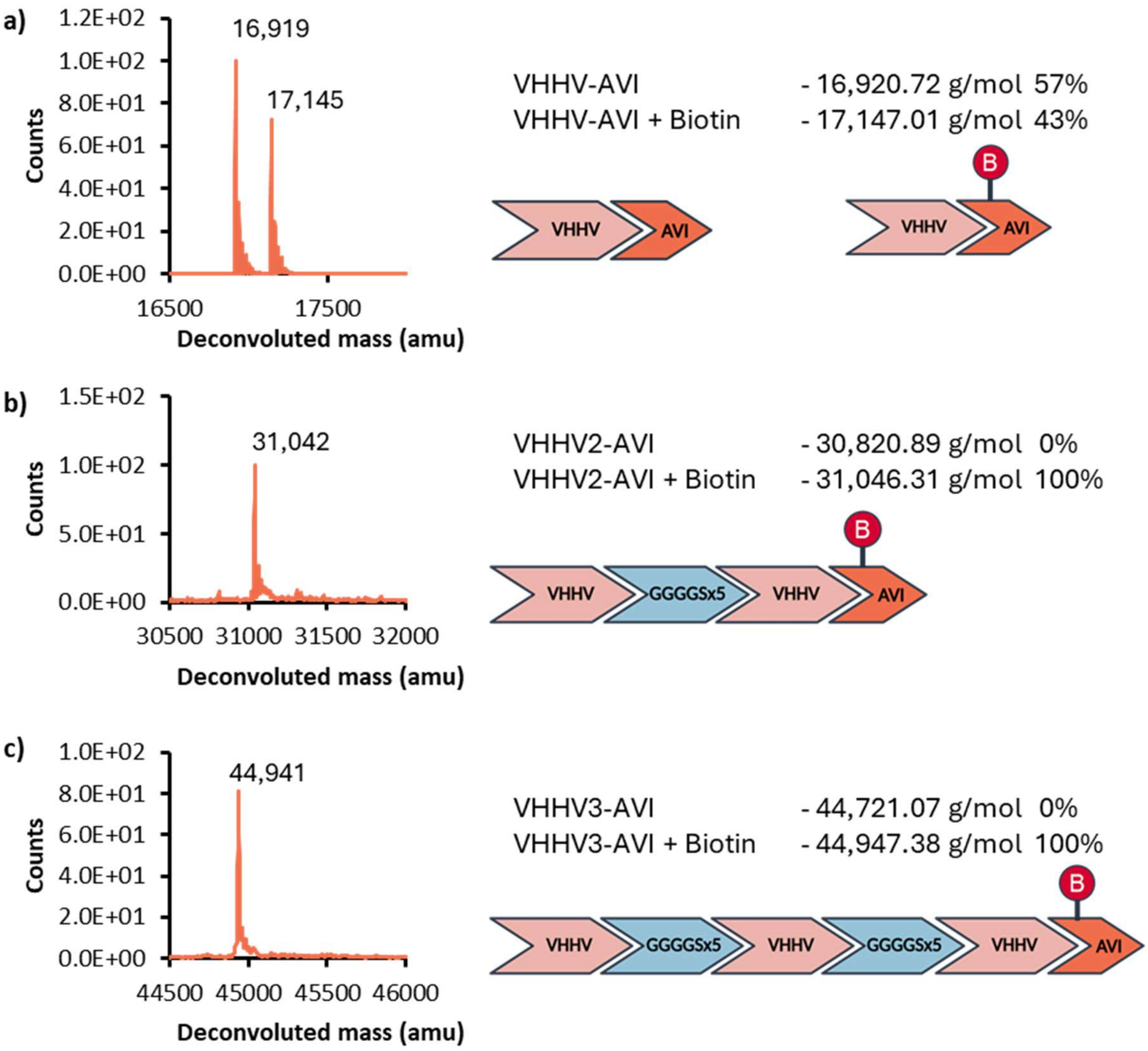

Figure 5. 8 LC-MS spectra for the AVI-tagged nanobodies co-expressed with BirA to evaluate biotinylation efficiency. The mass addition from the biotin is expected to be 244.31 g/mol. **a**) VHHV-AVI (16,20.72 g/mol), observed masses of 16,919 and 17,145 correspond to the non-biotinylated and biotinylated versions respectively peak integration indicated a 43% distribution of the biotinylated version. **b**) VHHV2-AVI (30,820.89 g/mol) observed mass of 31,042 correspond to the biotinylated version. **c**) VHHV3-AVI (44,721.07 g/mol) observed mass of 44,941 correspond to the biotinylated version.

5.2.7 Polystreptavidin AuNP development

Streptavidin is a widely used protein in biosensor development due to its exceptionally strong affinity for biotin. This strong interaction makes it a popular choice for surface functionalisation and signal generation in various biosensing platforms.[96,131] One notable application is in LFAs, where streptavidin is often employed to functionalise the nitrocellulose membranes forming the test line. Instead of immobilising the capture reagent (e.g., an antibody) directly on the test pad, it is allowed to interact with the target analyte in solution. When the reaction mixture reaches the streptavidin-coated test line, the biotinylated capture reagent is rapidly and efficiently captured, forming a stable complex. This approach offers a key advantage: the antigen and capture antibody have more time to interact in solution, increasing the likelihood of binding and improving the sensitivity of the assay.[38]

By leveraging the strong streptavidin-biotin interaction, the capture reagent is effectively immobilised at the test line in the short timescales, enabling the detection of the target analyte. This strategy exploits one of the strongest known binding pairs in nature to enhance the performance and sensitivity of LFAs.[89]

In the present study, in addition to decorating nitrocellulose test lines with biotinylated nanobodies through immobilised streptavidin, biotinylated nanobodies will also be used to decorate streptavidin-coated AuNPs. This has been previously demonstrated by Chen *et al.*, where in vivo biotinylated nanobodies were used to decorate streptavidin functionalised AuNPs used for the development of a solution-based SPR biosensor.[96]

Similar to Fellows and colleagues, physisorption-mediated streptavidin immobilisation to AuNPs was pursued here due to its simplicity and scalability.[132] Streptavidin has been reported to adsorb to the surface of citrate-capped AuNPs efficiently. In this study, polystreptavidin, a polymerised version of streptavidin that is commonly used in LFAs, was used due to its high biotin binding capacity.

To study the optimal conditions for polystreptavidin physisorption, a bioconjugation optimisation screening was performed, where the nanoparticle and bioconjugate stability was monitored. In the optimisation screening, a range of polystreptavidin concentrations (125 µg/mL – 1 µg/mL) during physisorption were tested using a range of pH conditions from pH 5.0 to pH 10.0 in increments of 0.5 using 40 nm AuNPs.

UV-Vis spectroscopy was employed, monitoring the aggregation index defined as the absorbance at 580 nm over the absorbance at 530 nm, which is an indication of nanoparticle stability. Stability was evaluated before and after the addition of NaCl. Bioconjugates which remained stable after the addition of NaCl indicate coating of the nanoparticle surface with protein which acts as a protective layer.

The IEP of streptavidin, calculated to be 6.30 using PROPKA on APBS (PDB id: 6J6J), plays a crucial role in the aggregation behaviour of AuNPs during bioconjugation.[133,134] At low ionic strength, aggregation (aggregation index > 0.5) is observed only under specific conditions: PSA concentration at 25 µg/mL and at pH lower than 6.5 and 125 µg/mL at pH 5.5 (Figure 5.9 a). This observation aligns with the calculated IEP, where a pH below 6.5 results in a net positive charge for the protein, leading to nanoparticle aggregation.

At high ionic strength conditions, optimal bioconjugation requires a high concentration of PSA to sufficiently coat the nanoparticles and prevent salt-induced aggregation. Only the 125 µg/mL concentration of PSA maintained stability across the pH range tested, and this was only for pH values below 8.5 (Figure 5.9 b). The optimal conditions identified are 125 µg/mL

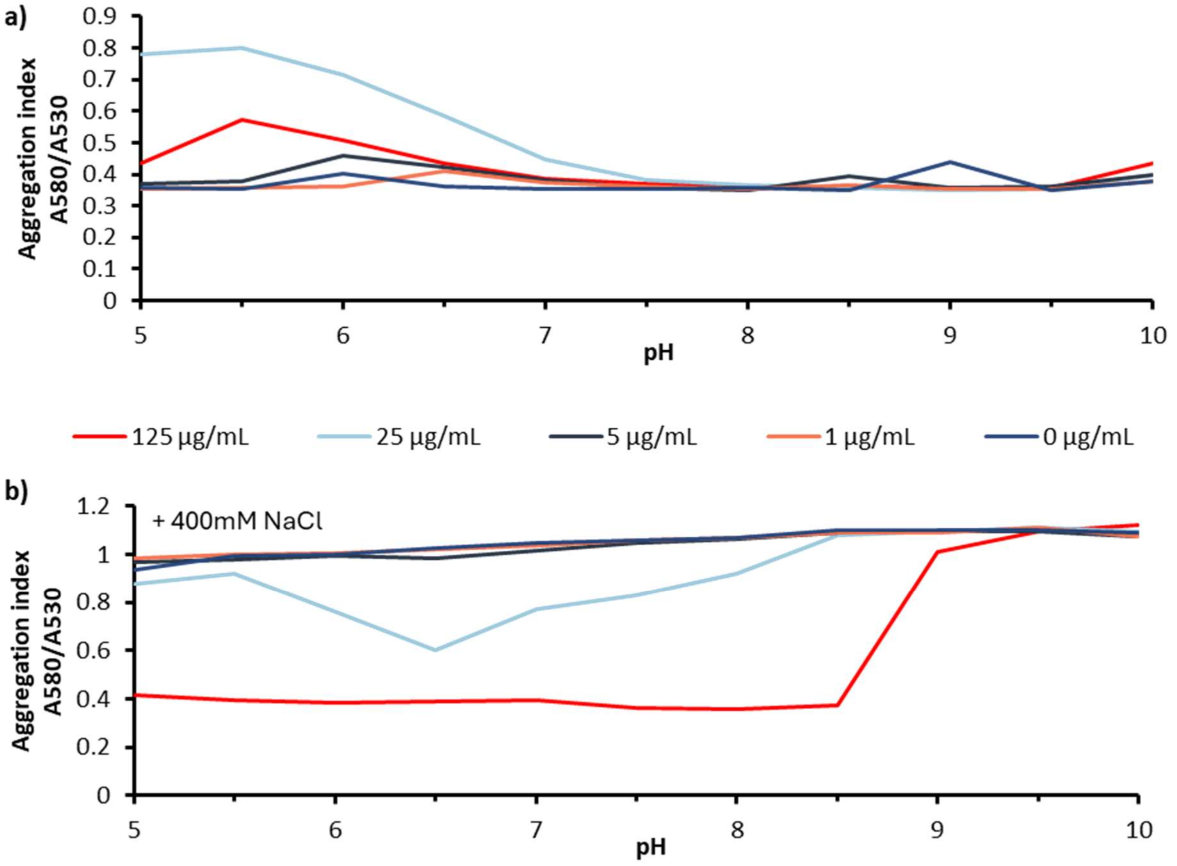

Figure 5. 9 Adsorption characteristics of PSA on 40 nm AuNPs. (**a**) Aggregation index plots of each conjugation reaction across a range of pH conditions. (**b**) Aggregation index plots of PSA-AuNP after increasing the NaCl concentration to 400 mM.

PSA at a pH of 8.5, providing a steric and charge-dense layer capable of shielding the nanoparticles. These conditions were chosen for subsequent experiments.

5.2.8 PSA-AuNP biconjugate characterisation and function evaluation

Using the optimal bioconjugation conditions of PSA to 40 nm AuNP, larger-scale (1 mL) conjugations were prepared to evaluate their colloidal stability through different processing stages. Following the initial bioconjugation reaction, PSA-AuNPs were blocked with BSA to ensure all nanoparticle surfaces were covered with protein. The conjugates were then washed three times via centrifugation to remove any unbound PSA, replacing the supernatant with blocking buffer.

To assess the impact of PSA immobilisation, blocking and washing on AuNP stability, the aggregation index and hydrodynamic diameter were studied after each step. The aggregation index of bare AuNPs remained relatively unchanged following physisorption of PSA (0.41 ± 0.03 SD vs. 0.43 ± 0.02 SD), indicating that the particles remain monodisperse (Figure 5.10a). Blocking and washing steps slightly increased the aggregation index (0.58 ± 0.03 SD and 0.54 ± 0.02 SD, respectively), indicating some loss of stability.

DLS confirms the immobilisation of PSA onto the nanoparticle surface, observed by an increase in hydrodynamic diameter from 43.5 ± 0.5 nm for bare AuNPs to 88.6 ± 1.4 nm for the AuNP-PSA (Figure 5.10a). The 45.1 nm increase is appreciably larger than the dimensions of the tetrameric streptavidin 5.9×5.3×4.8 nm, but this is expected as PSA, a polymerised version of streptavidin, was used here.[135]

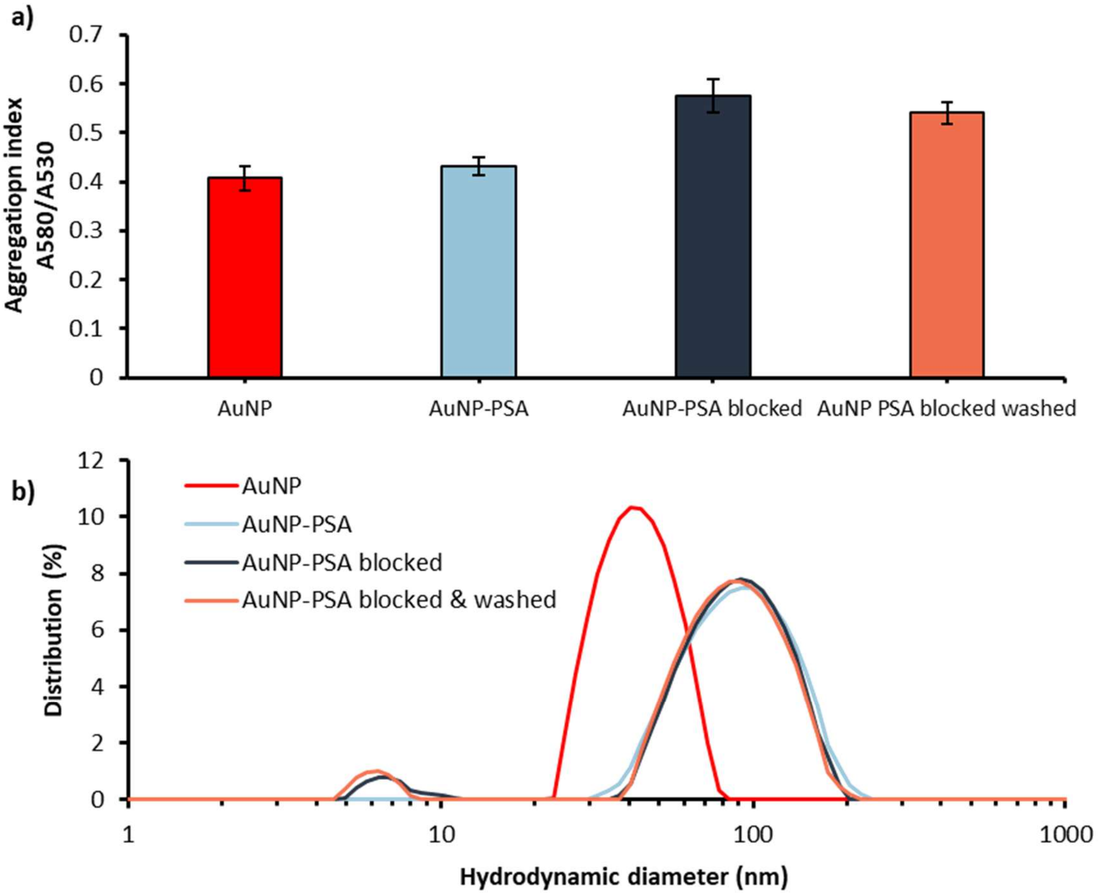

Figure 5. 10 Characterisation of PSA-AuNPs after different processing steps of a 1mL bioconjugation batch. (**a**) Aggregation index plots. Values are shown as the mean (n = 3) ± the standard deviation of the mean (**b**) Hydrodynamic diameter distribution plots (by intensity) of the PSA-AuNPs at different processing stages.

Interestingly, the hydrodynamic diameter decreased after blocking (82.8 ± 1.2 nm) and washing (77.8 ± 0.2 nm). This unexpected reduction might be attributed to the appearance of an additional peak of smaller size (~6 nm) in the diameter distribution plot after BSA addition (Figure 5.10a). This smaller peak may be contributing to an underestimation of the particle hydrodynamic diameter. The smaller peak could be from the BSA, which is present at relatively high concentrations (10 mg/mL) after the blocking step.

In addition to the stability of the PSA-AuNP bioconjugate, it is also important to evaluate its functionality. In this case, functionality is the ability of the bioconjugate to bind to biotin. The functionality was initially tested in a direct binding LFA format where test lines on nitrocellulose membranes were decorated with biotinylated BSA. In a 96 well-plate, 10 µL of different concentrations of PSA-AuNPs (232.2, 116.2, 58.1, 29.0, 14.5 and 0 pM) were dispensed, and the half dipstick immunoassay containing the BSA-biotin test lines were inserted into the well containing the bioconjugates. This enables the wicking of the bioconjugates over the nitrocellulose membrane and enables their binding to the BSA-biotin membrane, as shown in the scheme in Figure 5.11a. Following the assay operation, the signal was captured and quantified using a camera, and image analysis

To assess the functionality of PSA-AuNP conjugates, the limit of detection (LoD) was determined using image analysis of the LFAs. This analysis revealed an LoD of 17.2 pM for 40 nm PSA-AuNPs. This finding aligns with the work of Khlebtsov and colleagues, who established a relationship between LoD and AuNPs of different sizes dispensed on nitrocellulose membranes.[136] Their proposed calculation allows for the prediction of the absolute LoD based on nanoparticle diameter, providing a theoretical framework for understanding the observed sensitivity of these bioconjugates. Indeed, the measured LoD here (19.8 amol in 10 µL) closely matches their measured LoD for 40 nm AuNPs (18.9 amol). This strong agreement suggests that nearly all bioconjugates are immobilised on the nitrocellulose membrane even at these low concentrations, demonstrating a high degree of functionality for the PSA-AuNP bioconjugates.

To further evaluate the functionality of the PSA-AuNP, the number of binding sites was estimated using an inhibitory curve experiment performed on the same assay setup. In this experiment, PSA-AuNPs at a fixed concentration of OD1 or 0.11 nM were mixed with free biotin and incubated for 5 minutes before running on the BSA-biotin decorated strips. In this competitive assay format, the free biotin binds to the PSA on the bioconjugate and, at high enough concentrations, saturates the binding sites, preventing the bioconjugate from binding to the BSA-biotin test line.

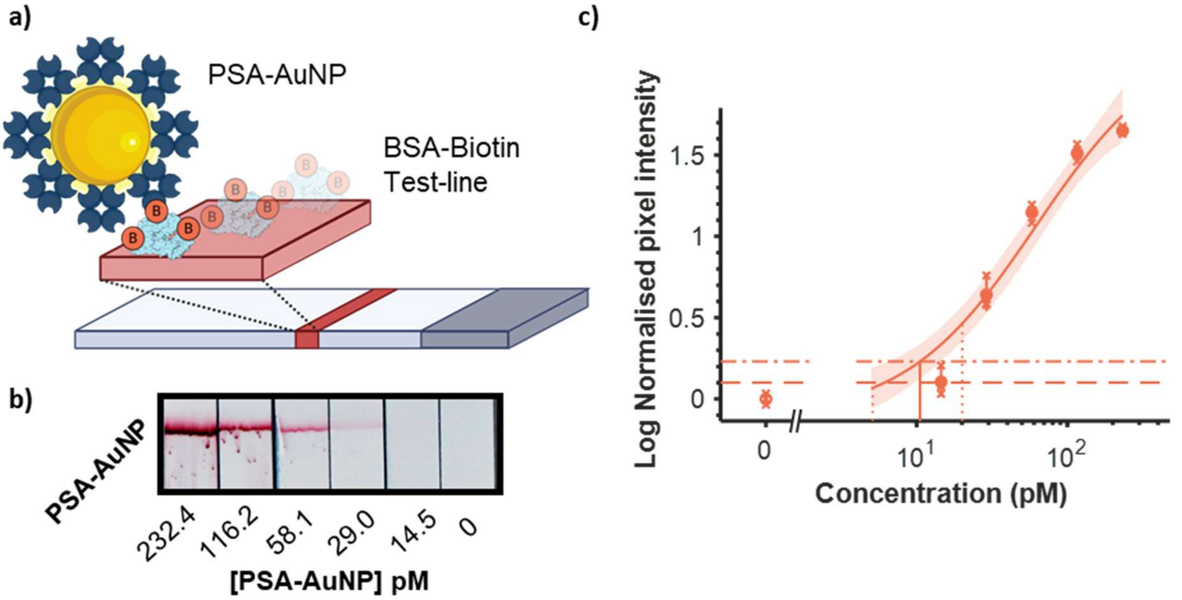

Figure 5. 11 PSA-AuNP LoD analysis (**a**) scheme of LFA prepared to test the functionality of PSA-AuNPs. In this assay, PSA-AuNPs are flown through nitrocellulose membranes decorated with BSA-biotin, enabling the direct capture of the PSA-AuNP on the test line. (**b**) Contrast-enhanced images of BSA-biotin LFA after running different concentrations of PSA-AuNPs. (**c**) Test line signal as a function of PSA-AuNP concentration to establish the LoD (n = 3), individual data points and their average are displayed as crosses and solid circles, respectively ± the standard deviation of the mean. Solid curves show the fitted Langmuir functions. Dashed lines show the 95% CI of the LoD calculation, while solid vertical lines show the LoD.

In this competitive assay format, the concentration of biotin that is required to reduce the signal by 50% (IC50) is calculated to be at 1.91 nM (Figure 5.12). This shows that 1.91 nM of free biotin is required to saturate the binding sites of 50% of the PSA-AuNPs during the 5 minutes of incubation in the plate and the time it takes to reach the test line when running the assay. A mechanistic mathematical model was employed to make a more accurate assessment of the number of binding sites during this multistep experiment. This model consists of solution-based calculations of the PSA-AuNP interaction with biotin for 5 minutes, occurring in the plate prior to the LFA assay, coupled with an advection-diffusion-reaction model to simulate the competitive LFA that follows. In the later part of the model, the interaction of the PSA-AuNP with biotin is simulated while the reactants are moving across the nitrocellulose membrane and the interaction of the PSA-AuNP with the BSA-biotin as the reactants move past the test-line. To achieve this model, a modified version of the competitive LFA model developed by Qian was created.[137] The modifications made to this model include a polyvalent interaction of PSA-AuNP to biotin such that it allows multiple biotins to bind each PSA-AuNP. This modification to LFA diffusion-advection-reaction systems has been developed and validated by Liu and colleagues in a non-competitive format.[76] A further modification is made to dynamically adjust the overall association and dissociation rates of the bioconjugate as its available receptors are depleted by biotin binding using equations 5.1 and 5.2.

In these simulations, particles with different numbers of binding sites (Nbs) were mixed together with concentrations of free biotin, matching the concentrations used in the experiment. During the simulations, the solution-based model would initially calculate the distribution of biotins bound per nanoparticle, the remaining free biotin and free particle. These results would then be entered into the competitive LFA model, where the signal was quantified at the end of the assay. IC50 was calculated for each bioconjugate with different binding sites and was used to compare with the IC50 calculated from the experiment.

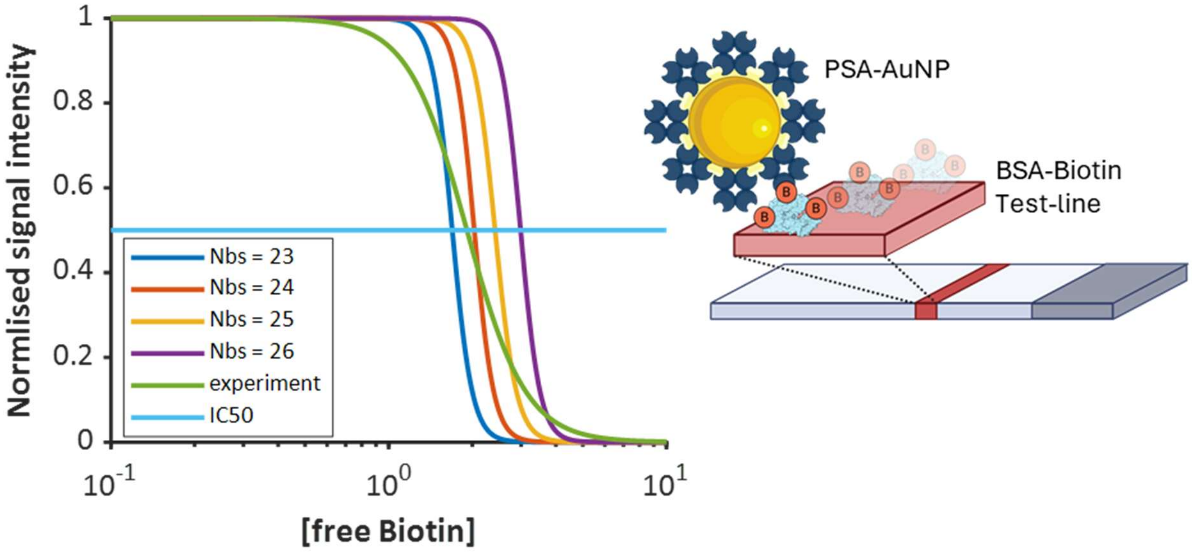

Figure 5. 12 Comparison of IC50 results from the experiment and the data generated using the diffusion-advection-reaction competitive model.

The closest IC50 match of the experiment to simulations was when the simulation was performed with a nanoparticle that had 24 binding sites (Figure 5.12), which resulted in a calculated IC50 value of 2.03. While the IC50 is a close match with the model, the shape of the dose-response curve is different. This discrepancy could be from a simplifying assumption in the model used: all bioconjugates have the same number of binding sites. In reality, there's likely a distribution of binding sites per bioconjugate. This variation in binding sites would affect the binding kinetics of each bioconjugate differently, influencing the overall dose-response curve.

5.2.9 Stability and function of nanobody-bound PSA-AuNPs

Detection nanobodies VHHV-AVI, VHHV2-AVI and VHHV3-AVI were decorated on the surface of PSA-AuNP by reacting the free nanobodies with blocked and purified PSA-AuNP bioconjugates. The reaction was carried out for 30 minutes at room temperature and at a large excess of detection nanobodies to PSA-AuNPs (7000-fold excess). The conditions chosen ensured complete saturation of the PSA-AuNP bioconjugate with detection nanobody. The solution-based model suggests that this should be completed within a few seconds, performing the reaction over 30 minutes ensured completion. The resulting nanobody-decorated PSA-AuNPs are referred to as VHHV-PSA-AuNP, VHHV2-PSA-AuNP, and VHHV3-PSA-AuNP.

Following bioconjugation, the nanobody-decorated bioconjugates were purified using three rounds of the standard centrifugation method to ensure the removal of free-detection nanobodies. The stability of the purified nanobody-decorated bioconjugates was determined using DLS and UV-Vis. Attaching the monovalent nanobody, VHHV-AVI, to the PSA-AuNP resulted in an increase in hydrodynamic diameter to 86.5 nm compared to that of the purified PSA-AuNP of 77.8 nm Figure 5.13a. This increase in hydrodynamic diameter of 8.7 nm is consistent with the anticipated increase in diameter from the formation of an additional monolayer using the monovalent nanobody. The aggregation index for VHHV-PSA-AuNP (0.57) showed a minor decrease in stability compared to bare AuNPs (aggregation index < 0.5), but it was similar to that of PSA-AuNP (0.54). This indicates that VHHV-AVI binding and the additional washing steps did not significantly affect the stability of the PSA-AuNPs.

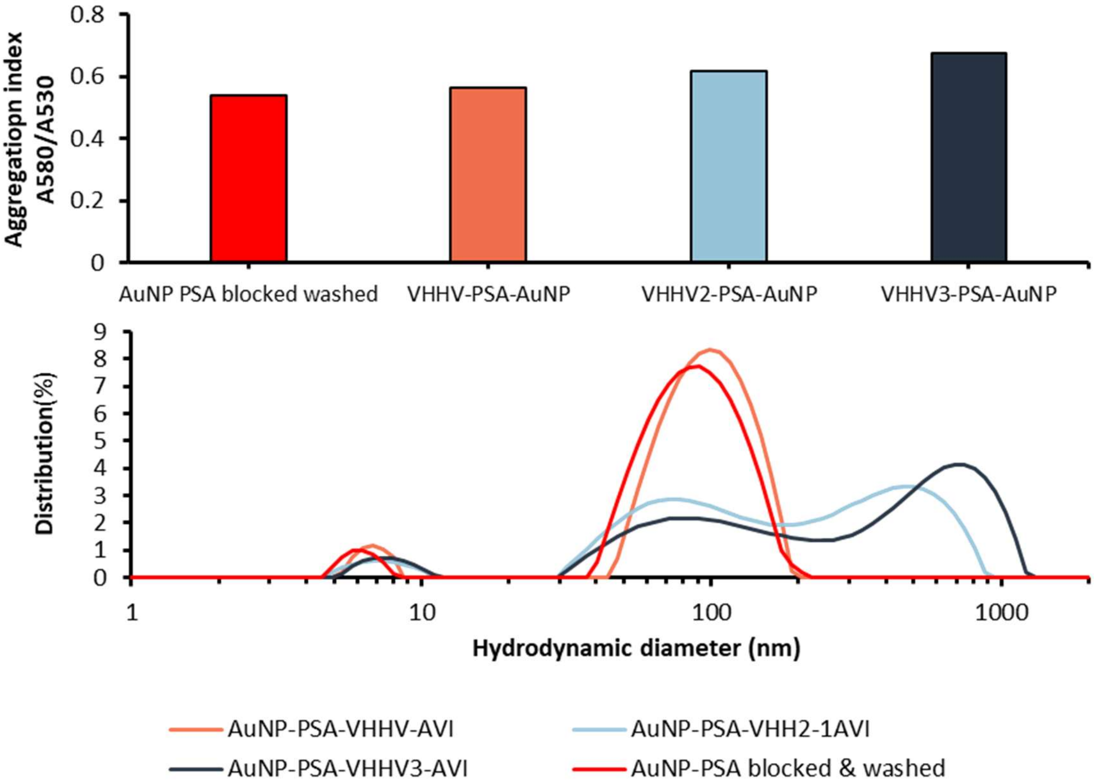

Figure 5. 13 Characterisation of PSA-AuNPs decorated with AVI-tagged nanobodies (**a**) Aggregation index plots. Values are shown as the mean ± the standard deviation of the mean (**b**) Hydrodynamic diameter distribution plots of the PSA-AuNPs decorated with different AVI-tagged nanobodies (by intensity).

In contrast, attaching the bivalent (VHHV2-AVI) and trivalent (VHHV3-AVI) nanobodies significantly destabilised the nanoparticles. DLS analysis of VHHV2-PSA-AuNP revealed a substantial increase in hydrodynamic diameter to 196.7 nm, with an additional peak at 420.3 nm, signifying aggregation. This was further confirmed by an increased aggregation index to 0.62. Similarly, attaching VHHV3 to PSA-AuNP resulted in significant aggregation, with a large hydrodynamic diameter (294.3 nm), an additional peak at 623.7 nm, and a higher aggregation index of 0.68.

The reason for this instability when using bivalent and trivalent nanobodies is not yet clear. However, the increased aggregation observed by DLS with increasing nanobody valency suggests that binder length may play a role. Despite the indications of bioconjugate aggregation, the residual nanoparticle stability motivated further evaluation as diagnostic probes

An LFA was developed to assess the functionality of the nanobody-decorated PSA-AuNPs as detection probes for the S1 protein of SARS-CoV-2. First, a suitable capture monoclonal antibody was selected via a competition-based biolayer interferometry (BLI) experiment. This experiment evaluated the simultaneous binding of VHHV and monoclonal antibodies (D001 or D003) to the S1 protein. Biotinylated VHHV nanobody was loaded onto a streptavidin-functionalised BLI sensor, followed by the addition of S1 protein and either D001 or D003 antibody. The results showed that D001 competes with VHHV for binding to the S1 protein as no signal is generated with its addition (Figure 5.14). D003 binds to a distinct site since an association is observed with its addition. Consequently, D003 was chosen as the capture antibody and spotted onto nitrocellulose strips at 1 mg/mL.

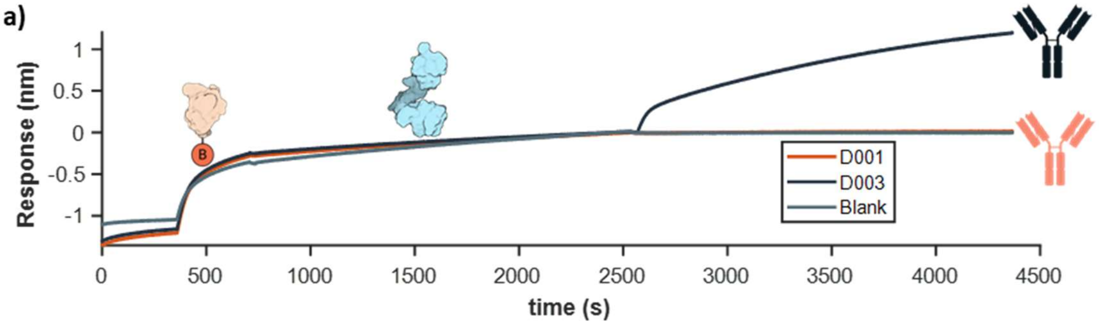

Figure 5. 14 Competition BLI is used to identify a compatible antibody pair with the VHHV nanobody. VHHV was first loaded onto the sensor, followed by the loading of S1 protein and then either D003 or D001 mAb. The absence of signal at the mAb loading step indicated overlapping epitopes, while the presence of signal indicated a suitable pair.

Next, the nanobody-decorated nanoparticles were mixed with either the S1 protein (500 ng/mL) or a blank buffer and run on the LFA strips. Analysis of the signal-to-noise ratio (SNR) revealed that VHHV-PSA-AuNP generated a moderate signal in the presence of the antigen (SNR = 3.88, Figure 5.15), indicating effective antigen detection. However, VHHV2-PSA-AuNP and VHHV3-PSA-AuNP produced significant non-specific signals, resulting in SNRs approaching 1 (1.37 and 1.22, respectively). This suggests that the diagnostic potential of these bioconjugates is limited as they would struggle to differentiate between positive and negative samples at the relatively high tested antigen concentrations. This could be tied to the significant nanoparticle aggregation observed from the VHHV2-PSA-AuNP and VHHV3-PSA-AuNP since aggregated bioconjugates have a greater tendency to generate non-specific signals.

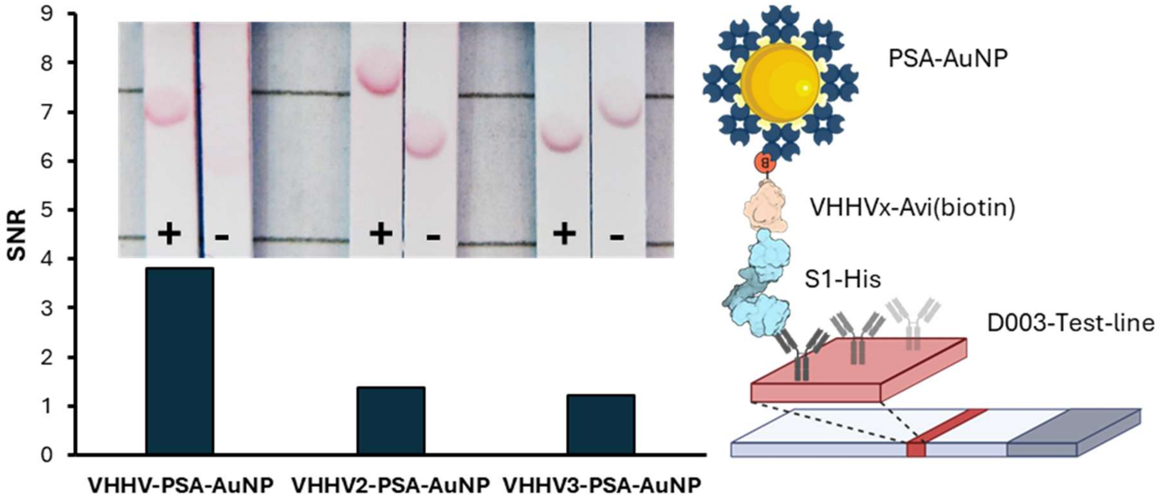

Figure 5. 15 Evaluation of nanobody decorated PSA-AuNP conjugates as detection probes in LFA. SNR plot shows the ratio of the signal generated in the positive assay over the signal generated in the blank assay. The scheme shows the immunocomplex formation at the test line comprising the D003 mAb, S1 protein and the nanobody decorated PSA-AuNP.

The combined challenges of nanoparticle instability, the low number of observed binding sites on the PSA-AuNPs, and the generation of non-specific signals prompted the exploration of alternative streptavidin bioconjugates. Specifically, commercially available streptavidin-coated AuNPs (SA-AuNP) were considered. These nanoparticles offer a more controlled and consistent surface than the complex PSA used in the PSA-AuNPs. This alternative approach promises to address the limitations encountered with the previous system and potentially improve assay performance. The following section will evaluate the characteristics of commercially available SA-AuNPs in combination with the in vivo biotinylated nanobodies. Their functionality as a detection probe in the S1 LFA will be evaluated.

5.2.10 Stability and function of nanobody-bound SA-AuNPs

The manufacturer claims the commercially sourced streptavidin conjugated AuNPs (SA-AuNPs) exhibit exceptional stability (2.5 M NaOH at 70° for 1 hour). Chemical bioconjugation of streptavidin to the stabilised AuNP ensures the functional and stable display of streptavidin. The switch to commercially sourced SA-AuNPs would eliminate the nanoparticle aggregation observed when using physisorbed PSA-AuNPs and facilitate the initial proof of concept of the modular LFA diagnostic. In future iterations of the modular LFA, optimisation of the physisorbed PSA-AuNP would aim to eliminate the nanoparticle aggregation observed and allow its integration into the modular LFA.

Bioconjugates displaying the AVI-tagged nanobodies, VHHV, VHHV2 and VHHV3 on streptavidin particles were prepared. SA-AuNPs were incubated with a 3000-fold excess of each nanobody for 1 hour to ensure complete saturation of streptavidin binding sites on the nanoparticle surface. Unbound nanobodies were removed by means of centrifugation, and particles were suspended in a running buffer containing 1% BSA and 0.1 % tween-20 in PBS. DLS confirmed the binding of the nanobodies to the nanoparticle surface and paired with UV-Vis to confirm the stability of the purified bioconjugates.

The observed hydrodynamic diameter of SA-AuNP of 84.2 ± 1.7 nm corresponds to that of the 40 nm AuNP, a layer of stabilising polymer linker and a layer of streptavidin. The decoration of AuNP-SA with AVI-tagged nanobodies increases hydrodynamic diameter, which is dependent on nanobody valency. The hydrodynamic diameter of VHHV-SA-AuNP of 87.8± 1.6 nm indicates an increase of 3.6 nm in diameter (Figure 5.16). This increase confirms the attachment of VHHV-AVI on the surface via the biotin handle but is appreciably smaller than the dimensions of VHHV (4.68 × 3.29 × 2.64). Since the AVI tag is on the C-terminus, a tail-on conformation of the nanobody is expected when it is attached to the streptavidin on the nanoparticle surface. Similarly, the binding of VHHV2-AVI and VHHV3-AVI on SA-AuNP exhibit hydrodynamic diameters of 90.4± 0.2 and 92.6± 1.5 nm, respectively. Although these changes in hydrodynamic diameter appear to be dependent on nanobody valency, they are still lower than what would be expected if they were bound on a tail-on configuration. UV-Vis spectroscopy indicated no loss in nanoparticle stability since the aggregation index measured for VHHV-SA-AuNP (0.52 ± 0.03), VHHV2-SA-AuNP (0.50 0.03) and VHHV3-SA-AuNP (0.50

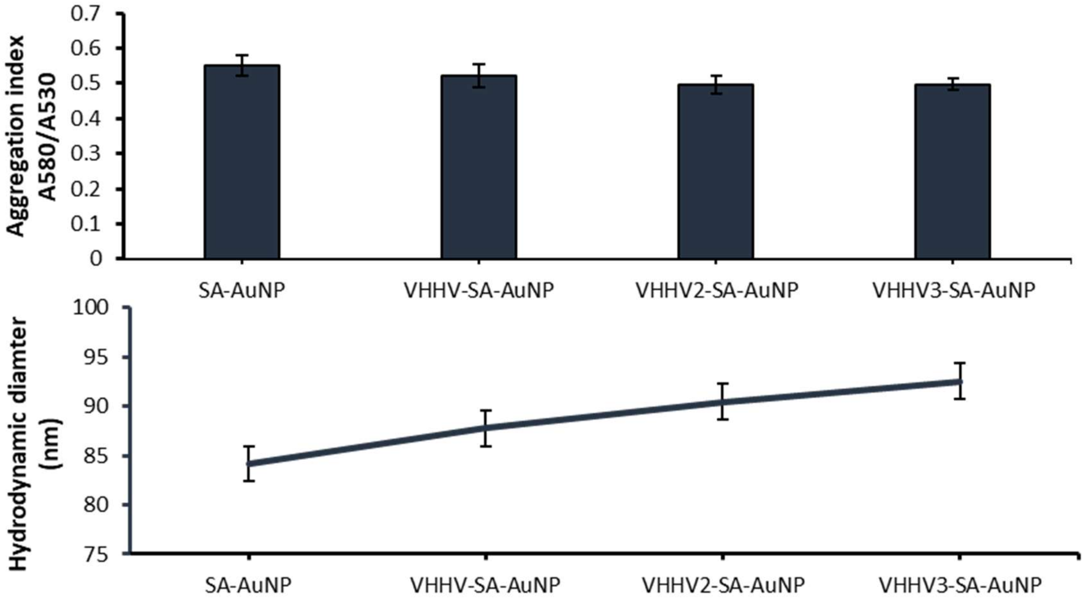

Figure 5. 16 Characterisation of nanobody decorated SA-AuNPs before and after attaching detection nanobodies (VHHV-AVI, VHHV2-AVI and VHHV-3 AVI) and purification cycles using centrifugation. The aggregation index is displayed as mean ± the standard deviation of the mean (n = 3). Hydrodynamic diameter displayed as mean (n = 3) ± the standard deviation of the mean

± 0.02) was not significantly different to that of SA-AuNP (0.55 ± 0.03, t > 0.05 vs all conjugates).

The stability maintained by the nanobody-decorated SA-AuNPs demonstrates a clear advantage over the less stable nanobody-decorated PSA-AuNPs. For this reason, these bioconjugates will be used in subsequent sections for the development of the modular LFA.

5.2.11 Modular display of detection nanobodies on SA-AuNPs in LFA

To systematically assess the performance of the nanobody-conjugated SA-AuNPs in LFAs, they were first optimised in a traditional LFA format using immobilised D003 mAb as the capture agent. This approach allows the isolation and evaluation of the performance of the nanoparticle-based detection system before integrating it into the full modular LFA, where both detection and capture nanobodies are displayed on streptavidin functionalised surfaces. The D003 antibody was printed on nitrocellulose strips using a biodot dispensing system in this simplified assay.

A critical factor influencing LFA performance is the running buffer pH, which can significantly impact antigen-antibody binding and off-target interactions, ultimately affecting both specific and nonspecific signal generation. Nonspecific signal refers to the signal generated by the AuNPs binding to the test line in the absence of the target antigen (S1 protein). To determine the optimal pH, running buffers were prepared at pH 7.0, 7.5, 8.0 (using HEPES), and 8.5 (using borate buffer). Each nanobody-decorated SA-AuNP conjugate (VHHV-SA-AuNP, VHHV2-SA-AuNP, VHHV3-SA-AuNP) was tested with 500 ng/mL of S1 protein or in blank

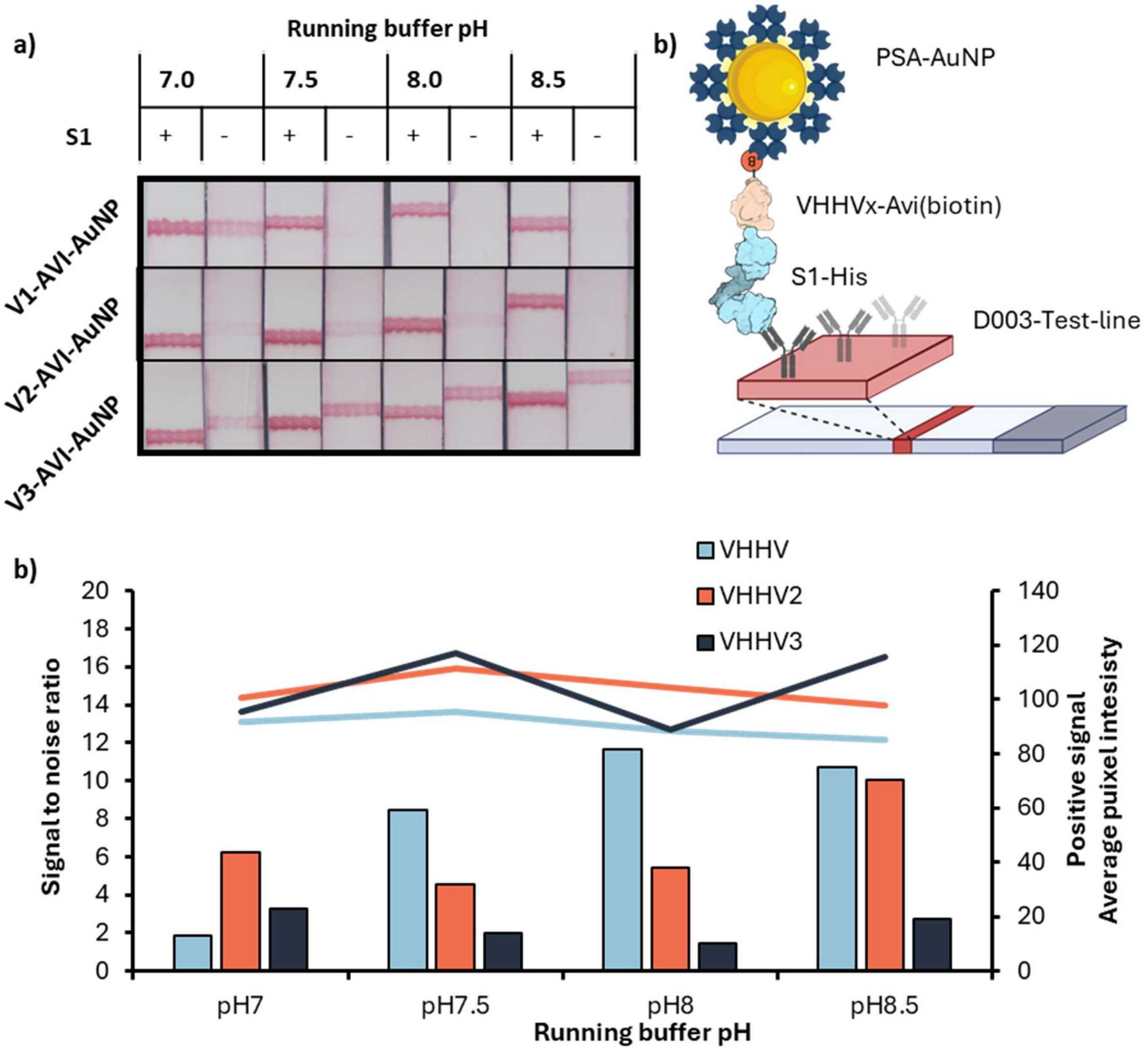

Figure 5. 17 LFA running buffer pH optimisation (**a**) Contrast-enhanced images of LFA with D003 mAb test lines were performed using nanobody decorated SA-AuNPs at different running buffer pHs. Positive samples contain 500 ng/mL of S1 protein, while negative samples contain no S1 protein. (**b**) Scheme of the LFA immunocomplex formation comprising the D003 mAb on the test line, S1 protein, and nanobody decorated SA-AuNP (**c**) bar plot shows the SNR for LFA run at each pH condition. The line shows the measured signal generated using the positive sample.

buffer at each pH. Image analysis quantified signal intensity, and the SNR was calculated to determine the optimal running buffer conditions.

A relatively weak dependence of signal intensity on pH in the presence of the S1 protein was observed. Signal intensity varied by less than 25% across the tested pH range (Figure 5.17). All bioconjugates produced the highest signal at pH 7.5. Notably, VHHV-SA-AuNP consistently produced less signal than VHHV2-SA-AuNP, potentially due to the increased affinity of the divalent nanobody, which may enhance binding to the S1 protein and improve capture efficiency. This effect is not observed when comparing VHHV2-SA-AuNP and VHHV3-SA-AuNP.

In contrast to the specific signal, the nonspecific signal showed a strong dependence on pH, leading to significant variations in SNR. The optimal running buffer for VHHV-SA-AuNP was pH 8.0 (SNR = 11.6). Increasing the pH to 8.5 leads to a slight reduction in the positive sample signal leading to a slight reduction in the SNR. The optimum pH for VHHV2-SA-AuNP is determined to be at pH 8.5 (SNR = 10.0), where the nonspecific signal is minimised, leading to a higher SNR. VHHV3-SA-AuNP consistently underperformed due to a higher nonspecific signal, achieving a maximum SNR of 3.3 at pH 7.0.

The observed trend suggests a relationship between nanobody valency and nonspecific signal generation. The increased surface area and flexibility of multivalent nanobodies, particularly with the addition of linker sequences, may provide more opportunities for nonspecific interactions with the capture antibody (D003) on the test line. These interactions could lead to signal generation even in the absence of the target analyte.

To assess the sensitivity of the nanobody-decorated SA-AuNPs, the LoD for S1 protein was determined using the same LFA format. Due to the high non-specific binding observed in previous optimisation experiments, VHHV3-SA-AuNP was excluded from this analysis. VHHV-SA-AuNP and VHHV2-SA-AuNP were tested at their respective optimal running pH conditions (pH 8.0 and pH 8.5, respectively). A series of LFAs with D003 mAb test lines were prepared and run using each bioconjugate with varying concentrations of the S1 protein. Signal intensity was quantified using image analysis, and the LoD was determined as the lowest S1 concentration, producing a signal statistically distinguishable from the background.

Interestingly, the LoD for the LFA using VHHV-SA-AuNP (146.1 pM ± 95.1 - 224.0 95% CI) was significantly higher than that using VHHV2-SA-AuNP (62.7 pM ± 37.5 - 104.0 95% CI $p = 0.02$, Figure 5.18). This difference highlights the impact of nanobody valency on sensitivity. The improved sensitivity with the bivalent nanobody (VHHV2) likely stems from its increased affinity for the S1 protein, leading to more efficient analyte capture. This observation is consistent with the findings presented in Chapter 4, where the superior binding kinetics of VHHV2 (K_D = 0.97 nM) compared to VHHV (K_D = 1.77 nM) were demonstrated using biolayer interferometry. Furthermore, VHHV2 exhibited a lower LoD (49.8 pM) than VHHV (79.9 pM) in ELISA assays. Notably, the enhancement in LoD observed in this LFA configuration (approximately 2.5-fold improvement with VHHV2) is even greater than that observed in ELISA or BLI.

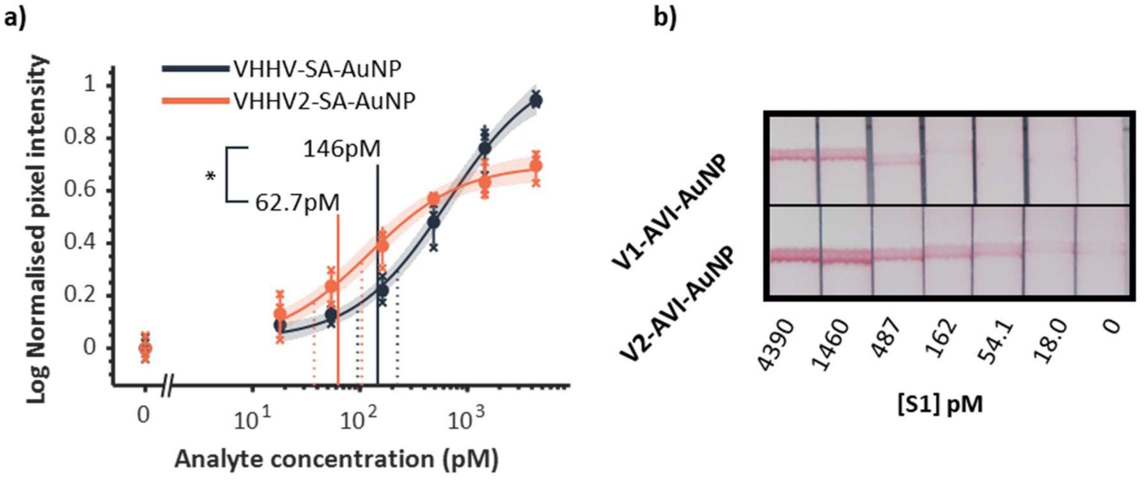

Figure 5. 18 LoD analysis of S1 LFA using VHHV-SA-AuNP and VHHV2-SA-AuNP. (**a**) LoD plot. Fitted Langmuir curves were used to calculate the LoD of each series. The shaded area around the fit shows the 95% CI of the fit. Solid straight lines show the LoD, while dotted lines show the 95% CI of the LoD. Crosses show individual data points, while solid circles show the mean ± the SD of the mean. (**b**) exemplar contrast-enhanced images of the dose-response LFA experiments. * – $p < 0.05$

This enhanced improvement in this LFA format could be attributed to the unique configuration of the bivalent nanobody on the AuNP surface. In the case of VHHV2-SA-AuNP, one nanobody is likely directly bound to the streptavidin surface, while the other remains pendant and freely diffusive. This "pendant" nanobody may provide increased flexibility and accessibility for antigen binding. Furthermore, this increased flexibility is then passed to the bound analyte and allows for more efficient capture of the analyte bioconjugate immunocomplex to the LFA test line. This phenomenon has been reported in other studies where increased antibody flexibility led to improved capture efficiency in LFAs.[59]

These results demonstrate the successful application of nanobody-decorated SA-AuNPs as detection probes in LFAs and highlight the significant improvement in analytical sensitivity achieved by employing the bivalent nanobody. This optimised nanoparticle-based detection system constitutes the first component of the fully modular LFA.

This modular approach offers a significant advantage over the direct physisorption of nanobodies onto AuNPs, as explored in Chapter 4, particularly concerning bioconjugate stability and the use of both monovalent and divalent nanobodies. In Chapter 4, the direct binding of monovalent and divalent nanobodies often led to substantial nanoparticle aggregation, which severely limited their use in LFAs. This limitation is elegantly overcome here by employing streptavidin-biotin-mediated immobilisation, allowing for the stable conjugation of both monovalent and divalent nanobodies. Essentially, the already stabilised streptavidin-coated AuNPs can be decorated with either monovalent or divalent VHHV nanobodies without compromising their stability.

However, this notable improvement in stability must be weighed against a significant increase in cost. Streptavidin-coated AuNPs are currently around 50 times more expensive than bare AuNPs. While this price would likely decrease with bulk synthesis or orders; this is a crucial consideration for LFA development, especially when aiming to satisfy the WHO ASSURED criteria, which emphasises affordability for distribution to low-income countries often most affected by communicable diseases.

Therefore, it's proposed that both decoration methods, modular (streptavidin-biotin) and direct physisorption, are relevant depending on the diagnostic requirements. They each offer distinct advantages and disadvantages regarding utility, cost, and the use of nanobodies with different valencies, providing flexibility for various LFA applications. Interestingly, the sensitivity achieved with VHHV2-SA-AuNP (LoD of 62.7 pM) is considerably better than that observed in Chapter 4 with directly physisorbed VHHV3, which exhibited an LoD of 247 pM. This difference is particularly noteworthy considering that the assay used in Chapter 4 employed a simplified format with the antigen directly bound to PSA test lines, potentially favouring higher sensitivity. The superior performance of the streptavidin-mediated display approach, despite its increased complexity compared to direct adsorption, underscores its potential for developing highly sensitive LFAs. The next section will focus on optimising the modular display of nanobodies on the LFA test line.

5.2.12 Modular display of capture nanobodies on the LFA test-line

With the functionality of nanobody-decorated SA-AuNPs as detection probes established, attention was turned to optimising the capture component of the modular LFA. The aim of this section is to evaluate the performance of the in vivo biotinylated nanobodies as capture reagents when displayed on PSA-functionalised test lines. To simplify the analysis and isolate the performance of the capture system, an LFA format was employed where the detection probe was a conventional antibody-conjugated AuNP, and the capture agent was the biotinylated nanobody immobilised on the test line. This strategy allowed the capture component to be optimised and evaluated independently before integration into the full modular LFA.

To serve as the detection probe in this LFA format, AuNPs conjugated with the D003 monoclonal antibody were prepared. The optimal pH and antibody concentration for conjugation were determined using the standard physisorption screening. This optimisation process ensured the generation of stable, purified D003-conjugated AuNPs with optimal functionality for use in the LFA.

The monomeric VHHV and its dimeric and trimeric forms all target the same epitope on the S1 protein. To develop a fully modular LFA, two nanobodies are required that bind distinct epitopes: one serving as the capture nanobody while the other as the detection nanobody. Therefore, the nanobody repertoire was expanded to include two additional nanobodies characterised earlier in this thesis: VHHE and Nb6.

To ensure compatibility and avoid competition for the same epitope, a competition-based BLI experiment was employed. Biotinylated VHHV was immobilised onto streptavidin BLI sensors, followed by the addition of S1 protein. The binding of either Nb6 or VHHE to the S1-VHHV complex was evaluated. This experiment confirmed the compatibility of VHHE with VHHV, consistent with findings in Chapter 3 (Figure 5.19). This result was anticipated as VHHV and VHHE, both developed by Koenig *et al.*, have been previously validated to bind distinct epitopes on the S1 protein.[34]

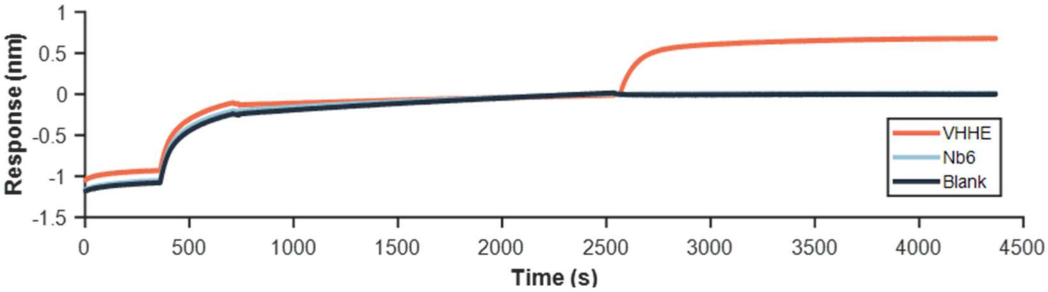

Figure 5. 19 Competition-based BLI is used to identify suitable nanobody pairs for VHHV to act as the capture nanobody in the modular LFA.

In contrast, Nb6 seemed to compete with VHHV for the same epitope, as evidenced by the lack of binding signal in the BLI experiment. This finding indicates that Nb6 is not suitable for use in conjunction with VHHV in the modular LFA.

The LFA used in this instance was performed by the mixing of buffer spiked with the analyte with the D003-AuNP and biotinylated AVI-tagged nanobody. After all the components are mixed in a well of a 96 well-plate and left to incubate for 5 minutes, an LFA strip with PSA on its test line is inserted into the well. The reaction mixture migrates across the nitrocellulose, and the immunocomplex has an opportunity to bind to the test line. A critical parameter influencing this type of LFA performance is the concentration of the capture nanobody.

Insufficient nanobody concentration can lead to suboptimal capture of the analyte-capture nanobody immunocomplex, reducing assay sensitivity. Conversely, excessive nanobody concentration can result in the "hook effect," where excess capture nanobody competes with the complete immunocomplex (AuNP conjugate – analyte – detection nanobody) for binding to the test line. Therefore, careful optimisation of capture nanobody concentration is crucial.

A series of LFAs were performed to determine the optimal concentration using D003-AuNPs as the detection probe and varying concentrations of capture nanobodies (100, 200 or 400 nM) on PSA-functionalised test lines. Four different nanobodies (VHHV, VHHV2, VHHV3, and VHHE) were tested to assess the impact of nanobody valency and binding characteristics on the optimal concentration. Each LFA was run with either S1 protein (500 ng/mL) or blank buffer to evaluate signal generation and nonspecific binding, which were used to calculate the SNR.

This investigation revealed a strong dependence of the SNR on the detection nanobody concentration, particularly for VHHV, VHHV2 and VHHE, where significant variations were observed (Figure 5.20). Interestingly, with VHHV and VHHV2, the SNR initially increased as

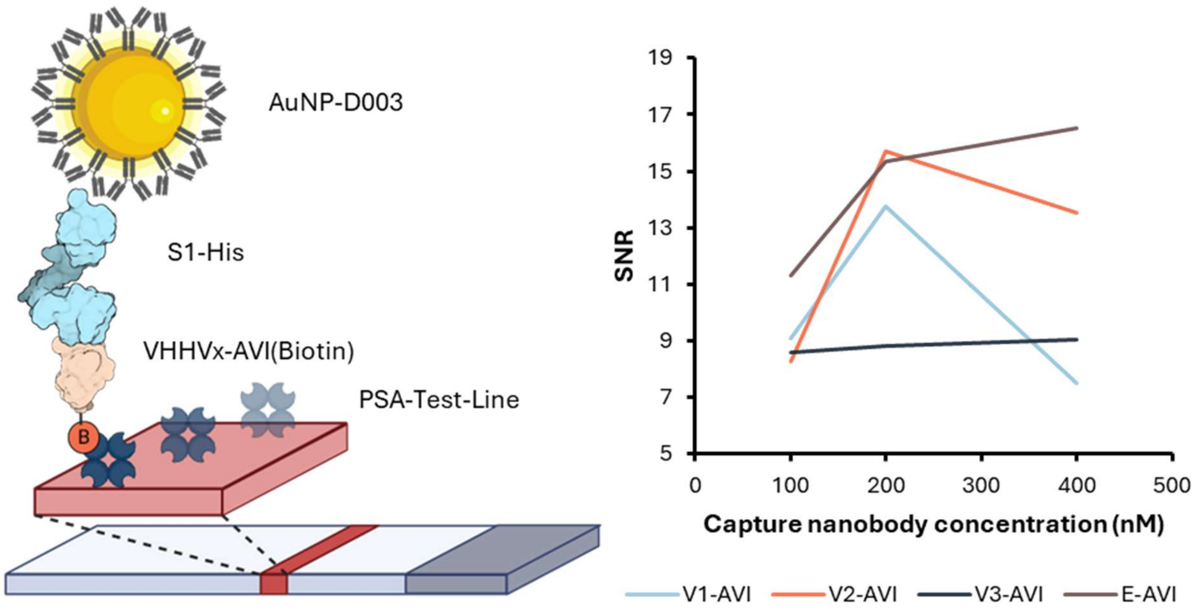

Figure 5. 20 Capture nanobody concentration optimisation. Scheme of the LFA showing the immunocomplex formation comprising the D003-AuNP bioconjugate, the S1 protein, capture biotinylated nanobody and PSA immobilised on the nitrocellulose. SNR plot of each detection nanobody run at different concentrations in the D003-AuNP LFA.

the nanobody concentration was raised from 100 nM to 200 nM but subsequently decreased at 400 nM. This trend suggests an initial improvement in analyte capture at 200 nM, followed by a decline in signal potentially due to the hook effect at higher concentrations. In contrast, the LFA using VHHV3 as the capture nanobody showed less sensitivity to concentration changes, exhibiting only a slight increase in SNR with increasing concentration. Furthermore, the maximum SNR achieved with VHHV3 (9.21) was notably lower than that of VHHV and VHHV2 (13.8 and 15.3, respectively), a result consistent with the experiments utilising VHHV3-AVI as the detection nanobody. VHHE demonstrated the highest SNR (16.5) among all nanobodies tested, with an optimal capture nanobody concentration of 400 nM.

To assess the influence of capture nanobody valency on assay sensitivity, the LoD for S1 protein was determined using LFAs with D003-AuNPs as the detection probe. The performance of VHHV, VHHV2, and VHHV3 as capture agents were compared, each used at their respective optimal concentration. A series of S1 protein concentrations were tested, and signal quantification was performed to determine the LoD achieved with each nanobody. These assays were operated by premixing the bioconjugate analyte and the capture nanobody in solution before running on PSA LFA strips.

This analysis revealed a significant improvement in LoD when comparing the assay using the monovalent VHHV-AVI nanobody to the bivalent VHHV2-AVI nanobody (116.0 [79.2 – 169.6]

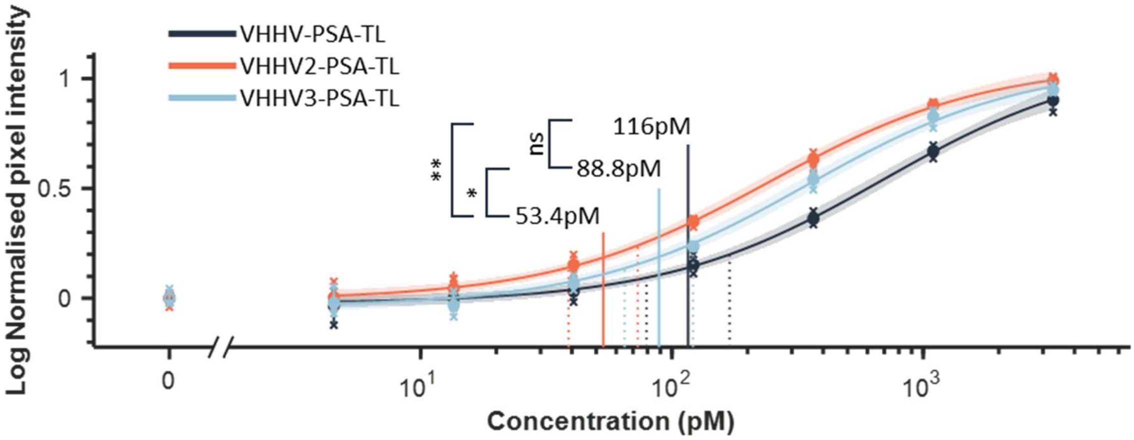

Figure 5. 21 LoD analysis of S1 LFA using D003-AuNP and biotinylated nanobodies as capture reagents on PSA-decorated nitrocellulose strips. The LoD plot shows the fitted Langmuir curves used to calculate the LoD of each series. The shaded area around the fit shows the 95% CI of the fit. Solid straight lines show the LoD, while dotted lines show the 95% CI of the LoD. Crosses show individual data points, while solid circles show the mean ± the SD of the mean. * – $p < 0.05$, ** – $p < 0.01$, ns – $p > 0.05$

pM 95% CI vs. 53.4 [38.8 – 73.1] pM 95% CI, $p < 0.005$ Figure 5.21). This enhancement in sensitivity is likely attributed to the increased valency of the bivalent nanobody, leading to improved binding kinetics and more efficient capture of the S1 protein. However, this improvement is slightly smaller than the enhancement observed when the bivalent nanobody was used as the detection probe on the nanoparticle surface.

This difference in improvement may be related to the “pendant nanobody" hypothesis proposed earlier. It was postulated that the enhanced performance of bivalent nanobodies as detection probes could be due to the increased flexibility and accessibility of the pendant nanobody when binding the analyte. When conjugated to the nanoparticle surface, the detection nanobody's movement and orientation are considered to be constrained by the size and surface properties of the nanoparticle. In this situation, the extra pendant provides a greater improvement in analyte capture. In contrast, when the nanobody is used as a capture nanobody, it is freely diffusive in solution and not restricted by the nanoparticle. Therefore, there is less to gain from additional nanobody domains regarding configuration and diffusivity.

Contrary to expectations, a reduction in sensitivity was observed with the trivalent VHHV3 nanobody (88.8 [64.8 - 121.4] pM 95% CI) compared to the bivalent VHHV2. This finding is unexpected since the trivalent nanobody exhibits a lower K_D and is anticipated to have more favourable binding kinetics, leading to more efficient analyte capture.

The reduced sensitivity observed with the trivalent nanobody might be attributed to several factors related to its increased size and complexity. Firstly, the larger size and diverse configurations accessible to the trivalent nanobody could lead to steric hindrance of the biotin handle, hindering its ability to bind to streptavidin on the test line. Secondly, while the added valency enhances affinity towards the target analyte, it might also increase avidity for off-target binding, increase background noise, and reduce sensitivity, which is consistent with the results. Thirdly, the freedom of the trivalent nanobody to adopt diverse configurations in solution could result in steric hindrance of its paratopes by other nanobody domains, reducing its ability to capture the antigen. Finally, the added complexity and size of the trivalent nanobody might increase its tendency for non-specific self-association, further reducing the effective concentration of active capture agents and reducing sensitivity.

5.2.13 Fully modular LFA

Having optimised both the modularly displayed nanobodies on nanoparticles and the nanobody-displayed nitrocellulose test lines, these components were integrated to create a fully modular LFA. This assay utilises VHHE-AVI as the capture reagent and VHHV-AVI as the detection probe, both immobilised via biotin-streptavidin interactions.

A two-step procedure is employed to perform the assay. First, the antigen is mixed with VHHE-AVI and incubated for 5 minutes. This mixture is then applied to the PSA-functionalised LFA strip, allowing the capture nanobody-antigen complex to form and become immobilised on the test line through the biotin handle. In the second step, pre-decorated VHHV-SA-AuNPs are introduced to the strip. The AuNPs, displaying the detection nanobody, bind to the analyte already immobilised on the test line, completing the immunoassay. The schematic in Figure 5.22 shows the process for performing the two-step assay.

This two-step process is crucial to prevent crosslinking of nanoparticles during assay operation. If the full immunocomplex (AuNP-SA, detection nanobody, analyte, and capture nanobody) were formed in solution, the complex would present a free biotin. This free biotin could interact with unoccupied receptors on the AuNP-SA surface, causing undesirable crosslinking and leading to loss of signal and aggregation. This concern is particularly relevant in scenarios where the AuNP-SA is not pre-functionalised with detection nanobodies and is decorated on-site during assay operation. In such cases, it is essential to prevent the capture nanobody from interacting with the unmodified AuNP-SA to avoid mixing of reagents and heterogeneous display of both detection and capture nanobodies on the conjugate, which could significantly impact assay sensitivity.

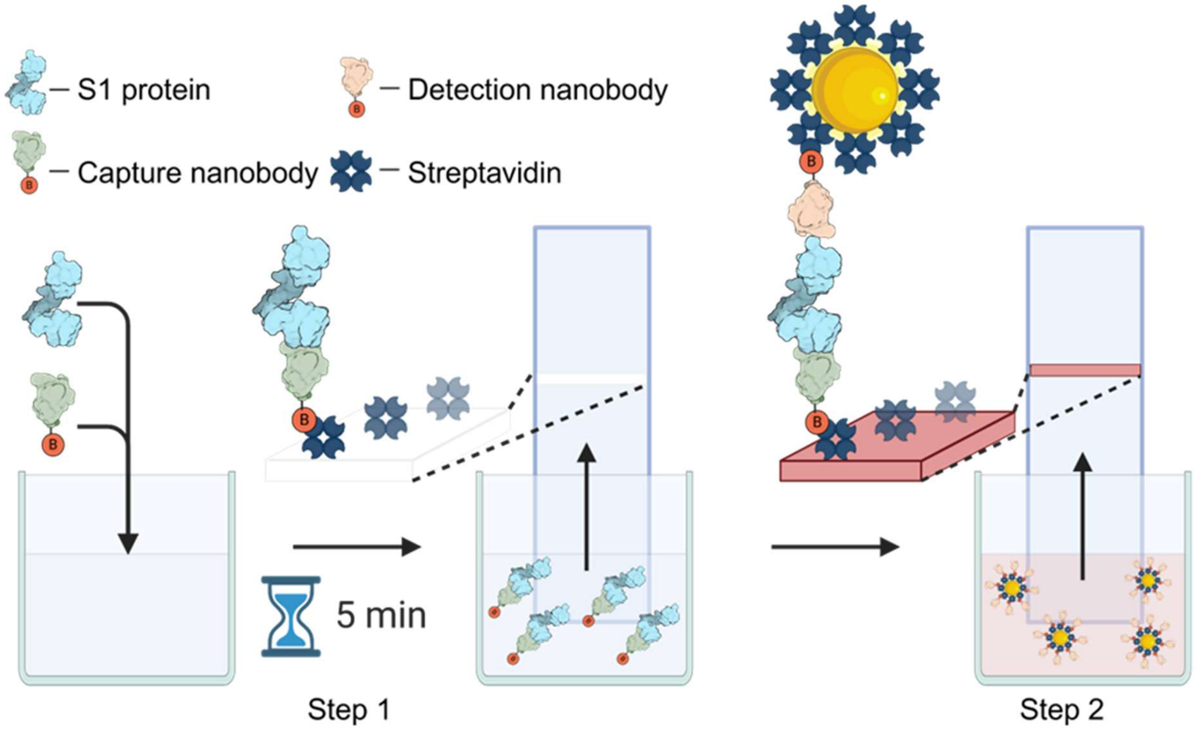

Figure 5. 22 Schematic showing the operation of the two-step modular LFA format. Step 1: Antigen is mixed with biotinylated capture nanobody (VHHE) and incubated. The complex is then applied to the PSA-functionalized LFA strip. Step 2: Pre-decorated VHHV-SA-AuNPs are added to the strip. The detection nanobody (VHHV) on the AuNP binds to the antigen captured on the test line, forming a visible signal.

This crosslinking issue could be mitigated by employing different tags for each nanobody. For example, the streptavidin-biotin interaction could be used for nanoparticle decoration, while a myc-tag and anti-myc tag antibody could be used to immobilise the capture nanobody on the test line. However, this work has prioritised displaying both nanobodies via streptavidin-biotin interactions due to the significant benefits in sensitivity and production simplicity. From a sensitivity perspective, the unparalleled affinity of the streptavidin-biotin interaction is crucial. While this is necessary for the efficient display of detection nanobodies on streptavidin-functionalised nanoparticles within PoC timescales (as demonstrated in earlier simulations), using this interaction for capture nanobody display further enhances sensitivity. The window for interaction between the tagged nanobody and the test line is limited to the brief time the mixture flows past the test tile, making efficient capture critical for maximising sensitivity. Furthermore, streptavidin-biotin display offers practical advantages. Streptavidin is more cost-effective than antibodies, as it can be expressed in bacteria, and it exhibits greater stability.

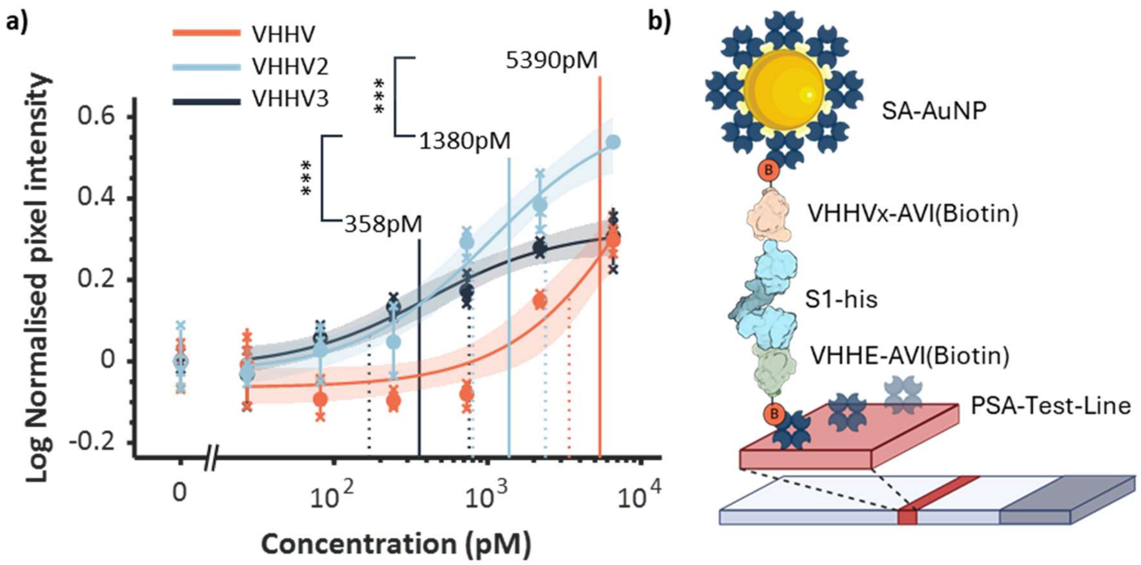

Figure 5. 23 (**a**) LoD analysis of dual modular display LFA. Each series represents the dose-response signal of each experiment utilising VHHV, VHHV2 or VHHV3 nanobodies as detection nanobodies on the SA-AuNP. Curves show the fitted Langmuir functions to each series, and the shade region around each curve shows the 95% CI of each fit. Vertical solid lines show the LoD of each series, while dotted vertical lines show the 95% CI of the LoD calculation. Crosses show individual data points, while solid circles show the mean. *** - p<0.005. (**b**) Scheme of the immunocomplex formation of the full modular LFA comprising the SA-AuNP, VHHV nanobody as the detection nanobody, the S1 protein analyte, the VHHE as the detection nanobody and PSA decorated on the TL.

From a production standpoint, tagging both nanobodies with biotin simplifies cloning and allows for identical production and purification protocols, streamlining the overall process.

In addition to the monovalent VHHV, the bivalent and trivalent versions of the detection nanobody were included in the experiments to probe the effect of nanobody valency on assay sensitivity. This investigation revealed a strong dependence of the detection nanobody valency on assay sensitivity. The least performing LFA was generated when using VHHV-AVI as the detection nanobody with a calculated LoD of 5390 pM (3400 – 8550 pM 95% CI), Figure 5.23. The LoD of the LFA utilising VHHV2-AVI as the detection nanobody generated a significantly lower LoD of 1380 pM (800 – 2380 pM 95% CI, $p < 0.005$). A further significant improvement in LoD was observed on the LFA using the VHHV3-AVI nanobody as the detection nanobody, generating a LoD of 358 pM (169 – 757 pM 95% CI, $p < 0.005$)

The observed improvement in the LoD with increased nanobody valency aligns, in part, with previous findings in this thesis and the broader literature. In a study by Mingxia *et al.,* the use of multivalent nanobodies in a sandwich ELISA achieved a 200-fold improvement in sensitivity compared to using monovalent nanobodies due to avidity and affinity improvements.[138] In the present study, the monomeric form of the S1 protein does not allow for avidity improvements (binding of multiple nanobodies to each antigen). This explains the comparatively modest improvements observed here. Similarly, in a study by Zhiqiang *et al.,* self-assembled nanobodies enhanced the sensitivity of a fluorescent-based LFA.[139] In this thesis, increased valency has been consistently shown to enhance nanobody affinity and improve performance in various immunoassays. For instance, in Chapter 4, BLI measurements demonstrated a decrease in the dissociation constant with increasing valency. This translated into improved sensitivity when these nanobodies were used as detection probes in ELISAs or when physisorbed onto gold nanoparticles.

Furthermore, in this chapter, using the bivalent version of VHHV to decorate SA-AuNPs in an LFA with D003 antibody test lines resulted in a significantly reduced LoD compared to the monovalent version. While experimentation with VHHV3 in that particular LFA format was hampered by excessive non-specific signals, the full modular assay, with VHHV3-AVI as the detection nanobody and VHHE as the capture nanobody, enabled further investigation. The reduction in non-specific signals in this format allowed for successful experimentation, demonstrating the anticipated relationship between increased valency and improved LoD. The trivalent VHHV3-AVI achieved a better LoD compared to both the divalent and monovalent forms, confirming the trend observed throughout this research. This finding aligns both with the expectation for improved LoD due to improved affinity and the pendant nanobody hypothesis proposed earlier, which states that having freely diffusive nanobodies pendant from the bioconjugate improves the LoD beyond what is expected from just improvements in affinity.

However, the relationship between valency and LoD observed for the detection nanobody in this experiment differed from that seen in the capture nanobody experiments. In the previous section, a decrease in LoD was noted when VHHV3-AVI was used as the capture nanobody compared to VHHV2-AVI. It was suggested that the dynamic and complex structure of VHHV3-AVI might lead to conformations that sterically hinder the paratopes and conceal the biotin tag, reducing its interaction with the antigen or the PSA test line.

Conversely, when VHHV3-AVI is decorated onto SA-AuNPs, its conformational flexibility might be restricted due to immobilisation on the nanoparticle surface. This restriction could reduce the tendency for steric hindrance, allowing for more efficient antigen binding and contributing to the improved LoD observed when VHHV3-AVI is used as the detection nanobody. This highlights the potential influence of nanoparticle immobilisation on the performance of multivalent nanobodies.

5.3 Considerations for clinical translation

In the initial proof-of-concept experiments, all assays were run in a running buffer. While the buffer used contained a relatively high concentration of BSA, it is not as complex as physiological samples like blood plasma or saliva. These matrices contain a complex and highly concentrated (80 g/L in blood plasma) mixture of proteins and cells that can impact assay performance. Affinity reagents and the analyte itself have a greater chance of off-target interactions in such matrices, potentially reducing specific signals and increasing non-specific signals.[20] This ultimately reduces the assay's sensitivity and increases LoD. Non-specific interactions can be controlled by the optimisation of the sample buffer. This can include adding surfactants or adjustments in ionic strength and pH. However, sample buffer adjustments need careful control, as they can disrupt both specific and non-specific interactions.[5]

In the current iteration of the modular LFAs, AuNP bioconjugates are used as prepared in the solution. To enable deployment, these nanoparticles would need to be dried for long-term storage at ambient conditions. Since the proposed modular LFA requires on-site decoration of SA-AuNPs with the detection nanobody, the bioconjugates would need to be dried in a tube, allowing the addition of the detection nanobody in solution to hydrate, resuspend, and decorate the bioconjugates. As demonstrated in Chapter 4, careful optimisation of the conjugate buffer is crucial to prevent aggregation during drying and enable resuspension without compromising functionality.

This system efficiently produces highly pure nanobodies for use in modular LFA. By using a dual expression system in *E. coli*, nanobodies are seamlessly expressed and biotinylated in vivo. This method is fast, cost-effective, and yields approximately 1-10 mg of nanobodies per litre of culture, depending on the nanobody. Based on our current yield, we estimate that a single litre of culture can generate enough material for 90,000 to 900,000 LFA tests. While promising, this may fall short of the scale required for global pandemic control. For example, over 3 billion LFAs were performed within the first two years of the SARS-CoV-2 pandemic.[72] In such situations, lab-scale bacterial fermentation and periplasmic expression of nanobodies would not meet the production demands for rapid LFA deployment, necessitating alternative approaches. One possibility is large-scale expression in yeast. Li *et al*. demonstrated nanobody production at 100 L scales in *Pichia pastoris*, reaching yields of 23 g/L.[140] However, a decrease in biotinylation efficiency was observed with increased nanobody yields. Future scale-up plans and studies should consider and investigate the biotinylation efficiency at higher nanobody yields and incorporate strategies to maximise biotinylation efficiency, such as continuous culture supplementation with biotin during induction.

In this study, SARS-CoV-2 was used as a model system to demonstrate the feasibility of a fully modular LFA. While the S1 protein is a relevant biomarker for SARS-CoV-2 detection, the N protein is more commonly used in antigen tests due to its lower risk of mutational escape and higher concentration in infected individuals. The N protein concentration in saliva ranges from 10 to 10,000 pg/mL between 1 and 7 days post-infection.[141] The current modular LFA sensitivity lies at the higher end of this range, enabling detection at peak infection but potentially limiting early detection and disease spread control. The modular design is readily adaptable to technologies developed for ultra-sensitive LFAs. These include using quantum nanodiamonds or platinum nanocatalysts instead of AuNPs, achieving orders of magnitude greater sensitivity.[38,40] Other strategies involve signal detection technologies like thermal contrasting or Raman spectroscopy.[142,143] Thus, the LFA could be adapted for diseases requiring detection of analytes at very low concentrations, such as HIV, where p24 levels in blood plasma range from 0.1 to 1000 pg/mL.[144] For diseases with higher analyte concentrations, the modular LFA using AuNPs and colourimetric readout could be configured for diagnostic use. For instance, the dengue and Zika virus non-structural proteins are present in blood serum at 120 ng/mL and 30 ng/mL, respectively.[145]

5.4 Conclusions and future work

This chapter detailed the development and evaluation of a novel, fully modular LFA based on in vivo biotinylated nanobodies. This platform offers a streamlined approach to LFA design by utilising the high-affinity streptavidin-biotin interaction for immobilising both capture and detection nanobodies onto prefabricated LFA cassettes and AuNP bioconjugates.

Mathematical modelling was used to guide the choice of affinity reagents for modular attachment of nanobodies onto AuNPs to be used in LFA. The interactions of polyvalent bioconjugates with tagged nanobodies using a solution-based simulation provided insights into how different affinity systems perform in various display scenarios. It was demonstrated that strong affinity is crucial to enable decoration within the rapid timescales of PoC when the decoration step would be performed manually by the user during assay operation. It was also shown that in-line decoration would be feasible with streptavidin-biotin interaction, potentially simplifying the assay. However, careful optimisation would be required to balance decoration efficiency and free detection nanobody concentration. It was also shown that the affinity repertoire could be expanded beyond the ultra-low affinity to include conventional antibody-antigen affinities for bioconjugate decoration. However, this must be performed in a laboratory setting since bioconjugate purification would be required. The work in this section showcases the use of mathematical modelling to guide the design of LFA components. Advancements in this model that include more complex interactions could improve its accuracy. This includes factors like non-specific binding and heterogeneous distributions of binding sites per nanoparticle. Furthermore, in this work, the model was used to qualitatively evaluate the different systems. Future studies should aim to validate the model by generating reagents under various conditions and comparing their performance to the model's predictions.

This chapter successfully demonstrated the generation of an in vivo nanobody biotinylation system using *E. coli* co-transformed with plasmids containing AVI-tagged nanobodies and a plasmid encoding for biotin ligase. This approach enabled the co-expression of BirA and AVI-tagged nanobodies, allowing seamless simultaneous expression and biotinylation. Protein characterisation revealed 100% biotinylation in expression cultures with moderate protein yield, but this efficiency was reduced when the protein yield increased. Furthermore, protein yield was found to be dependent on nanobody valency, with smaller nanobodies achieving multi-fold improved protein yields. Future studies should investigate the mechanisms behind incomplete biotinylation and reduced protein yield with increased nanobody valency, as these factors could pose challenges to scaling up this system.

The in vivo biotinylated nanobodies were successfully integrated into various LFAs as detection and capture reagents through modular display on both the nanoparticles and the nitrocellulose membranes. Using an antibody that was confirmed to pair with VHHV, LFAs were developed for the detection of the S1 protein using biotinylated nanobodies as either detection reagents, capture reagents, or both. In configurations using a combination of nanobody and antibody, the LFA achieved low picomolar sensitivity for the detection of the S1 protein. Notably, using the divalent nanobody as the detection reagent significantly enhanced the LFA's sensitivity beyond expectations based on observations from monovalent to divalent nanobody transitions in other assays. Using nanobodies as the capture probe with antibody-conjugated nanoparticles, detecting the S1 protein revealed more complex relationships between nanobody valency and assay sensitivity. While the expected improvement was observed when comparing the monovalent version to the divalent version, an unexpected decrease in sensitivity was noted when comparing the trivalent version to the divalent version. It was suggested that the trivalent nanobody may adopt configurations that conceal the biotin handle or its antigen-binding sites, hindering its performance in the assay. In the LFA utilising biotinylated nanobodies as both detection and capture reagents, pM sensitivity was achieved for detecting the S1 protein in spike buffer samples.

While this proof-of-concept study highlights the potential of the modular LFA platform, further research is needed to address challenges related to assay performance in complex matrices, drying and storage of AuNP bioconjugates, scalability of nanobody production, sensitivity for early disease detection, and adaptability to diverse applications.

Despite these challenges, the modular LFA platform holds promise for revolutionising diagnostics by enabling rapid adaptation to emerging threats, facilitating point-of-care testing, and improving healthcare accessibility, particularly in resource-limited settings. Future research will focus on refining the platform and expanding its applications to address diverse diagnostic needs.

6 Final summary and perspectives

LFA technology is a robust diagnostic tool that enables the cost-effective, rapid, and scalable detection of various diseases. However, challenges remain when these assays need to be quickly developed and deployed at scale, which can be hindered by manufacturing and supply chain bottlenecks. This can lead to discrepancies in availability, particularly in resource-limited settings despite their low cost. These limitations can hinder the timely availability of crucial diagnostic tools, as exemplified by the SARS-CoV-2 pandemic, where testing shortages significantly impacted global containment efforts. Therefore, it is essential to establish innovative tools and strategies that facilitate the accelerated development and scalable deployment of LFAs while mitigating vulnerabilities to manufacturing bottlenecks. This will ensure equal access to these vital diagnostics and enhance global preparedness for future health crises.

6.1 Review of thesis outline and conclusions

This thesis has investigated the possibility of using nanobodies as biorecognition alternatives to traditional antibodies, exploiting their quick development, adaptability and cheap manufacture to enable quicker LFA development and the generation of versatile LFAs. The first issue addressed in this thesis is the instability observed when nanobodies are physisorbed onto gold nanoparticles (AuNP), especially when exposed to solutions with elevated ionic strengths.

The work in Chapter 3 focused on studying the stability of nanobody AuNP bioconjugates prepared through physisorption, the simplest and most common conjugation technique for the preparation of diagnostic bioconjugates. By examining the physisorption of nanobodies in their native form and under different bioconjugation conditions such as pH, AuNP diameter and ionic strength, insights into adsorption characteristics of nanobodies and the extent of the bioconjugate stability were gained. These were studied using UV-Vis spectroscopy and DLS.

These findings were used to propose mechanisms leading to bioconjugate instability and serve as the benchmark for subsequent studies that aimed to improve bioconjugate stability. Another area of focus in Chapter 3 was the exploration of common modifications to physisorption towards improving resulting bioconjugate stability. The lead nanobody VHHV was engineered to present a free cysteine and tested for changes in adsorption characteristics and the resulting bioconjugate stability. This modification resulted in modest improvement in bioconjugate stability when the cysteine-bearing nanobody is physisorbed in its dimeric form. This finding encouraged subsequent studies that would explore multivalent nanobodies. Another modification to physisorption explored is the addition of carbonate buffer during physisorption. This was also found to increase resistance to salt-induced aggregation moderately.

Chapter 4 investigated a novel modification strategy involving the incorporation of nanobodies into multivalent chains, aiming to improve the resulting bioconjugate stability when these are physisorbed onto AuNPs. Nanobody VHHV was engineered into a divalent and trivalent versions by fusing nanobody domains using a flexible linker to enable free configuration. Characterisation of the engineered nanobodies revealed improvement in the nanobody affinity to the target antigen with increased valency, translating into drastic improvements in sensitivity when used as detection probes in ELISA. Distinct improvements in stability were observed when the trimeric nanobody was physisorbed onto AuNPs compared to the monovalent and divalent forms exhibiting a high degree of resistance to salt-induced aggregation. The stability was maintained through bioconjugate processing, which included blocking, washing, and freeze-drying. Furthermore, pM sensitivity for the target antigen was achieved using the trivalent nanobody bioconjugate as a label in an LFA format even after the required bioconjugate processing. Higher-order polyvalent nanobodies and other nanobodies incorporated into multivalent fusions provided functional insights for nanobody multivalent state and protein yield. The study of these nanobodies physisorbed onto AuNPs also revealed insights of nanobody characteristics and their ability to form stable bioconjugates when used in multivalent form for bioconjugate synthesis. The results in this chapter offer a significant contribution to nanobody-based LFA, which was hindered by the inability of nanobodies to provide sufficient protection for LFA applications. The work in this chapter can be used to design bioconjugation workflows and improve bioconjugate stability by engineering nanobodies into multivalent fusions.

Chapter 5 shifted the focus to developing an adaptable modular display LFA system, capitalising on the straightforward protein engineering of nanobodies. Specifically, a fully modular LFA was developed where in vivo biotinylated nanobodies were modularly displayed on streptavidin-functionalised nitrocellulose pads and streptavidin-coated AuNPs. Mathematical modelling guided the selection of affinity reagents for optimal nanobody display on AuNPs, demonstrating the importance of strong affinity for rapid, user-friendly point-of-care testing. The model also highlighted the potential for streamlined "in-line" decoration and the feasibility of incorporating a broader range of affinity strengths. An efficient *E. coli*-based system for in vivo biotinylation of nanobodies was successfully established, although challenges related to biotinylation efficiency and protein yield were observed with increasing nanobody valency. These biotinylated nanobodies were integrated into LFAs targeting the SARS-CoV-2 S1 protein, demonstrating picomolar sensitivity in configurations utilising both nanobody and antibody components. Notably, divalent nanobodies significantly enhanced assay sensitivity when used as detection reagents, while the impact of valency on capture nanobodies was more complex. This proof-of-concept study demonstrates the potential of the fully modular LFA platform. However, further research is needed to optimise assay performance in complex matrices, address nanobody production scalability, and enhance sensitivity for early disease detection. The LFA developed in this chapter is envisioned to be adaptable to any target disease using a suitable nanobody pair. Stockpiling prefabricated LFA cassettes allows for rapid deployment and activation in response to emerging infectious threats, minimising the impact of manufacturing bottlenecks and supply chain disruptions. Furthermore, the cost-effective production of nanobodies facilitates their generation even in resource-limited settings, promoting broader access to these crucial reagents. Collectively, this strategy enables a quicker and more comprehensive response to disease outbreaks, significantly improving global pandemic preparedness.

Collectively, the work in this thesis has provided a deep analysis of the potential of nanobodies to be used as biorecognition reagents in diagnostics. Various engineered and native nanobodies were used in this thesis across multiple immunoassay formats, providing functional insights of nanobody structure characteristics and sensitivity achieved.

6.2 Future work

6.2.1 Comparison with antibody-based LFA

A key motivation for exploring nanobodies as alternatives to full-size antibodies in diagnostic platforms like LFAs is their smaller size. This would allow for denser packing of functional recognition elements on biosensor surfaces, such as AuNPs and nitrocellulose membranes. This increased density has long been recognised to enhance analyte capture, improving analytical sensitivity. While this thesis demonstrated the feasibility and advantages of using nanobodies in LFAs, a comprehensive, quantitative comparison of functional loading and its direct correlation to sensitivity gains between nanobodies and antibodies of comparable affinities was not fully explored. Therefore, future studies should prioritise a systematic investigation employing a diverse library of nanobodies and antibodies with a range of affinities for a standard target analyte. This would allow for a direct, side-by-side comparison of their respective abilities to form densely functionalised layers on various LFA components and, crucially, to establish a clear relationship between paratope density and the resulting analytical sensitivity in an LFA format. Such studies would provide valuable insights into the fundamental advantages of nanobodies and inform the design of next-generation LFAs with optimised performance characteristics.

6.2.2 Study orientation effects

In Chapter 5, a significant improvement in the limit of detection (LoD) was observed when nanobodies were modularly displayed on streptavidin-functionalised AuNPs compared to bioconjugates prepared through conventional physisorption. This notable gain in analytical sensitivity, a critical parameter for expanding the applicability and robustness of LFAs, could be attributed, at least in part, to favourable orientation effects. In the modular system, nanobodies are attached to the streptavidin-coated nanoparticle surface via a C-terminal biotin tag. This ensures a uniform orientation where the antigen-binding site is projected outwards, away from the nanoparticle surface. In contrast, nanobodies physisorbed directly onto AuNPs can adopt random orientations, potentially hindering the accessibility of their paratopes for analyte binding. This difference in display likely contributes to the improved LoD observed with the modular approach. Future studies should quantify the number of immobilised nanobodies in both the modular and physisorbed systems to gain deeper insights into the contribution of orientation effects to analytical sensitivity. Furthermore, estimating the proportion of nanobodies presenting their paratopes in an optimal configuration for analyte binding would be valuable. Techniques such as quantifying the amount of unbound nanobody in the supernatant post-conjugation, coupled with methods for assessing the functional activity of immobilised nanobodies, similar to the enzymatic assays used to determine the number of active antibodies on nanoparticle surfaces in previous studies, could provide valuable data.[59,60] These studies could confirm the orientation-sensitivity relationship and enable future experimentation to increase this effect further.

6.2.3 Investigating conformational changes of physisorbed nanobodies

This thesis thoroughly investigated the extent to which nanobodies prevent salt-induced aggregation when physisorbed onto AuNPs. By examining various protein characteristics, including structure, exposed functional groups, and amino acid composition, insights were gained into the complex interplay between protein properties, the physisorption process, and the resulting bioconjugate stability. Initial mechanisms contributing to aggregation under different ionic strength conditions were proposed, including the potential for protein-mediated cross-linking and conformational changes of the nanobody upon adsorption to the nanoparticle surface. However, a complete understanding of the underlying mechanisms driving aggregation, and particularly the reasons why nanobodies offer limited protection against it, is not yet achieved. Therefore, future studies should focus on elucidating these proposed aggregation mechanisms. A key aspect will be investigating potential conformational changes of nanobodies upon physisorption using techniques like circular dichroism (CD) spectroscopy, which can provide valuable information on protein secondary structure alterations. Additionally, nuclear magnetic resonance (NMR) spectroscopy could be employed to identify the specific attachment points and binding interfaces between nanobodies and the AuNP surface. By confirming the precise mechanisms leading to salt-induced aggregation and understanding the limitations of nanobodies in this context, would enable rational design strategies to engineer the next generation of nanobody constructs. These improved nanobodies would be specifically tailored to enhance colloidal stability and mitigate aggregation, unlocking their full potential in LFA and other diagnostic applications.

6.2.4 Clinical translation of nanobody-based LFA

While this thesis has demonstrated the potential of nanobodies for use in LFA, several considerations and optimisation steps need to be taken to enable their use in the clinic. This thesis generated several LFAs using physisorbed or modularly displayed nanobodies. These LFAs were designed to detect the SARS-CoV-2 S1 protein. This model system was chosen based on the availability of an extensive library of nanobodies against this target. Still, a more appropriate biomarker for detecting SARS-CoV-2 is the nucleocapsid protein, which is present in higher concentrations in infected individuals. Similarly, a biomarker that is compatible with nanobodies and present in concentrations that can be detected with LFA should be selected for detecting other diseases. Furthermore, the LFA performed in this thesis involved samples consisting of running buffers spiked with the antigen. Transitioning to physiological samples can significantly impact the assay's sensitivity by affecting both specific and non-specific interactions of assay components, which require subsequent optimisation. Parameters such as sample viscosity, pH and ionic strength should be considered. Another consideration is the preparation of reagents for long-term storage. In Chapter 4, trivalent nanobody bioconjugate was investigated for performance after freeze-drying. While the sensitive detection after this processing step is a promising initial finding, there are still considerations to be made for the ability of the bioconjugate to be stored in a desiccated format and used. In the study in Chapter 4, the bioconjugate was freeze-dried in a 96-well plate. To enable their use in LFAs, bioconjugates are dried on conjugate pads attached to LFA pads, offering resuspension of the bioconjugates during assay operation. The trimeric bioconjugate generated here and future nanobody-based bioconjugates should be evaluated for their ability to be stored and desiccated on conjugate pads. These studies should determine the stability of the bioconjugates after being resuspended from storage on a conjugate pad, and their functionality in detecting the analyte. This could require the optimisation of the bioconjugate storage buffer using cryoprotective additives such as sucrose, as used in Chapter 4. Furthermore, these studies should be coupled with accelerated ageing studies to asswss the effect of long-term storage.

7 Bibliography

1 B. Ince and M. K. Sezgintürk, *TrAC Trends in Analytical Chemistry*, 2022, **157**, 116725.

2 M. A. Connolly, M. Gayer, M. J. Ryan, P. Salama, P. Spiegel and D. L. Heymann, *The Lancet*, 2004, **364**, 1974–1983.

3 Gov.uk, 100 days mission to respond to future pandemic threats, https://www.gov.uk/government/publications/100-days-mission-to-respond-to-future-pandemic-threats, (accessed 22 November 2024).

4 WHO, The top 10 causes of death, https://www.who.int/news-room/fact-sheets/detail/the-top-10-causes-of-death, (accessed 6 December 2024).

5 C. Parolo, A. Sena-Torralba, J. F. Bergua, E. Calucho, C. Fuentes-Chust, L. Hu, L. Rivas, R. Álvarez-Diduk, E. P. Nguyen, S. Cinti, D. Quesada-González and A. Merkoçi, *Nat Protoc*, 2020, **15**, 3788–3816.

6 P. Peng, C. Liu, Z. Li, Z. Xue, P. Mao, J. Hu, F. Xu, C. Yao and M. You, *TrAC Trends in Analytical Chemistry*, 2022, **152**, 116605.

7 F. Watzinger, K. Ebner and T. Lion, *Mol Aspects Med*, 2006, **27**, 254–298.

8 Y. Liu, L. Zhan, Z. Qin, J. Sackrison and J. C. Bischof, *ACS Nano*, 2021, **15**, 3593–3611.

9 M. Naseri, Z. M. Ziora, G. P. Simon and W. Batchelor, *Rev Med Virol*, 2022, **32**, e2263.

10 K. J. Land, D. I. Boeras, X.-S. Chen, A. R. Ramsay and R. W. Peeling, *Nat Microbiol*, 2018, **4**, 46–54.

11 A. Sena-Torralba, R. Álvarez-Diduk, C. Parolo, A. Piper and A. Merkoçi, *Chem Rev*, 2022, **122**, 14881–14910.

12 B. Bruijns, R. Tiggelaar, J. Knotter and A. van Dam, *Sensors*, 2023, **23**, 6201.

13 D. Cherkaoui, D. Huang, B. S. Miller, V. Turbé and R. A. McKendry, *Biosens Bioelectron*, 2021, **189**, 113328.

14 I. Montesinos, D. Gruson, B. Kabamba, H. Dahma, S. Van den Wijngaert, S. Reza, V. Carbone, O. Vandenberg, B. Gulbis, F. Wolff and H. Rodriguez-Villalobos, *Journal of Clinical Virology*, 2020, **128**, 104413.

15 E. Mermiga, V. Pagkali, C. Kokkinos and A. Economou, *Molecules*, 2023, **28**, 8135.

16 K. Omidfar, F. Riahi and S. Kashanian, *Biosensors (Basel)*, 2023, **13**, 837.

17 E. B. Bahadır and M. K. Sezgintürk, *TrAC Trends in Analytical Chemistry*, 2016, **82**, 286–306.

18 L. J. Harris, E. Skaletsky and A. McPherson, *J Mol Biol*, 1998, **275**, 861–872.

19 M. L. Chiu, D. R. Goulet, A. Teplyakov and G. L. Gilliland, *Antibodies*, 2019, **8**, 55.

20 A. Frutiger, A. Tanno, S. Hwu, R. F. Tiefenauer, J. Vörös and N. Nakatsuka, *Chem Rev*, 2021, **121**, 8095–8160.

21 N. C. HUGHES-JONES, *Br Med Bull*, 1963, **19**, 171–177.

22 V. Kamat and A. Rafique, *Anal Biochem*, 2017, **536**, 16–31.

23 J. He, in *The Immunoassay Handbook*, Elsevier, 2013, pp. 381–393.

24 A. V. Bartosh, D. V. Sotnikov, O. D. Hendrickson, A. V. Zherdev and B. B. Dzantiev, *Biosensors (Basel)*, 2020, **10**, 17.

25 D. Gasperino, T. Baughman, H. V. Hsieh, D. Bell and B. H. Weigl, *Annual Review of Analytical Chemistry*, 2018, **11**, 219–244.

26 J. K. H. Liu, *Annals of Medicine & Surgery*, 2014, **3**, 113–116.

27 G. Winter, A. D. Griffiths, R. E. Hawkins and H. R. Hoogenboom, *Annu Rev Immunol*, 1994, **12**, 433–455.

28 C. M. Hammers and J. R. Stanley, *Journal of Investigative Dermatology*, 2014, **134**, 1–5.

29 Y. jia Jin, D. Yu, X. long Tian, H. xian Li, X. chao Zhou, Y. Kong, W. Zhang, L. Zhang, C. Lei, Z. lin Yang, C. Tu, Y. ling Wu and T. lei Ying, *Acta Pharmacol Sin*, 2022, **43**, 954–962.

30 N. E. Weisser and J. C. Hall, *Biotechnol Adv*, 2009, **27**, 502–520.

31 M. IA. Ahmad, C. G. Amorim, L. F. Abu Qatouseh and M. C. B. S. M. Montenegro, *Microchemical Journal*, 2024, **196**, 109628.

32 A. Mohseni, M. Molakarimi, M. Taghdir, R. H. Sajedi and S. Hasannia, *J Biomol Struct Dyn*, 2019, **37**, 3686–3696.

33 M. Schoof, B. Faust, R. A. Saunders, S. Sangwan, V. Rezelj, N. Hoppe, M. Boone, C. B. Billesbølle, C. Puchades, C. M. Azumaya, H. T. Kratochvil, M. Zimanyi, I. Deshpande, J. Liang, S. Dickinson, H. C. Nguyen, C. M. Chio, G. E. Merz, M. C. Thompson, D. Diwanji, K. Schaefer, A. A. Anand, N. Dobzinski, B. S. Zha, C. R. Simoneau, K. Leon, K. M. White, U. S. Chio, M. Gupta, M. Jin, F. Li, Y. Liu, K. Zhang, D. Bulkley, M. Sun, A. M. Smith, A. N. Rizo, F. Moss, A. F. Brilot, S. Pourmal, R. Trenker, T. Pospiech, S. Gupta, B. Barsi-Rhyne, V. Belyy, A. W. Barile-Hill, S. Nock, Y. Liu, N. J. Krogan, C. Y. Ralston, D. L. Swaney, A. García-Sastre, M. Ott, M. Vignuzzi, P. Walter, A. Manglik, C. M. Azumaya, C. Puchades, M. Sun, J. R. Braxton, A. F. Brilot, M. Gupta, F. Li, K. E. Lopez, A. Melo, G. E. Merz, F. Moss, J. Paulino, T. H. Pospiech, S. Pourmal, A. N. Rizo, A. M. Smith, P. V. Thomas, F. Wang, Z. Yu, M. S. Dickinson, H. C. Nguyen, D. Asarnow, M. G. Campbell, C. M. Chio, U. S. Chio, D. Diwanji, B. Faust, M. Gupta, N. Hoppe, M. Jin, J. Li, Y. Liu, G. E. Merz, S. Sangwan, T. K. M. Tsui, R. Trenker, D. Trinidad, E. Tse, K. Zhang, F. Zhou, N. Herrera, H. T. Kratochvil, U. Schulze-Gahmen, M. C. Thompson, I. D. Young, J. Biel, I. Deshpande, X. Liu, C. B. Billesbølle, C. Nowotny, A. M. Smith, J. Zhao, A. Bowen, N. Hoppe, Y.-L. Li, P. Nguyen, M. Safari, K. Schaefer, N. Whitis, M. Moritz, T. W. Owens, A. Diallo, K. Kim, J. K. Peters, E. W. Titus, J. Chen, L. Doan, S. Flores, V. L. Lam, Y. Li, M. Lo, A. C. Thwin, S. Wankowicz, Y. Zhang, D. Bulkley, A. Joves, A. Joves, L. McKay, M. Tabios, O. S. Rosenberg, K. A. Verba, D. A. Agard, Y. Cheng, J. S. Fraser, A. Frost, N. Jura, T. Kortemme, N. J. Krogan, A. Manglik, D. R. Southworth and R. M. Stroud, *Science (1979)*, 2020, **370**, 1473–1479.

34 P.-A. Koenig, H. Das, H. Liu, B. M. Kümmerer, F. N. Gohr, L.-M. Jenster, L. D. J. Schiffelers, Y. M. Tesfamariam, M. Uchima, J. D. Wuerth, K. Gatterdam, N. Ruetalo, M. H. Christensen, C. I. Fandrey, S. Normann, J. M. P. Tödtmann, S. Pritzl, L. Hanke, J. Boos, M. Yuan, X. Zhu, J. L. Schmid-Burgk, H. Kato, M. Schindler, I. A. Wilson, M. Geyer, K. U. Ludwig, B. M. Hällberg, N. C. Wu and F. I. Schmidt, *Science*, 2021, **371**, 1–15.

35 X. Wang, T. Sun, W. Shen, M. Liu, W. Liu, H. Zuo, Y. Zhang, L. Geng, W. Wang, C. Shao and J. Bai, *Sens Actuators B Chem*, 2023, **394**, 134419.

36 Bárbara Sofia Fialho Simões, PhD Thesis, University of Birmingham, 2021.

37 S. Y. Doerflinger, J. Tabatabai, P. Schnitzler, C. Farah, S. Rameil, P. Sander, A. Koromyslova and G. S. Hansman, *mSphere*, 2016, **1**, 1–16.

38 C. N. Loynachan, M. R. Thomas, E. R. Gray, D. A. Richards, J. Kim, B. S. Miller, J. C. Brookes, S. Agarwal, V. Chudasama, R. A. McKendry and M. M. Stevens, *ACS Nano*, 2018, **12**, 279–288.

39 M. M. Kijanka, A. S. A. van Brussel, E. van der Wall, W. P. T. M. Mali, P. J. van Diest, P. M. P. van Bergen en Henegouwen and S. Oliveira, *EJNMMI Res*, 2016, **6**, 14.

40 B. S. Miller, L. Bezinge, H. D. Gliddon, D. Huang, G. Dold, E. R. Gray, J. Heaney, P. J. Dobson, E. Nastouli, J. J. L. Morton and R. A. McKendry, *Nature*, 2020, **587**, 588–593.

41 Z. Li, Y. Wang, J. Wang, Z. Tang, J. G. Pounds and Y. Lin, *Anal Chem*, 2010, **82**, 7008–7014.

42 J. Li, H. Duan, P. Xu, X. Huang and Y. Xiong, *RSC Adv*, 2016, **6**, 26178–26185.

43 D. Chekkaramkodi, S. El Turk, M. Ali and H. Butt, *Sci Rep*, 2024, **14**, 29736.

44 X. Liu, M. Atwater, J. Wang and Q. Huo, *Colloids Surf B Biointerfaces*, 2007, **58**, 3–7.

45 D. K. Kim, Y. J. Hwang, C. Yoon, H. O. Yoon, K. S. Chang, G. Lee, S. Lee and G. R. Yi, *Physical Chemistry Chemical Physics*, 2015, **17**, 20786–20794.

46 J. Turkevich, P. C. Stevenson and J. Hillier, *Discuss Faraday Soc*, 1951, **11**, 55.

47 E. Calucho, C. Parolo, L. Rivas, R. Álvarez-Diduk and A. Merkoçi, in *Comprehensive Analytical Chemistry*, Elsevier B.V., 2020, vol. 89, pp. 313–359.

48 X. Liu, J. Li, Y. Huang, X. Wang, X. Zhang and X. Wang, *Environ Sci Technol*, 2017, **51**, 6156–6164.

49 A. J. Sheridan, K. C. Thompson and J. M. Slater, *Biophys Chem*, 2022, **290**, 106896.

50 S. H. Brewer, W. R. Glomm, M. C. Johnson, M. K. Knag and S. Franzen, *Langmuir*, 2005, **21**, 9303–9307.

51 Y. Wang, Z. Gao, Z. Han, Y. Liu, H. Yang, T. Akkin, C. J. Hogan and J. C. Bischof, *Sci Rep*, 2021, **11**, 898.

52 L. Zhan, S. Z. Guo, F. Song, Y. Gong, F. Xu, D. R. Boulware, M. C. McAlpine, W. C. W. Chan and J. C. Bischof, *Nano Lett*, 2017, **17**, 7207–7212.

53 M. H. Jazayeri, H. Amani, A. A. Pourfatollah, H. Pazoki-Toroudi and B. Sedighimoghaddam, *Sens Biosensing Res*, 2016, **9**, 17–22.

54 L. Zhang, Y. Mazouzi, M. Salmain, B. Liedberg and S. Boujday, *Biosens Bioelectron*, 2020, **165**, 112370.

55 A. Wang, K. Vangala, T. Vo, D. Zhang and N. C. Fitzkee, *The Journal of Physical Chemistry C*, 2014, **118**, 8134–8142.

56 J.-P. Ayrton, C. Ho, H. Zhang, V. Chudasama, S. Frank and M. R. Thomas, *Nanoscale*, 2024, **16**, 19881–19896.

57 S. Thobhani, S. Attree, R. Boyd, N. Kumarswami, J. Noble, M. Szymanski and R. A. Porter, *J Immunol Methods*, 2010, **356**, 60–69.

58 J. Goossens, H. Sein, S. Lu, M. Radwanska, S. Muyldermans, Y. G. J. Sterckx and S. Magez, *Analytical Methods*, 2017, **9**, 3430–3440.

59 D. A. Richards, M. R. Thomas, P. A. Szijj, J. Foote, Y. Chen, J. C. F. Nogueira, V. Chudasama and M. M. Stevens, *Nanoscale*, 2021, **13**, 11921–11931.

60 K. Tripathi and J. D. Driskell, *ACS Omega*, 2018, **3**, 8253–8259.

61 G. Ruiz, K. Tripathi, S. Okyem and J. D. Driskell, *Bioconjug Chem*, 2019, **30**, 1182–1191.

62 K. Siriwardana, A. Wang, K. Vangala, N. Fitzkee and D. Zhang, *Langmuir*, 2013, **29**, 10990–10996.

63 O. Awotunde, S. Okyem, R. Chikoti and J. D. Driskell, *Langmuir*, 2020, **36**, 9241–9249.

64 T. Robson, D. S. H. Shah, A. S. Solovyova and J. H. Lakey, *ACS Appl Nano Mater*, 2018, **1**, 3590–3599.

65 M. Iarossi, C. Schiattarella, I. Rea, L. De Stefano, R. Fittipaldi, A. Vecchione, R. Velotta and B. Della Ventura, *ACS Omega*, 2018, **3**, 3805–3812.

66 M. Ben Haddada, D. Hu, M. Salmain, L. Zhang, C. Peng, Y. Wang, B. Liedberg and S. Boujday, *Anal Bioanal Chem*, 2017, **409**, 6227–6234.

67 S. L. Filbrun and J. D. Driskell, *Analyst*, 2016, **141**, 3851–3857.

68 S. Dominguez-Medina, L. Kisley, L. J. Tauzin, A. Hoggard, B. Shuang, A. S. D. S. Indrasekara, S. Chen, L. Y. Wang, P. J. Derry, A. Liopo, E. R. Zubarev, C. F. Landes and S. Link, *ACS Nano*, 2016, **10**, 2103–2112.

69 K. E. Woods, Y. R. Perera, M. B. Davidson, C. A. Wilks, D. K. Yadav and N. C. Fitzkee, *Journal of Physical Chemistry C*, 2016, **120**, 27944–27953.

70 W. Ma, A. Saccardo, D. Roccatano, D. Aboagye-Mensah, M. Alkaseem, M. Jewkes, F. Di Nezza, M. Baron, M. Soloviev and E. Ferrari, *Nat Commun*, 2018, **9**, 1489.

71 H. Hsieh, J. Dantzler and B. Weigl, *Diagnostics*, 2017, **7**, 29.

72 J. Budd, B. S. Miller, N. E. Weckman, D. Cherkaoui, D. Huang, A. T. Decruz, N. Fongwen, G.-R. Han, M. Broto, C. S. Estcourt, J. Gibbs, D. Pillay, P. Sonnenberg, R. Meurant, M. R. Thomas, N. Keegan, M. M. Stevens, E. Nastouli, E. J. Topol, A. M. Johnson, M. Shahmanesh, A. Ozcan, J. J. Collins, M. Fernandez Suarez, B. Rodriguez, R. W. Peeling and R. A. McKendry, *Nature Reviews Bioengineering*, 2023, **1**, 13–31.

73 T. Huynh, C. E. Anderson, D. J. Gasperino, S. P. Harston, H. V. Hsieh, R. Marzan, J. R. Williford, C. I. Oncina, V. A. Glukhova, D. M. Cate, K. P. Nichols and B. H. Weigl, in *2019 IEEE Global Humanitarian Technology Conference (GHTC)*, IEEE, 2019, pp. 1–4.

74 S. Qian and H. H. Bau, *Anal Biochem*, 2003, **322**, 89–98.

75 M. S. Ragavendar and C. M. Anmol, in *2012 Annual International Conference of the IEEE Engineering in Medicine and Biology Society*, IEEE, 2012, pp. 2408–2411.

76 Z. Liu, J. Hu, A. Li, S. Feng, Z. Qu and F. Xu, *Sens Actuators B Chem*, 2017, **248**, 699–707.

77 N. R. Bennett, J. L. Watson, R. J. Ragotte, A. J. Borst, D. L. See, C. Weidle, R. Biswas, E. L. Shrock, P. J. Y. Leung, B. Huang, I. Goreshnik, R. Ault, K. D. Carr, B. Singer, C. Criswell, D. Vafeados, M. Garcia Sanchez, H. M. Kim, S. Vázquez Torres, S. Chan and D. Baker, 2024, preprint, DOI: 10.1101/2024.03.14.585103.

78 I. Zimmermann, P. Egloff, C. A. J. Hutter, B. T. Kuhn, P. Bräuer, S. Newstead, R. J. P. Dawson, E. R. Geertsma and M. A. Seeger, *Nat Protoc*, 2020, **15**, 1707–1741.

79 P. C. Fridy, Y. Li, S. Keegan, M. K. Thompson, I. Nudelman, J. F. Scheid, M. Oeffinger, M. C. Nussenzweig, D. Fenyö, B. T. Chait and M. P. Rout, *Nat Methods*, 2014, **11**, 1253–1260.

80 J. P. Salvador, N. Vasylieva, I. Gonzalez-Garcia, M. Jin, R. Caster, J. B. Siegel and B. D. Hammock, *ACS Food Science and Technology*, 2022, **2**, 1276–1282.

81 M. Kamel, S. Maher, H. El-Baz, F. Salah, O. Sayyouh and Z. Demerdash, *Trop Med Infect Dis*, 2022, **7**, 1–13.

82 P. Chen, Q. Yang, S. Li, X. Liu, B. Li, J. Zhang, J. Wang, X. Yue and Y. Wang, *Anal Chem*, 2024, **96**, 17602–17611.

83 T. Hattori, M. Umetsu, T. Nakanishi, S. Sawai, S. Kikuchi, R. Asano and I. Kumagai, *Bioconjug Chem*, 2012, **23**, 1934–1944.

84 G. P. Anderson, L. C. Shriver-Lake, J. L. Liu and E. R. Goldman, *Antibodies*, 2022, **11**, 1–10.

85 C. A. Holstein, A. Chevalier, S. Bennett, C. E. Anderson, K. Keniston, C. Olsen, B. Li, B. Bales, D. R. Moore, E. Fu, D. Baker and P. Yager, *Anal Bioanal Chem*, 2016, **408**, 1335–1346.

86 Bioporto, gRAD Lateral Flow, https://bioporto.com/grad/, (accessed 3 January 2025).

87 B. S. Miller, M. R. Thomas, M. Banner, J. Kim, Y. Chen, Q. Wei, D. K. Tseng, Z. S. Göröcs, A. Ozcan, M. M. Stevens and R. A. McKendry, *Biosens Bioelectron*, 2022, **207**, 114133.

88 C. A. Holstein, M. Griffin, J. Hong and P. D. Sampson, *Anal Chem*, 2015, **87**, 9795–9801.

89 J. D. Bishop, H. V. Hsieh, D. J. Gasperino and B. H. Weigl, *Lab Chip*, 2019, **19**, 2486–2499.

90 C. E. Z. Chan, A. H. Y. Chan, A. P. C. Lim and B. J. Hanson, *J Immunol Methods*, 2011, **373**, 79–88.

91 E. R. Gray, J. C. Brookes, C. Caillat, V. Turbé, B. L. J. Webb, L. A. Granger, B. S. Miller, L. E. McCoy, M. El Khattabi, C. T. Verrips, R. A. Weiss, D. M. Duffy, W. Weissenhorn and R. A. McKendry, *ACS Infect Dis*, 2017, **3**, 479–491.

92 C. K. Kariuki and S. Magez, *Protein Expr Purif*, 2021, **185**, 1–9.

93 E. A. Bastos-Soares, R. M. O. Sousa, A. F. Gómez, J. Alfonso, A. M. Kayano, F. B. Zanchi, M. E. Funes-Huacca, R. G. Stábeli, A. M. Soares, S. S. Pereira and C. F. C. Fernandes, *Int J Biol Macromol*, 2020, **165**, 2244–2252.

94 G. Gonzalez-Sapienza, M. A. Rossotti and S. Tabares-da Rosa, *Front Immunol*, 2017, **8**, 1–12.

95 Y. H. Lee, H. Medhi, X. Liu, I. H. Ha, K. T. Nam and H. Ploegh, *ACS Appl Mater Interfaces*, 2023, **15**, 59258–59268.

96 X. Chen, S. Kang, M. A. Ikbal, Z. Zhao, Y. Pan, J. Zuo, L. Gu and C. Wang, *Biosens Bioelectron*, 2022, **202**, 1–10.

97 G. P. Anderson, J. L. Liu, L. C. Shriver-Lake, D. Zabetakis, V. A. Sugiharto, H.-W. Chen, C.-R. Lee, G. N. Defang, S.-J. L. Wu, N. Venkateswaran and E. R. Goldman, *Anal Chem*, 2019, **91**, 9424–9429.

98 G. Bao, M. Tang, J. Zhao and X. Zhu, *EJNMMI Res*, 2021, **11**, 6.

99 M. J. Pollitt, G. Buckton, R. Piper and S. Brocchini, *RSC Adv*, 2015, **5**, 24521–24527.

100 J. S. Gebauer, M. Malissek, S. Simon, S. K. Knauer, M. Maskos, R. H. Stauber, W. Peukert and L. Treuel, *Langmuir*, 2012, **28**, 9673–9679.

101 nanoComposix, Citrate Surface, https://nanocomposix.com/pages/citrate-surface, (accessed 12 December 2024).

102 Bárbara Sofia Fialho Simões, PhD Thesis, University of Birmingham, 2021.

103 B. N. Khlebtsov, R. S. Tumskiy, A. M. Burov, T. E. Pylaev and N. G. Khlebtsov, *ACS Appl Nano Mater*, 2019, **2**, 5020–5028.

104 D. Kim, Y. Kim, S. Hong, J. Kim, N. Heo, M.-K. Lee, S. Lee, B. Kim, I. Kim, Y. Huh and B. Choi, *Sensors*, 2016, **16**, 2154.

105 C. Fang, Z. Chen, L. Li and J. Xia, *J Pharm Biomed Anal*, 2011, **56**, 1035–1040.

106 J. X. Xu, Md. S. Alom, R. Yadav and N. C. Fitzkee, *Nat Commun*, 2022, **13**, 1–11.

107 V. Humblot, F. Tielens, N. B. Luque, H. Hampartsoumian, C. Méthivier and C. M. Pradier, *Langmuir*, 2014, **30**, 203–212.

108 T. Pleiner, M. Bates, S. Trakhanov, C.-T. Lee, J. E. Schliep, H. Chug, M. Böhning, H. Stark, H. Urlaub and D. Görlich, *Elife*, 2015, **4**, 1–21.

109 J. E. Pinto Torres, J. Goossens, J. Ding, Z. Li, S. Lu, D. Vertommen, P. Naniima, R. Chen, S. Muyldermans, Y. G.-J. Sterckx and S. Magez, *Sci Rep*, 2018, **8**, 1–15.

110 D. V. Sotnikov, I. V. Safenkova, A. V. Zherdev, V. G. Avdienko, I. V. Kozlova, S. S. Babayan, V. Ya. Gergert and B. B. Dzantiev, *Applied Sciences*, 2020, **10**, 475.

111 C. Zhang, X. Wu, D. Li, J. Hu, D. Wan, Z. Zhang and B. D. Hammock, *Analytical Methods*, 2021, **13**, 1757–1765.

112 nanoComposix, Carbonate Surface, https://nanocomposix.com/pages/carbonate-surface, (accessed 11 December 2024).

113 B. Saha, T. H. Evers and M. W. J. Prins, *Anal Chem*, 2014, **86**, 8158–8166.

114 A. Kausaite-Minkstimiene, A. Ramanaviciene, J. Kirlyte and A. Ramanavicius, *Anal Chem*, 2010, **82**, 6401–6408.

115 C. Huang, J. Huang, S. Zhu, T. Tang, Y. Chen and F. Qian, *Chem Eng Sci*, 2023, **270**, 118521.

116 Y. Xiang, S. Nambulli, Z. Xiao, H. Liu, Z. Sang, W. P. Duprex, D. Schneidman-Duhovny, C. Zhang and Y. Shi, *Science (1979)*, 2020, **370**, 1479–1484.

117 A. M. Alkilany, S. R. Abulateefeh, K. K. Mills, A. I. Bani Yaseen, M. A. Hamaly, H. S. Alkhatib, K. M. Aiedeh and J. W. Stone, *Langmuir*, 2014, **30**, 13799–13808.

118 D. Prakashan, N. S. Shrikrishna, M. Byakodi, K. Nagamani and S. Gandhi, *J Med Virol*, 2023, **95**, 1–12.

119 M. De Groeve, B. Laukens and P. Schotte, *Microb Cell Fact*, 2023, **22**, 135.

120 A. de Marco, 2022, pp. 145–157.

121 WHO, *Use of SARS-CoV-2 antigen-detection rapid diagnostic tests for COVID-19 self-testing*, .

122 C. E. Anderson, T. Huynh, D. J. Gasperino, L. F. Alonzo, J. L. Cantera, S. P. Harston, H. V. Hsieh, R. Marzan, S. K. McGuire, J. R. Williford, C. I. Oncina, V. A. Glukhova, J. D. Bishop, D. M. Cate, B. D. Grant, K. P. Nichols and B. H. Weigl, *Anal Bioanal Chem*, 2022, **414**, 2607–2618.

123 J. Erickson, B. Goldstein, D. Holowka and B. Baird, *Biophys J*, 1987, **52**, 657–662.

124 H. C. Berg and E. M. Purcell, *Biophys J*, 1977, **20**, 193–219.

125 L. Deng, E. N. Kitova and J. S. Klassen, *J Am Soc Mass Spectrom*, 2013, **24**, 49–56.

126 R. F. Delgadillo, T. C. Mueser, K. Zaleta-Rivera, K. A. Carnes, J. González-Valdez and L. J. Parkhurst, *PLoS One*, 2019, **14**, e0204194.

127 B. S. Miller, C. Parolo, V. Turbé, C. E. Keane, E. R. Gray and R. A. McKendry, *Chemistry - A European Journal*, 2018, **24**, 9783–9787.

128 D. C. Ranawakage, T. Takada and Y. Kamachi, *Sci Rep*, 2019, **9**, 6895.

129 M. Fairhead and M. Howarth, *Methods in Molecular Biology*, 2015, **1266**, 171–184.

130 Z. Sun, J. Lv, X. Liu, Z. Tang, X. Wang, Y. Xu and B. D. Hammock, *Anal Chem*, 2018, **90**, 10628–10634.

131 T. Lakshmipriya, S. C. B. Gopinath and T.-H. Tang, *PLoS One*, 2016, **11**, e0151153.

132 T. Fellows, L. Ho, S. Flanagan, R. Fogel, D. Ojo and J. Limson, *Analyst*, 2020, **145**, 5180–5193.

133 E. Jurrus, D. Engel, K. Star, K. Monson, J. Brandi, L. E. Felberg, D. H. Brookes, L. Wilson, J. Chen, K. Liles, M. Chun, P. Li, D. W. Gohara, T. Dolinsky, R. Konecny, D. R. Koes, J. E. Nielsen, T. Head-Gordon, W. Geng, R. Krasny, G. W. Wei, M. J. Holst, J. A. McCammon and N. A. Baker, *Protein Science*, 2018, **27**, 112–128.

134 M. H. M. Olsson, C. R. SØndergaard, M. Rostkowski and J. H. Jensen, *J Chem Theory Comput*, 2011, **7**, 525–537.

135 X. Fan, J. Wang, X. Zhang, Z. Yang, J.-C. Zhang, L. Zhao, H.-L. Peng, J. Lei and H.-W. Wang, *Nat Commun*, 2019, **10**, 2386.

136 B. N. Khlebtsov, R. S. Tumskiy, A. M. Burov, T. E. Pylaev and N. G. Khlebtsov, *ACS Appl Nano Mater*, 2019, **2**, 5020–5028.

137 S. Qian and H. H. Bau, *Anal Biochem*, 2004, **326**, 211–224.

138 M. Sun, Y. Sun, Y. Yang, M. Zhao, D. Cao, M. Zhang, D. Xia, T. Wang, Y. Gao, S. Wang, H. Wang, X. Cai and T. An, *Int J Biol Macromol*, 2024, **258**, 128896.

139 Z. Li, W. Zhang, Q. Zhang, P. Li and X. Tang, *ACS Nano*, 2023, **17**, 19359–19371.

140 X. Li, P. Qiao, Y. Zhang, G. Liu, M. Zhu, J. Gai and Y. Wan, *Protein Expr Purif*, 2024, **218**, 106441.

141 D. Shan, J. M. Johnson, S. C. Fernandes, H. Suib, S. Hwang, D. Wuelfing, M. Mendes, M. Holdridge, E. M. Burke, K. Beauregard, Y. Zhang, M. Cleary, S. Xu, X. Yao, P. P. Patel, T. Plavina, D. H. Wilson, L. Chang, K. M. Kaiser, J. Nattermann, S. V. Schmidt, E. Latz, K. Hrusovsky, D. Mattoon and A. J. Ball, *Nat Commun*, 2021, **12**, 1931.

142 Y. Wang, Z. Qin, D. R. Boulware, B. S. Pritt, L. M. Sloan, I. J. Gonzalez, D. Bell, R. R. Rees-Channer, P. Chiodini, W. C. W. Chan and J. C. Bischof, *Anal Chem*, 2016, **88**, 11774–11782.

143 W. Wang, S. Srivastava, A. Garg, C. Xiao, S. Hawks, J. Pan, N. Duggal, G. Isaacman-VanWertz, W. Zhou, L. C. Marr and P. J. Vikesland, *Environ Sci Technol*, 2024, **58**, 4926–4936.

144 C. N. Loynachan, PhD thesis, Imperial College London, 2018.

145 I. Bosch, H. de Puig, M. Hiley, M. Carré-Camps, F. Perdomo-Celis, C. F. Narváez, D. M. Salgado, D. Senthoor, M. O'Grady, E. Phillips, A. Durbin, D. Fandos, H. Miyazaki, C.-W. Yen, M. Gélvez-Ramírez, R. V. Warke, L. S. Ribeiro, M. M. Teixeira, R. P. Almeida, J. E. Muñóz-Medina, J. E. Ludert, M. L. Nogueira, T. E. Colombo, A. C. B. Terzian, P. T. Bozza, A. S. Calheiros, Y. R. Vieira, G. Barbosa-Lima, A. Vizzoni, J. Cerbino-Neto, F. A. Bozza, T. M. L. Souza, M. R. O. Trugilho, A. M. B. de Filippis, P. C. de Sequeira, E. T. A. Marques, T. Magalhaes, F. J. Díaz, B. N. Restrepo, K. Marín, S. Mattar, D. Olson, E. J. Asturias, M. Lucera, M. Singla, G. R. Medigeshi, N. de Bosch, J. Tam, J. Gómez-Márquez, C. Clavet, L. Villar, K. Hamad-Schifferli and L. Gehrke, *Sci Transl Med*, 2017, **9**, 29.

146 E. Jurrus, D. Engel, K. Star, K. Monson, J. Brandi, L. E. Felberg, D. H. Brookes, L. Wilson, J. Chen, K. Liles, M. Chun, P. Li, D. W. Gohara, T. Dolinsky, R. Konecny, D. R. Koes, J. E. Nielsen, T. Head-Gordon, W. Geng, R. Krasny, G. W. Wei, M. J. Holst, J. A. McCammon and N. A. Baker, *Protein Science*, 2018, **27**, 112–128.

147 J. Jumper, R. Evans, A. Pritzel, T. Green, M. Figurnov, O. Ronneberger, K. Tunyasuvunakool, R. Bates, A. Žídek, A. Potapenko, A. Bridgland, C. Meyer, S. A. A. Kohl, A. J. Ballard, A. Cowie, B. Romera-Paredes, S. Nikolov, R. Jain, J. Adler, T. Back, S. Petersen, D. Reiman, E. Clancy, M. Zielinski, M. Steinegger, M. Pacholska, T. Berghammer, S. Bodenstein, D. Silver, O. Vinyals, A. W. Senior, K. Kavukcuoglu, P. Kohli and D. Hassabis, *Nature*, 2021, **596**, 583–589.

148 M. Mirdita, K. Schütze, Y. Moriwaki, L. Heo, S. Ovchinnikov and M. Steinegger, *Nat Methods*, 2022, **19**, 679–682.

8 Appendix

8.1 Protein and nucleotide sequences used

VHHV nanobody with C-terminus hexahistidine tag

MGQVQLVETGGGLVQPGGSLRLSCAASGFTFSSYAMGWARQVPGKGLEWVSYIYSDGSTEYQDSVKG
RFTISRDNAKSTVYLQMNSLKPEDTAVYYCATEGSLGGWGRDFGSWGQGTQVTVSSLEHHHHHH*

ATGGGCCAGGTGCAACTGGTTGAGACCGGTGGCGGTCTGGTGCAACCGGGCGGTAGCCTGCGTCT
GAGCTGCGCGGCGAGCGGTTTCACCTTTAGCAGCTATGCGATGGGTTGGGCGCGTCAGGTGCCGG
GTAAAGGTCTGGAGTGGGTTAGCTACATCTATAGCGACGGCAGCACCGAATACCAAGATAGCGTTAA
GGGTCGTTTCACCATTAGCCGTGACAACGCGAAAAGCACCGTGTATCTGCAGATGAACAGCCTGAAG
CCGGAGGATACCGCGGTTTACTATTGCGCGACCGAAGGTAGCCTGGGCGGTTGGGGCCGTGACTT
TGGTAGCTGGGGCCAGGGTACCCAAGTGACCGTTAGCAGCCTCGAGCACCACCACCACCACCACT
GA

VHHE nanobody with C-terminus hexahistidine tag

MGQVQLVETGGGFVQPGGSLRLSCAASGVTLDYYAIGWFRQAPGKEREGVSCIGSSDGRTYYSDSVKG
RFTISRDNAKNTVYLQMNSLKPEDTAVYYCALTVGTYYSGNYHYTCSDDMDYWGKGTLVTVSSLEHHHH
HH*

ATGGGCCAAGTTCAGCTAGTAGAAACAGGTGGAGGGTTCGTGCAGCCGGGTGGTTCTCTGCGTCTCT
CCTGCGCGGCTAGCGGCGTTACCCTGGACTACTACGCGATCGGCTGGTTTCGCCAGGCGCCGGG
TAAGGAGCGCGAGGGTGTGAGCTGTATTGGCTCGTCTGACGGCCGTACTTACTACTCCGACAGCGTT
AAGGGCCGTTTCACCATCTCCCGTGACAACGCGAAAAACACCGTCTACCTGCAAATGAACAGCCTG
AAACCGGAAGATACCGCAGTTTATTACTGCGCCTTGACCGTTGGCACCTATTACAGCGGTAATTATCA
CTATACGTGCAGCGATGATATGGATTATTGGGGTAAGGGTACGTTGGTGACCGTGTCGAGCCTCGAGC
ACCACCACCACCACCACTGA

Nb6 nanobody with C-terminus hexahistidine tag

MGQVQLVESGGGLVQAGGSLRLSCAASGIIFGRNAMGWYRQAPGKERELVAGITRRGSITYYADSVKGR
FTISRDNAKNTVYLQMNSLKPEDTAVYYCAADPASPAPGDYWGQGTQVTVSSLEHHHHHH*

ATGGGCCAAGTTCAGCTAGTAGAATCAGGTGGAGGGTTGGTCCAAGCCGGTGGTAGCCTGCGTCTCT
CTTGTGCGGCGTCCGGCATTATCTTCGGCCGCAACGCAATGGGTTGGTATCGTCAGGCACCGGGCA
AAGAACGCGAGCTGGTGGCGGGTATCACCCGTCGCGGTTCGATCACCTATTACGCCGACTCCGTGA
AAGGCCGTTTTACCATTAGCCGTGACAACGCGAAGAACACTGTTTACCTGCAAATGAATTCTCTGAAG
CCAGAGGATACCGCAGTTTACTACTGCGCGGCTGATCCGGCGAGCCCGGCTCCGGGCGACTATTG
GGGTCAGGGTACGCAGGTTACGGTGAGCAGCCTCGAGCACCACCACCACCACCACTGA

Cys-VHHV nanobody with C-terminus hexahistidine tag

CMGQVQLVETGGGLVQPGGSLRLSCAASGFTFSSYAMGWARQVPGKGLEWVSYIYSDGSTEYQDSVK
GRFTISRDNAKSTVYLQMNSLKPEDTAVYYCATEGSLGGWGRDFGSWGQGTQVTVSSLEHHHHHH*

TGTATGGGCCAGGTGCAACTGGTTGAGACCGGTGGCGGTCTGGTGCAACCGGGCGGTAGCCTGCG
TCTGAGCTGCGCGGCGAGCGGTTTCACCTTTAGCAGCTATGCGATGGGTTGGGCGCGTCAGGTGCC

GGGTAAAGGTCTGGAGTGGGTTAGCTACATCTATAGCGACGGCAGCACCGAATACCAAGATAGCGTT
AAGGGTCGTTTCACCATTAGCCGTGACAACGCGAAAAGCACCGTGTATCTGCAGATGAACAGCCTGA
AGCCGGAGGATACCGCGGTTTACTATTGCGCGACCGAAGGTAGCCTGGGCGGTTGGGGCCGTGAC
TTTGGTAGCTGGGGCCAGGGTACCCAAGTGACCGTTAGCAGCCTCGAGCACCACCACCACCACCA
CTGA

VHHV-Cys nanobody with C-terminus hexahistidine tag

MGQVQLVETGGGLVQPGGSLRLSCAASGFTFSSYAMGWARQVPGKGLEWVSYIYSDGSTEYQDSVKG
RFTISRDNAKSTVYLQMNSLKPEDTAVYYCATEGSLGGWGRDFGSWGQGTQVTVSSLEHHHHHHC*

ATGGGCCAGGTGCAACTGGTTGAGACCGGTGGCGGTCTGGTGCAACCGGGCGGTAGCCTGCGTCT
GAGCTGCGCGGCGAGCGGTTTCACCTTTAGCAGCTATGCGATGGGTTGGGCGCGTCAGGTGCCGG
GTAAAGGTCTGGAGTGGGTTAGCTACATCTATAGCGACGGCAGCACCGAATACCAAGATAGCGTTAA
GGGTCGTTTCACCATTAGCCGTGACAACGCGAAAAGCACCGTGTATCTGCAGATGAACAGCCTGAAG
CCGGAGGATACCGCGGTTTACTATTGCGCGACCGAAGGTAGCCTGGGCGGTTGGGGCCGTGACTT
TGGTAGCTGGGGCCAGGGTACCCAAGTGACCGTTAGCAGCCTCGAGCACCACCACCACCACCACT
GTTGA

VHHV2 nanobody with C-terminus hexahistidine tag

MGQVQLVETGGGLVQPGGSLRLSCAASGFTFSSYAMGWARQVPGKGLEWVSYIYSDGSTEYQDSVKG
RFTISRDNAKSTVYLQMNSLKPEDTAVYYCATEGSLGGWGRDFGSWGQGTQVTVSSGGGGSGGGGS
GGGGSQVQLVETGGGLVQPGGSLRLSCAASGFTFSSYAMGWARQVPGKGLEWVSYIYSDGSTEYQDS
VKGRFTISRDNAKSTVYLQMNSLKPEDTAVYYCATEGSLGGWGRDFGSWGQGTQVTVSSLEHHHHHH
*

ATGGGCCAGGTGCAACTGGTTGAGACCGGTGGCGGTCTGGTGCAACCGGGCGGTAGCCTGCGTCT
GAGCTGCGCGGCGAGCGGTTTCACCTTTAGCAGCTATGCGATGGGTTGGGCGCGTCAGGTGCCGG
GTAAAGGTCTGGAGTGGGTTAGCTACATCTATAGCGACGGCAGCACCGAATACCAAGATAGCGTTAA
GGGTCGTTTCACCATTAGCCGTGACAACGCGAAAAGCACCGTGTATCTGCAGATGAACAGCCTGAAG
CCGGAGGATACCGCGGTTTACTATTGCGCGACCGAAGGTAGCCTGGGCGGTTGGGGCCGTGACTT
TGGTAGCTGGGGCCAGGGTACCCAAGTGACCGTTAGCAGCGGCGGAGGTGGATCTGGCGGAGGT
GGATCGGGCGGAGGTGGATCACAGGTGCAACTGGTTGAGACCGGTGGCGGTCTGGTGCAACCGG
GCGGTAGCCTGCGTCTGAGCTGCGCGGCGAGCGGTTTCACCTTTAGCAGCTATGCGATGGGTTGGG
CGCGTCAGGTGCCGGGTAAAGGTCTGGAGTGGGTTAGCTACATCTATAGCGACGGCAGCACCGAAT
ACCAAGATAGCGTTAAGGGTCGTTTCACCATTAGCCGTGACAACGCGAAAAGCACCGTGTATCTGCA
GATGAACAGCCTGAAGCCGGAGGATACCGCGGTTTACTATTGCGCGACCGAAGGTAGCCTGGGCG
GTTGGGGCCGTGACTTTGGTAGCTGGGGCCAGGGTACCCAAGTGACCGTTAGCAGCCTCGAGCAC
CACCACCACCACCACTGA

VHHV3 nanobody with C-terminus hexahistidine tag

MGQVQLVETGGGLVQPGGSLRLSCAASGFTFSSYAMGWARQVPGKGLEWVSYIYSDGSTEYQDSVKG
RFTISRDNAKSTVYLQMNSLKPEDTAVYYCATEGSLGGWGRDFGSWGQGTQVTVSSGGGGSGGGGS
GGGGSQVQLVETGGGLVQPGGSLRLSCAASGFTFSSYAMGWARQVPGKGLEWVSYIYSDGSTEYQDS
VKGRFTISRDNAKSTVYLQMNSLKPEDTAVYYCATEGSLGGWGRDFGSWGQGTQVTVSSGGGGSGGG
GSGGGGSQVQLVETGGGLVQPGGSLRLSCAASGFTFSSYAMGWARQVPGKGLEWVSYIYSDGSTEYQ
DSVKGRFTISRDNAKSTVYLQMNSLKPEDTAVYYCATEGSLGGWGRDFGSWGQGTQVTVSSLEHHHH
HH*

ATGGGCCAGGTGCAACTGGTTGAGACCGGTGGCGGTCTGGTGCAACCGGGCGGTAGCCTGCGTCT
GAGCTGCGCGGCGAGCGGTTTCACCTTTAGCAGCTATGCGATGGGTTGGGCGCGTCAGGTGCCGG
GTAAAGGTCTGGAGTGGGTTAGCTACATCTATAGCGACGGCAGCACCGAATACCAAGATAGCGTTAA
GGGTCGTTTCACCATTAGCCGTGACAACGCGAAAAGCACCGTGTATCTGCAGATGAACAGCCTGAAG
CCGGAGGATACCGCGGTTTACTATTGCGCGACCGAAGGTAGCCTGGGCGGTTGGGGCCGTGACTT
TGGTAGCTGGGGCCAGGGTACCCAAGTGACCGTTAGCAGCGGCGGAGGTGGATCTGGCGGAGGT
GGATCGGGCGGAGGTGGATCACAGGTGCAACTGGTTGAGACCGGTGGCGGTCTGGTGCAACCGG
GCGGTAGCCTGCGTCTGAGCTGCGCGGCGAGCGGTTTCACCTTTAGCAGCTATGCGATGGGTTGGG
CGCGTCAGGTGCCGGGTAAAGGTCTGGAGTGGGTTAGCTACATCTATAGCGACGGCAGCACCGAAT
ACCAAGATAGCGTTAAGGGTCGTTTCACCATTAGCCGTGACAACGCGAAAAGCACCGTGTATCTGCA
GATGAACAGCCTGAAGCCGGAGGATACCGCGGTTTACTATTGCGCGACCGAAGGTAGCCTGGGCG
GTTGGGGCCGTGACTTTGGTAGCTGGGGCCAGGGTACCCAAGTGACCGTTAGCAGCGGCGGAGGT
GGATCTGGCGGAGGTGGATCGGGCGGAGGTGGATCACAGGTGCAACTGGTTGAGACCGGTGGCG
GTCTGGTGCAACCGGGCGGTAGCCTGCGTCTGAGCTGCGCGGCGAGCGGTTTCACCTTTAGCAGC
TATGCGATGGGTTGGGCGCGTCAGGTGCCGGGTAAAGGTCTGGAGTGGGTTAGCTACATCTATAGCG
ACGGCAGCACCGAATACCAAGATAGCGTTAAGGGTCGTTTCACCATTAGCCGTGACAACGCGAAAA
GCACCGTGTATCTGCAGATGAACAGCCTGAAGCCGGAGGATACCGCGGTTTACTATTGCGCGACCG
AAGGTAGCCTGGGCGGTTGGGGCCGTGACTTTGGTAGCTGGGGCCAGGGTACCCAAGTGACCGTT
AGCAGCCTCGAGCACCACCACCACCACCACTGA

VHHV-AVI-HRV3 with C-terminus hexahistidine tag

MGQVQLVETGGGLVQPGGSLRLSCAASGFTFSSYAMGWARQVPGKGLEWVSYIYSDGSTEYQDSVKG
RFTISRDNAKSTVYLQMNSLKPEDTAVYYCATEGSLGGWGRDFGSWGQGTQVTVSSGLNDIFEAQKIE
WHELEVLFQGPLEHHHHHH*

ATGGGCCAGGTGCAACTGGTTGAGACCGGTGGCGGTCTGGTGCAACCGGGCGGTAGCCTGCGTCT
GAGCTGCGCGGCGAGCGGTTTCACCTTTAGCAGCTATGCGATGGGTTGGGCGCGTCAGGTGCCGG
GTAAAGGTCTGGAGTGGGTTAGCTACATCTATAGCGACGGCAGCACCGAATACCAAGATAGCGTTAA
GGGTCGTTTCACCATTAGCCGTGACAACGCGAAAAGCACCGTGTATCTGCAGATGAACAGCCTGAAG
CCGGAGGATACCGCGGTTTACTATTGCGCGACCGAAGGTAGCCTGGGCGGTTGGGGCCGTGACTT
TGGTAGCTGGGGCCAGGGTACCCAAGTGACCGTTAGCAGCGGCCTGAACGACATCTTCGAGGCTC
AGAAAATCGAATGGCACGAACTGGAAGTGCTGTTTCAG

VHHV2-AVI-HRV3 with C-terminus hexahistidine tag

MGQVQLVETGGGLVQPGGSLRLSCAASGFTFSSYAMGWARQVPGKGLEWVSYIYSDGSTEYQDSVKG
RFTISRDNAKSTVYLQMNSLKPEDTAVYYCATEGSLGGWGRDFGSWGQGTQVTVSSGGGGSGGGGS
GGGGSQVQLVETGGGLVQPGGSLRLSCAASGFTFSSYAMGWARQVPGKGLEWVSYIYSDGSTEYQDS
VKGRFTISRDNAKSTVYLQMNSLKPEDTAVYYCATEGSLGGWGRDFGSWGQGTQVTVSSGGGGSGGG
GSGGGGSQVQLVETGGGLVQPGGSLRLSCAASGFTFSSYAMGWARQVPGKGLEWVSYIYSDGSTEYQ
DSVKGRFTISRDNAKSTVYLQMNSLKPEDTAVYYCATEGSLGGWGRDFGSWGQGTQVTVSSLEHHHH
HH*

ATGGGCCAGGTGCAACTGGTTGAGACCGGTGGCGGTCTGGTGCAACCGGGCGGTAGCCTGCGTCT
GAGCTGCGCGGCGAGCGGTTTCACCTTTAGCAGCTATGCGATGGGTTGGGCGCGTCAGGTGCCGG
GTAAAGGTCTGGAGTGGGTTAGCTACATCTATAGCGACGGCAGCACCGAATACCAAGATAGCGTTAA
GGGTCGTTTCACCATTAGCCGTGACAACGCGAAAAGCACCGTGTATCTGCAGATGAACAGCCTGAAG
CCGGAGGATACCGCGGTTTACTATTGCGCGACCGAAGGTAGCCTGGGCGGTTGGGGCCGTGACTT
TGGTAGCTGGGGCCAGGGTACCCAAGTGACCGTTAGCAGCGGCGGAGGTGGATCTGGCGGAGGT

GGATCGGGCGGAGGTGGATCACAGGTGCAACTGGTTGAGACCGGTGGCGGTCTGGTGCAACCGG
GCGGTAGCCTGCGTCTGAGCTGCGCGGCGAGCGGTTTCACCTTTAGCAGCTATGCGATGGGTTGGG
CGCGTCAGGTGCCGGGTAAAGGTCTGGAGTGGGTTAGCTACATCTATAGCGACGGCAGCACCGAAT
ACCAAGATAGCGTTAAGGGTCGTTTCACCATTAGCCGTGACAACGCGAAAAGCACCGTGTATCTGCA
GATGAACAGCCTGAAGCCGGAGGATACCGCGGTTTACTATTGCGCGACCGAAGGTAGCCTGGGCG
GTTGGGGCCGTGACTTTGGTAGCTGGGGCCAGGGTACCCAAGTGACCGTTAGCAGCGGCCTGAAC
GACATCTTCGAGGCTCAGAAAATCGAATGGCACGAACTGGAAGTGCTGTTTCAGGGCCCGCTCGAG
CACCACCACCACCACCACTGA

VHHV3-AVI-HRV3 with C-terminus hexahistidine tag

MGQVQLVETGGGLVQPGGSLRLSCAASGFTFSSYAMGWARQVPGKGLEWVSYIYSDGSTEYQDSVKG
RFTISRDNAKSTVYLQMNSLKPEDTAVYYCATEGSLGGWGRDFGSWGQGTQVTVSSGGGGSGGGGS
GGGGSQVQLVETGGGLVQPGGSLRLSCAASGFTFSSYAMGWARQVPGKGLEWVSYIYSDGSTEYQDS
VKGRFTISRDNAKSTVYLQMNSLKPEDTAVYYCATEGSLGGWGRDFGSWGQGTQVTVSSGGGGSGGG
GSGGGGSQVQLVETGGGLVQPGGSLRLSCAASGFTFSSYAMGWARQVPGKGLEWVSYIYSDGSTEYQ
DSVKGRFTISRDNAKSTVYLQMNSLKPEDTAVYYCATEGSLGGWGRDFGSWGQGTQVTVSSGLNDIFE
AQKIEWHELEVLFQGPLEHHHHHH*

ATGGGCCAGGTGCAACTGGTTGAGACCGGTGGCGGTCTGGTGCAACCGGGCGGTAGCCTGCGTCT
GAGCTGCGCGGCGAGCGGTTTCACCTTTAGCAGCTATGCGATGGGTTGGGCGCGTCAGGTGCCGG
GTAAAGGTCTGGAGTGGGTTAGCTACATCTATAGCGACGGCAGCACCGAATACCAAGATAGCGTTAA
GGGTCGTTTCACCATTAGCCGTGACAACGCGAAAAGCACCGTGTATCTGCAGATGAACAGCCTGAAG
CCGGAGGATACCGCGGTTTACTATTGCGCGACCGAAGGTAGCCTGGGCGGTTGGGGCCGTGACTT
TGGTAGCTGGGGCCAGGGTACCCAAGTGACCGTTAGCAGCGGCGGAGGTGGATCTGGCGGAGGT
GGATCGGGCGGAGGTGGATCACAGGTGCAACTGGTTGAGACCGGTGGCGGTCTGGTGCAACCGG
GCGGTAGCCTGCGTCTGAGCTGCGCGGCGAGCGGTTTCACCTTTAGCAGCTATGCGATGGGTTGGG
CGCGTCAGGTGCCGGGTAAAGGTCTGGAGTGGGTTAGCTACATCTATAGCGACGGCAGCACCGAAT
ACCAAGATAGCGTTAAGGGTCGTTTCACCATTAGCCGTGACAACGCGAAAAGCACCGTGTATCTGCA
GATGAACAGCCTGAAGCCGGAGGATACCGCGGTTTACTATTGCGCGACCGAAGGTAGCCTGGGCG
GTTGGGGCCGTGACTTTGGTAGCTGGGGCCAGGGTACCCAAGTGACCGTTAGCAGCGGCGGAGGT
GGATCTGGCGGAGGTGGATCGGGCGGAGGTGGATCACAGGTGCAACTGGTTGAGACCGGTGGCG
GTCTGGTGCAACCGGGCGGTAGCCTGCGTCTGAGCTGCGCGGCGAGCGGTTTCACCTTTAGCAGC
TATGCGATGGGTTGGGCGCGTCAGGTGCCGGGTAAAGGTCTGGAGTGGGTTAGCTACATCTATAGCG
ACGGCAGCACCGAATACCAAGATAGCGTTAAGGGTCGTTTCACCATTAGCCGTGACAACGCGAAAA
GCACCGTGTATCTGCAGATGAACAGCCTGAAGCCGGAGGATACCGCGGTTTACTATTGCGCGACCG
AAGGTAGCCTGGGCGGTTGGGGCCGTGACTTTGGTAGCTGGGGCCAGGGTACCCAAGTGACCGTT
AGCAGCGGCCTGAACGACATCTTCGAGGCTCAGAAAATCGAATGGCACGAACTGGAAGTGCTGTTT
CAGGGCCCGCTCGAGCACCACCACCACCACCACTGA